

1       MEASUREMENT OF ELECTROWEAK PRODUCTION OF  
2                   SAME-SIGN W BOSON PAIRS WITH ATLAS

3                   William Kennedy DiClemente

4                   A DISSERTATION  
5                   in  
6                   Physics and Astronomy

7                   Presented to the Faculties of The University of Pennsylvania  
8                   in Partial Fulfillment of the Requirements for the Degree of Doctor of Philosophy  
9                   2019 *Last compiled: April 2, 2019*

10                  

---

  
11                  I. Joseph Kroll, Professor, Physics  
12                   Supervisor of Dissertation

13                  

---

  
14                  Joshua Klein, Professor, Physics  
15                   Graduate Group Chairperson

16                  Dissertation Committee  
17                  Elliot Lipeles, Associate Professor, Physics  
18                  Christopher Mauger, Associate Professor, Physics  
19                  Burt Ovrut, Professor, Physics  
20                  Justin Khoury, Professor, Physics  
21                  I. Joseph Kroll, Professor, Physics

22 MEASUREMENT OF ELECTROWEAK PRODUCTION OF SAME-SIGN W BOSON PAIRS  
23 WITH ATLAS

24 COPYRIGHT  
25 2019  
26 William Kennedy DiClemente

27 All rights reserved.

---

## Acknowledgements

---

29 It would be impossible to properly thank everyone who has helped me along this journey; nevertheless  
30 I will attempt to be as thorough as possible.

31 First and foremost, I would like to thank my family. My parents, Gwynne Kennedy and John  
32 DiClemente, for always believing in me and listening to me attempt to explain what it is I am  
33 working on. My many feline friends past and present—Stella, Lucky, Julia, Elise, Lucille, Tweedie,  
34 Ruby, and Sylvie—for keeping me warm during the winter holidays back home. My girlfriend Amber  
35 Wright, for tolerating me these past few months and doing your best to keep me relatively sane.

36 Thanks to my advisor Joe Kroll for guiding me through the past six years at Penn; your advice  
37 both in physics and in life has been invaluable to my growth as a physicist and a person. Additional  
38 thanks to the rest of the ATLAS faculty at Penn: Elliot Lipeles, Evelyn Thomson, and Brig Williams.  
39 The amount of open collaboration between students and faculty irrespective of who works for whom  
40 has helped me learn so much.

41 I would also like to extend thanks to two important figures from before my time at Penn. Firstly,  
42 to Gardner Friedlander, my high school physics teacher who first got me interested in the subject.  
43 You were the first to show me how I could use a pen and paper to predict events in real life, a  
44 fascination of mine that has continued into my work here, just with much harder math and on a more  
45 fundamental scale. Secondly, my undergraduate research advisor, Al Goshaw, at Duke University.  
46 You gave a college freshman who thought particle physics was “pretty neat” the opportunity to do  
47 meaningful research with one of the leading collaborations in the field. Without either of you, I  
48 likely would not be in this position today.

49 Thanks to the members of the Inner Detector Alignment group, including but not limited to  
50 Anthony Morley for his guidance on my qualification task, and to Shih-Chieh Hsu, Pierfrancesco  
51 Butti, Matthias Danninger, Salvador Marti, and Steffen Henkelmann for numerous collaborative

52 alignment efforts.

53 The entire  $W^\pm W^\pm jj$  13 TeV analysis group, and those with whom I worked most closely: Philip  
54 Sommer, Emily Duffield, Rustem Ospanov, Stefanie Todt, and Liqing Zhang. Special thanks to  
55 Rustem for pushing me to find my voice in the analysis. Thanks to my  $W^\pm W^\pm jj$  HL-LHC prospects  
56 collaborators Claire Lee and Karolos Potamiamos.

57 Lastly, thanks to my fellow Penn ATLAS graduate students, Bijan Haney, Joey Reichert, Khilesh  
58 Mistry, Leigh Schaefer, Bill Balunas, Christian Herwig, Elodie Ressegue, and many more, for lis-  
59 tening to my ramblings, answering my many questions, and for countless entertaining lunchtime  
60 discussions.

# ABSTRACT

62 MEASUREMENT OF ELECTROWEAK PRODUCTION OF SAME-SIGN W BOSON PAIRS  
 63 WITH ATLAS

William Kennedy DiClemente

J. Kroll

66 This thesis presents two studies of electroweak same-sign  $W^\pm W^\pm jj$  scattering with the ATLAS  
 67 experiment. The first is a measurement of the fiducial cross section at  $\sqrt{s} = 13$  TeV using  $36.1 \text{ fb}^{-1}$   
 68 of data recorded in 2015 and 2016. The electroweak production is observed with a signal significance  
 69 of  $6.9\sigma$ , and the fiducial cross section is measured to be  $\sigma_{\text{meas}}^{\text{fid}} = 2.91^{+0.51}_{-0.47}(\text{stat})^{+0.28}_{-0.29}(\text{sys}) \text{ fb}$ . The  
 70 second is a study on the future prospects for the  $W^\pm W^\pm jj$  process at the planned High-Luminosity  
 71 LHC, with a projected  $\sqrt{s} = 14$  TeV and  $3000 \text{ fb}^{-1}$  of data. The expected electroweak production  
 72 cross section is determined with a total uncertainty of 6%, and the purely longitudinal scattering  
 73 component is extracted with an expected significance of  $1.8\sigma$ . Additionally, some time is taken to  
 74 detail the alignment of the ATLAS Inner Detector subsystems, as good alignment performance is  
 75 essential for making high-quality physics measurements.

---

# Contents

---

77	Acknowledgements	iii
78	Abstract	v
79	Contents	vi
80	List of Tables	x
81	List of Figures	xiii
82	Preface	xx
83	1 Introduction	1
84	2 Theoretical Framework	3
85	2.1 Introduction to the Standard Model . . . . .	3
86	2.2 Electroweak symmetry breaking and the Higgs boson . . . . .	6
87	2.3 Electroweak vector boson scattering . . . . .	9
88	3 LHC and the ATLAS Detector	13
89	3.1 The Large Hadron Collider . . . . .	13
90	3.2 The ATLAS Detector . . . . .	16
91	3.2.1 The Inner Detector . . . . .	17
92	3.2.1.1 Pixel Detector . . . . .	18
93	3.2.1.2 Semiconductor Tracker . . . . .	19
94	3.2.1.3 Transition Radiation Tracker . . . . .	19

95	3.2.2	The Calorimeters . . . . .	20
96	3.2.2.1	Liquid Argon Calorimeter . . . . .	21
97	3.2.2.2	Tile Calorimeter . . . . .	22
98	3.2.3	The Muon Spectrometer . . . . .	23
99	3.3	Particle reconstruction . . . . .	23
100	3.3.1	Track reconstruction . . . . .	24
101	3.3.2	Electron reconstruction . . . . .	25
102	3.3.3	Muon reconstruction . . . . .	28
103	<b>4</b>	<b>Alignment of the ATLAS Inner Detector</b>	<b>32</b>
104	4.1	The alignment method . . . . .	33
105	4.1.1	Alignment levels . . . . .	37
106	4.1.2	Alignment coordinate systems . . . . .	38
107	4.2	Early 2015 alignment of the ATLAS detector . . . . .	40
108	4.2.1	June alignment procedure . . . . .	40
109	4.2.2	Alignment results . . . . .	42
110	4.2.2.1	Residual distributions from collisions . . . . .	43
111	4.2.2.2	Track parameter resolution from cosmic rays . . . . .	47
112	4.2.3	Error scaling . . . . .	48
113	4.3	Level 2 alignment of the TRT . . . . .	50
114	4.4	Momentum bias from sagitta deformations . . . . .	51
115	4.4.1	Sagitta bias monitoring with electron $E/p$ . . . . .	52
116	4.4.1.1	Measuring $\langle E/p \rangle$ . . . . .	53
117	4.4.1.2	Results in 13TeV data . . . . .	55
118	<b>5</b>	<b>Measurement of same-sign <math>WW</math> production at <math>\sqrt{s} = 13</math> TeV with ATLAS</b>	<b>58</b>
119	5.0.1	Experimental overview of vector boson scattering . . . . .	58
120	5.0.2	Same-sign $W^\pm W^\pm$ scattering . . . . .	59
121	5.0.3	Overview of backgrounds . . . . .	61
122	5.1	Data and Monte Carlo samples . . . . .	63
123	5.1.1	Monte Carlo samples . . . . .	64
124	5.2	Object and event selection . . . . .	66
125	5.2.1	Object selection . . . . .	66

---

126	5.2.1.1	Muon candidate selection . . . . .	66
127	5.2.1.2	Electron candidate selection . . . . .	67
128	5.2.1.3	Jet candidate selection . . . . .	69
129	5.2.1.4	Treatment of overlapping objects . . . . .	69
130	5.2.2	Signal event selection . . . . .	70
131	5.3	Background estimations . . . . .	71
132	5.3.1	Estimation of the $WZ$ background . . . . .	72
133	5.3.2	Estimation of the $V\gamma$ background . . . . .	73
134	5.3.3	Estimation of backgrounds from charge misidentification . . . . .	75
135	5.3.3.1	Validation of the charge misidentification estimate . . . . .	77
136	5.3.4	Estimation of non-prompt backgrounds with the fake-factor method . . . . .	78
137	5.3.4.1	Overview of the default fake-factor method . . . . .	79
138	5.3.4.2	The fake-factor with $p_T^{\text{cone}}$ . . . . .	81
139	5.3.4.3	Application of the fake-factor . . . . .	82
140	5.3.4.4	Systematic uncertainties . . . . .	86
141	5.3.4.5	Results of the fake-factor . . . . .	87
142	5.3.4.6	Validation of the fake-factor . . . . .	90
143	5.3.5	Reduction of $WZ$ background using custom overlap removal . . . . .	90
144	5.4	Cross section measurement . . . . .	95
145	5.4.1	Maximum likelihood fit . . . . .	95
146	5.4.2	Definition of the fiducial volume . . . . .	97
147	5.4.3	Cross section extraction . . . . .	98
148	5.5	Summary of uncertainties . . . . .	99
149	5.5.1	Experimental uncertainties . . . . .	99
150	5.5.2	Theoretical uncertainties . . . . .	100
151	5.5.2.1	Uncertainties from EWK-QCD interference . . . . .	102
152	5.6	Results . . . . .	103
153	5.7	Beyond the Standard Model extensions of $W^\pm W^\pm jj$ . . . . .	105
154	5.7.1	Doubly charged Higgs bosons . . . . .	106
155	5.7.2	Anomalous quartic couplings . . . . .	108
156	<b>6</b>	<b>Prospects for same-sign <math>WW</math> at the High Luminosity LHC</b>	<b>111</b>
157	6.0.3	Analysis Overview . . . . .	112

158	6.1	Theoretical motivation . . . . .	113
159	6.1.1	Experimental sensitivity to longitudinal polarization . . . . .	113
160	6.2	Monte Carlo samples . . . . .	114
161	6.3	Background estimations . . . . .	115
162	6.3.1	Truth-based isolation . . . . .	116
163	6.4	Object and event selection . . . . .	117
164	6.4.1	Object selection . . . . .	117
165	6.4.2	Event selection . . . . .	117
166	6.5	Selection optimization . . . . .	118
167	6.5.1	Random grid search algorithm . . . . .	119
168	6.5.2	Inputs to the optimization . . . . .	120
169	6.5.3	Results of the optimization . . . . .	121
170	6.6	Results . . . . .	122
171	6.6.1	Event yields . . . . .	122
172	6.6.2	Uncertainties . . . . .	126
173	6.6.3	Cross section measurement . . . . .	127
174	6.6.4	Longitudinal scattering significance . . . . .	127
175	<b>7</b>	<b>Conclusion</b>	<b>131</b>
176	<b>A</b>	<b>Additional material on <math>W^\pm W^\pm jj</math> measurement at <math>\sqrt{s} = 13\text{TeV}</math></b>	<b>132</b>
177	A.1	Impact of experimental uncertainty on MC background estimations . . . . .	132
178	A.2	Pre-fit event yields . . . . .	134
179	<b>B</b>	<b>Additional material on <math>W^\pm W^\pm jj</math> prospects at the HL-LHC</b>	<b>135</b>
180	B.1	Truth isolation . . . . .	135
181	B.1.1	TRUTH1++ derivations . . . . .	136
182	B.1.2	Check of truth-based isolation . . . . .	137
183	B.1.3	Loose isolation working point . . . . .	137
184	B.2	Plots of other optimization variables . . . . .	140
185	<b>Bibliography</b>		<b>142</b>

---

## List of Tables

---

187	4.1	The four alignment levels for each of the detector subsystems and their components (first introduced in Section 3.2). The total number of alignable structures and degrees of freedom (DoF) to be aligned are given for each level. . . . .	39
188			
189			
190	4.2	Summary of the highest level of alignment applied to each ID subsystem when deriving the June alignment. . . . .	42
191			
192	4.3	Estimated value of the error scaling term $b$ for each subdetector component with the June alignment. . . . .	49
193			
194	5.1	Predicted cross sections for EQK and QCD production of diboson processes relevant to VBS at $\sqrt{s} = 13\text{TeV}$ using the SHERPA MC generator. The numbers for the $W^\pm W^\pm jj$ process are bolded. Leptons are required to have $p_T \geq 25\text{ GeV}$ and lie within $ \eta  \leq 2.5$ with $m_{ll} > 20\text{ GeV}$ , and at least two jets are required with $p_T \geq 30\text{ GeV}$ and $ \eta  < 4.5$ . The VBS contributions are enhanced by requiring the dijet invariant mass $m_{jj} > 500\text{ GeV}$ and dijet separation $\Delta y_{jj} > 2.4$ . . . . .	61
195			
196			
197			
198			
199			
200	5.2	Summary of MC samples used in the analysis. . . . .	65
201			
202	5.3	Muon selection criteria. All muons are required to pass the preselection (top), and then either the signal (middle) or loose (bottom) criteria is applied to the preselected electrons. . . . .	67
203			
204	5.4	Electron selection criteria. All electrons are required to pass the preselection (top), and then either the signal (middle) or loose (bottom) criteria is applied to the preselected electrons. . . . .	68
205			
206	5.5	Jet selection criteria. All jets are required to pass the above selection in order to be used in the analysis. . . . .	69
207			
208	5.6	Summary of the overlap removal procedure used in the analysis. If the criteria in the “check” column is met, in the “result” column, the object on the left of the arrow is removed in favor of the object on the right. . . . .	70
209			
210			
211	5.7	Summary of trigger requirements for electrons and muons for $\sqrt{s} = 13\text{TeV}$ data collected in 2015 and 2016. At least one of the triggers must be satisfied. . . . .	71
212			
213	5.8	The signal event selection. . . . .	72
214	5.9	Event yields in the $WZ$ control region before normalization. All lepton flavor channels are combined. . . . .	73
215			
216	5.10	Selection criteria for the $V\gamma$ control region. . . . .	74

217	5.11	Event yields in the $V\gamma$ control region. The $V\gamma$ scale factor of 1.77 is calculated by scaling up the $Z\gamma$ and $Z$ +jets backgrounds to account for the difference between the data and predicted total background. . . . .	75
220	5.12	Selection criteria for the same-sign inclusive validation region. . . . .	78
221	5.13	Event selection for the dijet region used for calculating the fake-factor. The selected lepton can pass either the nominal (signal) or loose selections. In the case of the nominal leptons, the $p_T > 27$ GeV requirement is replaced with $p_T > 15$ GeV. . . . .	84
224	5.14	Values of the fake-factor in each $p_T$ bin and for each individual systematic source. . . . .	89
225	5.15	Estimated yields for the fake lepton background. The estimated yield is shown in the first column together with the statistical uncertainty followed by the systematic uncertainties from variations of the the fake-factors within their statistical (stat.) and systematic (syst.) uncertainties. The labels $f_e$ and $f_\mu$ indicate the fake-factors for electrons and muons, respectively. . . . .	89
230	5.16	Selection criteria for the same-sign top fakes validation region. . . . .	90
231	5.17	Custom OR definition. Leptons must pass this selection in order to be counted for the trilepton veto. . . . .	94
233	5.18	Definition of the fiducial volume. . . . .	97
234	5.19	Impact of various systematic effects on the fiducial cross section measurement. The impact of a given source of uncertainty is computed by performing the fit with the corresponding nuisance parameter varied up or down by one standard deviation from its nominal value. . . . .	100
238	5.20	List of sources of experimental uncertainties on the reconstruction of physics objects. . . . .	101
239	5.21	Impact of experimental uncertainties for the $W^\pm W^\pm jj$ EWK processes in all channels. . . . .	101
240	5.22	Impact of experimental uncertainties for the $WZ$ process in all channels. . . . .	101
241	5.23	The set of generator level cuts used for generating the interference samples with <code>MadGraph</code> . . . . .	102
242	5.24	Cross sections for each different $W^\pm W^\pm jj$ production mode (inclusive, EWK only, QCD only, and interference only) generated using <code>MadGraph</code> . The cross sections are calculated using a minimal set of generator level cuts from events where the $W$ decays to a muon. . . . .	103
245	5.25	Table of the data and prediction event yields in the signal region after the fit. Numbers are shown for the six lepton flavor and charge channels and for all channels combined. The background estimations from the fake-factor are included in the “Non-prompt” category, and backgrounds from $V\gamma$ production and electron charge misidentification are combined in the “ $e/\gamma$ conversions” category. Finally, $ZZ$ , $VVV$ , and $t\bar{t}V$ backgrounds are combined in the “Other prompt” category. . . . .	104
251	5.26	Observed 95% confidence limits set by CMS at $\sqrt{s} = 13$ TeV on the nine dimension-eight operators that modify the $WWWW$ QGC listed in Equation 5.33. . . . .	110
253	6.1	Summary of MC samples used in the analysis. . . . .	115
254	6.2	Truth-based isolation requirements for electrons and muons. . . . .	116
255	6.3	Summary of the signal event selection. . . . .	118
256	6.4	Updates to the $W^\pm W^\pm jj$ event selection criteria after optimization. Cuts not listed remain unchanged from the default selection in Table 6.3. . . . .	122
258	6.5	Signal and background event yields using the default event selection for an integrated luminosity of $\mathcal{L} = 3000 \text{ fb}^{-1}$ . Events containing a fake or charge-flipped electron are removed from their respective sources and combined into a single entry each. . . . .	123
261	6.6	Signal and background event yields using the optimized event selection for an integrated luminosity of $\mathcal{L} = 3000 \text{ fb}^{-1}$ . Events containing a fake or charge-flipped electron are removed from their respective sources and combined into a single entry each. . . . .	124
264	6.7	Summary of estimated experimental and rate uncertainties. . . . .	126

---

265	A.1	Impact of experimental uncertainties for the $W^\pm W^\pm jj$ QCD processes in all channels . . . . .	132
266	A.2	Impact of experimental uncertainties for triboson process in all channels. . . . .	133
267	A.3	Impact of experimental uncertainties for $t\bar{t}V$ processes in all channels. . . . .	133
268	A.4	Impact of experimental uncertainties for the $W\gamma$ process in all channels. . . . .	133
269	A.5	Impact of experimental uncertainties for the $Z\gamma$ process in all channels. . . . .	133
270	A.6	Impact of experimental uncertainties for the $ZZ$ process in all channels. . . . .	134
271	A.7	Table of the data and prediction event yields in the signal region before the fit. Numbers 272 are shown for the six lepton flavor and charge channels and for all channels combined. 273 Here the $WZ$ background yields are normalized to the data in the $WZ$ control region. The 274 background estimations from the fake-factor are included in the “Non-prompt” category, 275 and backgrounds from $V\gamma$ production and electron charge misidentification are combined 276 in the “ $e/\gamma$ conversions” category. Finally, $ZZ$ , $VVV$ , and $t\bar{t} + V$ backgrounds are 277 combined in the “Other prompt” category. . . . .	134
278	B.1	Event yields prior to applying any form of truth-based isolation criteria. . . . .	135
279	B.2	Event yields after applying a test version of the truth-based isolation. . . . .	136
280	B.3	Electron and muon isolation requirements for the loose working point. . . . .	137
281	B.4	Event yields broken down by sample and by background type using the loose isolation 282 workingpoint. Events containing a fake or charge-flipped electron are removed from their 283 respective sample and added to the “fakes” and “charge flip” rows, respectively. Errors 284 include statistical uncertainty and estimated systematic rate uncertainty based on the 285 background process. . . . .	138
286	B.5	Event yields broken down by background type using the tight isolation workingpoint. 287 Events containing a fake or charge-flipped electron are removed from their respective 288 sample and added to the “fakes” and “charge flip” rows, respectively. Errors include sta- 289 tistical uncertainty and estimated systematic rate uncertainty based on the background process. . . . .	139

---

## List of Figures

---

292    2.1	Summary of several Standard Model total and fiducial production cross section measurements compared to the corresponding theoretical predictions calculated at NLO or higher. The dark colored error bar represents the statistical uncertainty, and the light colored error bar represents the full uncertainty (including systematic and luminosity uncertainties). The data/theory ratio, luminosity used and reference for each measurement are also shown. . . . .	4
298    2.2	An illustration of the potential term $V(\phi)$ in Equation 2.6 for the cases where $\mu^2 > 0$ (left) and $\mu^2 < 0$ (right). The right-hand plot shows the Higgs potential, or “Mexican hat potential”, with the minimum at $ \phi  = \sqrt{-\frac{\mu^2}{\lambda}}$ rather than at $ \phi  = 0$ as in the left-hand plot. . . . .	7
302    2.3	A graphical representation of the EWSB mechanism involving the $SU(2) \times U(1)$ bosons and the Higgs field. The $W^\pm$ and $Z$ bosons each obtain mass by eating a degree of freedom (dof) from the Higgs field, and in the process gain a longitudinal polarization mode, while the photon stays massless (with two dof) and the SM Higgs boson $h$ remains. . . . .	9
306    2.4	Feynman diagram of a generic VBS process. The gray circle represents any interaction with two incoming and two outgoing vector bosons, including any of the diagrams shown in Figures 2.5 and 2.6. . . . .	10
309    2.5	Leading order $VV \rightarrow VV$ Feynman diagrams involving EWK bosons. From left to right: $s$ -channel, $t$ -channel, $u$ -channel, and the quartic gauge coupling. . . . .	10
311    2.6	Leading order $VV \rightarrow VV$ Feynman diagrams involving the exchange of a Higgs boson. From left to right: $s$ -channel, $t$ -channel, and $u$ -channel. . . . .	10
313    2.7	Cross sections in nanobarns for five different longitudinally polarized VBS processes as a function of center of mass energy $\sqrt{s}$ . Without a Higgs boson (left), the cross sections grow unbounded with $\sqrt{s}$ . With a 120 GeV Higgs boson (right), the cross sections no longer diverge. . . . .	12
317    3.1	The CERN accelerator complex. For LHC collisions, protons are accelerated by the Linac 2 (purple), the PSB (light purple), the PS (magenta), and the SPS (light blue) before entering the LHC ring (dark blue). . . . .	14
320    3.2	Peak instantaneous luminosity delivered to ATLAS during 13TeV $pp$ data taking as a function of time. . . . .	15
322    3.3	Integrated luminosity collected by ATLAS as a function of time at 13TeV from 2015-2018. . . . .	15

323    3.4	Distribution of the mean number of interactions per bunch crossing for the 2015 and 324    2016 $pp$ collision data at 13TeV. . . . .	16
325    3.5	Cut-away view of the ATLAS detector. . . . .	17
326    3.6	The barrel layers of the Pixel, SCT, and TRT detectors making up the Inner Detector. .	18
327    3.7	Cut-away view of the ATLAS calorimeter systems. . . . .	20
328    3.8	Diagram of the cells within the LAr barrel. The accordion structure can be seen in the 329    cut-away view. . . . .	22
330    3.9	Measured LH electron ID efficiencies in $Z \rightarrow ee$ events for the <b>LooseLH</b> (blue), <b>MediumLH</b> 331    (red), and <b>TightLH</b> (black) working points as a function of electron $E_T$ . The bottom 332    panel shows data-to-simulation ratios. . . . .	26
333    3.10	Measured isolation efficiencies for the <b>LooseTrackOnly</b> (black), <b>Loose</b> (red), <b>GradientLoose</b> 334    (blue), and <b>Gradient</b> (yellow) working points as a function of electron $E_T$ . The bottom 335    panel shows data-to-simulation ratios. . . . .	28
336    3.11	Muon reconstruction efficiencies in $Z \rightarrow \mu\mu$ events for the <b>Loose</b> (yellow), <b>Medium</b> (red), 337    and <b>Tight</b> (blue) ID working points as a function of muon $\eta$ . The drop in efficiency for 338 <b>Medium</b> and <b>Tight</b> muons in the range $ \eta  < 0.1$ is due to the exclusion of CT and ME 339    muons, which are used to recover acceptance in this region. Collision data (solid points) 340    is compared to simulation (open points) and the ratio is in the lower panel. . . . .	30
341    3.12	Muon isolation efficiencies in $Z \rightarrow \mu\mu$ events for the <b>Loose</b> (left) and <b>GradientLoose</b> 342    (right) working points as a function of muon $p_T$ . Collision data (black) is compared to 343    simulation (red) and the ratio is in the lower panel. . . . .	31
344    4.1	Graphical representation of the effect of a misaligned detector element. The reconstructed 345    particle track (dashed arrow) differs from the actual trajectory of the particle (solid 346    arrow) due to a shift in the third detector element. The cyan lines represent the track- 347    to-hit residuals. . . . .	33
348    4.2	Graphical representation of a track-hit residual in the local $x$ direction according to 349    Equation 4.2. The sensor in this example measures a particle hit in the local $x$ and $y$ 350    directions, with each having its own residual. . . . .	34
351    4.3	Flow chart depicting the ID alignment chain. . . . .	36
352    4.4	A schematic representation of the Inner Detector in the longitudinal plane with the global 353    coordinate system overlaid on top. The Pixel detector and IBL are shown in blue, the 354    SCT in green, and the TRT in red. The local coordinates for each subdetector module 355    are inset on the right. . . . .	39
356    4.5	The $d_0$ distributions with respect to the reconstructed primary vertex using 13TeV col- 357    lision data sample rconstructed using the June (black) and March (green) alignments. 358    The data is compared to a MC simulation using a perfect detector geometry (red). The 359    distributions are normalized to the same number of entries. . . . .	43
360    4.6	Local $x$ (left) and local $y$ (right) residual distributions of the IBL planar sensors using 361    13TeV collision data sample reconstructed using the June (black) and March (green) 362    alignments. The data is compared to a MC simulation using a perfect detector geometry 363    (red). The distributions are normalized to the same number of entries. . . . .	44
364    4.7	The mean of the local $x$ (left) and local $y$ (right) residual distributions as a function of 365    the global $z$ position of each IBL module using 13TeV collision data sample reconstruc- 366    ted using the June (black) and March (green) alignments. The data is compared to a MC 367    simulation using a perfect detector geometry (red). . . . .	45

368	4.8	Local $x$ (left) and local $y$ (right) residual distributions for the Pixel barrel (excluding the IBL) using 13TeV collision data sample reconstructed using the June (black) and March (green) alignments. The data is compared to a MC simulation using a perfect detector geometry (red). The distributions are normalized to the same number of entries. . . . .	45
372	4.9	Local $x$ (left) and local $y$ (right) residual distributions for the Pixel endcaps using 13TeV collision data sample reconstructed using the June (black) and March (green) alignments. The data is compared to a MC simulation using a perfect detector geometry (red). The distributions are normalized to the same number of entries. . . . .	46
376	4.10	Local $x$ residual distributions for the SCT barrel (left) and end-caps (right) using 13TeV collision data sample reconstructed using the June (black) and March (green) alignments. The data is compared to a MC simulation using a perfect detector geometry (red). The distributions are normalized to the same number of entries. . . . .	46
380	4.11	Residual distributions for the TRT barrel (left) and end-caps (right) using 13TeV collision data sample reconstructed using the June (black) and March (green) alignments. The data is compared to a MC simulation using a perfect detector geometry (red). The distributions are normalized to the same number of entries. . . . .	47
384	4.12	Representation of splitting a single cosmic ray track passing through the entire detector (left) into two separate tracks (right). . . . .	48
386	4.13	Distribution of the difference in the impact parameter $\Delta d_0$ (left) and charge over transverse momentum $\Delta q/p_T$ (right) between the two cosmic ray split tracks. The June (black) and March (green) alignments are compared. The distributions are normalized to the same number of entries. . . . .	48
390	4.14	Pull distributions in local $x$ (left) and $y$ (right) for the IBL using 13TeV collision data sample after applying the error scaling. . . . .	49
392	4.15	Residual means by straw layer in two TRT $\phi$ -sectors affected by a tilt misalignment. The tilts in each of the three modules are clearly visible in the red points representing the reconstructed data prior to alignment. After four iterations of L2 alignment, the residual means in the gray points are flat. . . . .	50
396	4.16	Two dimensional map of residuals in the first layer of the TRT barrel vs $z$ and $\phi$ . Each bin represents the mean of a Gaussian fit to the TRT residuals in that bin. The map on the left is after the L3 (wire-by-wire) alignment of the TRT performed in 2010, and the map on the right is after the L2 alignment at the end of 2015. The $z$ -axis for both plots use the same scale. . . . .	51
401	4.17	Representation of a curl distortion in the detector. The image represents a cutaway view of the transverse plane of the barrel region. The deformation is represented by the red arrows, and the impact on the reconstructed positive (blue) and negative (green) tracks are shown. The dashed lines represent the true particle trajectories, and the solid lines represent the reconstructed trajectories. . . . .	52
406	4.18	Geometric definition of the sagitta $s$ in relation to the length of the chord $l$ and the radius $R$ of a circular arc. . . . .	53
408	4.19	$E/p$ distributions of electrons and positrons in two different $\eta\phi$ bins of the detector. The left hand plot is taken from a region with no momentum bias where $\langle E/p \rangle^+ = \langle E/p \rangle^-$ , while the right hand plot shows an 8% disagreement in $\langle E/p \rangle$ between electrons and positrons. . . . .	54
412	4.20	Sagitta bias in the $\sqrt{s} = 13\text{TeV}$ data collected by ATLAS in 2016 as a function of $\eta$ and $\phi$ for the prompt (left) and reprocessed (right) alignments using the $E/p$ method. . . . .	56
414	4.21	Sagitta bias in the $\sqrt{s} = 13\text{TeV}$ data collected by ATLAS in 2016 projected along $\eta$ for the prompt (gray) and reprocessed (blue) alignments using the $E/p$ method. . . . .	56

416	4.22 Sagitta bias in the $\sqrt{s} = 13\text{TeV}$ data collected by ATLAS in 2017 as a function of $\eta$ and $\phi$ in reconstructed electrons (left) and after two iterations of momentum corrections (right) from the $E/p$ method. . . . .	56
419	4.23 Sagitta bias in the $\sqrt{s} = 13\text{TeV}$ data collected by ATLAS in 2017 projected along $\eta$ in reconstructed electrons (gray) and after one (red) and two (blue) iterations of momentum corrections from the $E/p$ method. . . . .	57
422	5.1 Tree-level Feynman diagrams for VBS EWK $VVjj$ production including triple gauge couplings involving $W$ and/or $Z$ bosons (top left and top middle), quartic gauge coupling (top right), or the exchange of a Higgs boson ( $s$ -channel bottom left and $t$ -channel bottom right). The labels are quarks ( $q$ ), fermions ( $f$ ), and gauge bosons ( $V = W, Z$ ). . . . .	60
426	5.2 Tree-level Feynman diagrams for non-VBS EWK $VVjj$ production. The labels are quarks ( $q$ ), fermions ( $f$ ), and gauge bosons ( $V = W, Z$ ). . . . .	60
428	5.3 Tree-level Feynman diagrams for QCD $VVjj$ production. The labels are quarks ( $q$ ), fermions ( $f$ ), and gauge bosons ( $V = W, Z$ ). . . . .	60
430	5.4 Leading order Feynman diagrams for VBS EWK production of $W^\pm W^\pm jj$ events. The leftmost diagram contains a quartic gauge coupling vertex, and the rightmost diagram contains an exchange of a Higgs boson. . . . .	62
433	5.5 $W^\pm W^\pm jj$ VBS event topology containing two leptons (1 and 2) with the same electric charge, two neutrinos, and two forward tagging jets (3 and 4) with large rapidity separation $\Delta y$ . . . . .	62
436	5.6 Generator level comparisons at $\sqrt{s} = 7\text{TeV}$ of dijet invariant mass ( $m_{jj}$ , left) and dijet rapidity ( $\Delta y_{jj}$ , right) in EWK (red) and QCD (blue) $W^\pm W^\pm jj$ events with no selection cuts applied. . . . .	63
439	5.7 ATLAS event display of a $pp \rightarrow W^+W^+ \rightarrow \mu^+\nu_\mu\mu^+\nu_\mu jj$ event. The muons are represented by the red lines travelling from the ID through the MS, and the forward jets are represented by the blue cones with yellow energy deposits in the calorimeters. The direction of the $E_T^{\text{miss}}$ in the transverse plane is indicated by the gray dashed line in the inset image. . . . .	64
444	5.8 Leading lepton $p_T$ (left) and $\eta$ (right) distributions in the $WZ$ control region before normalization. All lepton channels are combined. . . . .	73
446	5.9 Trilepton invariant mass $m_{lll}$ distribution in the $WZ$ control region before normalization. All lepton channels are combined. . . . .	74
448	5.10 Charge misidentification rates for electrons as a function of $ \eta $ and $p_T$ . Rates are calculated from $Z \rightarrow e^+e^-$ MC after applying scale factors to approximate the charge mis-ID rates in data. . . . .	76
451	5.11 Dilepton invariant mass distribution $m_{ll}$ for the $ee$ channel in the same-sign inclusive VR. . . . .	78
452	5.12 $p_T$ distributions for the leading (left) and subleading (right) electron for the $ee$ channel in the same-sign inclusive VR. In these plots, the cut requiring $m_{ee}$ to fall within the $Z$ mass window has been inverted in order to test the modelling away from the $Z$ peak. . . . .	79
455	5.13 Graphical representation of how the fake factor method is used to estimate the fake background in a given $NN$ region. . . . .	80
457	5.14 $\Delta p_T$ distributions for nominal (blue) and loose (red) muons in simulated $t\bar{t}$ events. Each muon has been matched to a truth-level jet. Both distributions are normalized to unit area. . . . .	82
460	5.15 $\Delta p_T$ distributions for muons (top) and electrons (bottom) in simulated $t\bar{t}$ events. Each lepton has been matched to a truth-level jet, and that truth jet has had its $p_T$ corrected to include all truth muons within a cone of $\Delta R < 0.4$ . The nominal leptons are in black. $\Delta p_T$ is calculated for the loose leptons using $p_T$ (red) and $p_T + p_T^{\text{cone}}$ (blue). . . . .	83

464	5.16 Distributions of $p_T^{\text{cone}}/p_T$ for nominal (black) and loose (red) muons in simulated $t\bar{t}$ events.	84
465	5.17 The measured fake-factor as a function of muon $p_T + p_T^{\text{cone}}$ . The error bars represent the statistical uncertainty only.	85
466		
467	5.18 The measured fake-factor as a function of electron $p_T + p_T^{\text{cone}}$ in the central ( $ \eta  < 1.37$ , blue) and forward ( $ \eta  > 1.37$ , red) regions of the detector. The error bars represent the statistical uncertainty only.	86
468		
469		
470	5.19 Systematic variations in the fake-factor as a function of muon $p_T + p_T^{\text{cone}}$ . The individual fake-factors obtained for each systematic variation are displayed with their statistical uncertainties.	87
471		
472		
473	5.20 Systematic variations in the fake-factor as a function of electron $p_T + p_T^{\text{cone}}$ in the central ( $ \eta  < 1.37$ , top) and forward ( $ \eta  > 1.37$ , bottom) regions of the detector. The individual fake-factors obtained for each systematic variation are displayed with their statistical uncertainties.	88
474		
475		
476		
477	5.21 Distributions of the subleading lepton $p_T$ in the same-sign top fakes VR for $\mu^\pm\mu^\pm$ events (top right), $e^\pm e^\pm$ events (top left), $\mu^\pm e^\pm$ events (bottom left), and all events combined (bottom right). All errors are statistical only.	91
478		
479		
480	5.22 Pseudorapidity ( $\eta$ ) distributions of truth muons (top) and electrons (bottom) for Sherpa $W^\pm W^\pm jj$ and $WZ$ MC samples. The blue vertical lines represent the allowed $\eta$ range for each lepton flavor. The numbers correspond to the number of raw MC events that fall within and outside of the allowed $\eta$ range for each MC sample.	92
481		
482		
483		
484	5.23 Distributions of $p_{T,\text{ratio}}(\mu, j)$ for EWK and QCD $W^\pm W^\pm jj$ signal (black) and $WZ$ background (teal) for truth-matched third muons in events that pass the trilepton veto. Both distributions are normalized to unit area. The associated efficiency curves are on the right where efficiency is defined as the percentage of total events that would pass a cut on $p_{T,\text{ratio}}(\mu, j)$ at a given value on the $x$ -axis.	92
485		
486		
487		
488		
489	5.24 Distributions of $\Delta R(\mu, j)$ for EWK and QCD $W^\pm W^\pm jj$ signal (black) and $WZ$ background (teal) for truth-matched third muons in events that pass the trilepton veto. Both distributions are normalized to unit area. The associated efficiency curves are on the right where efficiency is defined as the percentage of total events that would pass a cut on $\Delta R(\mu, j)$ at a given value on the $x$ -axis.	93
490		
491		
492		
493		
494	5.25 Distributions of $p_{T,\text{ratio}}(e, j)$ for EWK and QCD $W^\pm W^\pm jj$ signal (black) and $WZ$ background (teal) for truth-matched third electrons in events that pass the trilepton veto. Both distributions are normalized to unit area. The associated efficiency curves are on the right where efficiency is defined as the percentage of total events that would pass a cut on $p_{T,\text{ratio}}(e, j)$ at a given value on the $x$ -axis.	93
495		
496		
497		
498		
499	5.26 Two-dimensional plots of $p_{T,\text{ratio}}(\mu, j)$ vs $\Delta R(\mu, j)$ for truth-matched third muons in events that pass the trilepton veto for EWK and QCD $W^\pm W^\pm jj$ signal (left) and $WZ$ background (right). The blue overlay indicates the area in which the third leptons will pass the custom OR and result in the event failing the trilepton veto.	94
500		
501		
502		
503	5.27 Visual representation of the different kinematic regions relevant to the cross section measurement. The acceptance factor $\mathcal{A}$ converts from the truth level total phase space to the truth level fiducial region, and the efficiency correction $\mathcal{C}$ translates the fiducial region in to the reconstruction level signal region.	98
504		
505		
506		

507	5.28 The dijet invariant mass $m_{jj}$ distributions for data and predicted signal and background in the signal region after the fit. The shaded band represents the statistical and systematic uncertainties added in quadrature. Note that the bins have been scaled such that they represent the number of events per 100 GeV in $m_{jj}$ . The background estimations from the fake-factor are included in the “Non-prompt” category, and backgrounds from $V\gamma$ production and electron charge misidentification are combined in the “ $e/\gamma$ conversions” category. Finally, $ZZ$ , $VVV$ , and $t\bar{t}+V$ backgrounds are combined in the “Other prompt” category. . . . .	104
515	5.29 The event yields for data and predicted signal and background in the $WZ$ and low- $m_{jj}$ control regions after the fit. The shaded band represents the statistical and systematic uncertainties added in quadrature. The background estimations from the fake-factor are included in the “Non-prompt” category, and backgrounds from $V\gamma$ production and electron charge misidentification are combined in the “ $e/\gamma$ conversions” category. Finally, $ZZ$ , $VVV$ , and $t\bar{t}V$ backgrounds are combined in the “Other prompt” category. . . . .	105
521	5.30 Comparison of the measured $W^\pm W^\pm jj$ EWK fiducial cross section with theoretical calculations from <b>SHERPA v2.2.2</b> and <b>POWHEG-BOX v2</b> . The light orange band represents the total experimental uncertainty on the measured value, and the dark orange hashed band is the statistical uncertainty. For the simulations, the light blue band represents the total theoretical uncertainty, and the dark blue hashed band are the scale uncertainties. The theory predictions do not include the interference between the EWK and QCD production. . . . .	106
528	5.31 CMS observed and expected upper limits for the $H^{\pm\pm} \rightarrow W^\pm W^\pm$ cross section at 95% CL at $\sqrt{s} = 13\text{TeV}$ as a function of $H^{\pm\pm}$ mass. The region above the observed limit is excluded by the measurement. . . . .	107
531	5.32 ATLAS observed and expected upper limits for the $H^{\pm\pm} H^{\mp\mp} \rightarrow W^\pm W^\pm W^\mp W^\mp$ cross section at 95% CL at $\sqrt{s} = 13\text{TeV}$ as a function of $H^{\pm\pm}$ mass. The region above the observed limit is excluded by the measurement. . . . .	108
534	5.33 Invariant mass distributions of the $2l2\nu$ system in $pp \rightarrow e^+\nu_e\mu^+\nu_\mu jj$ events at LO and NLO with the <b>VBFNLO</b> MC generator. SM predictions are compared to those with the anomalous coupling $\frac{f_{T,1}}{\Lambda^4} = 200\text{TeV}^{-4}$ . The left plot shows the differential cross section for each prediction, and the right plot shows the $K$ -factors for the SM and anomalous coupling predictions as well as the cross section ratio between the anomalous coupling and SM predictions at LO and NLO. . . . .	110
540	6.1 Comparison of the leading (left) and subleading (right) lepton $p_T$ distributions for purely longitudinal (LL, black) and mixed polarization (LT+TT, cyan) $W^\pm W^\pm jj$ events. . . . .	113
542	6.2 Comparison of the azimuthal dijet separation ( $ \Delta\phi_{jj} $ ) for purely longitudinal (LL, black) and mixed polarization (LT+TT, cyan) $W^\pm W^\pm jj$ events. . . . .	114
544	6.3 A visual representation of a two-dimensional rectangular grid (left) and a random grid (right) in variables $x$ and $y$ . The signal events are the black circles, and the red squares are the background events. Each intersection of gray dashed lines represents a cut point to be evaluated by the optimization. . . . .	120
548	6.4 Leading (top) and subleading (bottom) jet $p_T$ distributions. The default and optimized cuts are represented by the red and green dashed lines, respectively. The $W^\pm W^\pm jj$ EWK signal (black points) is normalized to the same area as the sum of the backgrounds (colored histogram). . . . .	123
552	6.5 Lepton-jet centrality distribution. The default and optimized cuts are represented by the red and green dashed lines, respectively. The $W^\pm W^\pm jj$ EWK signal (black points) is normalized to the same area as the sum of the backgrounds (colored histogram). . . . .	124

---

555    6.6	$p_T$ distributions for the leading jet using the default (left) and optimized (right) event 556    selections for all channels combined. . . . .	125
557    6.7	$p_T$ distributions for the subleading jet using the default (left) and optimized (right) event 558    selections for all channels combined. . . . .	125
559    6.8	$p_T$ distributions for lepton-jet centrality $\zeta$ using the default (left) and optimized (right) 560    event selections for all channels combined. . . . .	126
561    6.9	Projections of the statistical (black), theoretical (blue), systematic (yellow), and total 562    (red) uncertainties on the measured cross section as a function of integrated luminosity 563    using the optimized event selection. . . . .	128
564    6.10	Dijet azimuthal separation ( $ \Delta\phi_{jj} $ ) for the low $m_{jj}$ region ( $520 < m_{jj} < 1100$ GeV, top) 565    and the high $m_{jj}$ region ( $m_{jj} > 1100$ GeV, bottom). The purely longitudinal (LL, gray) 566    is plotted separately from the mixed and transverse (LT+TT, cyan) polarizations. . . . .	129
567    6.11	Projections of the expected longitudinal scattering significance as a function of inte- 568    grated luminosity when considering all sources of uncertainties (black) or only statistical 569    uncertainties (red). . . . .	130
570    B.1	Number of truth particles within $\Delta R < 0.4$ of a selected muon or electron using the 571    ATLAS standard TRUTH1 (left) and the custom TRUTH1++ (right) derivations in $t\bar{t}$ sim- 572    ulation. The complete truth record is stored in the TRUTH1++ derivation, and this is best 573    seen in the first bin, where the lepton has no nearby truth particles. . . . .	136
574    B.2	Leading lepton $p_T$ distribution. The default and optimized cuts are represented by the 575    red and green dashed lines, respectively. The $W^\pm W^\pm jj$ EWK signal (black points) is 576    normalized to the same area as the sum of the backgrounds (colored histogram). . . . .	140
577    B.3	Dilepton invariant mass distribution. The default and optimized cuts are represented by 578    the red and green dashed lines, respectively. The $W^\pm W^\pm jj$ EWK signal (black points) 579    is normalized to the same area as the sum of the backgrounds (colored histogram). . . . .	140
580    B.4	Dijet invariant mass distribution. The default and optimized cuts are represented by the 581    red and green dashed lines, respectively. The $W^\pm W^\pm jj$ EWK signal (black points) is 582    normalized to the same area as the sum of the backgrounds (colored histogram). . . . .	141

---

## Preface

---

584 This thesis presents the major highlights of my work with the ATLAS experiment as a graduate  
585 student at the University of Pennsylvania from Fall of 2013 until early Spring of 2019.

586 The first step of working on the experiment is to complete a *qualification task* in order to be  
587 included on the author list of ATLAS publications. These tasks are an opportunity to contribute  
588 to the experiment as a whole, such as maintaining detector hardware or monitoring physics perfor-  
589 mance. For my qualification task, I worked with the Inner Detector Alignment group which works  
590 to make sure we have accurate knowledge of the locations of each and every sensor in the tracking  
591 detector. My qualification task involved investigating a possible momentum bias in the Monte Carlo  
592 (MC) simulated data. The MC is supposed to be reconstructed with a perfect detector geometry  
593 which should in principle be free of any momentum biases. Ultimately I determined that the size of  
594 the biases were small enough to be negligible compared to what is seen in the real data, and that  
595 they could be corrected for if necessary.

596 My work with the alignment group would continue for the duration of my time here at Penn. In  
597 early 2015, at the start of the LHC’s second data-taking run (Run 2), I assisted with the validation  
598 of the first set of alignment constants using  $\sqrt{s} = 13$  TeV proton-proton collision data. At this point  
599 I took over the responsibility of alignment of the TRT subdetector. The TRT was aligned to high  
600 accuracy in Run 1, and over the course of my time working on alignment, the TRT never required  
601 a straw-by-straw alignment; however it did require a module-level alignment at the end of 2015.  
602 My final responsibility in the alignment group was monitoring momentum biases using the energy-  
603 momentum ratio ( $E/p$ ) of electrons. For the large data reprocessing, the  $E/p$  method served as a  
604 cross check to a similar method using  $Z$  boson events for monitoring and aligning out momentum  
605 biases in the detector. The results from both methods were also used in the uncertainties for the  
606 tracking measurements.

607 On the analysis side, I had previous experience in Standard Model (SM) electroweak physics  
608 from my time as an undergraduate at Duke University, and it remained a point of interest for  
609 me in graduate school. As such, I was happy to work with fellow Penn students on the cross  
610 section measurement of SM  $WZ$  diboson production with the early  $\sqrt{s} = 13$  TeV ATLAS data.  
611 My contribution to the analysis was primarily on the software side, as I maintained and updated  
612 the analysis framework. While the  $WZ$  measurement is not covered by this thesis, it provided me  
613 with invaluable analysis experience in electroweak physics, as well as a detailed understanding of a  
614 major background to many diboson processes. The results for this analysis can be found published  
615 in Physics Letters B in 2016 [1].

616 The final two analyses I worked on involved the scattering of same-sign  $W$  bosons, and they make  
617 up the majority of this thesis. The first analysis is a measurement of the  $W^\pm W^\pm jj$  cross section  
618 at  $\sqrt{s} = 13$  TeV. This measurement along with that of the CMS collaboration represent the first  
619 observation of the  $W^\pm W^\pm jj$  scattering process. My primary contribution to the analysis is in the  
620 estimation of the fake lepton background, where we implemented a brand new version of the fake-  
621 factor method using particle isolation variables. I also did a preliminary study of the interference  
622 between electroweak and strong production of  $W^\pm W^\pm jj$  events, assisted in the production of data  
623 samples for use with the analysis framework, and used my familiarity with the  $WZ$  process to  
624 optimize the rejection of this background. Ultimately the results of this optimization were not  
625 included in the final result; however, it is still covered in the thesis in the hopes that it will be useful  
626 for similar analyses in the future. The formal publication for this measurement will likely be coming  
627 out within the next few months.

628 The second  $W^\pm W^\pm jj$  analysis is a study on the prospects for a measurement of the process at the  
629 upgraded High-Luminosity LHC, scheduled to begin operation in 2026. Here my main contribution  
630 was an optimization of the event selection using a Random Grid Search algorithm. Through the  
631 optimization we expect to take advantage of the higher center of mass energy and greater volume of  
632 data and tighten certain selection cuts to increase the strength of the  $W^\pm W^\pm jj$  signal. In addition, I  
633 once again maintained and updated the analysis framework and produced the group's data samples,  
634 and I also developed a truth-based particle isolation criteria in order to reduce contributions from  
635 backgrounds involving the top quark. The results of this prospects study will be published as a part  
636 of the annual Yellow Report for the High-Luminosity LHC.

637

Will K. DiClemente  
Philadelphia, February 2019

# CHAPTER 1

## Introduction

640 The Large Hadron Collider (LHC) at CERN is the most powerful collider experiment in the world.  
641 At the time of its construction, the largest unanswered question in the Standard Model (SM) was  
642 the mechanism behind electroweak symmetry breaking (EWSB). As a result, one of the primary  
643 goals of the experiment is to learn as much as possible about this mechanism. Thus far, the LHC  
644 has succeeded in discovering a particle consistent with the long-awaited Higgs boson. In addition,  
645 measurements of many SM processes have been performed for the first time or at better precision  
646 than before thanks to the high collision energy and large volume of data collected by the LHC.

647 Processes involving the scattering of two massive electroweak (EWK) gauge bosons are of par-  
648 ticular interest at the LHC for two main reasons. Firstly, they allow for tests of the self-interactions  
649 predicted by the EWK gauge theory through triple and quartic gauge couplings. While the triple  
650 couplings have been studied by previous experiments as well as at the LHC, the quartic couplings  
651 of the massive gauge bosons have not been accessible previously. Thus, processes involving these  
652 couplings can be measured and compared to the SM predictions for the first time. Secondly, the scat-  
653 tering of two massive gauge bosons is sensitive to the underlying EWSB mechanism. The  $W^\pm$  and  
654  $Z$  bosons are given non-zero masses—and consequently a longitudinal polarization mode—through  
655 the Higgs mechanism, and thus their interactions serve as a direct probe of the symmetry breaking  
656 sector.

657 This thesis presents two separate analyses dealing with the scattering of two same-sign  $W^\pm$   
658 bosons with the LHC’s ATLAS experiment. The  $W^\pm W^\pm jj$  process is a particularly interesting one:  
659 it has access to the  $WWWW$  quartic gauge coupling, production modes that involve the exchange  
660 of a Higgs boson, and relatively low backgrounds. Evidence of EWK  $W^\pm W^\pm jj$  production was first  
661 seen by the ATLAS and CMS experiments at  $\sqrt{s} = 8$  TeV, however the data set was too small to

662 claim observation of the process. The first analysis covered here is the follow up to the above ATLAS  
663 measurement, measuring the EWK fiducial cross section at  $\sqrt{s} = 13$  TeV with a larger data sample.  
664 The second analysis explores the prospects for future measurements of the  $W^\pm W^\pm jj$  process at the  
665 planned High-Luminosity LHC (HL-LHC). A measurement of the production cross section as well  
666 as sensitivity to the purely longitudinal component of the  $W^\pm W^\pm$  scattering is presented.

667 In addition to the SM measurements, a part of this thesis is devoted to alignment of the detector  
668 components making up ATLAS's Inner Detector (ID). Precise knowledge of the locations of detector  
669 elements is essential for accurate particle track reconstruction, which in turn results in improved  
670 resolutions for physics measurements. The ATLAS alignment algorithm determines the positions  
671 of each ID sensor through minimizing the distance between reconstructed particle tracks and the  
672 sensor hit position. Special emphasis is given to the monitoring of momentum biases that may exist  
673 in the ID even after alignment.

674 The first few chapters of this thesis are intended to provide context for the main topics. Chapter 2  
675 gives a brief introduction to the Standard Model with a focus on the EWSB mechanism and vector  
676 boson scattering. The experimental apparatus—the LHC and the ATLAS detector—are detailed in  
677 Chapter 3. The next three chapters present the main body of work. Chapter 4 covers the alignment  
678 of the ATLAS Inner Detector. Chapters 5 and 6 detail the ATLAS  $\sqrt{s} = 13$  TeV  $W^\pm W^\pm jj$  cross  
679 section measurement and the  $\sqrt{s} = 14$  TeV HL-LHC  $W^\pm W^\pm jj$  prospects study, respectively.

## CHAPTER 2

# Theoretical Framework

682 This chapter outlines the theoretical groundwork for the rest of the thesis. An overview of the Stan-  
683 dard Model of particle physics (SM) is given in Section 2.1, followed by the electroweak symmetry  
684 breaking mechanism involving the Higgs boson in Section 2.2. Finally, Section 2.3 will go into detail  
685 on the interests of electroweak vector boson scattering (VBS).

### 686 2.1 Introduction to the Standard Model

687 The Standard Model of particle physics serves as a mathematical description of the fundamental  
688 particles of the universe and their interactions. It has been developed over the course of the past  
689 century, incorporating both predictions from theory and results from experiments. All in all, the SM  
690 has proven to be very accurate in describing the particle interactions seen in experiments, as can be  
691 seen in the summary plot in Figure 2.1 comparing ATLAS measurements to their SM predictions.

692 The SM is a quantum field theory (QFT) [3, 4] in which the fundamental particles are represented  
693 as excited states of their corresponding fields. The spin- $\frac{1}{2}$  fermionic fields give rise to the quarks  
694 and leptons comprising ordinary matter, the spin-1 fields correspond to the electroweak bosons and  
695 the gluon which mediate the electroweak and strong forces, respectively, and finally the scalar Higgs  
696 field is responsible for electroweak symmetry breaking. The excitations and interactions of the fields  
697 are governed by the SM Lagrangian, which is invariant under local transformations of the group  
698  $SU(3) \times SU(2) \times U(1)$ .

699 The first quantum field theory to be developed was quantum electrodynamics (QED) [5], which  
700 describes the electromagnetic interaction. The theory predicts the existence of a  $U(1)$  gauge field  
701 that interacts with the electrically charged fermions. This field corresponds to the photon. A key

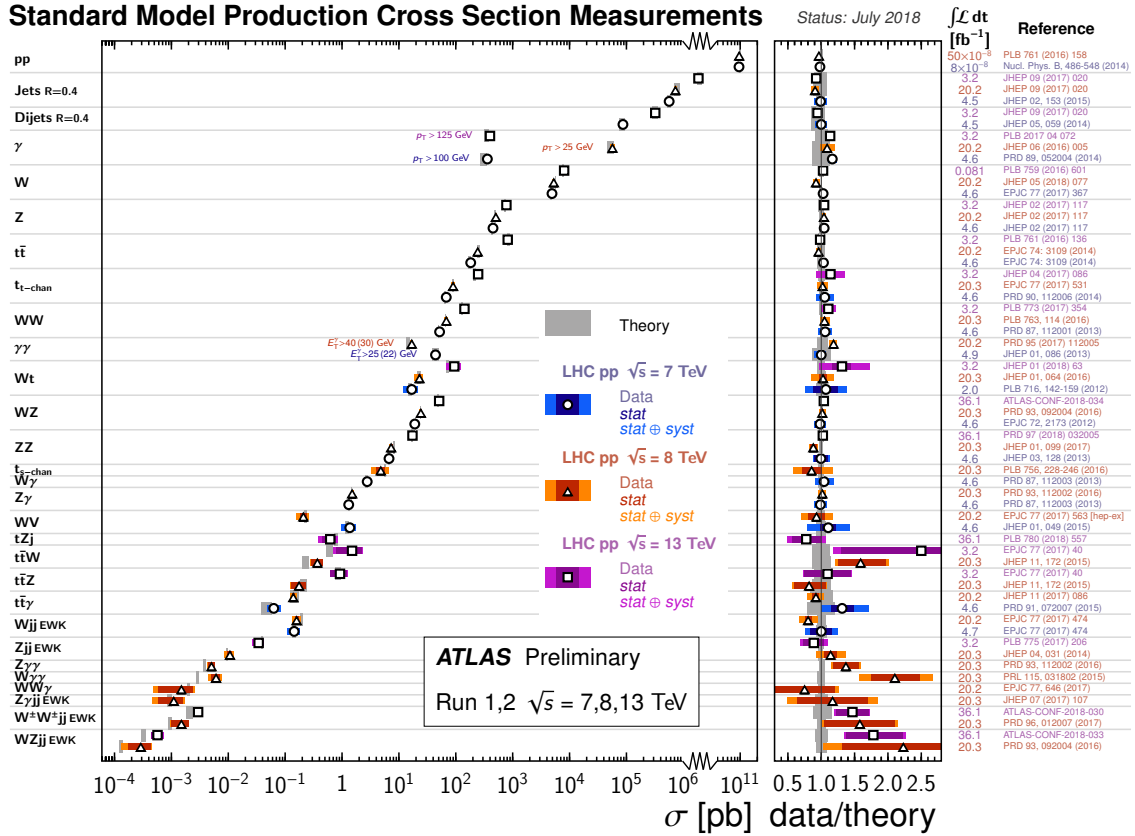


Figure 2.1: Summary of several Standard Model total and fiducial production cross section measurements compared to the corresponding theoretical predictions calculated at NLO or higher. The dark colored error bar represents the statistical uncertainty, and the light colored error bar represents the full uncertainty (including systematic and luminosity uncertainties). The data/theory ratio, luminosity used and reference for each measurement are also shown [2].

702 aspect of QED is that it is perturbative: the coupling constant  $\alpha = e^2/4\pi$  is small, where  $e$  is  
703 electrical charge of the field, allowing for the use of perturbation theory in calculations. In this case,  
704 calculations can be written as a power series in  $\alpha$ , where successive higher order terms contribute  
705 less to the final result. The accuracy of perturbative calculations is an essential tool for being able  
706 to make predictions from the SM.

707 The strong interaction—the theory of quarks and gluons—has also been described using QFT as  
708 quantum chromodynamics (QCD). The symmetry group for QCD is SU(3), and its eight generators  
709 correspond to the eight differently charged, massless gluons [6]. Unlike in QED, which has the  
710 familiar positive and negative electric charges, the strong force has three “colors”. Color charge

combined with the non-Abelian nature of  $SU(3)$ , which allows the gluons to interact with each other, result in the most well-known property of QCD: color confinement. In order to increase the separation between two color-charged quarks, the amount of energy required increases until it becomes energetically favorable to pair-produce a new quark-antiquark pair, which then bind to the original quarks. The end result of this is that only color-neutral objects exist in isolation. What this means for the strong coupling constant  $\alpha_s$  is that its value at the low energies where confinement occurs is large, on the order of  $\alpha_s \sim 1$ . The consequence of this is that perturbation theory cannot be used to approximate these interactions. While this appears at first to be a critical problem for prediction, fortunately it turns out that  $\alpha_s$  “runs”, or decreases in magnitude at higher energy [7, 8]. This so-called “asymptotic freedom” allows QCD to be calculated perturbatively [9] at energies accessible by collider experiments including the LHC.

The last gauge field corresponds to the weak interaction. Ultimately, the weak  $SU(2)$  and the electromagnetic  $U(1)$  mix to form the  $SU(2) \times U(1)$  *electroweak* (EWK) interaction [10, 11]. A more detailed description of the mixing will be discussed in conjunction with electroweak symmetry breaking (EWSB) in Section 2.2; however, a summary of the resulting EWK interaction is presented here, at the risk of some repeated information to follow. There are three weak isospin bosons arising from the  $SU(2)$  group ( $W_\mu^1$ ,  $W_\mu^2$ , and  $W_\mu^3$ ) and one weak hypercharge boson from the  $U(1)$  group ( $B_\mu$ ). The  $W_3$  and  $B$  bosons mix according to the weak mixing angle  $\theta_W$  to form the  $Z$  boson and the photon according to

$$\begin{pmatrix} \gamma \\ Z \end{pmatrix} = \begin{pmatrix} \cos \theta_W & \sin \theta_W \\ -\sin \theta_W & \cos \theta_W \end{pmatrix} \begin{pmatrix} B_\mu \\ W_\mu^3 \end{pmatrix}. \quad (2.1)$$

The value of  $\theta_W$  is not predicted by the SM; it is one example of an experimental input to the theory, measured to be  $\sin^2 \theta_W = 0.23153 \pm 0.00016$  [12]. The charged  $W^\pm$  bosons are a mixture of the remaining  $W_\mu^1$  and  $W_\mu^2$  bosons:

$$W^\pm = \frac{1}{\sqrt{2}}(W_\mu^1 \mp iW_\mu^2). \quad (2.2)$$

Unlike the photon (and the gluon of QCD), the  $W^\pm$  and  $Z$  bosons are massive. This means that even though  $SU(2)$  is non-Abelian, the range of interaction is short and confinement does not occur. Lastly, the EWK interaction is chiral, only coupling to the left-handed component of the fermion fields.

One final field remains within the SM: the scalar Higgs field. It was originally proposed in the 1960’s to explain the masses of the  $W^\pm$  and  $Z$  bosons [13, 14, 15] and is the mechanism for the

739 EWSB process. The particle associated with the field is a massive scalar boson, the Higgs boson,  
740 which was recently discovered by ATLAS and CMS in 2012 [16, 17] with a mass of 125 GeV.

## 741 2.2 Electroweak symmetry breaking and the Higgs boson

742 The results of electroweak mixing and the implications of the Higgs field have been introduced  
743 in the previous section. If the EWK theory were an unbroken symmetry, the associated  $W^\pm$  and  
744  $Z$  bosons would be massless; however, when first observed experimentally [18, 19], they were found  
745 to be quite heavy; currently, their masses are known to be approximately 80 GeV and 91 GeV,  
746 respectively [20]. The following presents the Higgs mechanism, including how it “spontaneously  
747 breaks” the EWK symmetry, resulting in the massive  $W^\pm$  and  $Z$  bosons and the massless photon.

748 Beginning by writing the Higgs field as a complex scalar doublet

$$\phi = \begin{pmatrix} \phi^+ \\ \phi^0 \end{pmatrix} = \sqrt{\frac{1}{2}} \begin{pmatrix} \phi_1 + i\phi_2 \\ \phi_3 + i\phi_4 \end{pmatrix}, \quad (2.3)$$

749 a simple Lagrangian  $\mathcal{L}$  can be written as

$$\mathcal{L} = (\mathcal{D}_\mu \phi)^\dagger (\mathcal{D}^\mu \phi) - \mu^2 \phi^\dagger \phi - \lambda(\phi^\dagger \phi)^2, \quad (2.4)$$

750 where  $\lambda > 0$  and  $\mu^2$  are constants (the sign of  $\mu^2$  will be addressed shortly).  $\mathcal{D}_\mu$  is the covariant  
751 derivative defined such that  $\mathcal{L}$  is invariant under a local  $SU(2) \times U(1)$  gauge transformation:

$$\mathcal{D}_\mu \phi = \left( \partial_\mu + \frac{ig}{2} \tau_a W_\mu^a + \frac{ig'}{2} B_\mu \right) \phi. \quad (2.5)$$

752 Here,  $W_\mu^a$  ( $a = 1, 2, 3$ ) are the  $SU(2)$  fields with generators  $\tau_a$  and coupling constant  $g$ , and  $B_\mu$  is  
753 the  $U(1)$  field with coupling constant  $g'$ .

754 Isolating the Lagrangian’s potential term,

$$V(\phi) = \mu^2 \phi^\dagger \phi + \lambda(\phi^\dagger \phi)^2, \quad (2.6)$$

755 a choice must be made on the sign of  $\mu^2$ . The case of interest is when  $\mu^2 < 0$ , which results in  
756 the so-called “Mexican hat potential” shown in Figure 2.2. The potential is minimized along the  
757 collection of points

$$\phi^\dagger \phi = \frac{1}{2} (\phi_1^2 + \phi_2^2 + \phi_3^2 + \phi_4^2) = -\frac{\mu^2}{2\lambda}. \quad (2.7)$$

758 This means that the minimum of the potential is not at  $\phi = 0$  (as it would be in the case where  
759  $\mu^2 > 0$ ), but rather at a value

$$v \equiv \sqrt{-\frac{\mu^2}{\lambda}}. \quad (2.8)$$

760 With no loss of generality due to the SU(2) symmetry,  $\phi_1 = \phi_2 = \phi_4 = 0$  can be imposed on  
 761 Equation 2.7, leaving  $\phi_3^2 = v^2$ . Finally, the *vacuum expectation value* (VEV) of the field can be  
 762 written:

$$\langle \phi \rangle = \sqrt{\frac{1}{2}} \begin{pmatrix} 0 \\ v \end{pmatrix}. \quad (2.9)$$

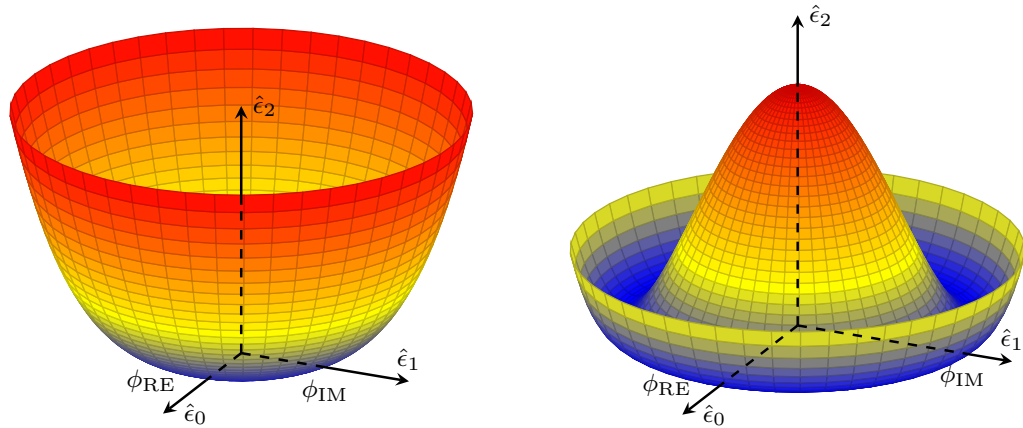


Figure 2.2: An illustration of the potential term  $V(\phi)$  in Equation 2.6 for the cases where  $\mu^2 > 0$  (left) and  $\mu^2 < 0$  (right). The right-hand plot shows the Higgs potential, or ‘‘Mexican hat potential’’, with the minimum at  $|\phi| = \sqrt{-\frac{\mu^2}{\lambda}}$  rather than at  $|\phi| = 0$  as in the left-hand plot.

763 The VEV can be substituted back into the original Lagrangian of Equation 2.4, and, following  
 764 quite a bit of math [21], a collection of mass terms can be identified:

$$\mathcal{L} \subset \mathcal{L}_M \equiv \frac{1}{8} v^2 g^2 \left[ (W_\mu^1)^2 + (W_\mu^2)^2 \right] + \frac{1}{8} v^2 \left[ g^2 (W_\mu^3)^2 - 2gg' W_\mu^3 B^\mu + g'^2 (B_\mu)^2 \right]. \quad (2.10)$$

765 Focusing on the first term for the moment, if Equation 2.2 for the physical  $W^\pm$  bosons is substituted  
 766 in, the mass term becomes

$$M_W^2 W^+ W^- = \left( \frac{1}{2} vg \right)^2 W^+ W^-, \quad (2.11)$$

767 which then simplifies to

$$M_W = \frac{1}{2} vg. \quad (2.12)$$

768 With a bit of clever forward-thinking, the second term of Equation 2.10 can be rewritten as

$$\frac{1}{8} v^2 \left[ g W_\mu^3 - g' B_\mu \right]^2 + 0 \left[ g' W_\mu^3 - g B_\mu \right]^2 = \frac{1}{2} M_Z^2 Z_\mu^2 + \frac{1}{2} M_A^2 A_\mu^2, \quad (2.13)$$

769 where  $Z_\mu^2$  and  $A_\mu^2$  represent the physical  $Z$  boson and photon, respectively:

$$Z_\mu = \frac{gW_\mu^3 - g'B_\mu}{\sqrt{g^2 + g'^2}} \quad (2.14)$$

770

$$A_\mu = \frac{g'W_\mu^3 - gB_\mu}{\sqrt{g^2 + g'^2}}. \quad (2.15)$$

771 From this, it can be seen that the photon is massless ( $M_A = 0$  in Equation 2.13), and the mass of  
772 the  $Z$  boson is identified as

$$M_Z = \frac{1}{2}v\sqrt{g^2 + g'^2}. \quad (2.16)$$

773 Lastly, the Higgs field can couple directly to the fermions. Taking the electron as an example,  
774 an additional Lagrangian term can be written:

$$\mathcal{L}_e = -G_e[\bar{e}_L\phi e_R + \bar{e}_R\phi^\dagger e_L], \quad (2.17)$$

775 where  $e_L$  and  $e_R$  are the left-handed doublet and right-handed singlet, respectively, and  $\phi$  is as in  
776 Equation 2.3. The symmetry can be spontaneously broken by a perturbation about the VEV of the  
777 form

$$\phi = \sqrt{\frac{1}{2}} \begin{pmatrix} 0 \\ v + h(x) \end{pmatrix}. \quad (2.18)$$

778  $\mathcal{L}_e$  then becomes

$$\begin{aligned} \mathcal{L}_e &= -\frac{G_e}{\sqrt{2}}v(\bar{e}_L e_R + \bar{e}_R e_L) - \frac{G_e}{\sqrt{2}}(\bar{e}_L e_R + \bar{e}_R e_L)h \\ &= -m_e \bar{e}e - \frac{m_e}{v} \bar{e}eh, \end{aligned} \quad (2.19)$$

779 which gives a value for the electron mass of  $m_e = \frac{G_e v}{\sqrt{2}}$ . From the second term above, it can be seen  
780 that the strength of the Higgs coupling to the electron is proportional to the mass of the electron.  
781 The rest of the fermion couplings follow from this example.

782 What is accomplished here is quite remarkable. The weak and electromagnetic interactions have  
783 been unified into a single  $SU(2) \times U(1)$  interaction, and the physical bosons observed in nature  
784 arise as mixtures of the four gauge fields. Three of the four degrees of freedom in the scalar field  
785  $\phi$  of Equation 2.3, are absorbed (or “eaten”) by the  $W^\pm$  and  $Z$  bosons, giving them a longitudinal  
786 polarization mode corresponding to a massive particle, and the fourth generates the Higgs boson.  
787 This process is summarized in Figure 2.3. Additionally, it is shown that the Higgs couples to  
788 fermions in proportion to their mass. From experimental measurements, the value of the VEV  
789 has been determined to be  $v \approx 246$  GeV [20]. However, it should be noted that the theory does  
790 not predict the mass of the Higgs boson or of the fermions; these must all be determined from  
791 experiment.

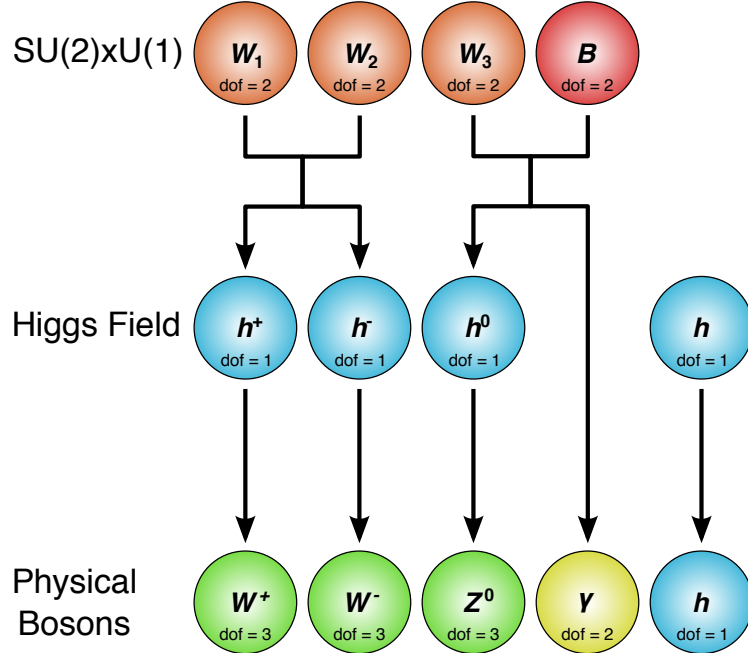


Figure 2.3: A graphical representation of the EWSB mechanism involving the  $SU(2) \times U(1)$  bosons and the Higgs field. The  $W^\pm$  and  $Z$  bosons each obtain mass by eating a degree of freedom (dof) from the Higgs field, and in the process gain a longitudinal polarization mode, while the photon stays massless (with two dof) and the SM Higgs boson  $h$  remains.

### 792 2.3 Electroweak vector boson scattering

793 Due to the non-Abelian nature of the EWK interaction, the associated gauge bosons are allowed  
 794 to self-interact. This results in triple and quartic couplings of gauge bosons (TGCs and QGCs,  
 795 respectively). The SM allowed TGCs are the  $WW\gamma$  and  $WWZ$  vertices, which can be measured  
 796 experimentally via diboson production or through vector boson fusion (VBF). The QGCs predicted  
 797 by the SM are  $WWZ\gamma$ ,  $WW\gamma\gamma$ ,  $WWZZ$ , and  $WWWW$ , and these vertices are accessible via  
 798 triboson production or vector boson scattering (VBS)<sup>1</sup> [22]. VBS processes are defined by a  $VV \rightarrow$   
 799  $VV$  signature, where  $V$  represents one of the EWK gauge bosons ( $W^\pm$ ,  $Z$ , or  $\gamma$ ), as shown in  
 800 Figure 2.4. The actual interaction between the incoming and outgoing vector bosons can be mediated  
 801 by the exchange of a virtual  $V$ , directly via a QGC (both are shown in Figure 2.5), or by the exchange  
 802 of a Higgs boson (as in Figure 2.6).

803 As detailed in the previous section, the Higgs mechanism produces three Goldstone bosons and a

<sup>1</sup>Vector boson fusion and scattering typically refer to the  $s$ -channel and  $t$ -channel exchanges of a vector boson, respectively; however, often both are used interchangeably to describe the  $VV \rightarrow VV$  process. Therefore, for the remainder of this thesis, *vector boson scattering* will refer to both the VBF and VBS production mechanisms.

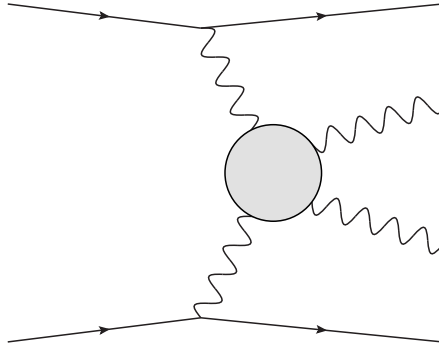


Figure 2.4: Feynman diagram of a generic VBS process. The gray circle represents any interaction with two incoming and two outgoing vector bosons, including any of the diagrams shown in Figures 2.5 and 2.6.

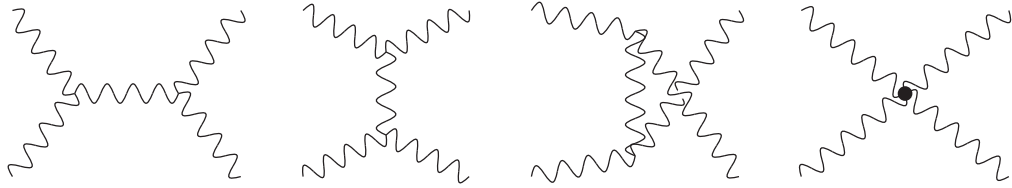


Figure 2.5: Leading order  $VV \rightarrow VV$  Feynman diagrams involving EWK bosons. From left to right:  $s$ -channel,  $t$ -channel,  $u$ -channel, and the quartic gauge coupling.

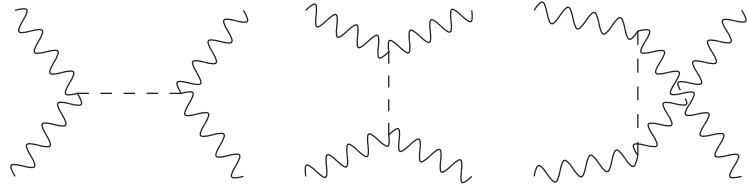


Figure 2.6: Leading order  $VV \rightarrow VV$  Feynman diagrams involving the exchange of a Higgs boson. From left to right:  $s$ -channel,  $t$ -channel, and  $u$ -channel.

804 Higgs boson. The Goldstone bosons are then “eaten” by the physical gauge bosons, giving them mass  
 805 and consequently a longitudinal polarization<sup>2</sup>. In fact, according to the Electroweak Equivalence  
 806 Theorem, the high-energy interactions of longitudinal gauge bosons can be accurately described by  
 807 the Goldstone bosons of the EWSB mechanism [23]. Thus, the scattering of the massive gauge  
 808 bosons is inextricably linked to EWSB.

809 It turns out that without a light SM Higgs boson, the scattering amplitude of longitudinally

---

<sup>2</sup>A massless spin-1 boson can have one of two transverse polarization states, while a massive spin-1 boson can also be longitudinally polarized. As a result, only the massive  $W^\pm$  and  $Z$  bosons, and not the massless photon, are sensitive to EWSB.

810 polarized vector bosons grows with center-of-mass energy and ultimately violates unitarity above  
 811  $\sqrt{s} \approx 1.2$  TeV [24, 25]. The equations for the two transverse ( $\epsilon_{\pm}^{\mu}$ ) and longitudinal ( $\epsilon_L^{\mu}$ ) polarization  
 812 vectors of a gauge boson of mass  $M_V$  can be written as

$$\epsilon_{\pm}^{\mu} = \frac{1}{\sqrt{2}}(0, 0, \pm i, 0) \quad (2.20)$$

813 and

$$\begin{aligned} \epsilon_L^{\mu} &= \frac{1}{M_V}(|\vec{p}|, 0, 0, E) \\ &= \frac{p^{\mu}}{M_V} + v^{\mu}, \end{aligned} \quad (2.21)$$

814 where  $v^{\mu}$  is of the order  $M_V/E$  and becomes small in the high energy limit [26]. From this, it can  
 815 be seen that  $\epsilon_L^{\mu}$  grows with the momentum of the boson  $p^{\mu}$ . Thus, the dominant contribution to the  
 816 VBS process at high energy comes from the longitudinally polarized gauge bosons [27].

817 The high-energy behavior of longitudinally polarized vector boson scattering can be explored in  
 818 the case of opposite-sign  $W^+W^- \rightarrow W^+W^-$  scattering. In the high-energy limit ( $s \gg M_W^2, M_H^2$ ),  
 819 the amplitude of  $W^+W^-$  scattering without considering the Higgs contributions (the appropriate  
 820 diagrams from Figure 2.5) can be written as

$$\mathcal{M}_{\text{gauge}} = -\frac{g^2}{4M_W^2}u + \mathcal{O}\left(\left[\frac{E}{M_W}\right]^0\right), \quad (2.22)$$

821 where  $g$  is the EWK coupling and  $u$  is one of the Mandelstam variables [25]. The  $\mathcal{O}(E^4)$  terms  
 822 cancel out between the TGC and QGC diagrams [27]. What is left is an amplitude proportional to  
 823  $E^2$  that diverges as  $E/M_W \rightarrow \infty$ . However, the amplitude from the diagrams involving the Higgs  
 824 boson (the relevant diagrams from Figure 2.6) is

$$\mathcal{M}_{\text{Higgs}} = -\frac{g^2}{4M_W^2} \left[ \frac{(s - M_W^2)^2}{s - m_H^2} + \frac{(t - M_W^2)^2}{t - M_H^2} \right], \quad (2.23)$$

825 which reduces to

$$\mathcal{M}_{\text{Higgs}} = \frac{g^2}{4M_W^2}u + \mathcal{O}\left(\left[\frac{E}{M_W}\right]^0\right) \quad (2.24)$$

826 in the high-energy limit. Adding the two equations together cancels out the  $E^2$  term and leaves only  
 827 terms constant in energy. Therefore, with a SM Higgs, the scattering amplitude for longitudinally  
 828 polarized  $W$  bosons no longer diverges. Plots of the cross section of several  $VV \rightarrow VV$  scattering  
 829 processes are shown in Figure 2.7 with and without a SM Higgs boson.

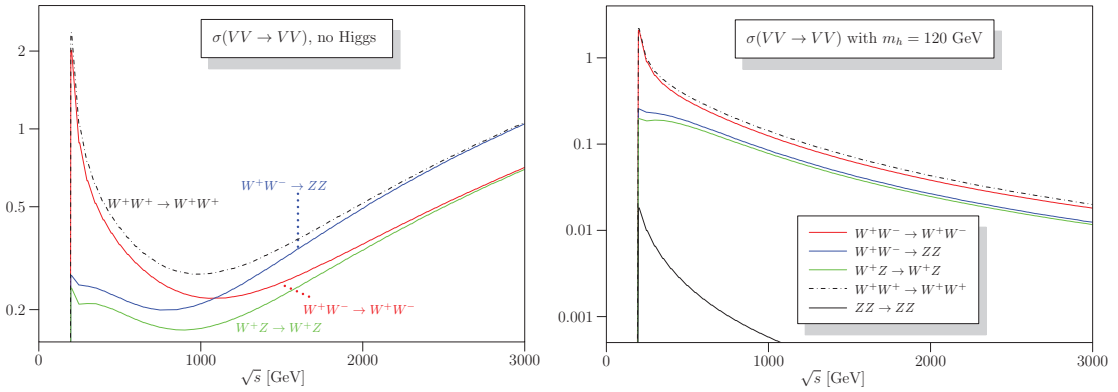


Figure 2.7: Cross sections in nanobarns for five different longitudinally polarized VBS processes as a function of center of mass energy  $\sqrt{s}$ . Without a Higgs boson (left), the cross sections grow unbounded with  $\sqrt{s}$ . With a 120 GeV Higgs boson (right), the cross sections no longer diverge. Plots taken from [28].

830

## CHAPTER 3

831

# LHC and the ATLAS Detector

832 This chapter covers the experimental apparatus relevant to this thesis: the Large Hadron Collider  
833 (LHC) and the ATLAS detector in Sections 3.1 and 3.2, respectively. Some time is taken in Sec-  
834 tion 3.3 to overview the methods used to identify and measure various particle types within ATLAS.

835 **3.1 The Large Hadron Collider**

836 The Large Hadron Collider (LHC) [29] is the most powerful particle accelerator in the world, colliding  
837 two beams of protons at a center of mass energy of  $\sqrt{s} = 13$  TeV. It is operated by the European  
838 Organization for Nuclear Research (CERN) and consists of a 27 km ring located beneath the France–  
839 Switzerland border. A chain of smaller accelerators incrementally boost the protons<sup>3</sup> up to higher  
840 and higher energies before they reach the final collision energy within the main LHC ring. Collisions  
841 occur at each of four detector experiments situated around the ring: ATLAS [30], ALICE [31],  
842 CMS [32], and LHCb [33].

843 Protons are obtained from hydrogen atoms stripped of their electrons by an electric field. A  
844 beam of protons is first accelerated up to 50 MeV in the Linac 2 accelerator, then to 1.4 GeV in the  
845 Proton Synchrotron Booster (PSB), 25 GeV in the Proton Synchrotron (PS), and finally to 450 GeV  
846 in the Super Proton Synchrotron (SPS). Two beams are then injected into the LHC ring in running  
847 in opposite directions where they accelerate up to the collision energy of 6.5 TeV. Each consists of  
848 bunches containing on the order of  $10^{11}$  protons separated by 25 ns [34]. A schematic of the CERN  
849 accelerator complex, including the chain of accelerators mentioned above, is shown in Figure 3.1.

---

<sup>3</sup>The LHC can also collide beams of heavy ions; however, this thesis focuses exclusively on the proton-proton collisions.

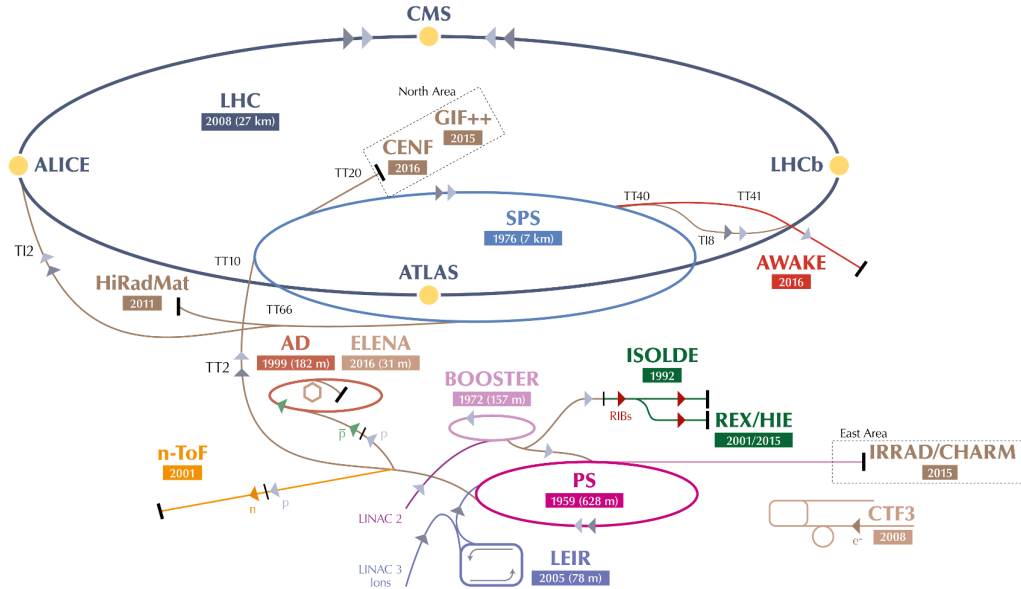


Figure 3.1: The CERN accelerator complex. For LHC collisions, protons are accelerated by the Linac 2 (purple), the PSB (light purple), the PS (magenta), and the SPS (light blue) before entering the LHC ring (dark blue) [35].

850 In addition to a high center of mass energy, the LHC must also deliver enough data to measure  
 851 rare processes. The amount of data collected is measured in terms of *luminosity*. The instantaneous  
 852 luminosity  $\mathcal{L}$  is defined in terms of the number of events per second  $\frac{dR}{dt}$  and the production cross  
 853 section  $\sigma_p$ :

$$\mathcal{L} = \frac{1}{\sigma_p} \frac{dR}{dt}. \quad (3.1)$$

854 The calculation itself can be quite tricky, as it depends on a number of factors including the number  
 855 of particles per bunch, the spread of the beam, and the crossing angle of the beams [36].

856 The LHC was originally designed to operate at an instantaneous luminosity of  $1.0 \times 10^{34} \text{ cm}^{-2}\text{s}^{-1}$ ;  
 857 however, this number was exceeded by the end of the 2016 data taking period, with a peak luminosity  
 858 of  $1.38 \times 10^{34} \text{ cm}^{-2}\text{s}^{-1}$ . By the end of Run 2 in December 2018, the LHC was running at more  
 859 than twice the design luminosity [37]. The instantaneous luminosity of proton-proton collisions as  
 860 a function of time in 2015 and 2016 are shown in Figure 3.2.

861 The total amount of data collected is reported in terms of *integrated* luminosity, which is simply  
 862 the time integral of the instantaneous luminosity. By the end of Run 2 (2015-2018), approximately  
 863  $140 \text{ fb}^{-1}$  of 13 TeV data collected by the ATLAS detector is available for physics, as shown in  
 864 Figure 3.3. The  $36.1 \text{ fb}^{-1}$  collected during the first two years (2015 and 2016) is used for the

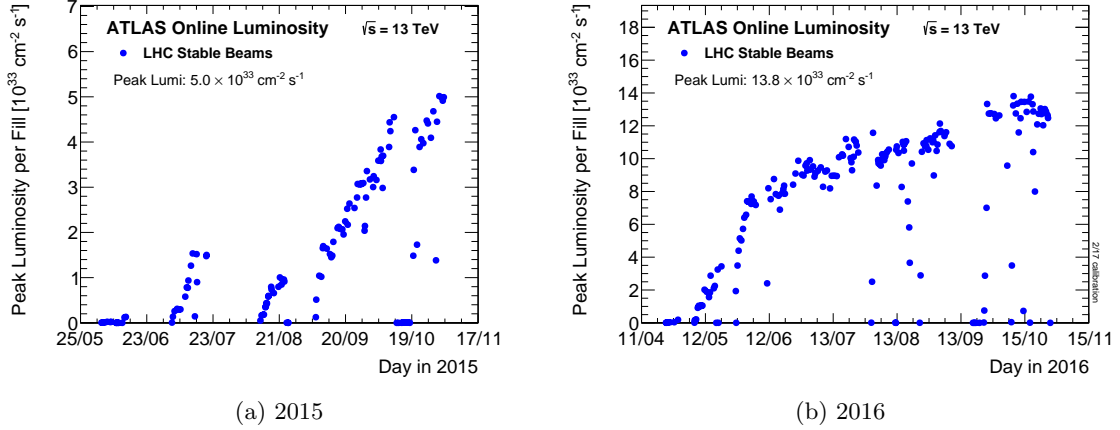


Figure 3.2: Peak instantaneous luminosity delivered to ATLAS during 13 TeV  $pp$  data taking as a function of time [37].

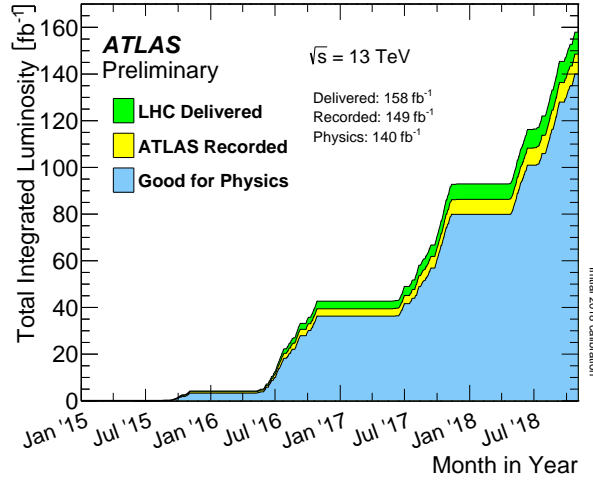


Figure 3.3: Integrated luminosity collected by ATLAS as a function of time at 13 TeV from 2015-2018 [37].

analysis later in this thesis.

Due to the high instantaneous luminosity, more than one  $pp$  interaction occurs in a single bunch crossing, referred to as *pileup*. During the 2016 data taking campaign, the average number of interactions per bunch crossing  $\langle\mu\rangle$  was approximately 24 but has increased to upwards of 37 in 2017 and 2018 [37]. Figure 3.4 contains the average  $\mu$  for the 2015-2016 data set used for analysis in this thesis. The high pileup is a challenge for accurately reconstructing an individual collision.

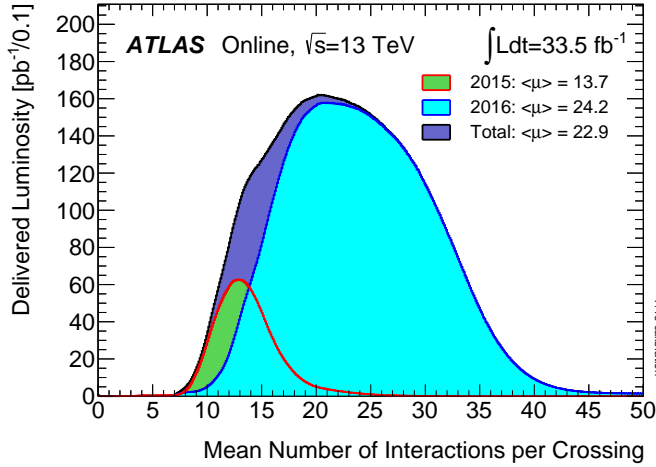


Figure 3.4: Distribution of the mean number of interactions per bunch crossing for the 2015 and 2016  $pp$  collision data at 13 TeV [37].

### 871 3.2 The ATLAS Detector

872 ATLAS (A Toroidal LHC ApparatuS) is a general-purpose particle detector. It contains several sub-  
 873 detector systems designed to measure different types of particles. Starting from the beam line and  
 874 working outwards, the Pixel Detector (PIX), Semiconductor Tracker (SCT), and Transition Radia-  
 875 tion Tracker (TRT) make up the Inner Detector (ID) and are responsible for measuring the trajec-  
 876 tories and momenta of charged particles. Next are two calorimeters, the Liquid Argon Calorimeter  
 877 (LAr) the Tile Calorimeter (TileCal), which stop electromagnetic and hadronic objects and measure  
 878 their energies. Finally, the outermost Muon Spectrometer (MS) measures muon tracks as they leave  
 879 the detector, as they are too heavy to be stopped by the calorimeters. The ATLAS detector and its  
 880 subsystems are shown in Figure 3.5.

881 ATLAS uses a global, right-handed coordinate system with the origin at the center of the detector  
 882 (the nominal interaction point). The  $x$ -axis points from the origin inwards to the center of the LHC  
 883 ring, the  $y$ -axis points upwards, and the  $z$ -axis points along the beam line. Due to the azimuthal  
 884 symmetry of the detector, it is useful to use cylindrical coordinates  $(r, \phi)$  in the plane transverse to  
 885 the  $z$ -axis, where  $\phi$  is the azimuthal angle. Instead of using the polar angle  $\theta$  to describe particle  
 886 trajectories, pseudorapidity is used instead:

$$\eta = -\ln(\tan(\theta/2)). \quad (3.2)$$

887 Pseudorapidity has the useful property that differences in  $\eta$  are invariant under Lorentz boosts along

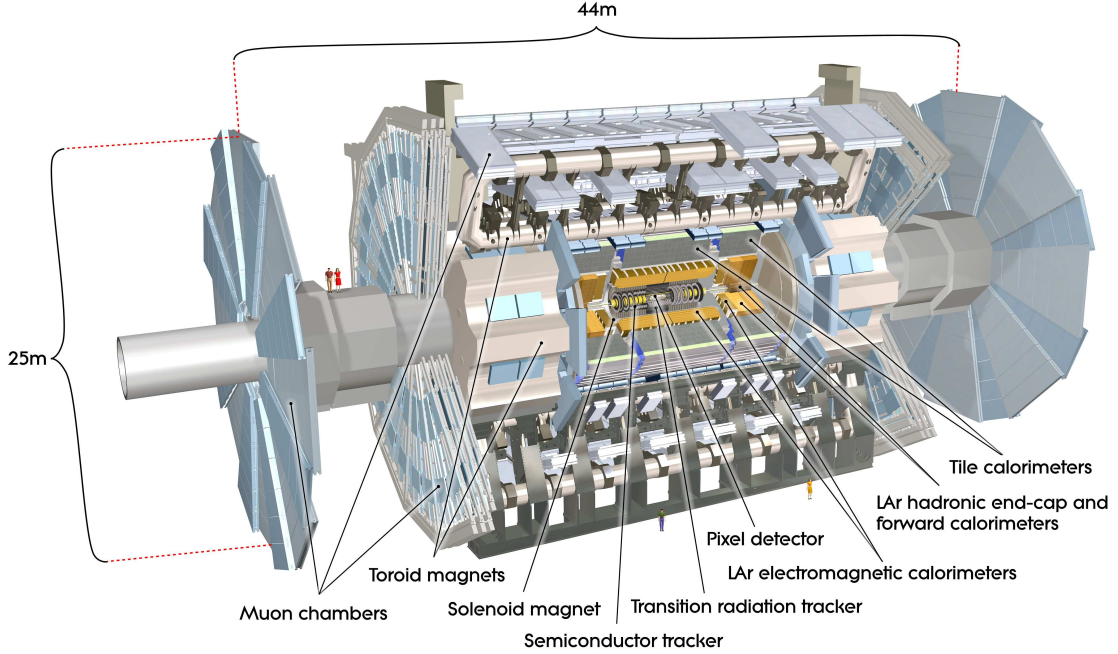


Figure 3.5: Cut-away view of the ATLAS detector [30].

the  $z$ -axis. The angular separation between two particles  $p_i$  and  $p_j$  is often expressed in terms of the quantity  $\Delta R$ , defined as

$$\Delta R(p_i, p_j) = \sqrt{\Delta\eta_{i,j}^2 + \Delta\phi_{i,j}^2}, \quad (3.3)$$

where  $\Delta\phi_{i,j} \in [-\pi, \pi]$  since  $\phi$  is periodic in  $2\pi$  and “wraps around” the detector in the azimuthal direction.

### 3.2.1 The Inner Detector

The ID [38, 39] is a tracking system that reconstructs the trajectories of charged particles. It spans just over a meter in radius, with the innermost layer of sensors at a radius of 33.25 cm from the beam line. Charged particles traveling through the ID leave *hits* in each sensor they pass through, and a *track* representing the path of the particle is fit to the hits according to the procedure outlined in Section 3.3.1. The ID’s pseudorapidity coverage extends out to  $|\eta| < 2.5$ . A solenoid magnet outside the ID produces a 2 T magnetic field that bends the particles, allowing for their momenta in the direction transverse to the field to be measured according to

$$p_T = q \cdot B \cdot r, \quad (3.4)$$

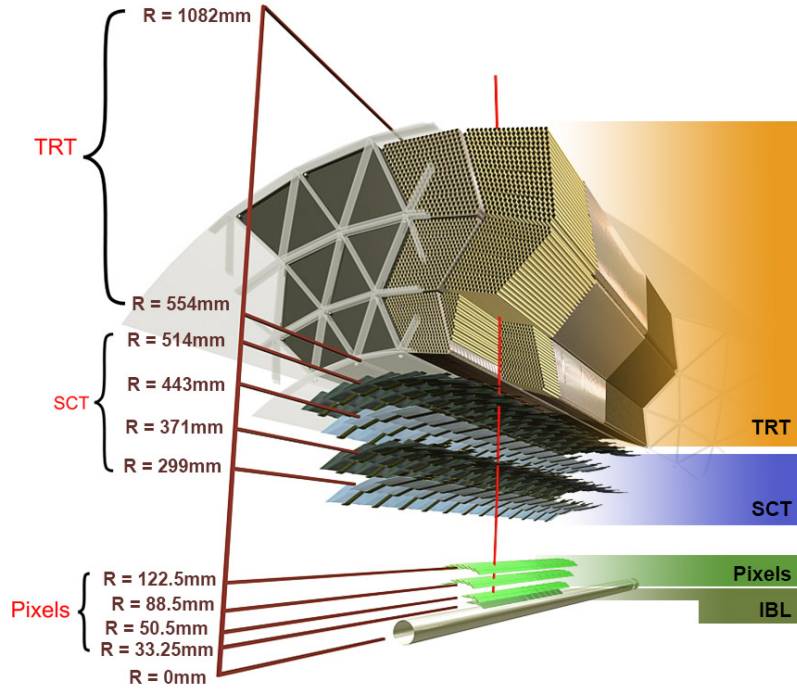


Figure 3.6: The barrel layers of the Pixel, SCT, and TRT detectors making up the Inner Detector.

900 where  $q$  is the charge of the particle ( $\pm 1$ ),  $B$  is the strength of the magnetic field, and  $r$  is the radius  
901 of the track's curvature. A cut-away view of the barrel region of the ID is shown in Figure 3.6.

902 **3.2.1.1 Pixel Detector**

903 The Pixel Detector consists of four cylindrical barrel layers<sup>4</sup> and three endcap disks on either side.  
904 It is the innermost subdetector of the ID with coverage up to  $|\eta| < 2.5$ . The individual sensors  
905 measure  $50 \mu\text{m} \times 400 \mu\text{m}$  and are installed on silicon wafers that make up the layers. All in all, there  
906 are 1744 wafers with 80 million readout channels. The sensors themselves are silicon semiconducting  
907 diodes that provide a signal when a charged particle passes through. The Pixel Detector has the  
908 finest resolution of all the ID subdetectors, at  $10 \mu\text{m}$  in the  $r\text{-}\phi$  plane and  $40 \mu\text{m}$  in the  $z$  direction.

909 During the upgrade period between Run 1 and Run 2, a new innermost layer was added to the  
910 Pixel detector barrel: the Insertable B-Layer (IBL) [40]. The IBL lies closest to the interaction  
911 point, at a radius of 33.25 cm from the beam line, and it is relied upon to provide high-precision

---

<sup>4</sup>For now, the outer three barrel layers will be covered in conjunction with the endcaps; the innermost layer will be described separately.

912 measurements close to the interaction point. Its addition allows better precision in detecting dis-  
913 placed vertices from  $b$ -jets, for example. The IBL consists of 280 silicon pixel modules arranged on  
914 14 staves that run parallel to the beam line. Each stave consists of 12 two-chip planar modules in  
915 the middle ( $|\eta| < 2.7$ ) with four 3D sensors [41] on either side ( $2.7 < |\eta| < 3.0$ ). The IBL's pixel  
916 sensors are  $50 \mu\text{m} \times 250 \mu\text{m}$  in size and have a resolution of  $10 \mu\text{m}$  in  $r\text{-}\phi$  and  $75 \mu\text{m}$  in  $z$  [42].

917 **3.2.1.2 Semiconductor Tracker**

918 The next subdetector of the ID is the SCT, which has four barrel layers and nine endcap disks per  
919 side which provide coverage up to  $|\eta| < 2.5$ . The SCT operates on the same principle as the Pixel  
920 Detector, but the sensitive elements are larger silicon “strips” placed on the wafers. This shape  
921 change assissts in covering the larger surface area required by the increasing detector radius. Each  
922 detector layer is actually made up of two layers of wafers, placed back-to-back with an angle of  
923 40 mrad between them. The resolution in the  $r\text{-}\phi$  plane is very fine at  $17 \mu\text{m}$ , but, due to the strip  
924 shape, the resolution along  $z$  is rather poor at  $580 \mu\text{m}$ .

925 **3.2.1.3 Transition Radiation Tracker**

926 The outermost component of the ID is the TRT [43, 44, 45], which uses a completely different  
927 technology from the Pixel and SCT to identify particle hits. The TRT is unique in that it combines  
928 a drift tube tracker with transition radiation detection to assist with electron identification. The  
929 TRT's sensitive elements are drift tubes (referred to as “straws”) that are 4 mm in diameter and  
930 consist of a cylindrical cathode with an anode wire running through the center. Each straw is filled  
931 with a gas mixture including xenon or argon which provides ionizing radiation when high energy  
932 particles pass through them. The resulting electrons drift to the anode and register a voltage,  
933 indicating a hit in the detector element.

934 Between the straws are polyethelene fibers in the barrel and polypropylene foil in the endcaps  
935 in order to encourage particles to emit transition radiation photons. These photons also ionize the  
936 gas within the straws, leading to a higher signal. The TRT takes advantage of the fact that lighter  
937 particles are more likely to emit transition radiation by using a ternary output: zero, low-threshold,  
938 and high-threshold. High-threshold hits are generally caused by electrons due to their low mass,  
939 and this can help in identifying electron tracks from backgrounds.

940 There are over 100,000 straws in the barrel of the TRT, and nearly 250,000 in the endcaps. The  
941 TRT provides pseudorapidity coverage up to  $|\eta| < 2.0$  with a resolution in the  $r\text{-}\phi$  plane of  $130 \mu\text{m}$ .

942 Since the drift tubes are insensitive along the direction of the wire, the TRT does not provide a  
 943 measurement along the  $z$  direction.

944 **3.2.2 The Calorimeters**

945 ATLAS utilizes two different calorimeters, the Liquid Argon and Tile Calorimeters [46, 47], in order  
 946 to measure electromagnetic and hadronic objects. The general principle behind both calorimeters is  
 947 the same: an incoming particle showers as it passes through, eventually coming to a stop, and the  
 948 resulting energy deposits are read out. Both are sampling calorimeters, which consist of alternating  
 949 layers of a dense material to induce the showering (called the *absorber*) and a second material which  
 950 measures the energy (called the *active material*). An advantage to this type of calorimeter is that  
 951 a very dense absorber can be used in order to produce a shower in a limited space, even if it is  
 952 unsuitable for measuring the energy from the shower. However, as a result, some of the energy is  
 953 deposited in the absorbers, and the total shower energy must be estimated. ATLAS's calorimeter  
 954 systems are shown in Figure 3.7.

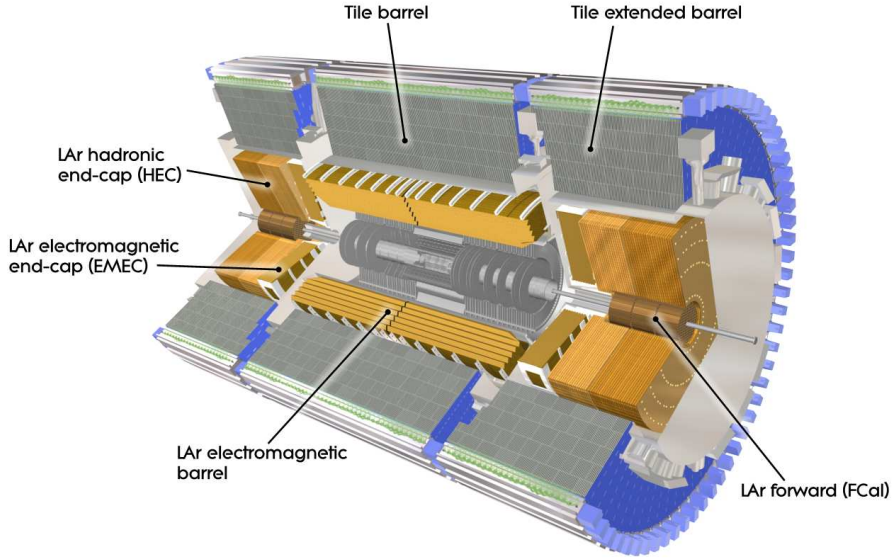


Figure 3.7: Cut-away view of the ATLAS calorimeter systems [48].

955 Electromagnetic objects, such as electrons and photons, shower via cascades of bremsstrahlung  
 956 photons and  $e^+e^-$  pairs. The radiation length  $X_0$  is defined as the mean distance over which an  
 957 electron's energy is reduced to  $1/e$  of its original value, or  $E(x) = E_0 e^{-x/X_0}$ . The majority of the

958 shower energy is deposited in the first few radiation lengths. The longitudinal shower depth scales  
 959 logarithmically with particle energy, and the transverse shower width is described by the Molière  
 960 radius<sup>5</sup> of the material.

961 Hadronic showers (referred to as *jets*) are the result of quarks or gluons which hadronize and  
 962 shower primarily via the strong interaction. Hadronic showers are generally wider than the electro-  
 963 magnetic showers described above. The longitudinal depth of the hadronic shower scales with the  
 964 nuclear interaction length of the material  $\lambda$ , defined as the mean distance for the number of particles  
 965 in a hadronic jet to be reduced to  $1/e$  of the initial number. In addition, about 1/3 of the shower  
 966 products are neutral pions  $\pi^0$  which decay electromagnetically via the process described above.

### 967 3.2.2.1 Liquid Argon Calorimeter

968 The LAr Calorimeter contains four individual calorimeters: the electromagnetic barrel (EMB) and  
 969 endcaps (EMEC), and the hadronic endcap (HEC) and forward calorimeter (FCal). The entire  
 970 calorimeter is surrounded by a cryostat held at a temperature around 90 K.

971 Focusing on the electromagnetic components first, the EMB covers  $|\eta| < 1.475$  and the two  
 972 EMECs cover  $1.375 < |\eta| < 3.2$ . They consist of alternating layers of lead absorber and liquid  
 973 argon. The exact thickness of the lead depends on the location within the detector, ranging from  
 974 1.1-2.2 mm. The absorbers are folded into an accordion shape, where the folding angles are varied  
 975 in order to keep the thickness of the liquid argon gap constant across the barrel (about 2.1 mm).  
 976 The electromagnetic calorimeter is thick enough that the minimum number of radiation lengths a  
 977 particle travels through is 24  $X_0$ , including the material from other subdetectors.

978 There are four layers within the EMB and EMEC, including an innermost pre-sampler that helps  
 979 correct for energy lost before the shower reaches the calorimeter. The next three layers consist of  
 980 differently shaped cells successively reducing in granularity. The first layer consists of narrow strips  
 981 for fine-grained  $\eta$  resolution, while the majority of the shower energy is deposited in the second  
 982 layer; the third layer captures most of the energy that escapes the previous two. The accordion  
 983 shape as well as the sizes of the cells in the EMB are shown in Figure 3.8.

984 The HEC is located directly behind the EMEC and covers  $1.5 < |\eta| < 3.2$ . It uses thick copper  
 985 plates as the absorber (25 mm in the front wheels and 50 mm in the rear wheels) separated by 8.5 mm  
 986 gaps filled with liquid argon. Rather than the accordion shape, the HEC cells are rectangular.

---

<sup>5</sup>A cone with a radius equal to the Molière radius ( $M_R$ ) will contain approximately 90% of the shower energy. At a radius of  $2M_R$ , 95% of the energy will be contained.

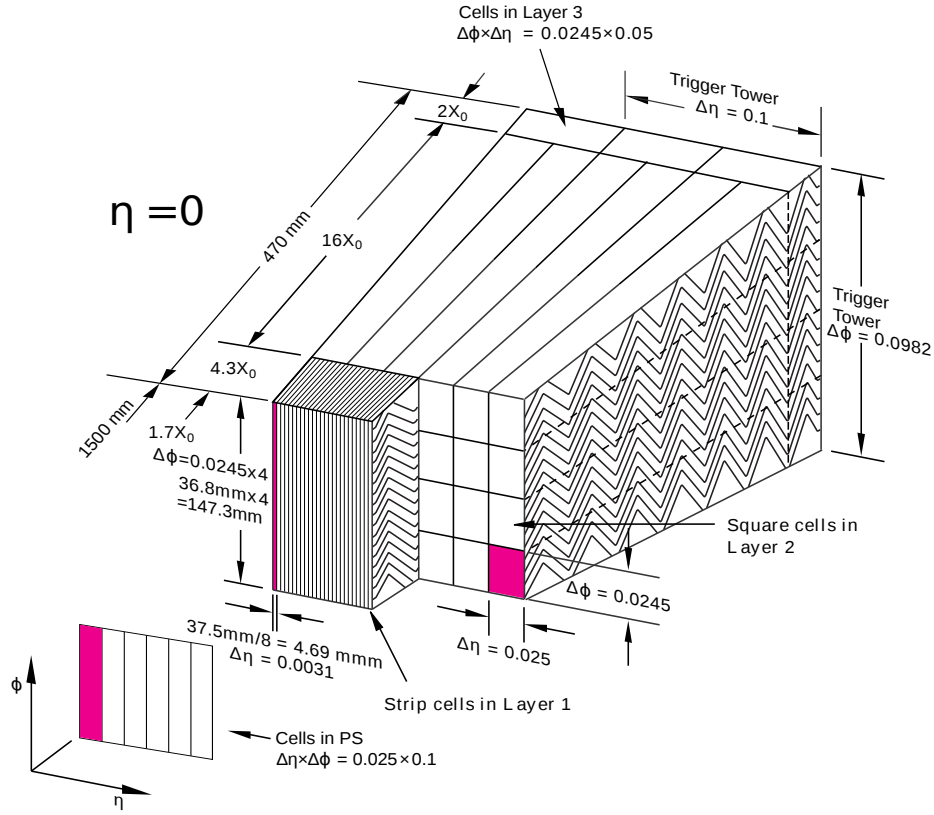


Figure 3.8: Diagram of the cells within the LAr barrel. The accordion structure can be seen in the cut-away view [46].

987     The FCal provides coverage for hadronic jets over the range  $3.2 < |\eta| < 4.9$ . Each FCal endcap  
 988     consists of three layers. The first is an electromagnetic calorimeter with a copper absorber, while the  
 989     other two hadronic layers use a tungsten absorber. Due to the high particle flux entering the FCal,  
 990     the liquid argon gaps are very narrow, and electrodes are embedded into the absorbers parallel to  
 991     the beam line.

### 992     3.2.2.2 Tile Calorimeter

993     The TileCal consists of a barrel and two “extended barrel” sections which cover the range  $|\eta| < 1.7$ .  
 994     It consists of alternating layers of steel plates and polystyrene scintillator tiles as the absorbers and  
 995     active material, respectively. The total thickness of the TileCal is approximately  $9 \lambda$ . As the shower  
 996     passes through the scintillators, photons are emitted that are picked up by wavelength shifting fibers  
 997     and passed to photomultiplier tubes.

**3.2.3 The Muon Spectrometer**

The outermost subdetector in ATLAS is the Muon Spectrometer [49]. Due to the high mass of muons compared to electrons, they pass through the calorimeters, necessitating their own detector. The MS is a high-resolution spectrometer which provides tracking for muon reconstruction within  $|\eta| < 2.7$ . A set of toroid magnets generate an azimuthal magnetic field that bends the muons for momentum measurements, much like in the ID. Four different technologies are used in the MS:

- Monitored Drift Tubes (MDT) are used across the entire  $\eta$  range for precision measurements of the tracks with a per-hit resolution in the range of 60-80  $\mu\text{m}$ . These consist of an aluminum tube filled with a gas mixture containing argon and an anode wire running through the middle of the tube. When a muon passes through, the gas is ionized, and the electrons are collected on the wire.
- Cathode Strip Chambers (CSC) are used for the forward regions of the endcaps (above  $|\eta| > 2.0$ ). They operate on a similar principle to the MDTs, with strips containing a mesh of anode wires running in parallel instead of tubes with a single wire each.
- Resistive Plate Chambers (RPC) in the barrel are primarily used to provide input for the muon trigger system. They consist of pairs of plastic resistive plates with a 2 mm gap between them filled with a gas mixture. Electrodes are attached to the plates to create a potential between them, and muons passing through ionize the gas and lead to electric discharges which in turn reduce the potential.
- Thin Gap Chambers (TGC) are used for triggering in the endcaps. The TGCs are arranged on circular disks consisting of two rings, and are similar in function to the CSCs but with a different gas mixture.

**3.3 Particle reconstruction**

In order to convert the raw detector readouts to information about a given particle, various sets of reconstruction algorithms are run. This includes building particle trajectories in the ID, as well as identifying and measuring electrons and muons. A brief overview of these reconstruction methods follow in order to provide context for when these objects are used later in the thesis.

1025    **3.3.1 Track reconstruction**

1026    *Track reconstruction* is the process by which a particle’s trajectory is reconstructed from the raw  
1027    measurements recorded in the ID. The ATLAS track reconstruction algorithm [50] follows three  
1028    main steps: clusterization, track finding, and ambiguity solving.

1029    The first step, clusterization, uses hits from the Pixel and SCT detectors. Neighboring pixels or  
1030    silicon strips that registered a hit in a sensor are grouped together into clusters using a connected  
1031    component analysis. Each cluster represents a *space-point*, or a three-dimensional measurement  
1032    corresponding to the point where the particle intersected the sensor. Since the SCT sensors consist  
1033    of two strip layers on top of each other (as described in Section 3.2.1.2), clusters from each layer  
1034    combine to form a single space-point. It is possible to have overlapping clusters from multiple  
1035    particles in a single sensor, and care is taken that these *merged clusters* are identified and handled  
1036    accordingly.

1037    Next, track seeds are formed using sets of three space-points. This number allows for a first  
1038    momentum estimate to be made while still allowing for as large a number of track combinations as  
1039    possible. The impact parameters of a track seed—the distance of closest approach to the collision—  
1040    are estimated by assuming a perfect helical trajectory in a uniform magnetic field. In order to ensure  
1041    the quality of a track seed, criteria on the momentum and impact parameters are imposed as well as  
1042    a requirement that at least one additional space-point lies along the preliminary trajectory. Finally,  
1043    a combinatorial Kalman filter [51] builds track candidates from the track seeds by incorporating  
1044    additional space-points lying along the preliminary trajectory. The filter allows for multiple track  
1045    candidates to be fit to the same track seed if more than one set of space-points is compatible.

1046    The final step of the reconstruction process is the ambiguity solving. Each collected track  
1047    candidate is processed individually before being sorted by its *track score*, a metric for quantifying  
1048    the likelihood that a given track candidate correctly represents the particle’s trajectory. The track  
1049    score is determined from a number of factors. Each cluster along the track candidate increases  
1050    the score by a weighted amount that incorporates the intrinsic resolution of the relevant detector’s  
1051    sensors in addition to other factors. Conversely, if a track candidate passes through a sensor but  
1052    there is no associated cluster (called a *hole*), the score is reduced. The  $\chi^2$  of the track fit contributes  
1053    as well in order to promote tracks with high quality fits. Finally, the logarithm of the momentum  
1054    adds to the score to suppress tracks with incorrectly assigned clusters, as these tracks typically have  
1055    low momenta. A track candidate is rejected by the ambiguity solver if its score is too low, or if it  
1056    fails to meet a basic set of quality criteria. If a cluster would be shared by more than one track, at

1057 most two tracks are allowed to pass through it. In this case, preference is given to tracks already  
 1058 passing through the ambiguity solver, which by construction results in the two highest scoring tracks  
 1059 using the shared cluster being kept.

1060 Following this procedure, TRT hits can be incorporated into the track fit through *TRT track*  
 1061 *extension* [52]. Compatible sets of TRT measurements are found for tracks found in the silicon  
 1062 detectors surviving the ambiguity solving. The algorithm requires that the original silicon-only  
 1063 track not be modified by the inclusion of the TRT hits; it is simply an extension of the existing  
 1064 track.

1065 What is described above is the *inside-out* reconstruction algorithm; there is also an *outside-in*  
 1066 reconstruction that begins in the TRT. This algorithm is not covered in detail here, as much of the  
 1067 process is similar to the above. The general workflow begins with finding track segments in the  
 1068 TRT, constructing the track candidates including the silicon hits, and finally ambiguity solving.

### 1069 3.3.2 Electron reconstruction

1070 Electron reconstruction [53] uses information from both the ID and the electromagnetic calorimeters.  
 1071 The characteristic signature of an electron in ATLAS is a charged particle track in the ID that is  
 1072 matched in  $\eta\phi$  to localized clusters of energy deposited in the calorimeter.

1073 Calorimeter cluster candidates are seeded from localized energy deposits according to a sliding-  
 1074 window algorithm [54]. The clusters are a  $3 \times 5$  rectangle of calorimeter towers in  $\eta \times \phi$  with a  
 1075 total transverse energy greater than 2.5 GeV. In the event that two clusters overlap, if the  $E_T$   
 1076 of the clusters vary by more than 10%, the highest  $E_T$  cluster is kept, otherwise the candidate  
 1077 with the highest  $E_T$  in the central tower is kept. The ID tracks are those generated using the  
 1078 algorithm detailed above in Section 3.3.1, and tracks with a nearby calorimeter cluster are re-fit  
 1079 using a Gaussian-sum filter designed to take into account bremsstrahlung effects [55].

1080 To reconstruct the final electron candidate, the refit track and the cluster are subject to the final  
 1081 matching criteria:

$$|\eta_{\text{cluster}} - \eta_{\text{track}}| < 0.05 \quad \text{and} \quad (3.5)$$

$$-0.10 < q \times \Delta\phi_{\text{cluster, track}} < 0.05 \quad \text{or} \quad -0.10 < q \times \Delta\phi_{\text{res}} < 0.05,$$

1082 where  $q$  is the charge of the track and  $\Delta\phi_{\text{res}}$  is the azimuthal separation between the cluster position  
 1083 and the track after rescaling its momentum to the energy of the cluster. If multiple tracks satisfy the  
 1084 above criteria, the primary track is selected by an algorithm that takes into account the center of

1085 each cluster relative to the parameters of the candidate track. Finally, the clusters are reconstructed  
 1086 about the seed cluster using a larger window size,  $3 \times 7$  in the barrel and  $5 \times 5$  in the endcaps, and  
 1087 the energy is calibrated to the original electron energy using techniques described in [56, 57].

1088 **Electron identification** To determine whether an electron candidate is a signal electron or back-  
 1089 ground object, an identification criteria (ID) is implemented, covered in more detail in [53, 58]. Elec-  
 1090 tron ID is performed using a multivariate likelihood technique (LH) that simultaneously evaluates  
 1091 a list of measurements of an electron candidate, including both tracking and calorimeter clustering  
 1092 information. To cover the different requirements of various physics and performance studies, four  
 1093 different likelihood working points are constructed corresponding to increasing thresholds for the  
 1094 LH discriminant: `VeryLooseLH`, `LooseLH`, `MediumLH`, and `TightLH`. Each successive working point is  
 1095 a subset of its predecessors. The efficiencies of the `LooseLH`, `MediumLH`, and `TightLH` working points  
 1096 as a function of electron  $E_T$  are shown in Figure 3.9.

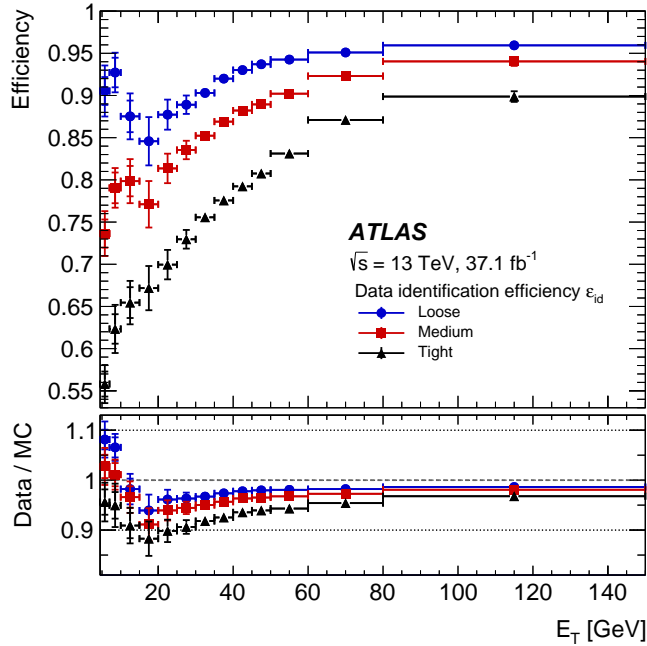


Figure 3.9: Measured LH electron ID efficiencies in  $Z \rightarrow ee$  events for the `LooseLH` (blue), `MediumLH` (red), and `TightLH` (black) working points as a function of electron  $E_T$ . The bottom plot shows data-to-simulation ratios. Plot taken from [53].

1097 **Electron isolation** Signal electrons, such as those from the decay of a  $W$  boson, tend to have  
 1098 little detector activity nearby in both the ID and the calorimeters. Background electrons, such as  
 1099 those from photon conversions or jets, are often produced in association with other particles. To  
 1100 take advantage of this, variables are constructed to quantify the amount of activity within a cone of  
 1101 a specified radius in  $\Delta R$  about an electron in both the tracking systems and the calorimeters.

1102 The track-based isolation consists of the sum of the transverse momentum of tracks within a cone  
 1103 of a specified radius about an electron (not including the electron itself). The tracks are required to  
 1104 have  $p_T > 1$  GeV, satisfy basic quality requirements, and be associated with the vertex from which  
 1105 the electron originated. Additionally, particles from bremsstrahlung radiation are considered part of  
 1106 the original electron and are subtracted from the isolation cone. A variable cone radius dependent  
 1107 on the  $p_T$  of the electron is used in order to compensate for busy detector environments:

$$\Delta R = \min\left(\frac{10 \text{ GeV}}{p_T}, R_{\max}\right), \quad (3.6)$$

1108 where  $R_{\max}$  is the largest allowed cone size, typically set at 0.2 for electrons.

1109 Calorimeter isolation is a bit more difficult due to the size of the energy deposits relative to the  
 1110 cone size, as parts of an energy cluster can lie outside of the cone. As such, topological clusters [59]  
 1111 (topo clusters) are seeded by calorimeter cells with deposited energy greater than four times the  
 1112 expected noise-level of that cell. The cluster is then expanded to incorporate electromagnetic and  
 1113 hadronic cells recording an energy greater than two times their expected noise-levels until no adjacent  
 1114 clusters remain satisfying the requirement. The isolation cone is then the sum of the  $E_T$  of all  
 1115 positive-energy topo clusters whose barycenters fall within a cone of radius  $\Delta R < 0.2$ . The electron's  
 1116 energy is subtracted by removing the cells within a rectangle around the electron.

1117 When applying the isolation selection, *relative isolation* is used, defined as the ratio of the track-  
 1118 or calorimeter-based isolation variable divided by the electron  $p_T$ . Four isolation working points are  
 1119 defined targeting specific values of efficiency. **Loose** and **LooseTrackOnly** target a fixed efficiency  
 1120 value across the  $p_T$  and  $\eta$  spectrum of the electrons, with the latter not applying a cut on calorimeter  
 1121 isolation. **Gradient** and **GradientLoose** target a  $p_T$ -dependent fixed efficiency that is uniform in  
 1122  $\eta$ . The efficiencies for these working points as a function of electron  $E_T$  are shown in Figure 3.10.  
 1123 Additional working points are also provided that instead use fixed values for the relative track and  
 1124 calorimeter isolation cuts.

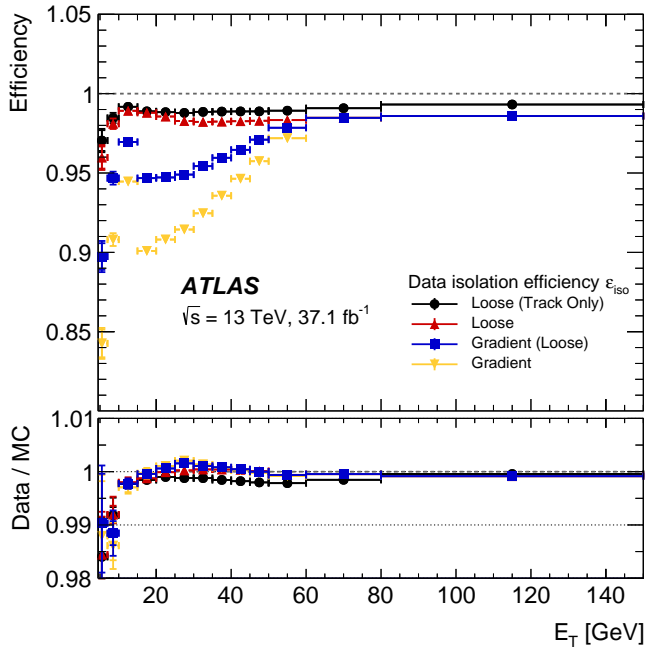


Figure 3.10: Measured isolation efficiencies for the `LooseTrackOnly` (black), `Loose` (red), `GradientLoose` (blue), and `Gradient` (yellow) working points as a function of electron  $E_T$ . The bottom panel shows data-to-simulation ratios. Plot taken from [53].

### 1125 3.3.3 Muon reconstruction

1126 Muon reconstruction [60, 61] first occurs independently in the ID and the MS, and then the infor-  
 1127 mation from both is combined to form the final muon tracks used in analysis. Muons in the ID are  
 1128 reconstructed as a charged particle track following the standard procedure detailed in Section 3.3.1.

1129 In the MS, hits within each muon chamber are collected into segments, with separate algorithms  
 1130 for each of the four different detector components described in Section 3.2.3. Muon track candidates  
 1131 are then built by fitting together segments using a combinatorial search seeded by segments in the  
 1132 middle layers first, and then expanding to the outer and inner layers. A track must contain at least  
 1133 two matching segments, except in the transition region between the barrel and endcap where a single  
 1134 segment can be used. In the event that a segment is shared by multiple tracks, an overlap removal  
 1135 algorithm decides which track should keep the segment, or if it should remain shared. Finally, the  
 1136 hits within each track candidate are fit using a global  $\chi^2$ , and the track is accepted if the  $\chi^2$  satisfies  
 1137 a set of selection criteria.

1138 The ID and MS tracks are then combined according to several different reconstruction criteria

1139 determined by the available information from the ID, MS, and calorimeters. This results in four  
 1140 different muon “types”:

- 1141     • Combined (CB): Independent tracks in the ID and MS are combined with a global track refit  
 1142        using both sets of hits. MS hits may be added or removed if it improves the quality of the  
 1143        track fit. Muons are typically reconstructed outside-in, matching a MS track to one in the ID;  
 1144        however, an inside-out matching is also used as a complementary approach.
- 1145     • Segment-tagged (ST): An ID track is classified as a muon if it can be extrapolated to at least  
 1146        one track segment in the MDT or CSC chambers. These are used when a muon only crosses  
 1147        one layer of the MS, either due to low  $p_T$  or falling in a region of reduced acceptance.
- 1148     • Calorimeter-tagged (CT): An ID track is classified as a muon if it can be matched to a calorime-  
 1149        ter energy deposit compatible with a minimum ionizing particle. These muons are generally  
 1150        lower in purity than the other types, but they are useful for recovering acceptance in the region  
 1151         $|\eta| < 0.1$  where the MS is only partially instrumented.
- 1152     • Extrapolated (ME): The muon is reconstructed using a MS track that is loosely compatible  
 1153        with having originated from the interaction point. The MS track must transverse at least  
 1154        two layers of the MS in the central region and three in the forward region. These muons are  
 1155        generally used to extend the acceptance of muon reconstruction in the forward regions not  
 1156        covered by the ID ( $2.5 < |\eta| < 2.7$ ).

1157 **Muon identification** Muon identification serves to select signal muons with a high quality mo-  
 1158 mentum measurement from backgrounds (mainly from pions and kaons). For CB muons, three  
 1159 variables are used:

- 1160     •  $q/p$  significance: The absolute value of the difference in  $q/p$  of the muons (where  $q$  is the  
 1161        muon’s charge) as measured by the ID and the MS divided by the corresponding uncertainties  
 1162        added in quadrature.
  - 1163     •  $\rho'$ : The absolute value of the difference between the  $p_T$  measurements in the ID and the MS  
 1164        divided by the  $p_T$  of the combined track.
  - 1165     • The normalized  $\chi^2$  of the combined track fit.
- 1166 Additional requirements are imposed on the number of hits within the ID to ensure the tracks’  
 1167 momenta are well measured.

1168 There are three primary muon identification working points<sup>6</sup> of increasing background rejection:  
 1169 **Loose**, **Medium**, and **Tight**. **Loose** muons include all four types listed above, but CT and ST muons  
 1170 are restricted to the region  $|\eta| < 0.1$ . The default recommendation for analysis are **Medium** muons,  
 1171 which only include CB and ME tracks. Finally, **Tight** muons are made up of CB muons with hits in  
 1172 at least two components of the MS and that pass the **Medium** requirements. Each successive working  
 1173 point is a subset of the previous one, and the cuts on the three variables listed above are tightened  
 1174 in each step. The muon reconstruction efficiency for each of these three working points in  $Z \rightarrow \mu\mu$   
 1175 events is shown in Figure 3.11.

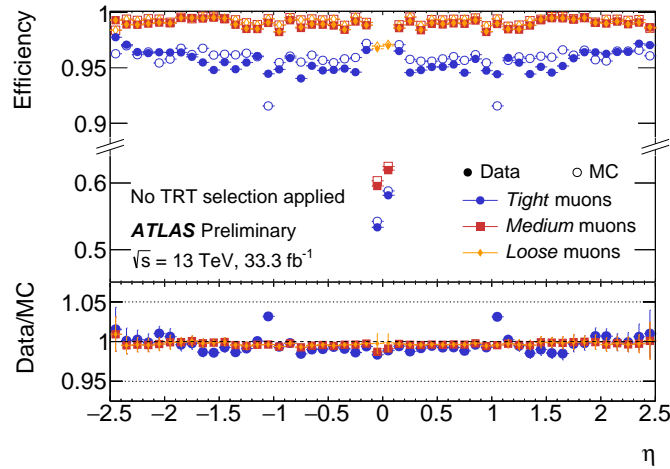


Figure 3.11: Muon reconstruction efficiencies in  $Z \rightarrow \mu\mu$  events for the **Loose** (yellow), **Medium** (red), and **Tight** (blue) ID working points as a function of muon  $\eta$ . The drop in efficiency for **Medium** and **Tight** muons in the range  $|\eta| < 0.1$  is due to the exclusion of CT and ME muons, which are used to recover acceptance in this region. Collision data (solid points) is compared to simulation (open points) and the ratio is in the lower panel. Plot taken from [62].

1166 **Muon isolation** Isolation for muons is handled in much the same way as for electrons (see Section  
 1167 3.3.2). A track-based variable is computed by summing the transverse momenta of tracks with  
 1168  $p_T > 1$  GeV within a cone of variable radius as in Equation 3.6 with  $R_{\max} = 0.3$ . The calorimeter-  
 1169 based isolation again uses topo clusters of radius  $\Delta R < 0.2$  with the energy deposit corresponding  
 1170 to the muon removed. Similar isolation working points are constructed using the same criteria as  
 1171 for electrons, and the efficiency of the **Loose** and **GradientLoose** working points as a function of  
 1172 muon  $p_T$  are shown in Figure 3.12.

<sup>6</sup>A fourth working point, **Highpt**, is optimized for high mass searches, such as  $W'$  and  $Z'$  resonances, and is not covered here.

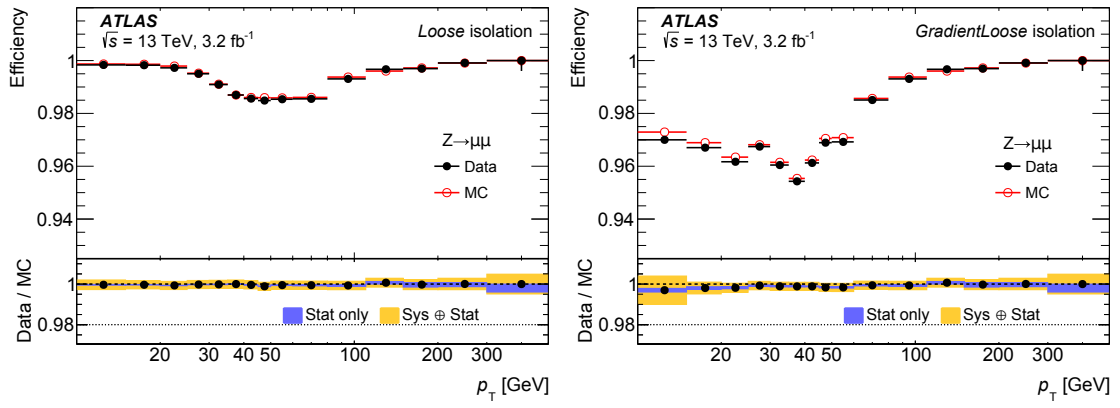


Figure 3.12: Muon isolation efficiencies in  $Z \rightarrow \mu\mu$  events for the Loose (left) and GradientLoose (right) working points as a function of muon  $p_T$ . Collision data (black) is compared to simulation (red) and the ratio is in the lower panel. Plots taken from [61].

## CHAPTER 4

---

# Alignment of the ATLAS Inner Detector

---

1185 As a charged particle passes through the ATLAS ID, it leaves *hits* in the sensors along its path  
 1186 in the form of ionization. The particle's trajectory, or *track*, can be reconstructed from a fit to  
 1187 these hits via the procedure described in Section 3.3.1. In order to reconstruct an accurate particle  
 1188 track, it is necessary to know where in space each hit occurred as precisely as possible, which in turn  
 1189 requires knowledge of the physical location of the sensor that registered the hit. If one of the sensors  
 1190 is displaced relative to its expected position in the known detector geometry, or *misaligned*, the  
 1191 assumed location of the corresponding hit will not match its actual location, resulting in inaccurate  
 1192 track parameters and a poor track fit. The first misalignments were a result of not knowing the  
 1193 exact positions of each sensor after the initial installation of the detector. Subsequent misalignments  
 1194 occur when sensors shift due to mechanical stress and strain, which can be the result of cycles in  
 1195 ATLAS's magnetic field, changes in operating temperatures, or when components are removed and  
 1196 replaced during maintenance. A visualization of how a misaligned detector element can affect the  
 1197 track reconstruction is shown in Figure 4.1.

1198 In order to correct the misalignments, the ID alignment procedure is applied to accurately  
 1199 determine the physical position and orientation of each detector element. The baseline accuracy of  
 1200 the alignment is required to be such that the track parameter resolutions are not degraded by more  
 1201 than 20% with respect to those derived from a perfect detector geometry<sup>7</sup> [38]. This corresponds to  
 1202 a precision of better than 10  $\mu\text{m}$  in the positioning of the elements of the silicon detectors [66].

1203 This chapter covers the ID alignment algorithm and procedure, its implementation during the  
 1204 2015 data taking period, and the steps taken to measure momentum biases that may exist after

---

<sup>7</sup>The so-called *perfect geometry* refers to the description of the ATLAS detector in which every sensor precisely matches its design specifications. The perfect geometry contains no misalignments, and the position of each sensor is known exactly.

1205 alignment.

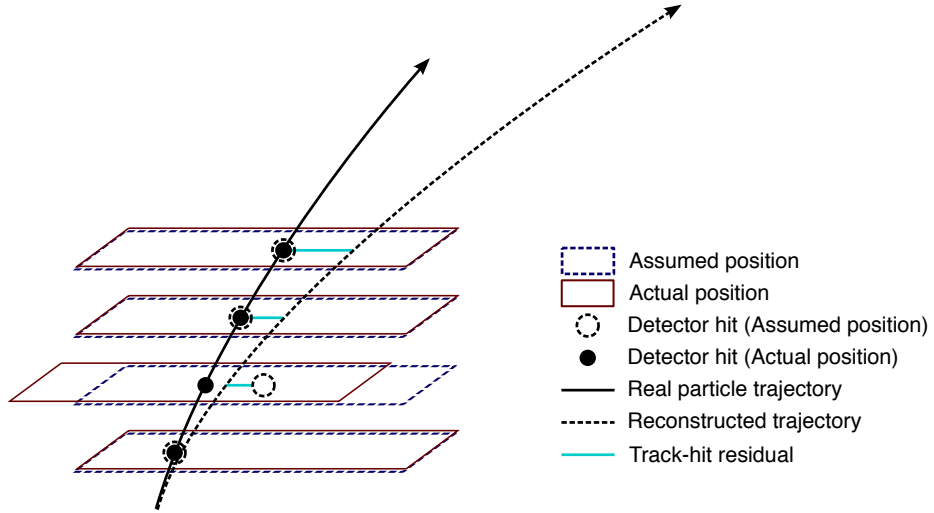


Figure 4.1: Graphical representation of the effect of a misaligned detector element. The reconstructed particle track (dashed arrow) differs from the actual trajectory of the particle (solid arrow) due to a shift in the third detector element. The cyan lines represent the track-to-hit residuals.

## 1206 4.1 The alignment method

1207 The alignment procedure uses a track-based algorithm that updates the locations of detector ele-  
 1208 ments in order to minimize the set of track-hit *residuals*. These residuals are defined as the distance  
 1209 between the where fitted track intersects a given detector element and the position of the actual hit  
 1210 recorded by the same element, shown by the cyan lines in Figure 4.1.

1211 Tracks in ATLAS are parameterized as five-dimensional vectors [64]:

$$\vec{\tau} = (d_0, z_0, \phi_0, \theta, q/p), \quad (4.1)$$

1212 where  $d_0$  and  $z_0$  are the transverse and longitudinal impact parameters with respect to the origin,  
 1213  $\phi_0$  is the azimuthal angle of the track at the point of closest approach to the origin,  $\theta$  is the polar  
 1214 angle, and  $q/p$  is the charge of the track divided by its momentum. The residual for the  $i^{\text{th}}$  hit of a  
 1215 given track can then be written in terms of the track parameters  $\vec{\tau}$  and a set of alignment parameters  
 1216  $\vec{a}$  that describe the hit location [65]:

$$r_i(\vec{\tau}, \vec{a}) = (\vec{m}_i - \vec{e}_i(\vec{\tau}, \vec{a})) \cdot \hat{k}, \quad (4.2)$$

1217 where  $\vec{e}_i$  is the intersection point of the extrapolated track with the sensor, and  $\vec{m}_i$  is the position  
 1218 of the associated hit within the sensor.  $\hat{k}$  is a unit vector corresponding to the direction of the

1219 measurement within the sensor, as shown in Figure 4.2.  $\vec{r}$  then is the vector of residuals for the  
 1220 track.

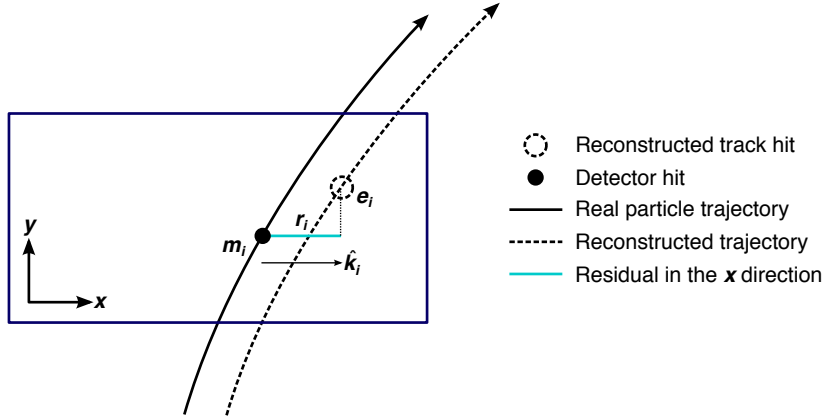


Figure 4.2: Graphical representation of a track-hit residual in the local  $x$  direction according to Equation 4.2. The sensor in this example measures a particle hit in the local  $x$  and  $y$  directions, with each having its own residual.

1221 A  $\chi^2$  function can be built from the residuals of all collected tracks:

$$\chi^2 = \sum_{\text{tracks}} \vec{r}^T V^{-1} \vec{r}, \quad (4.3)$$

1222 where  $V$  is the covariance matrix of the hit measurements. The  $\chi^2$  function is then minimized with  
 1223 respect to the alignment parameters  $\vec{a}$ , which contain all degrees of freedom being aligned. The  
 1224 minimization condition with respect to  $\vec{a}$  is

$$\frac{d\chi^2}{d\vec{a}} = 0 \rightarrow 2 \sum_{\text{tracks}} \left( \frac{d\vec{r}}{d\vec{a}} \right)^T V^{-1} \vec{r} = 0. \quad (4.4)$$

1225 This equation can be difficult to solve exactly, so the residual is rewritten as a first order Taylor  
 1226 expansion:

$$\vec{r} = \vec{r}_0 + \frac{d\vec{r}}{d\vec{a}} \delta \vec{a}, \quad (4.5)$$

1227 where  $\vec{r}_0$  is dependent on an initial set of track and alignment parameters  $\vec{r}_0$  and  $\vec{a}_0$ , respectively;  
 1228 the dependence of  $\vec{r}$  on the track parameters is included when evaluating the total derivative  $\frac{d\vec{r}}{d\vec{a}}$ .  
 1229 Equation 4.5 can then be inserted into the minimization condition from Equation 4.4 to give

$$\left[ \sum_{\text{tracks}} \left( \frac{d\vec{r}}{d\vec{a}} \right)^T V^{-1} \left( \frac{d\vec{r}}{d\vec{a}} \right) \right] \delta \vec{a} + \sum_{\text{tracks}} \left( \frac{d\vec{r}}{d\vec{a}} \right)^T V^{-1} \vec{r}_0 = 0. \quad (4.6)$$

1230 From this equation, the alignment matrix  $\mathcal{M}_a$  and alignment vector  $\vec{\nu}_a$  can be defined:

$$\mathcal{M}_a = \sum_{\text{tracks}} \left( \frac{d\vec{r}}{d\vec{a}} \right)^T V^{-1} \left( \frac{d\vec{r}}{d\vec{a}} \right) \quad (4.7)$$

1231

$$\vec{\nu}_a = \sum_{\text{tracks}} \left( \frac{d\vec{r}}{d\vec{a}} \right)^T V^{-1} \vec{r}_0. \quad (4.8)$$

1232 Finally, the alignment corrections  $\delta\vec{a}$  can be solved for by inverting the alignment matrix:

$$\delta\vec{a} = -\mathcal{M}_a^{-1} \vec{\nu}_a, \quad (4.9)$$

1233 which results in a system of linear equations of a size equal to the number of alignment degrees of  
1234 freedom [66].

1235 Inverting the full matrix and solving the resulting system of equations is referred to as *Global*  
1236  $\chi^2$  alignment [65]. This can be useful, as  $\mathcal{M}_a$  contains all the correlations between the structures  
1237 that are being aligned, or *alignable structures*. However, inverting the matrix is difficult when the  
1238 number of degrees of freedom becomes large—as the number of alignable structures increases, so  
1239 too does the size of the matrix  $\mathcal{M}_a$ . Eventually, inverting the matrix becomes too computationally  
1240 intensive to be practical.

1241 This problem is solved by the *Local*  $\chi^2$  algorithm [67]. In this case, the alignment matrix is  
1242 constructed to be block-diagonal, allowing for it to be easily inverted even for large numbers of  
1243 degrees of freedom. This is achieved by replacing the full derivative in Equation 4.6 with the partial  
1244 derivative  $\frac{\partial\vec{r}}{\partial\vec{a}}$ . The new alignment matrix  $\mathcal{M}'_a$  and alignment vector  $\vec{\nu}'_a$  become

$$\mathcal{M}'_a = \sum_{\text{tracks}} \left( \frac{\partial\vec{r}}{\partial\vec{a}} \right)^T V^{-1} \left( \frac{\partial\vec{r}}{\partial\vec{a}} \right) \quad (4.10)$$

1245

$$\vec{\nu}'_a = \sum_{\text{tracks}} \left( \frac{\partial\vec{r}}{\partial\vec{a}} \right)^T V^{-1} \vec{r}_0. \quad (4.11)$$

1246 Inverting  $\mathcal{M}'_a$  is considerably faster and requires less computing memory compared to  $\mathcal{M}_a$ , even for  
1247 large numbers of degrees of freedom; however, the correlations between the alignable structures is  
1248 lost. Due to the Taylor expansion used in Equation 4.6, several iterations of the alignment algorithm  
1249 may be necessary to converge on a final set of alignment constants. The Local  $\chi^2$  alignment typically  
1250 requires more iterations due to the loss of the correlation information [68].

1251 In practice, the ATLAS reconstruction is run over a set of events, and the resulting tracks are  
1252 fed to the alignment algorithm. The residuals are calculated, the alignment matrix is built and  
1253 inverted, and a new set of alignment constants is obtained. The convergence is checked in two ways:

- 1254 1. Measuring change in the  $\chi^2$  with respect to the previous iteration. If it is near zero, then the  
1255  $\chi^2$  is approaching its minimum.
- 1256 2. Looking at the residual distributions for different alignable structures. A well aligned detector  
1257 will have a residual distribution that is approximately Gaussian, with a mean of zero with a  
1258 width approximating the intrinsic resolution of the detector.
- 1259 If the above checks are satisfied, the process is finished, and the final set of alignment constants are  
1260 obtained; if not, another iteration is performed. A visual representation of the alignment chain is  
1261 shown in Figure 4.3.

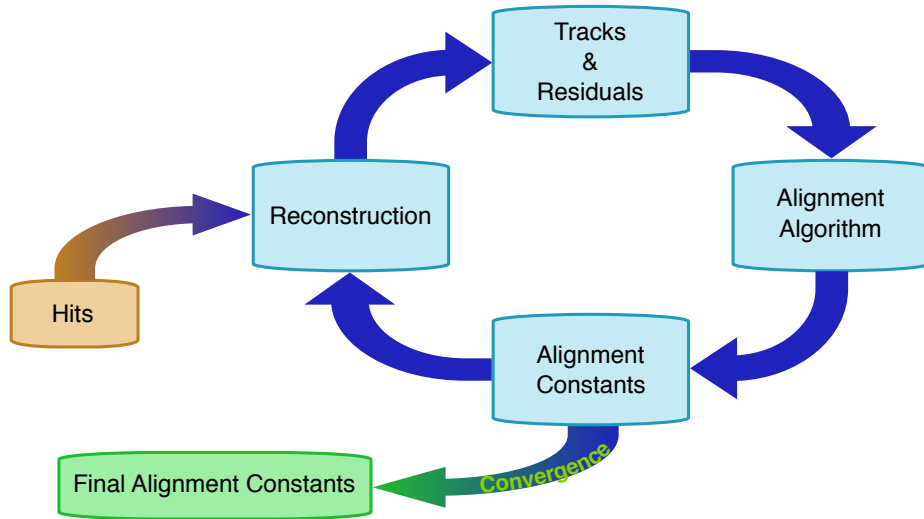


Figure 4.3: Flow chart depicting the ID alignment chain.

1262 Since a  $\chi^2$  minimization is used to align the detector, if there is a systematic misalignment in  
1263 the detector that does not adversely affect the  $\chi^2$ , the algorithm will be insensitive to it. These  
1264 misalignments are referred to as *weak modes*, and special care is taken to remove them [69]. One  
1265 potential impact of weak modes is a bias in the track momentum of reconstructed particles. This  
1266 particular effect is the subject of Section 4.4.

1267 The detector is aligned both in “real-time” as data is collected and during dedicated offline  
1268 alignment campaigns. The real-time alignment is performed in ATLAS’s *calibration loop*, which  
1269 comprises the first stage in the preparation of data for physics analysis. The calibration loop requires  
1270 the alignment—as well as various other detector calibrations—to be available within 48 hours for

initial data processing. A fast, coarse-grained alignment<sup>8</sup> is run on a subset of the available data containing full tracking information, and the results are propagated to the reconstruction of that particular dataset [70]. Due to the time constraints imposed on the calibration loop, a full sensor-by-sensor alignment is not possible.

The more thorough and finely tuned alignments are reserved for dedicated alignment campaigns, typically near the beginning and at the end of data taking campaigns. The former generally occurs once a sufficient amount of data is collected after a detector shutdown, in order to obtain a good baseline alignment for use in the remainder of the data taking period. One such alignment campaign, the initial offline alignment of the ATLAS detector at the beginning of Run 2, is the subject of Section 4.2. Once data taking is complete, a new set of alignment constants is derived for the full set of available data, and it is typically divided into several “blocks” to account for potential run-by-run shifts in the alignment constants. The data is then reprocessed using the newly derived detector geometry.

#### 4.1.1 Alignment levels

The alignment of the detector is performed at several levels of increasing granularity. This adds flexibility in being able to align only as finely as needed, and it also allows for global, detector-level misalignments to be corrected first before dealing with finer adjustments. The main alignment levels are as follows:

- Level 1 (L1) alignment involves moving entire subdetector components as a single unit. The entire Pixel detector (barrel and endcaps) is treated as a single structure, while the SCT and TRT barrel and endcaps are individually aligned. These often have the largest misalignments, but they are easily corrected and do not require large volumes of data to do so.
- Level 2 (L2) alignment treats individual layers in the silicon detectors (modules in the TRT) and end cap disks as individual alignable objects.
- Level 2.7 (L27) alignment was introduced with the addition of the IBL to the ID in Run 2. It involves the stave-by-stave alignment of the IBL and Pixel barrel<sup>9</sup>.

---

<sup>8</sup>The calibration loop runs up to a Level 2 alignment in the silicon detectors, which involves treating each layer of sensors as a single object. The alignment levels are defined in greater detail in Table 4.1.

<sup>9</sup>Even though the IBL is considered a part of the Pixel Detector, for the purposes of this Chapter, “Pixel” will refer to the original three layers of the Pixel barrel and its endcaps, and the IBL will be referenced separately.

1297     • Level 3 (L3) alignment treats each module in the silicon detectors and each straw in the TRT  
 1298       as an individual alignable object. It is the finest grained alignment available but also the most  
 1299       computationally intensive due to the large number of degrees of freedom. Due to the large  
 1300       number of individual detector elements being aligned, high statistics are required.

1301     The different alignment levels are listed in more detail in Table 4.1, including the number of alignable  
 1302       structures and associated degrees of freedom for each detector component.

1303     The implementation of the alignment algorithm in the software is flexible enough to allow each  
 1304       subsystem to be aligned individually at a specified level. Each alignable structure has six degrees of  
 1305       freedom: 3 translations ( $T_x, T_y, T_z$ ) and 3 rotations ( $R_x, R_y, R_z$ )<sup>10</sup>; however individual degrees of  
 1306       freedom may be turned on and off as required. In a typical alignment job, L1 and L2 contain few  
 1307       enough degrees of freedom that the Global  $\chi^2$  algorithm can be used, but L3 alignments (which can  
 1308       contain over 36,000 degrees of freedom in the silicon detectors alone) require the Local  $\chi^2$  algorithm.

#### 1309     **4.1.2 Alignment coordinate systems**

1310     The global coordinate system ( $x, y, z$ ) used by the ID alignment matches that of the ATLAS detector  
 1311       in general. The positions and orientations of individual detector modules of the ID are defined by  
 1312       a right-handed local coordinate system ( $x', y', z'$ ) where the origin is defined as the geometrical  
 1313       center of the module. The  $x'$ -axis for each silicon module is defined to point along the most sensitive  
 1314       direction of the module, the  $y'$ -axis is oriented along the long side of the module, and the  $z'$ -axis is  
 1315       orthogonal to the  $(x', y')$  plane. For the TRT straws, the  $x'$ -axis is perpendicular to both the wire  
 1316       and the radial direction, defined from the origin of the global frame to the straw center, the  $y'$ -axis  
 1317       points along the straw, and once again the  $z'$ -axis is orthogonal to the  $(x', y')$  plane. A depiction of  
 1318       the global and local coordinate systems for the ID is shown in Figure 4.4.

1319     When considering the alignment degrees of freedom listed earlier in Section 4.1.1, grouped collec-  
 1320       tions of modules, layers, or entire subdetectors use the global coordinate system; individual modules  
 1321       use their respective local coordinate systems. The translations  $T_i$  are with respect to the origin of  
 1322       the given reference frame, and the rotations  $R_i$  are taken about the Cartesian axes.

---

<sup>10</sup>The TRT is an exception, as the subdetector does not have any resolution along the length of the straw. Therefore, for the barrel,  $T_z$  is omitted. Similarly for the straws themselves, only two parameters are defined: translation with respect to the radial direction ( $T_\phi$ ) and rotation with respect to the radial axis ( $R_r$  for the barrel and  $R_z$  for the end-caps) [71].

Level	Description of alignable structure	Structures	DoF
1	IBL detector	1	6
	Whole Pixel detector	1	6
	SCT barrel and 2 end-caps	3	18
	TRT barrel and 2 end-caps ( $T_z$ fixed)	3	17
Total:		8	47
2	IBL detector	1	6
	Pixel barrel layers	3	18
	Pixel end-cap disks	$2 \times 3$	36
	SCT barrel layers	4	24
	SCT end-cap disks	$2 \times 9$	108
	TRT barrel 32 modules ( $T_z$ fixed)	$3 \times 32$	480
	TRT end-cap wheels	$2 \times 40$	480
Total:		208	792
2.7	IBL staves	14	84
	Pixel barrel staves	$22+38+52$	672
	Pixel end-cap disks	$2 \times 3$	18
	Total:		132
3	IBL modules	280	1,680
	Pixel modules	1,744	10,464
	SCT modules	4,088	24,528
	TRT barrel wires ( $T_\phi, R_r$ only)	105,088	210,176
	TRT end-cap wires ( $T_\phi, R_Z$ only)	245,760	491,520
	Total silicon sensors:	6,112	36,672
Total TRT wires:		350,848	701,696

Table 4.1: The four alignment levels for each of the detector subsystems and their components (first introduced in Section 3.2). The total number of alignable structures and degrees of freedom (DoF) to be aligned are given for each level.

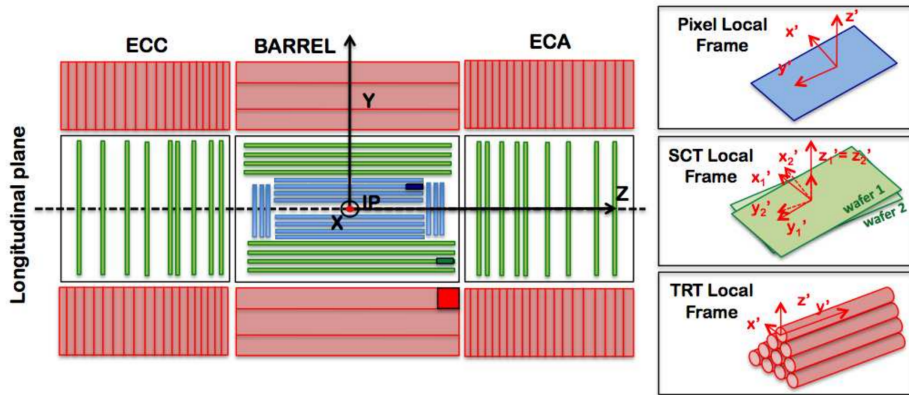


Figure 4.4: A schematic representation of the Inner Detector in the longitudinal plane with the global coordinate system overlaid on top. The Pixel detector and IBL are shown in blue, the SCT in green, and the TRT in red. The local coordinates for each subdetector module are inset on the right. Image taken from [72].

---

1323 **4.2 Early 2015 alignment of the ATLAS detector**

1324 At the end of Run 1, the LHC was shut down for upgrades and maintenance. During this time,  
 1325 a number of upgrades were performed on the ATLAS detector, including the installation of the  
 1326 Insertable B-Layer (IBL), mounted on a new beam pipe. These changes to the ID required some de-  
 1327 tector components to be removed temporarily, and many elements shifted relative to each other over  
 1328 the course of the maintenance process. In order to correct for these large detector movements prior to  
 1329 13 TeV data taking, an alignment was performed using cosmic ray data collected in early 2015 [72].  
 1330 This alignment was able to correct for the majority of the large detector-wide misalignments as well  
 1331 as determine the global position of the IBL at the micron level.

1332 In June of 2015, shortly after the data taking period began, the first track-based alignment of  
 1333 the refurbished ID was performed using the initial  $7.9 \text{ pb}^{-1}$  of  $\sqrt{s} = 13 \text{ TeV}$  proton-proton collision  
 1334 data [73]. Starting from the geometry determined by the cosmic ray alignment, referred to hereafter  
 1335 as the *March alignment*, an improved set of alignment constants (the *June alignment*) was derived  
 1336 from a data set of approximately 1.4 million selected tracks. A sample of Monte Carlo (MC) events  
 1337 containing approximately 2.7 million tracks from dijet events simulated using a perfect detector  
 1338 geometry is used as a comparison to the data; the MC events are reweighted to match the  $\eta$  and  $p_T$   
 1339 distributions found in the data. Additional validation of the alignment results uses a set of cosmic  
 1340 ray data collected by the detector during the LHC collisions.

1341 **4.2.1 June alignment procedure**

1342 The data set used as the input for the alignment is made up of a subset of physics events used for  
 1343 prompt reconstruction recorded at a rate of 10 Hz. To ensure that only high quality tracks are used  
 1344 for the alignment, each track is required to have transverse momentum  $p_T > 3 \text{ GeV}$ , contain at least  
 1345 one hit in the Pixel detector, at least seven hits in the combined silicon detectors (IBL, Pixel, and  
 1346 SCT), and at least 25 hits in the TRT.

1347 A full L3 alignment of the IBL was included in the March alignment; however, a realignment was  
 1348 still necessary. Since cosmic rays pass through the detector top-down, the staves on the sides of the  
 1349 IBL recorded fewer hits and thus could not be aligned as precisely as those on the top and bottom.  
 1350 Additionally, the IBL was operating at a temperature of  $-20^\circ\text{C}$  during the cosmic data taking, and  
 1351 it was set to  $-10^\circ\text{C}$  for collision data taking. This proved to be significant, as it was observed that  
 1352 the IBL staves experience a temperature-dependent, parabolic bowing in the local  $x$ -direction of  
 1353 approximately  $-10 \mu\text{m}/\text{K}$  [74]. As a result, a full L3 alignment of the IBL was essential in order to

1354 correct for the bowing. Due to it being a brand new element of the detector as well as its importance  
 1355 in vertexing and  $b$ -jet tagging, aligning the IBL sensors with a high degree of precision was one of  
 1356 the main goals of the June alignment.

1357 The June alignment was performed in two stages, with the first pass focusing on relative move-  
 1358 ments of the big structures and correcting for the bowing of the IBL. The March alignment corrected  
 1359 for these larger movements as well; however, it was observed during Run 1 that these sort of mis-  
 1360 alignments are introduced by changing conditions in the detector [69], such as adjustments in the  
 1361 cooling system settings or magnet power cycling, which may have occurred between the early cos-  
 1362 mic data taking and the first  $\sqrt{s} = 13$  TeV collisions. The silicon detectors were aligned at several  
 1363 different levels and the IBL was aligned at the module level; the TRT detector was kept fixed to  
 1364 act as a global reference frame. The full alignment chain for the first pass consisted of the following  
 1365 steps:

- 1366 1. The IBL, Pixel, and SCT detectors were aligned at L1. The SCT barrel was not aligned in  
   1367  $T_z$  in order to constrain global displacements along the  $z$ -axis, as the TRT is not sensitive to  
   1368 that degree of freedom.
- 1369 2. The IBL, and Pixel barrel and end-caps, and SCT barrel were aligned at L2. The SCT end-caps  
   1370 were aligned at L1.
- 1371 3. The IBL and pixel barrel were aligned at L27, using all six degrees of freedom. The Pixel  
   1372 end-cap disks were only aligned in the plane ( $T_x$ ,  $T_y$ , and  $R_z$ ). The SCT was treated the same  
   1373 as in the previous step.
- 1374 4. The IBL was aligned at L3 using all six degrees of freedom for each module.

1375 The primary goal for the second pass was to remove a bias in the transverse impact parameter  
 1376  $d_0$  found in the March alignment. In addition to the bias, the resolution of  $d_0$  was also observed  
 1377 to be poorer than expected. In order to correct for this, an additional constraint was passed to  
 1378 the alignment which added the impact parameter with respect to the beam spot as a pseudo-  
 1379 measurement [75]. With this setup, when the alignment algorithm minimizes the  $\chi^2$ , it will take  
 1380 care of the impact parameter minimization as well. Only the IBL and Pixel detectors were aligned  
 1381 in the second pass. The different alignment stages are listed below, with the beam spot constraint  
 1382 being used in each:

- 1383 1. The IBL and Pixel detectors were aligned at L2 with the SCT fixed.

- 1384     2. The IBL was aligned at L27
- 1385     3. The IBL and Pixel barrel and end-caps were aligned at L3.
- 1386     The set of alignment constants obtained at the end of the second pass represents the June alignment.
- 1387     The highest level of alignment each subdetector received over the course of the two passes is listed
- 1388     in Table 4.2.

Detector	Highest level of alignment	
IBL	L3	
Pixel	Barrel	L3
	End-caps	L3 ( $T_x$ , $T_y$ , and $R_z$ only)
SCT	Barrel	L2 (except $T_z$ )
	End-caps	L1
TRT	None	

Table 4.2: Summary of the highest level of alignment applied to each ID subsystem when deriving the June alignment.

### 1389 4.2.2 Alignment results

1390     Alignment quality is primarily assessed by looking at the track-hit residual distributions. If the  
 1391     detector is well aligned, the residuals will be Gaussian-distributed with a mean of zero and a width  
 1392     approximating the detector’s resolution. The residual distributions are constructed from the same  
 1393     selection of tracks that were used to perform the alignment, and are the focus of Section 4.2.2.1.  
 1394     A second check on the alignment involves observables sensitive to the track parameter resolution.  
 1395     In this case, cosmic rays are used, making use of a “split track” technique that takes advantage of  
 1396     the top-to-bottom cosmic ray trajectory (compared to the center-out trajectory of collision tracks).  
 1397     This method and the corresponding tests of the alignment are detailed in Section 4.2.2.2

1398         Additionally, the effect of the beam spot constrained alignment on the impact parameter  $d_0$   
 1399     needed to be checked. The  $d_0$  distributions for both the March and June alignments are compared  
 1400     to the MC simulation using a perfect geometry in Figure 4.5. In the March alignment, there is  
 1401     a clear bias of 18  $\mu\text{m}$  in the mean of the distribution and the width is nearly twice that of the  
 1402     perfect geometry. After the second pass of the June alignment, the mean has shifted to 1  $\mu\text{m}$  and  
 1403     the distribution has narrowed considerably. From this, it appears that the constrained alignment  
 1404     successfully removed the  $d_0$  bias.

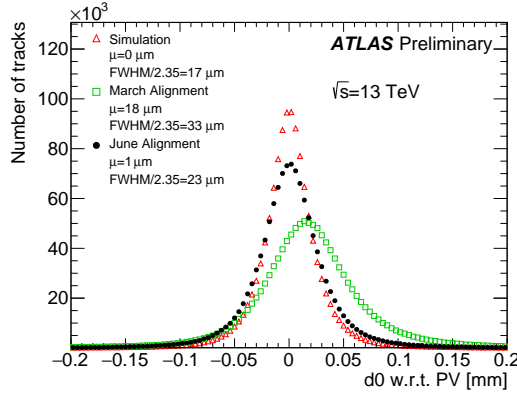


Figure 4.5: The  $d_0$  distributions with respect to the reconstructed primary vertex using 13 TeV collision data sample reconstructed using the June (black) and March (green) alignments. The data is compared to a MC simulation using a perfect detector geometry (red). The distributions are normalized to the same number of entries.

#### 1405 4.2.2.1 Residual distributions from collisions

1406 As mentioned previously, the primary focus of the June alignment campaign was on the IBL and the  
 1407 Pixel detectors. These subdetectors are the closest to the beam line and have the finest resolutions  
 1408 within the ID. The residual distributions in local  $x$  and  $y$  of the IBL planar sensors<sup>11</sup> are shown in  
 1409 Figure 4.6. These and subsequent figures in this section compare the June and March alignments to  
 1410 the perfectly-aligned MC simulation. Noticeable improvement in the distribution widths can be seen  
 1411 in both the local  $x$ - and  $y$ -directions, nearly matching the simulation in local  $x$ , the most sensitive  
 1412 direction.

1413 Due to the temperature-dependent bowing of the IBL, it is also interesting to look at the means of  
 1414 the residual distributions for each ring of IBL sensors along the beam line, as shown in Figure 4.7. A  
 1415 deformation is clearly visible in the March alignment in both measurement directions, and the shape  
 1416 in the local  $x$ -direction is consistent with an average stave bowing due to the different operating  
 1417 temperature of the IBL during the March alignment and the 13 TeV collisions. This feature was  
 1418 nearly eliminated in both directions through the L3 alignment of the IBL sensors.

1419 The local  $x$  and  $y$  residual distributions for the Pixel detector barrel and end-caps are shown  
 1420 in Figures 4.8 and 4.9. Even though the IBL is not included in the plots of the barrel, some of  
 1421 the noticeable improvement in the more sensitive local  $x$ -direction is an effect of the improved IBL  
 1422 alignment. Similarly, the relatively broad local  $y$  residual distribution in the barrel likely indicates

<sup>11</sup>The IBL contains 12 planar sensors in the center of a stave, with four 3D sensors on either end. Only the planar sensors are shown here due to low statistics in the 3D sensors as well as poor MC modeling of these sensors.

that further refinement of the IBL alignment was needed along that direction. Even so, the June alignment outperforms the March alignment and rivals the simulation in most of the plots.

Similar distributions for the SCT and TRT barrel and end-caps are shown in Figures 4.10 and 4.11, respectively. Much like with the Pixel residuals, there is a reduction in the width of the TRT residuals between the March and June alignments due to the alignment of the other subdetectors improving the quality of the track fit. Even though neither subdetector was aligned at module-level, the residuals indicate that the previous L3 alignment performed in Run 1 did not degrade significantly during the upgrade and maintenance period.

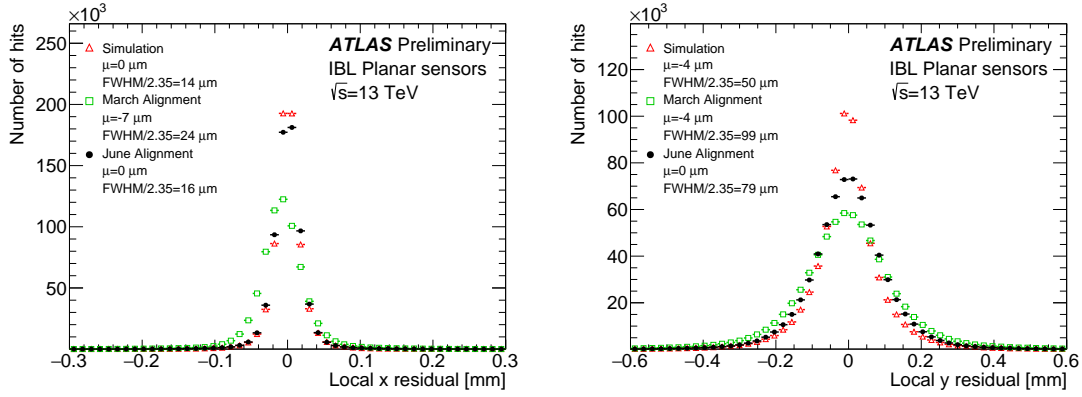


Figure 4.6: Local  $x$  (left) and local  $y$  (right) residual distributions of the IBL planar sensors using 13 TeV collision data sample reconstructed using the June (black) and March (green) alignments. The data is compared to a MC simulation using a perfect detector geometry (red). The distributions are normalized to the same number of entries.

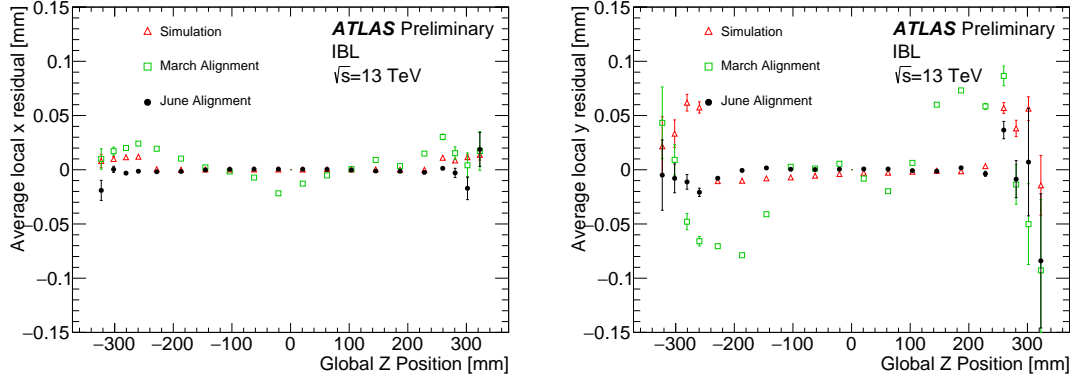


Figure 4.7: The mean of the local  $x$  (left) and local  $y$  (right) residual distributions as a function of the global  $z$  position of each IBL module using 13 TeV collision data sample reconstructed using the June (black) and March (green) alignments. The data is compared to a MC simulation using a perfect detector geometry (red).

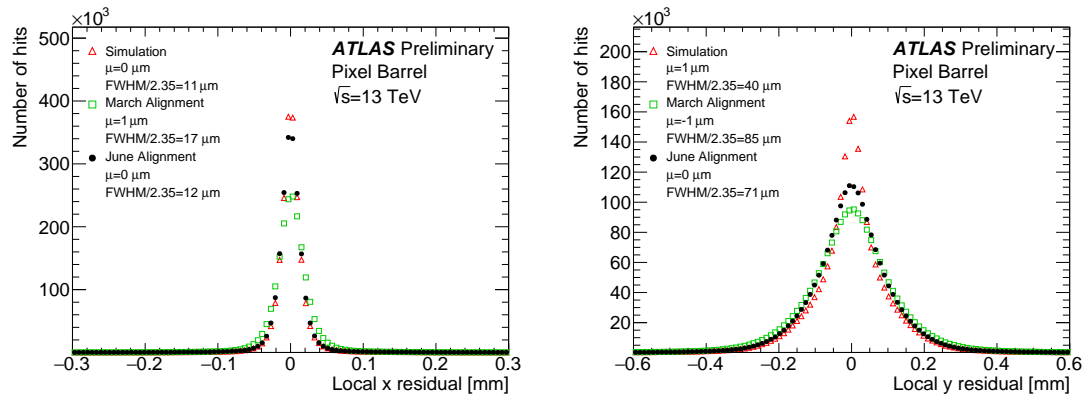


Figure 4.8: Local  $x$  (left) and local  $y$  (right) residual distributions for the Pixel barrel (excluding the IBL) using 13 TeV collision data sample reconstructed using the June (black) and March (green) alignments. The data is compared to a MC simulation using a perfect detector geometry (red). The distributions are normalized to the same number of entries.

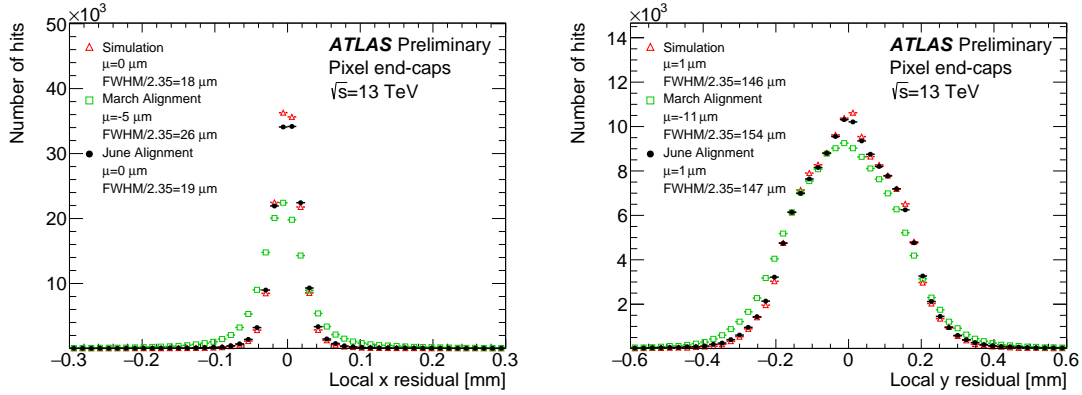


Figure 4.9: Local  $x$  (left) and local  $y$  (right) residual distributions for the Pixel end-caps using 13 TeV collision data sample reconstructed using the June (black) and March (green) alignments. The data is compared to a MC simulation using a perfect detector geometry (red). The distributions are normalized to the same number of entries.

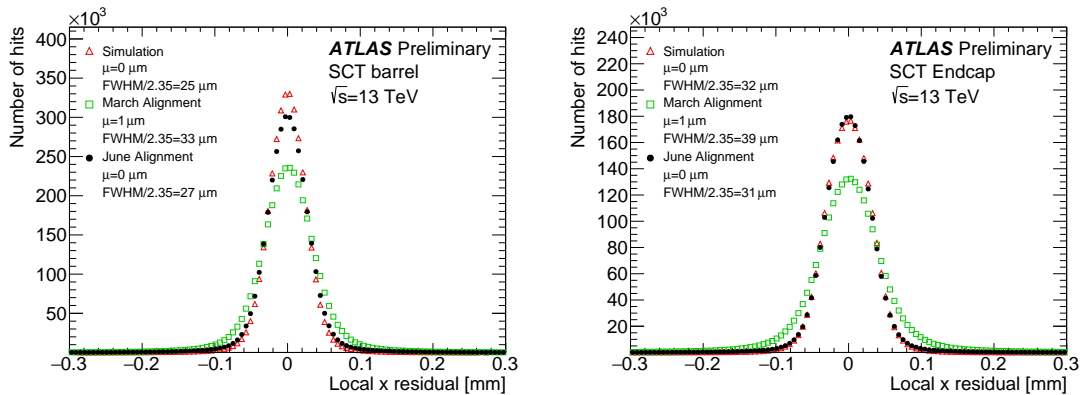


Figure 4.10: Local  $x$  residual distributions for the SCT barrel (left) and end-caps (right) using 13 TeV collision data sample reconstructed using the June (black) and March (green) alignments. The data is compared to a MC simulation using a perfect detector geometry (red). The distributions are normalized to the same number of entries.

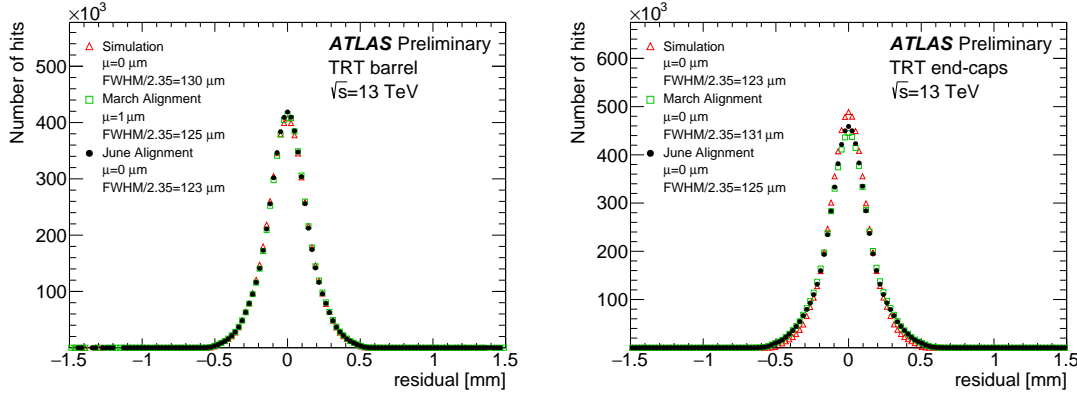


Figure 4.11: Residual distributions for the TRT barrel (left) and end-caps (right) using 13 TeV collision data sample reconstructed using the June (black) and March (green) alignments. The data is compared to a MC simulation using a perfect detector geometry (red). The distributions are normalized to the same number of entries.

#### 1431 4.2.2.2 Track parameter resolution from cosmic rays

1432 Cosmic ray data is very useful as an independent check on the alignment in the barrel of the detector.  
 1433 While tracks from proton-proton collisions originate within the detector and travel outwards, a  
 1434 cosmic ray that passes through the center of the detector leaves a track in both halves of the  
 1435 detector. If the cosmic ray is split in half, as in Figure 4.12, then it can be treated as two separate  
 1436 tracks each with nearly identical track parameters (some differences arise due to energy loss as the  
 1437 particle passes through the detector). The distribution of the difference in a given track parameter  
 1438  $\Delta\tau$  is approximately Gaussian with a variance  $\sigma^2(\Delta\tau)$ . Since both tracks come from the same  
 1439 particle, each track individually has a variance equal to  $\sigma^2(\Delta\tau)/2$ . The resolution of the track  
 1440 parameter is then given by the root mean square of the distribution divided by  $\sqrt{2}$ .

1441 Cosmic rays whose split tracks each have transverse momentum  $p_T > 2$  GeV and at least one,  
 1442 eight, and 25 hits in the barrels of the Pixel, SCT, and TRT detectors, respectively, were selected to  
 1443 measure a collection of track parameters. Figure 4.13 shows the difference in the impact parameter  
 1444  $\Delta d_0$  and the charge divided by the transverse momentum  $\Delta q/p_T$  of the selected split-track cosmic  
 1445 rays for both the March and June alignments. Both distributions show a reduction in width in the  
 1446 June alignment, corresponding to an improvement in the resolution of each track parameter. The  
 1447  $\Delta d_0$  plot in particular shows significant improvement with the June alignment, further validating  
 1448 the removal of the bias in the impact parameter.

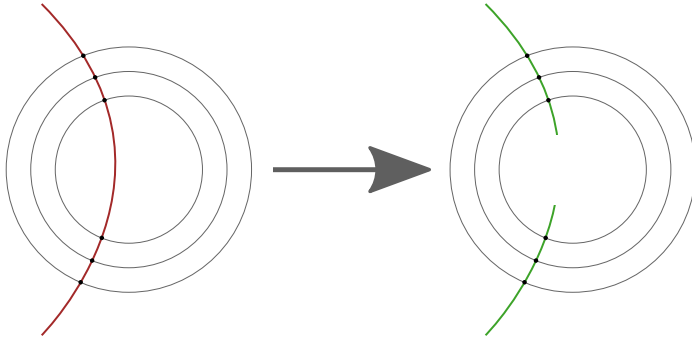


Figure 4.12: Representation of splitting a single cosmic ray track passing through the entire detector (left) into two separate tracks (right).

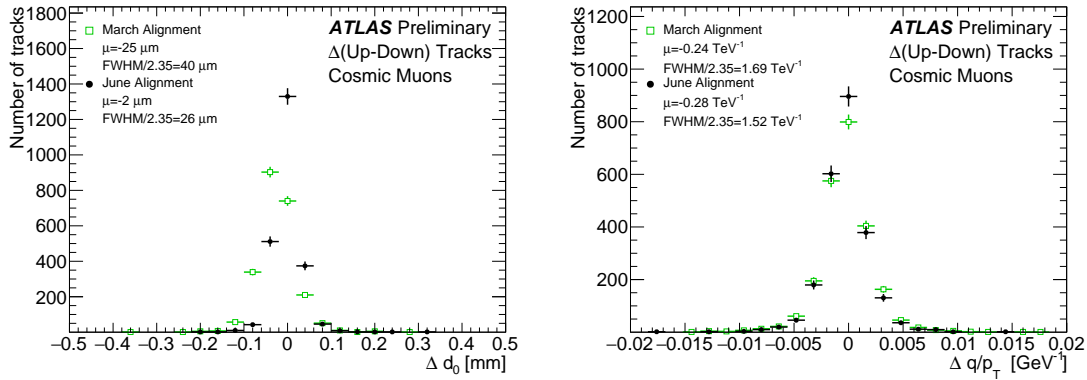


Figure 4.13: Distribution of the difference in the impact parameter  $\Delta d_0$  (left) and charge over transverse momentum  $\Delta q/p_T$  (right) between the two cosmic ray split tracks. The June (black) and March (green) alignments are compared. The distributions are normalized to the same number of entries.

#### 1449 4.2.3 Error scaling

1450 The final step in preparing the new set of June alignment constants deals with the adjustment of  
 1451 the hit errors, or *error scaling*. Knowledge of the exact position of a hit measurement on a track  
 1452 is limited by the accuracy with which the sensors' positions are known. Let  $\sigma$  represent the hit  
 1453 uncertainty used in track fitting, and  $\sigma_0$  be the detector's intrinsic uncertainty. If  $\sigma = \sigma_0$ , the pull  
 1454 of the track-hit residual distributions should form a Gaussian distribution centered at zero with unit  
 1455 width [66]. In the case of residual misalignment, the pull distributions' standard deviations will  
 1456 stray from unity. The hit uncertainty can be written as

$$\sigma = a \cdot \sigma_0 \oplus b, \quad (4.12)$$

1457 where  $a$  is a scaling factor, and  $b$  is a constant term which can be interpreted as a measure of any  
 1458 remaining misalignment of the detector elements. In the June alignment campaign, the value of  $a$   
 1459 was fixed at  $a = 1$ , and  $b$  was evaluated from the residual pull distributions for each subdetector in  
 1460 its sensitive directions.

1461 Once the value of  $b$  is determined, pull distributions derived from the new value of  $\sigma$  should  
 1462 have unit width. The error scaling values for each subdetector are listed in Table 4.3, and the pull  
 1463 distributions for the IBL after error scaling are shown in Figure 4.14

Detector	Coordinate	$b(\mu\text{m})$
IBL	$x$	6.4
	$y$	43.6
Pixel	$x$	5.2
	$y$	28.6
SCT	$x$	7.5
	$y$	0
TRT	$x$	10.8
	$r\phi$	8.6
TRT	$r\phi$	0
	$r\phi$	0

Table 4.3: Estimated value of the error scaling term  $b$  for each subdetector component with the June alignment.

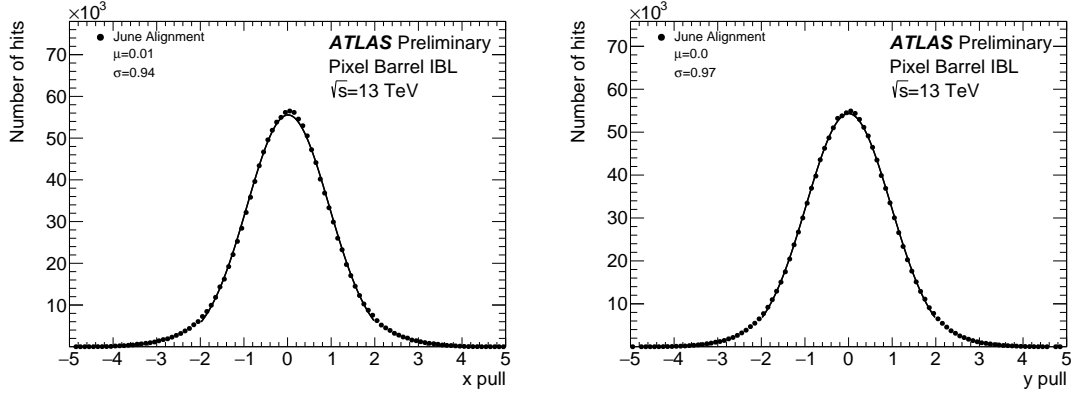


Figure 4.14: Pull distributions in local  $x$  (left) and  $y$  (right) for the IBL using 13 TeV collision data sample after applying the error scaling.

1464 **4.3 Level 2 alignment of the TRT**

1465 During validation of the final end-of-year reprocessing of the 2015 data, a misalignment was found in  
 1466 the barrel of the TRT detector, as several modules (triangular clusters of straws) showed rotations  
 1467 in the local  $y$  coordinate. The then-best available constants included a full L3 alignment of the  
 1468 silicon detectors and a separate L2 alignment of the TRT. However, not all degrees of freedom were  
 1469 enabled when the TRT was aligned. To correct for these tilts, an additional four iterations of L2  
 1470 alignment was performed on the TRT enabling all available degrees of freedom ( $T_x$ ,  $T_y$ ,  $R_x$ ,  $R_y$ , and  
 1471  $R_z$  in the barrel, and  $T_x$ ,  $T_y$ , and  $R_z$  for the endcaps). Plots of the residual means from TRT barrel  
 1472  $\phi$ -sectors containing modules affected by the tilt misalignment are shown in Figure 4.15 before and  
 1473 after the L2 alignment.

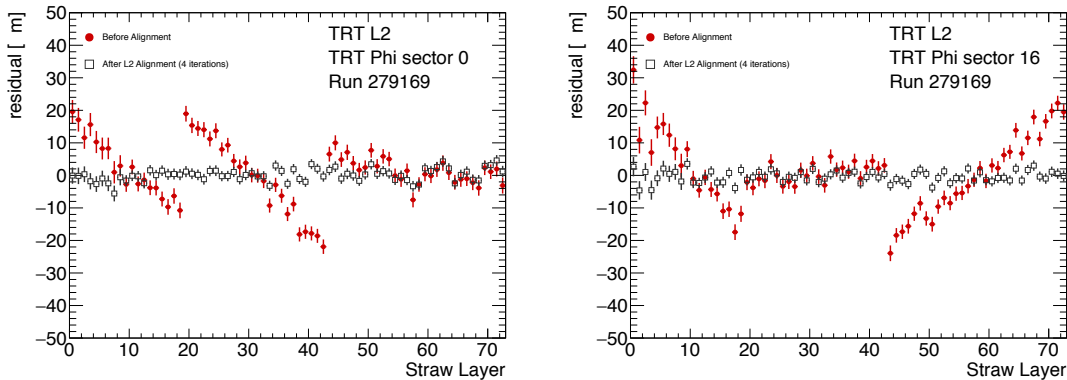


Figure 4.15: Residual means by straw layer in two TRT  $\phi$ -sectors affected by a tilt misalignment. The tilts in each of the three modules are clearly visible in the red points representing the reconstructed data prior to alignment. After four iterations of L2 alignment, the residual means in the gray points are flat.

1474 Following the L2 alignment, some additional time was taken to determine if a full wire-by-wire  
 1475 L3 alignment of the TRT was necessary. The TRT was last aligned at L3 during Run 1, but  
 1476 initial alignment campaigns in Run 2 did not show signs of misalignment (see, for example, the  
 1477 residual distributions shown earlier in Figure 4.11). In order to assess the alignment more carefully,  
 1478 two dimensional residual maps in  $\phi$  and  $z$  were constructed for each layer in the TRT barrel and  
 1479 endcaps using the current alignment. These maps were compared to a similar set using the L3  
 1480 alignment from 2010, from which it was determined that the straw-level alignment indeed hadn't  
 1481 degraded, and a new L3 alignment was not needed. The maps for the first layer of the TRT barrel  
 1482 are shown in Figure 4.16 for both sets of alignment constants.

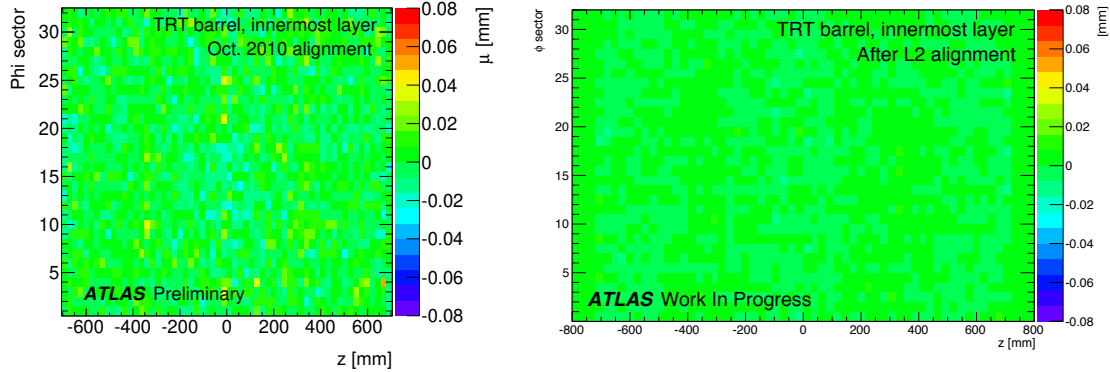


Figure 4.16: Two dimensional map of residuals in the first layer of the TRT barrel vs  $z$  and  $\phi$ . Each bin represents the mean of a Gaussian fit to the TRT residuals in that bin. The map on the left is after the L3 (wire-by-wire) alignment of the TRT performed in 2010, and the map on the right is after the L2 alignment at the end of 2015. The  $z$ -axis for both plots use the same scale. Left figure taken from [66].

#### 1483 4.4 Momentum bias from sagitta deformations

1484 A variety of weak mode deformations can exist in the detector even after alignment. As mentioned  
 1485 previously, these weak modes consist of misalignments which don't affect the  $\chi^2$  of the residuals and  
 1486 thus are not handled by the unconstrained alignment algorithm. In the presence of a weak mode,  
 1487 the description of the detector geometry can still provide efficient and high quality track fits, but  
 1488 there may also be systematic biases in one or more track parameters. Several weak modes, their  
 1489 impacts on the reconstruction, and the steps taken to eliminate them are detailed in [69, 76]. This  
 1490 section focuses specifically on *sagitta* deformations that result in a bias in the reconstructed track  
 1491 momentum.

1492 These sagitta distortions consist of detector movements orthogonal to the trajectory of the outgoing  
 1493 particle. The effect on the reconstructed track curvature is different for positively and negatively  
 1494 charged particles, resulting in a charge-antisymmetric bias. An example of this is illustrated by the  
 1495 curl deformation in Figure 4.17.

1496 In the plane transverse to ATLAS's magnetic field, outgoing particle tracks form circular arcs.  
 1497 The sagitta is defined as the distance from the center of this arc to the center of its base, as shown  
 1498 in Figure 4.18, and it represents the "amount of bending" in the track. In the case where the sagitta  
 1499  $s$  is considerably smaller than the detector radius  $R_0$ , which is a valid assumption when working

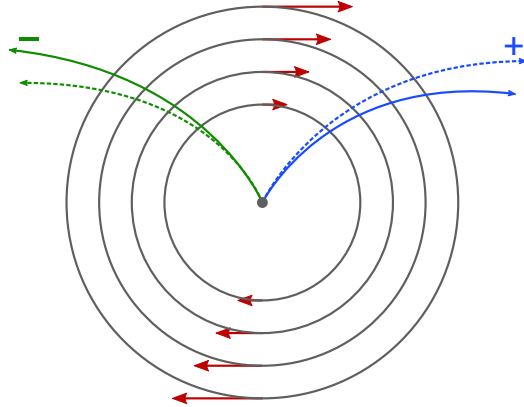


Figure 4.17: Representation of a curl distortion in the detector. The image represents a cutaway view of the transverse plane of the barrel region. The deformation is represented by the red arrows, and the impact on the reconstructed positive (blue) and negative (green) tracks are shown. The dashed lines represent the true particle trajectories, and the solid lines represent the reconstructed trajectories.

1500 with high momentum tracks, the transverse momentum of a particle of charge  $q$  can be written as

$$p_T \propto qB \frac{R_0^2}{8s}, \quad (4.13)$$

1501 where  $B$  is the strength of the detector's magnetic field [77]. If a sagitta bias is present, the track's  
1502 transverse momentum shifts by

$$q/p_T \rightarrow q/p_T + \delta_s \quad \text{or} \quad p_T \rightarrow p_T \cdot (1 + qp_T\delta_s)^{-1}, \quad (4.14)$$

1503 where  $\delta_s$  is a universal bias parameter that uniquely defines the deformation [76]. Finally, since the  
1504 reconstructed polar angle does not change under a sagitta deformation, the longitudinal component  
1505 of the momentum scales along with the transverse component, and an equivalent equation can be  
1506 written for the total momentum:

$$p \rightarrow p \cdot (1 + qp_T\delta_s)^{-1}. \quad (4.15)$$

#### 1507 4.4.1 Sagitta bias monitoring with electron $E/p$

1508 Since a sagitta bias results in changes in the momenta of particle tracks as measured by the ID, they  
1509 can be identified using independent measurements from other systems in the detector. One such  
1510 method involves using the energy-momentum ratio of electrons ( $E/p$ ). Since the electron's energy  
1511 is measured in ATLAS's calorimeter systems, it is not sensitive to any sagitta bias that may exist

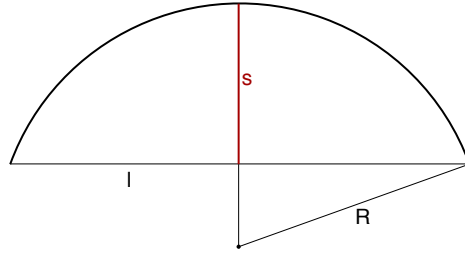


Figure 4.18: Geometric definition of the sagitta  $s$  in relation to the length of the chord  $l$  and the radius  $R$  of a circular arc.

in the ID and in the corresponding measurement of the track momentum. Under the assumption that the calorimeter response is independent of the charge of incoming particles, a charge-dependent momentum bias in the ID will manifest as a difference in the  $E/p$  ratio for electrons and positrons.

In the presence of a sagitta bias, the momentum will change according to Equation 4.15 and the average measured  $\langle E/p \rangle$  can be written as

$$\langle E/p \rangle^\pm \rightarrow \langle E/p \rangle^\pm \pm \langle E_T \rangle \delta_s , \quad (4.16)$$

where the approximation  $p_T \approx E_T$  is used. Assuming that  $\langle E/p \rangle^+ = \langle E/p \rangle^-$  in the absence of a bias, the sagitta bias parameter can be solved for:

$$\delta_s = \frac{\langle E/p \rangle^+ - \langle E/p \rangle^-}{2\langle E_T \rangle} . \quad (4.17)$$

If the kinematic selections for electrons and positrons are identical, the energy scale of the calorimeter will not factor into the  $\langle E/p \rangle$  difference; however, it will affect  $\langle E_T \rangle$ , which would scale the measured  $\delta_s$ . This is expected to be a small effect, as the energy scale for electrons has been measured at 13 TeV with uncertainties on the per-mil level across the entire detector [78].

#### 4.4.1.1 Measuring $\langle E/p \rangle$

The  $E/p$  ratio is measured using electrons and positrons from  $Z \rightarrow ee$  events in order to obtain a high purity sample of candidate particles. They are required to pass a basic selection criteria to ensure they are well measured in both the ID and the calorimeters:

- $E_T > 25$  GeV
- $|\eta| < 2.47$ , excluding the calorimeter's barrel-to-endcap transition region in  $1.37 < |\eta| < 1.52$
- Pass the MediumLH identification working point detailed in Section 3.3.2

- 1530     • Pass a selection of quality cuts, including a requirement that the electron be identified using  
 1531       cluster information in the calorimeter
- 1532     • The associated track must have at least one hit in the IBL, three in the Pixel detector, and  
 1533       five in the SCT detector.
- 1534   Events containing exactly two opposite-charge electrons passing this selection with an invariant mass  
 1535   within 30 GeV of the  $Z$  boson mass are then used for the  $E/p$  calculation.

1536   Since the size of the sagitta bias  $\delta_s$  is not expected to be constant across the entire detector,  
 1537   a two-dimensional rectangular grid is constructed binned in detector  $\eta$  and  $\phi$ . From the selected  
 1538   events, separate distributions of  $E/p$  are made for electrons and positrons within each bin. Each  
 1539   distribution is fit with Crystal Ball function<sup>12</sup>, and the peak of the distribution is taken as the value  
 1540   of  $\langle E/p \rangle$ . If there is no bias on the track momentum in the bin, the peaks for electrons and positrons  
 1541   should agree. Example  $E/p$  distributions including the Crystal Ball fits are shown in Figure 4.19.

1542   It is important to emphasize that deviations from one in the *ratio* of  $\langle E/p \rangle^+$  to  $\langle E/p \rangle^-$  points  
 1543   to a potential momentum biases. The value of  $\langle E/p \rangle$  itself is not expected to equal one exactly,  
 1544   as the track momentum on average tends to be slightly lower than the energy measurement in the  
 1545   calorimeter. This is due to the fact that if the electron were to radiate a photon, its momentum  
 1546   would change slightly, while it is likely that both the electron and the emitted photon would leave  
 1547   energy deposits near each other in the calorimeter and be reconstructed into the same object.

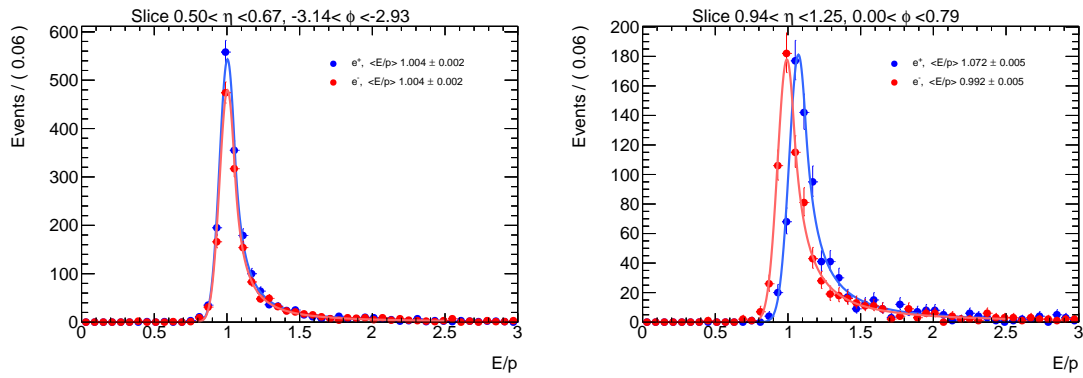


Figure 4.19:  $E/p$  distributions of electrons and positrons in two different  $\eta\phi$  bins of the detector. The left hand plot is taken from a region with no momentum bias where  $\langle E/p \rangle^+ = \langle E/p \rangle^-$ , while the right hand plot shows an 8% disagreement in  $\langle E/p \rangle$  between electrons and positrons.

<sup>12</sup>The Crystal Ball function is a probability density function consisting of a Gaussian core and a power-law tail.

1548 Once the  $\langle E/p \rangle^\pm$  distributions in each  $\eta\text{-}\phi$  bin have been extracted from the fits, a two dimensional map of  $\delta_s$  can be constructed using Equation 4.17. The map gives an overview of sagitta  
 1549 biases that may be present in the detector, and can be used by the alignment algorithm to reduce  
 1550 the bias in the next iteration. In this case, the tracks fed to the alignment have their momenta  
 1551 corrected according to  
 1552

$$q/p_{\text{corr}} = q/p_{\text{reco}}(1 - qp_{\text{T}}\delta_s), \quad (4.18)$$

1553 where  $p_{\text{reco}}$  is the reconstructed momentum of the track [76]. The corrected momentum is then  
 1554 constrained in the alignment.

#### 1555 4.4.1.2 Results in 13 TeV data

1556 The  $E/p$  method has been used to monitor sagitta biases in the detector several times over the  
 1557 course of Run 2. During this time, it has primarily served as an independent cross-check to a second  
 1558 method using  $Z \rightarrow \mu\mu$  events [76]. The  $Z \rightarrow \mu\mu$  method identifies individual track momentum  
 1559 biases through shifts in the reconstructed  $Z$  mass, which leaves it relatively insensitive to global  
 1560 sagitta biases. For this reason, the sagitta bias maps produced using this technique are normalized  
 1561 to those from the  $E/p$  method before being used to constrain the alignment. The results of two  
 1562 implementations of the  $E/p$  method are presented here.

- 1563 1. The first follows the end-of-year reprocessing of the entire ATLAS 2016 data set. Two sets  
 1564 of alignment constants are compared: the *prompt* alignment, which was derived shortly after  
 1565 each run was recorded, and the *reprocessed* alignment. The maps of the sagitta bias in each  
 1566 alignment calculated using the  $E/p$  method are shown in Figure 4.20, and the comparison of  
 1567 the  $\eta$  projection of the maps is shown in Figure 4.21.
- 1568 2. The second uses the 2017 data after reprocessing, and compares the effects of multiple iterations  
 1569 of the  $E/p$  method. In each iteration, the momenta of the electrons and positrons are corrected  
 1570 according to Equation 4.15 using the value of  $\delta_s$  computed in the previous iteration, and a  
 1571 new sagitta bias map is calculated. If the method is indeed characterizing the sagitta biases  
 1572 correctly, the corrections should converge quickly. The initial sagitta bias map is compared to  
 1573 the map after two such iterations in Figure 4.22, and the sagitta bias projected along  $\eta$  for  
 1574 each iteration is shown in Figure 4.23. Indeed, after just two iterations,  $\delta_s$  is consistent with  
 1575 zero in nearly all bins.

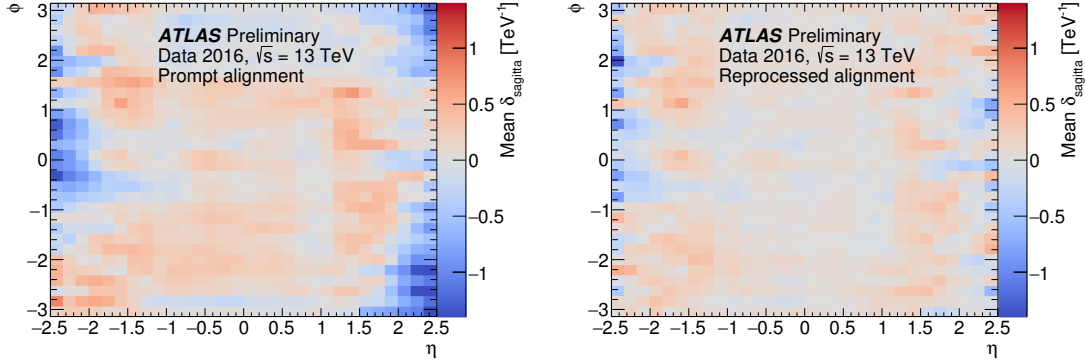


Figure 4.20: Sagitta bias in the  $\sqrt{s} = 13$  TeV data collected by ATLAS in 2016 as a function of  $\eta$  and  $\phi$  for the prompt (left) and reprocessed (right) alignments using the  $E/p$  method.

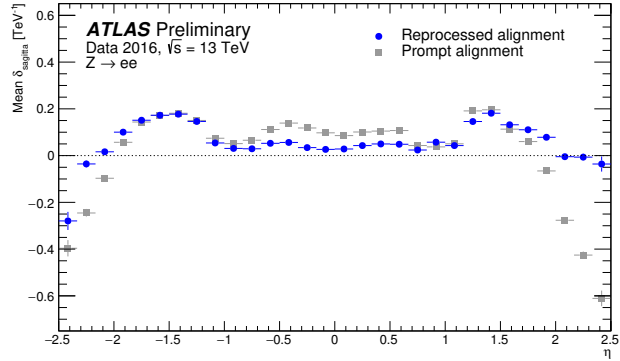


Figure 4.21: Sagitta bias in the  $\sqrt{s} = 13$  TeV data collected by ATLAS in 2016 projected along  $\eta$  for the prompt (gray) and reprocessed (blue) alignments using the  $E/p$  method.

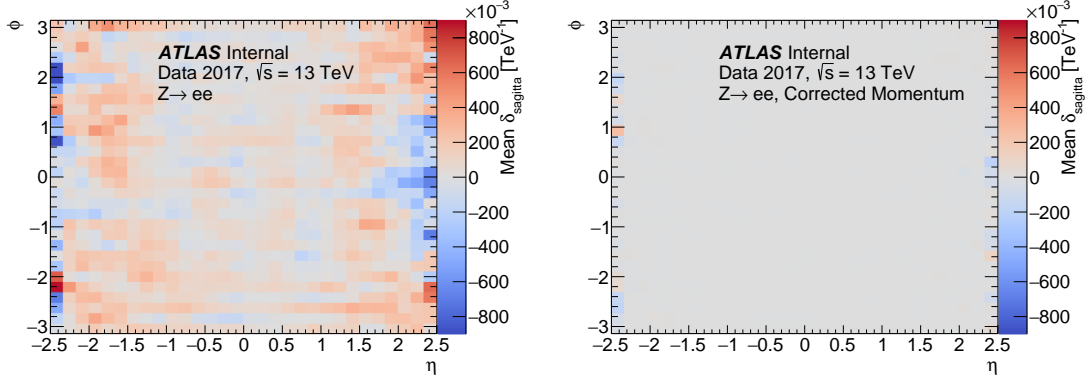


Figure 4.22: Sagitta bias in the  $\sqrt{s} = 13$  TeV data collected by ATLAS in 2017 as a function of  $\eta$  and  $\phi$  in reconstructed electrons (left) and after two iterations of momentum corrections (right) from the  $E/p$  method.

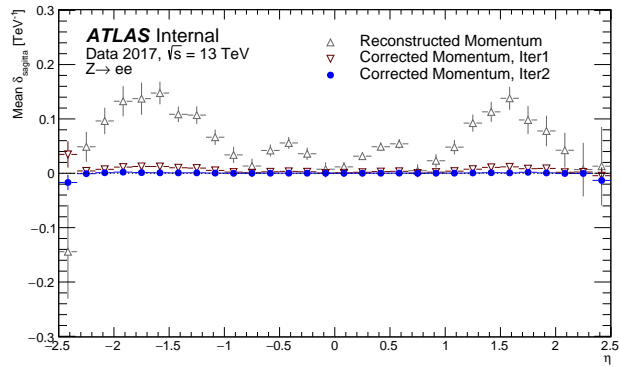


Figure 4.23: Sagitta bias in the  $\sqrt{s} = 13$  TeV data collected by ATLAS in 2017 projected along  $\eta$  in reconstructed electrons (gray) and after one (red) and two (blue) iterations of momentum corrections from the  $E/p$  method.

1576

## CHAPTER 5

1577

1578

# Measurement of same-sign $WW$ production at $\sqrt{s} = 13$ TeV with ATLAS

1579 Production of same-sign  $W$  boson pairs is a particularly interesting SM process. When produced  
1580 via vector boson scattering (VBS),  $W^\pm W^\pm jj$  is sensitive to the electroweak symmetry breaking  
1581 (EWSB) mechanism as well as potential Beyond the Standard Model (BSM) physics processes.  
1582  $W^\pm W^\pm jj$  events can be produced via electroweak-mediated (EWK) diagrams, of which VBS is a  
1583 subset, or QCD-mediated diagrams. The biggest advantage of same-sign  $W^\pm W^\pm jj$  over other VBS  
1584 processes lies in its ratio of electroweak (EWK) to QCD production cross sections. Despite the  
1585 opposite-sign  $W^\pm W^\mp$  having a larger total cross section, its EWK-mediated diagrams are much  
1586 smaller than its QCD-mediated diagrams, while for same-sign  $W^\pm W^\pm$  the EWK production is  
1587 considerably larger. This makes  $W^\pm W^\pm jj$  one of the premier channels for studying VBS at the  
1588 LHC.

1589 The first evidence of electroweak (EWK)  $W^\pm W^\pm jj$  production was seen by the ATLAS and CMS  
1590 experiments at  $\sqrt{s} = 8$  TeV with excesses of  $3.6\sigma$  [79] and  $2.0\sigma$  [80] over backgrounds, respectively.  
1591 More recently, ATLAS and CMS have both observed the EWK process at  $\sqrt{s} = 13$  TeV with  
1592 significances of  $6.9\sigma$  [81] and  $5.5\sigma$  [82], respectively. The ATLAS  $\sqrt{s} = 13$  TeV observation and  
1593 cross section measurement of EWK-produced  $W^\pm W^\pm jj$  is presented in this chapter [81, 83].

### 1594 5.0.1 Experimental overview of vector boson scattering

1595 VBS processes are very important to understand due to their sensitivity to the EWSB mechanism.  
1596 As explained in Section 2.3, in the absence of a light SM Higgs boson, the scattering amplitude of  
1597 longitudinally polarized vector bosons grows with center-of-mass energy. However, once the Higgs

1598 is introduced, the divergences cancel and the cross section no longer grows unbounded.

1599 With the discovery of the Higgs boson in 2012 [16, 17], the EWSB mechanism can now be directly  
 1600 studied. Due to the potential exchange of a Higgs boson in the VBS diagrams ( $W^\pm W^\pm jj$  itself does  
 1601 not contain an  $s$ -channel Higgs exchange), VBS processes are directly sensitive to properties of the  
 1602 Higgs. For example, the high-mass tail in the  $VV$  scattering system allows an approximation of the  
 1603 effective coupling strength of the Higgs to vector bosons that is independent of any assumptions  
 1604 on the Higgs width [84]. Additionally, the center of mass energy dependence of the  $VV$  scattering  
 1605 can reveal whether the Higgs boson unitarizes the longitudinal scattering amplitude fully or only  
 1606 partially [85].

1607 VBS events are characterized by two quarks from the colliding protons each radiating a vector  
 1608 boson which then scatter and decay in the detector. The incoming quarks carry a large amount of  
 1609 momentum and only deflect a small amount upon emitting the vector boson; as a result, they often  
 1610 enter the calorimeters very close to the beam line. Ignoring the decay products of the scattered  
 1611 bosons for now, these VBS events result in a final state of two vector bosons ( $V$ ) and two jets ( $j$ )  
 1612 at high pseudorapidities (called *forward jets* or *tag jets*) from the outgoing quarks. The shorthand  
 1613  $VVjj$  is used to represent this final state.

1614  $VVjj$  events can be produced via two different physical processes. The first involves purely  
 1615 electroweak interactions in the tree-level diagrams, of order  $\mathcal{O}(\alpha_{\text{EWK}}) = 6$  in the electroweak coupling  
 1616 constant, and will be referred to as *EWK production*. This can be further broken down into VBS  
 1617 and non-VBS events. In the VBS EWK production, the scattering occurs via triple or quartic gauge  
 1618 couplings, as well as the exchange of a Higgs boson. The non-VBS EWK production contains the  
 1619 same final state of two vector bosons and two outgoing quarks, but the bosons do not scatter. Due to  
 1620 gauge invariance, it is not possible to separate the VBS from the non-VBS productions [86]; therefore,  
 1621 both are included in the signal generation and are indistinguishable from one another. The second  
 1622 process involves a mix of the EWK and strong interactions, of order  $\mathcal{O}(\alpha_s) = 2 \otimes \mathcal{O}(\alpha_{\text{EWK}}) = 4$ , and  
 1623 will be referred to as *QCD production*. The tree-level Feynman diagrams for VBS EWK, non-VBS  
 1624 EWK, and QCD  $VVjj$  production are found in Figures 5.1, 5.2, and 5.3, respectively.

### 1625 5.0.2 Same-sign $W^\pm W^\pm$ scattering

1626 Same-sign  $W^\pm W^\pm jj$  scattering is considered to be one of the best channels for studying VBS at  
 1627 the LHC due to its favorable ratio of EWK to QCD production [84]. Since the VBS diagrams are  
 1628 the primary interest for analysis, the QCD production is considered a background. Therefore a

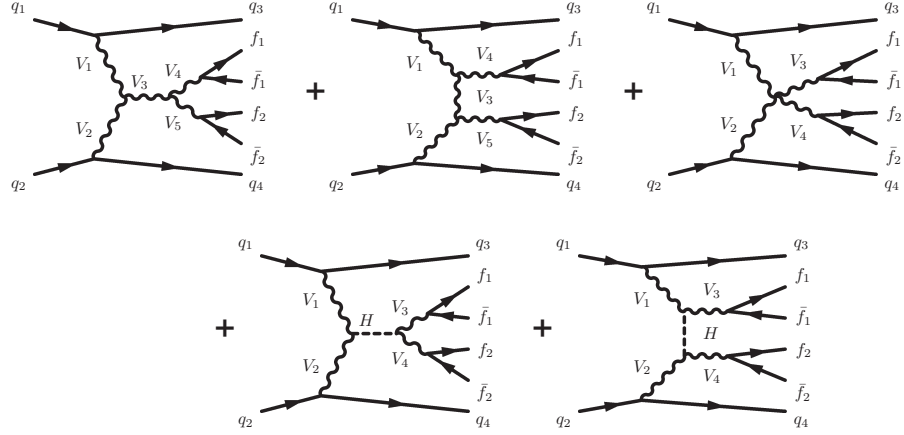


Figure 5.1: Tree-level Feynman diagrams for VBS EWK  $VVjj$  production including triple gauge couplings involving  $W$  and/or  $Z$  bosons (top left and top middle), quartic gauge coupling (top right), or the exchange of a Higgs boson ( $s$ -channel bottom left and  $t$ -channel bottom right). The labels are quarks ( $q$ ), fermions ( $f$ ), and gauge bosons ( $V = W, Z$ ).

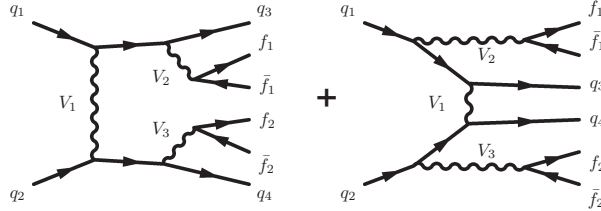


Figure 5.2: Tree-level Feynman diagrams for non-VBS EWK  $VVjj$  production. The labels are quarks ( $q$ ), fermions ( $f$ ), and gauge bosons ( $V = W, Z$ ).

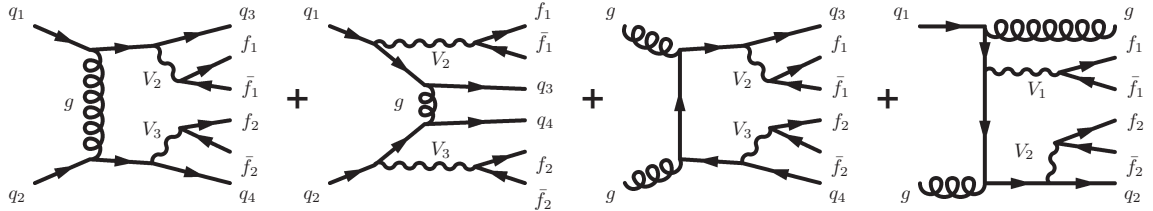


Figure 5.3: Tree-level Feynman diagrams for QCD  $VVjj$  production. The labels are quarks ( $q$ ), fermions ( $f$ ), and gauge bosons ( $V = W, Z$ ).

higher EWK-to-QCD ratio results in increased sensitivity to VBS. EWK and QCD cross sections at  $\sqrt{s} = 13$  TeV for six leptonic  $VVjj$  final states were calculated using the **SHERPA** MC generator in a VBS-enriched fiducial phase space in [87]. Despite its relatively low total cross section compared to some other  $VVjj$  processes, the EWK-to-QCD ratio for  $W^\pm W^\pm jj$  is 10-20 times higher than for other processes after applying VBS-enhancing selection criteria.

Final state	Process	$\sigma_{\text{EWK}}$ [fb]	$\sigma_{\text{QCD}}$ [fb]	$\sigma_{\text{EWK}}/\sigma_{\text{QCD}}$
$l^\pm l^\mp l^\pm l^\mp jj$	$ZZ$	0.098	0.100	0.98
$l^\pm l^\pm l^\mp \nu\nu jj$	$W^\pm Z$	2.34	4.38	0.53
$l^\pm l^\mp \nu\nu jj$	$W^\pm W^\mp, ZZ$	12.3	21.8	0.56
$l^\pm l^\pm \nu\nu jj$	<b><math>W^\pm W^\pm</math></b>	<b>3.97</b>	<b>0.346</b>	<b>11.47</b>
$l^\pm \nu\nu jj$	$W^\pm Z$	7.64	15.5	0.49
$\nu\nu\nu\nu jj$	$ZZ$	1.68	1.38	1.22

Table 5.1: Predicted cross sections for EQK and QCD production of diboson processes relevant to VBS at  $\sqrt{s} = 13$  TeV using the **SHERPA** MC generator. The numbers for the  $W^\pm W^\pm jj$  process are bolded. Leptons are required to have  $p_T \geq 25$  GeV and lie within  $|\eta| \leq 2.5$  with  $m_{ll} > 20$  GeV, and at least two jets are required with  $p_T \geq 30$  GeV and  $|\eta| < 4.5$ . The VBS contributions are enhanced by requiring the dijet invariant mass  $m_{jj} > 500$  GeV and dijet separation  $\Delta y_{jj} > 2.4$ . Numbers taken from [87].

This analysis studies  $W^\pm W^\pm jj$  scattering where both  $W$  bosons decay leptonically to  $e\nu$  or  $\mu\nu$ <sup>13</sup>.

The  $W^\pm W^\pm jj$  VBS final state consists of two leptons with the same electric charge, two neutrinos, and two high energy forward jets with a large invariant mass. Tree-level Feynman diagrams of VBS  $W^\pm W^\pm jj$  production can be found in Figure 5.4 and a visual representation of the VBS topology can be found in Figure 5.5.

The two tag jets in the characteristic VBS signature also serve as a powerful tool to suppress the QCD production mode. In EWK events, the two jets tend to have much higher separation and a larger combined invariant mass than the two leading jets in a QCD event. The two plots shown in Figure 5.6 highlight the differences in these dijet quantities between the two production modes. Finally, an ATLAS event display of a real  $W^\pm W^\pm jj$  candidate event is shown in Figure 5.7.

### 5.0.3 Overview of backgrounds

In addition to QCD production of  $W^\pm W^\pm jj$  events, there are several other processes with a final state of two same-sign leptons, two neutrinos, and two jets. However, due to the  $\pm 2$  final state charge,

<sup>13</sup>Throughout the rest of this chapter, unless stated otherwise,  $l$  denotes either electrons ( $e$ ) or muons ( $\mu$ ), and  $\nu$  denotes a neutrino. Additionally,  $e$ ,  $\mu$ , and  $\nu$  with no charge or anti-particle designation refer interchangeably to either the particle or anti-particle.

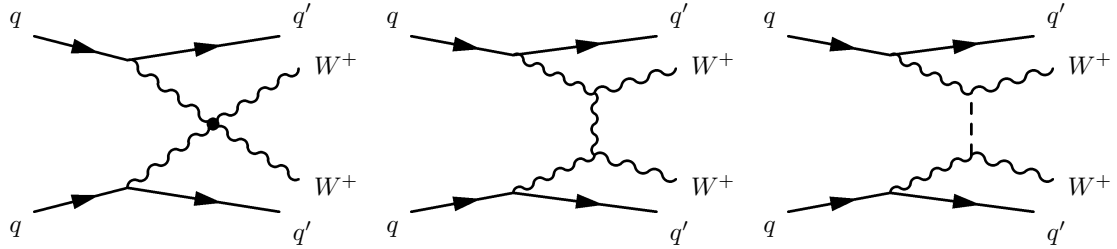


Figure 5.4: Leading order Feynman diagrams for VBS EWK production of  $W^\pm W^\pm jj$  events. The leftmost diagram contains a quartic gauge coupling vertex, and the rightmost diagram contains an exchange of a Higgs boson.

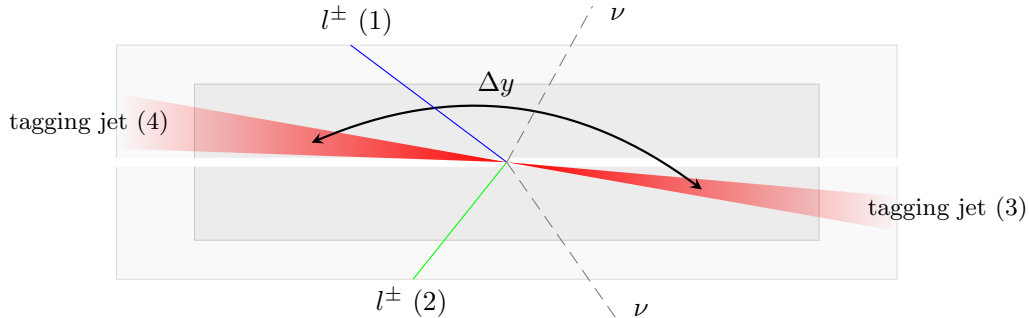


Figure 5.5:  $W^\pm W^\pm jj$  VBS event topology containing two leptons (1 and 2) with the same electric charge, two neutrinos, and two forward tagging jets (3 and 4) with large rapidity separation  $\Delta y$ .

1647 there is a considerable reduction in SM backgrounds (such as  $Z$  boson events) when compared to  
 1648 an analysis like opposite-sign  $W^\pm W^\mp jj$ .

1649 One of the largest background sources involves processes with prompt leptons<sup>14</sup>. These are events  
 1650 that contain two leptons with the same electric charge and one or more additional leptons that are  
 1651 “lost”, either by failing the selection criteria or falling outside of the detector’s acceptance. The  
 1652 number of processes that can contribute is limited by the requirement of same-sign leptons, and as a  
 1653 result this background is dominated by multi-boson processes, with the largest contribution coming  
 1654 from  $WZ$  events and smaller contributions from  $ZZ$  and  $t\bar{t} + V$  events. Triboson events where one  
 1655 boson decays hadronically also contribute to this background; however, the jets are generally softer  
 1656 and more central than in a typical VBS event, and the cuts applied on the forward jets suppress  
 1657 these contributions.

<sup>14</sup>Prompt leptons are those that are produced in the primary collision and are a direct decay product of the process of interest. Non-prompt leptons originate from some secondary process, such as a  $b$ -hadron decay. Jets that are mis-reconstructed as a lepton are also considered non-prompt.

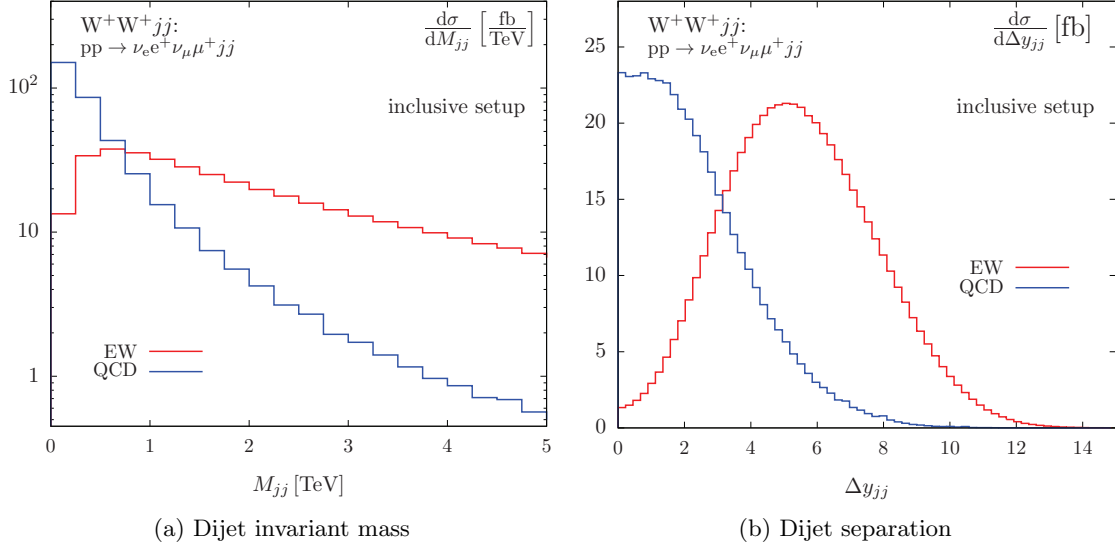


Figure 5.6: Generator level comparisons at  $\sqrt{s} = 7$  TeV of dijet invariant mass ( $M_{jj}$ , left) and dijet rapidity ( $\Delta y_{jj}$ , right) in EWK (red) and QCD (blue)  $W^\pm W^\pm jj$  events with no selection cuts applied. Plots taken from [88].

1658     The other dominant background comes from non-prompt, or “fake”, leptons. Here one or more  
 1659     leptons originate from the decay of another particle unrelated to the signal process, such as a heavy-  
 1660     flavor decay or photon conversion, or come from a jet that is misidentified as a lepton. This back-  
 1661     ground is mostly made up of events from  $t\bar{t}$  and  $W+jets$  processes, with a much smaller contribution  
 1662     from conversions in  $V\gamma$  events.

1663     Finally, opposite-sign lepton pairs can enter the signal region if one of the leptons is reconstructed  
 1664     with the wrong charge (called *charge misidentification*<sup>15</sup>). In practice, this only affects events with  
 1665     electrons, as the charge misidentification rate for muons is negligible [89]. This is a major background  
 1666     in events with two electrons, dominated by  $Z \rightarrow ee$  events; it is a much smaller contribution for  
 1667     events with one electron and one muon, where the primary contribution comes from  $t\bar{t}$  events.

## 1668     5.1 Data and Monte Carlo samples

1669     This analysis uses  $36.1 \text{ fb}^{-1}$  of  $\sqrt{s} = 13$  TeV proton-proton collisions recorded by ATLAS during  
 1670     the 2015 and 2016 data taking periods. The uncertainty in the combined integrated luminosity is  
 1671     2.1%. It is derived following a methodology similar to that detailed in [90] and using the LUCID-2

<sup>15</sup>Charge misidentification is also referred to interchangeably as *charge mis-ID* and *charge flip*.

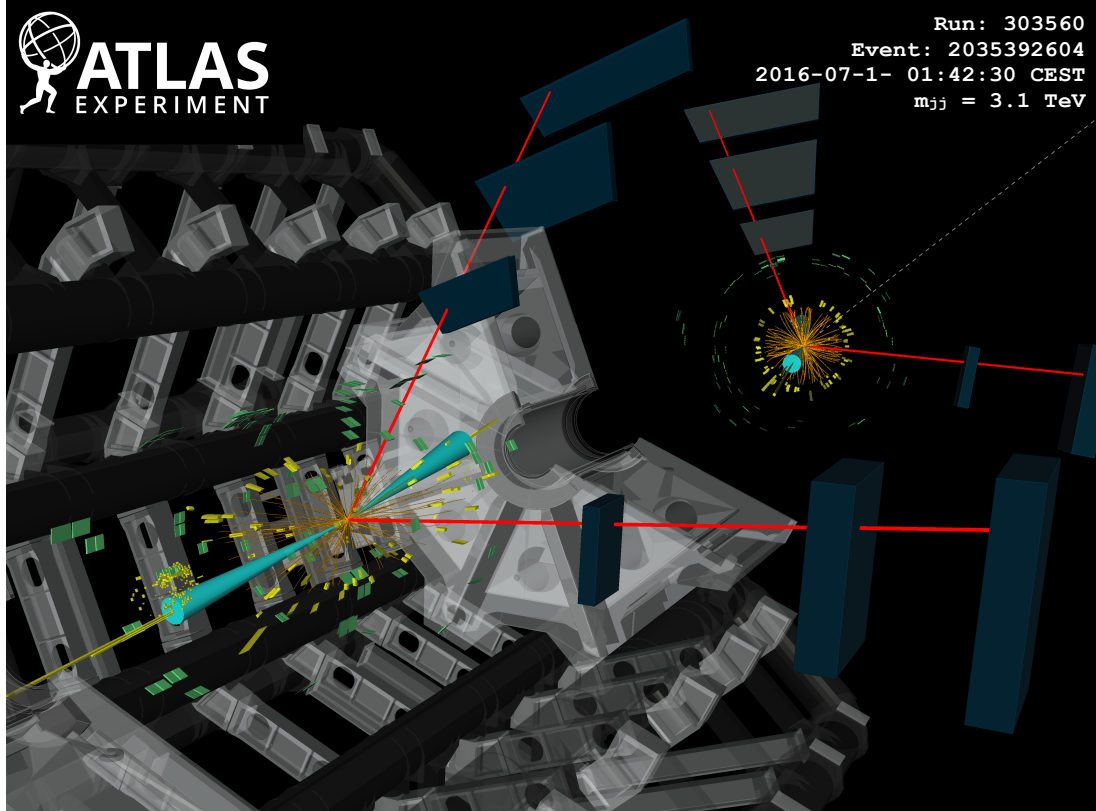


Figure 5.7: ATLAS event display of a  $pp \rightarrow W^+W^+ \rightarrow \mu^+\nu_\mu\mu^+\nu_\mu jj$  event. The muons are represented by the red lines travelling from the ID through the MS, and the forward jets are represented by the blue cones with yellow energy deposits in the calorimeters. The direction of the  $E_T^{\text{miss}}$  in the transverse plane is indicated by the gray dashed line in the inset image. Event display taken from [81].

1672 detector for the baseline luminosity measurements [91] from calibration of the luminosity scale using  
 1673  $x$ - $y$  beam-separation scans.

### 1674 5.1.1 Monte Carlo samples

1675 A number of Monte Carlo (MC) simulations are employed to model signal and background processes.  
 1676 In order to model the real collision data as closely as possible, each MC sample has been passed  
 1677 through a full simulation of the ATLAS detector in GEANT4 [92, 93], and events have been recon-  
 1678 structed using the same algorithms as the data. The simulation reproduces as closely as possible  
 1679 the momentum resolutions and calorimeter responses of the detector, and also includes the effects  
 1680 of pileup by including soft QCD interactions using PYTHIA v8.1 [94]. The MC samples used in this

Process	Generator	Comments
$W^\pm W^\pm jj$ (EWK)	SHERPA v2.2.2	Signal sample
$W^\pm W^\pm jj$ (EWK)	POWHEG-BOX v2	Systematics sample
$W^\pm W^\pm jj$ (QCD)	SHERPA v2.2.2	
Diboson	SHERPA v2.2.2	Both bosons decay leptonically ( $llll$ , $ll\nu\nu$ , $l\nu\nu\nu$ )
	SHERPA v2.2.1	One boson decays leptonically, the other hadronically
Triboson	SHERPA v2.1.1	
$W+jets$	SHERPA v2.2.1	
$Z+jets$	Madgraph5_aMC@NLO	
$V\gamma$	SHERPA v2.1.1	
$V\gamma jj$ (EWK)	SHERPA v2.2.4	
$t\bar{t}V$	Madgraph5_aMC@NLO	
$t\bar{t}$	POWHEG-BOX v2	
Single top	POWHEG-BOX v1	EWK $t$ -, $s$ -, & $Wt$ -channels

Table 5.2: Summary of MC samples used in the analysis.

1681 analysis are detailed in this section and summarized in Table 5.2.

1682 The  $W^\pm W^\pm jj$  samples are modeled using SHERPA v2.2.2 [95, 96, 97] with the NNPDF3.0 PDF  
 1683 set [98]. The EWK signal samples were generated by fixing the electroweak coupling constant to  
 1684  $\mathcal{O}(\alpha_W) = 6$ , and a QCD background sample was also generated with  $\mathcal{O}(\alpha_W) = 4$ . SHERPA includes  
 1685 up to one parton at next-to-leading order (NLO) and up to three at leading order (LO) in the strong  
 1686 coupling constant  $\alpha_s$ . A second  $W^\pm W^\pm jj$  EWK sample was generated using POWHEG-BOX v2 [99]  
 1687 with the NNPDF3.0 PDF set and at NLO accuracy. This sample is only used for systematic studies,  
 1688 as POWHEG-BOX does not include resonant triboson contributions in its matrix element, which are  
 1689 non-negligible at NLO [100].

1690 Diboson processes ( $VV$  where  $V = W, Z$ ) are simulated with SHERPA v2.2.2 for mixed hadronic  
 1691 and leptonic decays and SHERPA v2.2.1 for fully leptonic decays of the bosons. Similarly, triboson  
 1692 ( $VVV$ ) and  $V\gamma$  processes are simulated using SHERPA v2.1.1 with up to one parton at NLO and up  
 1693 to three at LO.  $W+jets$  processes are simulated with SHERPA v2.2.1 with up to two partons at NLO  
 1694 and four at LO. All the above SHERPA samples use the NNPDF3.0 PDF set and SHERPA's own parton  
 1695 showering. The  $Z+jets$  events are generated with Madgraph5\_aMC@NLO [101] at LO and interfaced  
 1696 with PYTHIA v8.1 for parton showering.

1697  $t\bar{t}$  events are generated using POWHEG-BOX v2 with the CT10 PDF set [102].  $t\bar{t}V$  samples are  
 1698 generated at NLO with Madgraph5\_aMC@NLO and the NNPDF3.0 PDF set interfaced with PYTHIA v8  
 1699 for parton showering. Finally, single top events are generated with POWHEG-BOX v1 and the CT10f4  
 1700 PDF set interfaced with PYTHIA v6 [103] for parton showering.

## 1701 5.2 Object and event selection

1702 This section details the selection criteria for objects used in the analysis as well as the selection for  
1703 signal events.

### 1704 5.2.1 Object selection

1705 Muons, electrons, and jets all must pass strict selection requirements to ensure that only high quality,  
1706 well measured objects are used. For leptons, a baseline selection is defined (called the *preselection*),  
1707 which all leptons must pass in order to be considered for the analysis. This preselection is an  
1708 intentionally loose set of criteria designed to have high acceptance in order to reject backgrounds  
1709 with additional leptons (such as  $WZ \rightarrow 3l\nu jj$ ). Signal leptons are then required to satisfy a much  
1710 tighter *signal selection* aimed at suppressing backgrounds from non-prompt or fake leptons. A third  
1711 set of lepton selection criteria, the *loose selection*, defines a sample enriched in non-prompt leptons,  
1712 and it is used in the fake-factor method for estimating the non-prompt background, discussed in  
1713 detail in Section 5.3.4. Jets are only required to pass one set of selection criteria. These selections  
1714 are outlined in the following subsections and summarized in Table 5.3 for muons, Table 5.4 for  
1715 electrons, and Table 5.5 for jets.

#### 1716 5.2.1.1 Muon candidate selection

1717 Cuts on muon momentum serve to reject low momentum leptons from background processes and from  
1718 additional collisions occurring in pileup events. Preselected muons must have transverse momentum  
1719  $p_T > 6$  GeV, and the signal muons must pass  $p_T > 27$  GeV. The  $p_T$  requirement for loose muons  
1720 is lower than for signal muons, at  $p_T > 15$  GeV, for reasons that are discussed in Section 5.3.4.3.  
1721 Muons are required to fall within the detector's  $\eta$  acceptance:  $|\eta| < 2.7$  for preselected muons, which  
1722 is tightened to  $|\eta| < 2.5$  for the signal muons.

1723 Cuts on the transverse and longitudinal impact parameters are applied to ensure that the can-  
1724 didate muon originated from the primary particle interaction and not some other source. The  
1725 preselection and the loose selection both have relaxed requirements on the transverse impact pa-  
1726 rameter significance ( $d_0/\sigma_{d_0}$ ) than the signal selection; all three have the same requirement on the  
1727 transverse impact parameter ( $|z_0 \times \sin \theta|$ ).

1728 Finally, the muon candidates are required to pass a particle identification and an isolation criteria  
1729 as defined in [61]. The methods used in constructing the identification and isolation working points  
1730 are described in more detail in Section 3.3.3. The muon identification serves to select prompt muons

with high efficiency and well measured momenta. This analysis uses two different working points: **Loose** for preselected muons and **Medium** for loose and signal muons, where **Medium** muons are a tighter subset of those that pass the **Loose** requirement. Muon isolation is a measurement of detector activity around the muon candidate, and it is measured with both track-based and calorimeter-based variables. The isolation working point used for the signal muons, **Gradient**, is defined such that there is 90% or better background rejection efficiency for 25 GeV muons, and 99% efficiency at 60 GeV. There is no minimum isolation requirement for preselected or loose muons. Loose muons are additionally required to fail one or both of the signal transverse impact parameter cut and signal isolation requirement.

Muon preselection	
Momentum cut	$p_T > 6$ GeV
Angular acceptance	$ \eta  < 2.7$
Longitudinal impact parameter	$ z_0 \times \sin \theta  < 0.5$ mm
Transverse impact parameter	$d_0/\sigma_{d_0} < 10$
Particle identification	<b>Loose</b>

Muon signal selection	
Momentum cut	$p_T > 27$ GeV
Angular acceptance	$ \eta  < 2.5$
Longitudinal impact parameter	$ z_0 \times \sin \theta  < 0.5$ mm
Transverse impact parameter	$d_0/\sigma_{d_0} < 3$
Particle identification	<b>Medium</b>
Particle isolation	<b>Gradient</b>

Muon loose selection	
Momentum cut	$p_T > 15$ GeV
Angular acceptance	$ \eta  < 2.5$
Longitudinal impact parameter	$ z_0 \times \sin \theta  < 0.5$ mm
Transverse impact parameter	$d_0/\sigma_{d_0} < 10$
Particle identification	<b>Medium</b>
Fail signal transverse impact parameter and/or isolation cuts	

Table 5.3: Muon selection criteria. All muons are required to pass the preselection (top), and then either the signal (middle) or loose (bottom) criteria is applied to the preselected electrons.

#### 5.2.1.2 Electron candidate selection

The electron candidate selections are very similar to those for muons. The momentum cut starts at  $p_T > 6$  GeV for the preselection, increases to  $p_T > 20$  GeV for loose electrons, and finally to

<sup>1743</sup>  $p_T > 27$  GeV for signal electrons. The  $|\eta|$  cut for electrons requires  $|\eta| < 2.47$  for all electrons,  
<sup>1744</sup> with the region  $1.37 \leq |\eta| \leq 1.52$  removed from loose and signal electrons. This is where the  
<sup>1745</sup> electromagnetic calorimeter transitions from the barrel to the endcaps and is not fully instrumented.  
<sup>1746</sup> Both the transverse and longitudinal impact parameter cuts are the same for all electron selections.

<sup>1747</sup> The electron particle identification uses a multivariate likelihood technique (LH) detailed in  
<sup>1748</sup> Section 3.3.2. Preselected electrons must pass the `LooseLH` working point with an additional re-  
<sup>1749</sup> quirement that there be a reconstructed track hit in the first layer of the pixel detector (a so-called  
<sup>1750</sup>  $B$ -layer hit). The LH requirement for the loose and signal electrons increases in tightness using  
<sup>1751</sup> `MediumLH` and `TightLH` electrons, respectively. As for isolation, the `Gradient` working point is re-  
<sup>1752</sup> quired for signal electrons only. The loose electrons must fail one or both of the signal identification  
<sup>1753</sup> and isolation requirements.

Electron preselection	
Momentum cut	$p_T > 6$ GeV
Angular acceptance	$ \eta  < 2.47$
Longitudinal impact parameter	$ z_0 \times \sin \theta  < 0.5$ mm
Transverse impact parameter	$d_0/\sigma_{d_0} < 5$
Particle identification	<code>LooseLH</code> + $B$ -layer hit

Electron signal selection	
Momentum cut	$p_T > 27$ GeV
Angular acceptance	$ \eta  < 2.47$ , excluding $1.37 \leq  \eta  \leq 1.52$
Longitudinal impact parameter	$ z_0 \times \sin \theta  < 0.5$ mm
Transverse impact parameter	$d_0/\sigma_{d_0} < 5$
Particle identification	<code>TightLH</code>
Particle isolation	<code>Gradient</code>

Electron loose selection	
Momentum cut	$p_T > 20$ GeV
Angular acceptance	$ \eta  < 2.47$ , excluding $1.37 \leq  \eta  \leq 1.52$
Longitudinal impact parameter	$ z_0 \times \sin \theta  < 0.5$ mm
Transverse impact parameter	$d_0/\sigma_{d_0} < 5$
Particle identification	<code>MediumLH</code>
Fail signal identification and/or isolation cuts	

Table 5.4: Electron selection criteria. All electrons are required to pass the preselection (top), and then either the signal (middle) or loose (bottom) criteria is applied to the preselected electrons.

1754 **5.2.1.3 Jet candidate selection**

1755 The final objects that need to pass selection are jets. Jets are clustered using the anti- $k_t$  algo-  
 1756 rithm [104] within a radius of  $\Delta R = 0.4$ . The jets are then calibrated using  $E_T$ - and  $\eta$ -dependent  
 1757 correction factors that are trained using MC simulations [105]. The calibrated jets are required  
 1758 to have  $p_T > 30$  GeV if they lie in the forward regions of the detector ( $2.4 < |\eta| < 4.5$ ) and  
 1759  $p_T > 25$  GeV in the central region ( $|\eta| \leq 2.4$ ). In order to suppress pileup jets, the so-called jet-  
 1760 vertex-tagger (JVT) discriminant associates a jet with the primary interaction vertex [106]; central  
 1761 jets with  $p_T > 60$  GeV are required to pass the **Medium** JVT working point, which corresponds to  
 1762 an average efficiency of over 92%. Finally, the jets are required to be separated from the selected  
 1763 leptons by at least  $\Delta R(j, l) > 0.3$ .

Jet selection	
Momentum cut	$p_T > 30$ GeV for $2.4 <  \eta  < 4.5$ $p_T > 60$ GeV for $ \eta  < 2.4$
JVT cut	<b>Medium</b>
Jet-lepton separation	$\Delta R(j, l) > 0.3$

Table 5.5: Jet selection criteria. All jets are required to pass the above selection in order to be used in the analysis.

1764 **5.2.1.4 Treatment of overlapping objects**

1765 In the event that one or more objects are reconstructed very close to each other, there is the possibility  
 1766 for double-counting if both originated from the same object. The procedure by which this ambiguity  
 1767 is resolved is called *overlap removal* (OR). The standard ATLAS recommendation for OR [107, 108]  
 1768 is implemented in this analysis and is summarized in Table 5.6.

1769 Since electrons leave a shower in the EM calorimeter, every electron has a jet associated with  
 1770 it. Therefore, any jets close to an electron (within  $\Delta R(e, j) < 0.2$ ) are rejected due to the high  
 1771 probability that they are the same object. On the other hand, when jets and electrons overlap  
 1772 within a larger radius of  $0.2 < \Delta R(e, j) < 0.4$ , it is likely that the electron and jet both are part of  
 1773 a heavy-flavor decay, and the electron is rejected.

1774 High energy muons can produce photons via bremsstrahlung radiation or collinear final state  
 1775 radiation which result in nearby energy deposits in the calorimeters. Non-prompt muons from  
 1776 hadronic decays produce a similar signature; however, in this case the jet has a higher track multi-  
 1777 plicity in the ID. It is possible to address both cases simultaneously by rejecting the jet when the

1778 ID track multiplicity is less than three, and otherwise rejecting the muon, for jets and muons within  
 1779  $\Delta R(\mu, j) < 0.4$ .

1780 In addition to the case above where muon bremsstrahlung results in a nearby reconstructed  
 1781 jet, the ID track from the muon and the calorimeter energy deposit from the photon can lead to an  
 1782 electron being reconstructed. In this case, if both a muon and an electron share a track in the ID, the  
 1783 muon is kept and the electron is rejected, unless the muon is calorimeter-tagged (see Section 3.3.3),  
 1784 in which case the muon is removed in favor of the electron.

Overlap	Check	Result (remove → keep)
Electron & Jet	$\Delta R(e, j) < 0.2$	Jet → Electron
	$0.2 < \Delta R(e, j) < 0.4$	Electron → Jet
Muon & Jet	$\Delta R(\mu, j) < 0.4$ and Jet $N_{ID}$ tracks $< 3$	Jet → Muon
	$\Delta R(\mu, j) < 0.4$ and Jet $N_{ID}$ tracks $\geq 3$	Muon → Jet
Electron & Muon	Shared ID track	Electron → Muon
	Shared ID track & muon is calo-tagged	Muon → Electron

Table 5.6: Summary of the overlap removal procedure used in the analysis. If the criteria in the “check” column is met, in the “result” column, the object on the left of the arrow is removed in favor of the object on the right.

### 1785 5.2.2 Signal event selection

1786 After the objects have been selected, cuts are applied on a per-event level to select  $W^\pm W^\pm jj$  signal  
 1787 events. The event selection is summarized in Table 5.8.

1788 The initial event selection chooses events that pass one or more of the trigger requirements listed  
 1789 in Table 5.7. At least one signal lepton is “matched” to a passed trigger in order to ensure that  
 1790 it was indeed a signal lepton that fired the trigger. A collection of *event cleaning* cuts must also  
 1791 be passed in order to remove events collected during periods in which one or more components of  
 1792 the detector were not operating optimally. Finally, the events are required to contain at least one  
 1793 interaction vertex. An event can have multiple reconstructed vertices from additional proton-proton  
 1794 collisions that occurred in the same bunch crossing. In this case, the *primary vertex* is determined  
 1795 by choosing the vertex with the largest sum of the  $p_T^2$  of its associated tracks.

1796 Events are then required to contain exactly two signal leptons with the same electric charge.  
 1797 The dilepton pair must have a combined invariant mass of  $m_{ll} \geq 20$  GeV in order to suppress  
 1798 low mass Drell-Yan backgrounds. Two additional selections are applied to events containing two  
 1799 electrons: both are required to have  $|\eta| < 1.37$  with an invariant mass at least 15 GeV away from  
 1800 the  $Z$ -boson mass to reduce events where one electron is reconstructed with the wrong charge (this

	2015 data	2016 data
Electrons	$p_T > 24$ GeV and Medium ID	$p_T > 26$ GeV and Tight ID and Loose isolation
	$p_T > 60$ GeV and Medium ID	$p_T > 60$ GeV and Medium ID
	$p_T > 120$ GeV and Loose ID	$p_T > 140$ GeV and Loose ID
Muons	$p_T > 20$ GeV and Loose isolation $p_T > 50$ GeV	$p_T > 26$ GeV and Medium isolation $p_T > 50$ GeV

Table 5.7: Summary of trigger requirements for electrons and muons for  $\sqrt{s} = 13$  TeV data collected in 2015 and 2016. At least one of the triggers must be satisfied.

1801 background will be discussed in more detail in Section 5.3.3). To suppress backgrounds from final  
 1802 states with more than two leptons, such as  $WZ$  or  $ZZ$ , events with more than two leptons passing  
 1803 the preselection are vetoed.

1804 Missing transverse energy ( $E_T^{\text{miss}}$ ) represents any particles that escape the detector without being  
 1805 measured, such as neutrinos, and it is defined as the magnitude of the vector sum of transverse  
 1806 momenta of all reconstructed objects. It can be difficult to calculate accurately, as it involves  
 1807 measurements from all subsystems within the detector, and it is sensitive to any corrections that may  
 1808 be applied to the reconstructed physics objects [109]. These corrections, including the momentum  
 1809 smearing for muons, energy scale and smearing for electrons, and jet calibrations, are propagated  
 1810 to the  $E_T^{\text{miss}}$  calculation. Events are required to contain  $E_T^{\text{miss}} > 30$  GeV in order to account for the  
 1811 two neutrinos from the  $W$  boson decays.

1812 At least two jets are required. The leading and subleading jets must have  $p_T > 65$  GeV and  
 1813  $p_T > 35$  GeV, respectively, and are referred to as the *tagging jets*. Events are vetoed if they contain  
 1814 one or more jets that have been tagged as a  $b$ -jet to suppress backgrounds from heavy flavor decays  
 1815 (especially top quark events). The  $b$ -tagging algorithm used by ATLAS is a boosted decision tree  
 1816 (BDT) called MV2c10, and this analysis uses a working point with 85% efficiency [110].

1817 Finally, cuts are applied on the VBS signature outlined in Section 5.0.2. The tagging jets are  
 1818 required to have a dijet invariant mass  $m_{jj} > 200$  GeV and be separated in rapidity by  $|\Delta y_{jj}| > 2.0$ .  
 1819 This preferentially selects the VBS EWK events over the QCD-produced  $W^\pm W^\pm jj$  events.

### 1820 5.3 Background estimations

1821 The major sources of background events are summarized in Section 5.0.3, and the methods used to  
 1822 estimate them are detailed in this section. Prompt backgrounds from  $ZZ$  and  $t\bar{t} + V$  are estimated  
 1823 directly from MC simulations. The shape of the  $WZ$  and  $V\gamma$  backgrounds are taken from MC, and  
 1824 the predicted yeilds are normalized to the data predictions in dedicated control regions, as outlined

Event selection	
Event preselection	Pass at least one trigger with a matched lepton Pass event cleaning At least one reconstructed vertex
Lepton selection	Exactly two leptons passing signal selection Both signal leptons with the same electric charge Dilepton mass $m_{ll} > 20$ GeV $ \eta  < 1.37$ and $ M_{ee} - M_Z  > 15$ GeV (ee-channel only) Veto events with more than two preselected leptons
Missing transverse energy	$E_T^{\text{miss}} \geq 30$ GeV
Jet selection	At least two jets Leading jet $p_T > 65$ GeV Subleading jet $p_T > 35$ GeV $m_{jj} > 200$ GeV $N_{b\text{-jet}} = 0$ $ \Delta y_{jj}  > 2.0$

Table 5.8: The signal event selection.

in Sections 5.3.1 and 5.3.2, respectively. Opposite sign events with a charge misidentified electron are estimated by a data-driven background method which is summarized in Section 5.3.3. Finally, a *fake-factor* method is used to estimate the contributions from non-prompt backgrounds and is the subject of Section 5.3.4.

### 5.3.1 Estimation of the $WZ$ background

The dominant background involving prompt leptons comes from  $WZ + \text{jets}$  events. The contribution is estimated from MC simulation and normalized to data in a control region enriched in  $WZ$  events. This region is defined by the same event selection as the signal region in Table 5.8, with the following changes applied to increase the purity of the  $WZ$  process:

- The third lepton veto is inverted, requiring a third lepton with  $p_T > 15$  GeV
- Two of the leptons must make a same-flavor opposite-sign pair. If more than one pair exists, the one with  $m_{ll}$  closest to the  $Z$  boson mass is chosen.
- The trilepton invariant mass is required to be  $m_{lll} > 106$  GeV to reduce contributions from  $Z\gamma$  and  $Z + \text{jets}$

Once the event yields in the control region are calculated, they are propagated to the final signal region fit, detailed in Section 5.4.1, in a single bin combining all the lepton channels. The systematic

1841 uncertainties of the  $WZ$  background are also calculated at this time. The event yields for the  $WZ$   
 1842 control region are listed in Table 5.9, and distributions of the leading lepton  $p_T$  and  $\eta$  as well as  
 1843 trilepton invariant mass  $m_{lll}$  are found in Figures 5.9 and 5.8, respectively.

Event yields in the $WZ$ control region	
$WZ$	$197.9 \pm 1.4$
$ZZ$	$14.1 \pm 0.3$
Triboson	$1.26 \pm 0.1$
top	$10.8 \pm 1.1$
$Z\gamma$	$3.1 \pm 1.1$
$Z+jets$	$2.5 \pm 1.4$
Total prediction	$229.7 \pm 2.5$
Data	$201 \pm 14.2$

Table 5.9: Event yields in the  $WZ$  control region before normalization. All lepton flavor channels are combined.

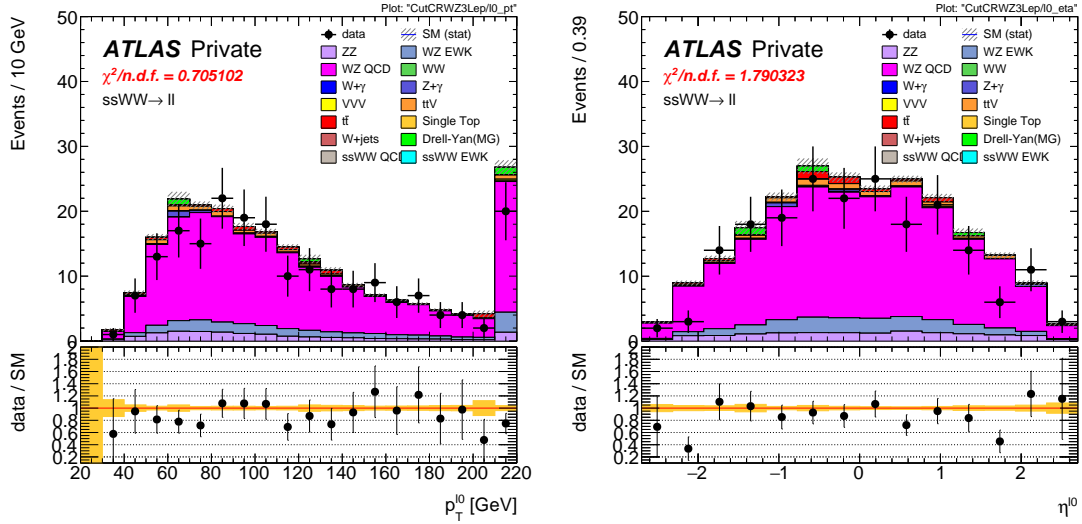


Figure 5.8: Leading lepton  $p_T$  (left) and  $\eta$  (right) distributions in the  $WZ$  control region before normalization. All lepton channels are combined.

### 1844 5.3.2 Estimation of the $V\gamma$ background

1845 Events from  $V\gamma$  processes can pass selection if the photon converts into an  $e^+e^-$  pair and one of the  
 1846 electrons passes the selection criteria. The background is estimated from MC simulations which are  
 1847 then scaled by a normalization factor calculated from a control region enriched in  $Z \rightarrow \mu\mu + \gamma$  events.

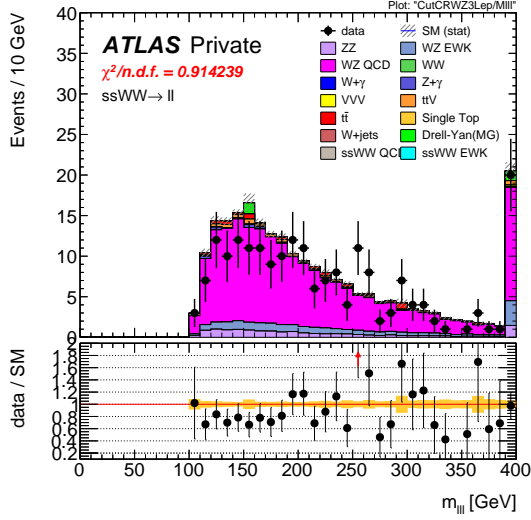


Figure 5.9: Trilepton invariant mass  $m_{lll}$  distribution in the  $WZ$  control region before normalization. All lepton channels are combined.

1848 This control region selects two opposite-sign muons and an additional electron that is assumed to  
 1849 come from the photon conversion. The full event selection is detailed in Table 5.10.

$V\gamma$ control region
Exactly two muons with $p_T > 27$ GeV and $p_T > 20$ GeV
Exactly one additional electron with $p_T > 15$ GeV
Remove overlap between $Z+jets$ and $Z\gamma$
Di-muon + photon invariant mass $75 < M_{\mu\mu\gamma} < 100$ GeV
$E_T^{\text{miss}} < 30$ GeV

Table 5.10: Selection criteria for the  $V\gamma$  control region.

1850 The  $Z\gamma$  MC samples available do not cover the full range of  $p_T^\gamma$  and  $\Delta R(\gamma, l)$ ; thus, additional  
 1851 Drell-Yan samples ( $Z+jets$ ) are used to fill out the phase space. Overlap between the two samples  
 1852 are removed to avoid double counting. Events with final state photons are checked at truth level<sup>16</sup>  
 1853 to ensure that the photon did not originate from a hadronic decay. Cuts on  $p_T^\gamma > 10$  GeV and  
 1854  $\Delta R(\gamma, l) > 0.1$  are then applied at generator level, and  $Z\gamma$  events that fail this additional selection  
 1855 and  $Z+jets$  events that pass it are removed.

1856 The normalization factor is calculated directly from the event yields in the  $V\gamma$  control region  
 1857 rather than in the signal fit, as is done for the  $WZ$  background. The event yields are listed in

<sup>16</sup>Truth particles are the particles produced directly by the MC generator before being passed through the full detector simulation, at which point they are considered *reconstruction-level* (or *reco-level*) particles.

1858 Table 5.11, and the normalization factor is determined to be 1.77. No MC events from  $Z\gamma$  processes  
 1859 survive the full event selection; thus, the scaling is only applied to the  $W\gamma$  background in the signal  
 1860 region. A systematic uncertainty of 44% is assigned to the background based off of the uncertainties  
 1861 in the calculation of the normalization factor.

Event yields in the $V\gamma$ control region	
$Z\gamma$	$24.6 \pm 3.3$
$Z+jets$	$3.0 \pm 1.5$
diboson + triboson	$6.7 \pm 0.3$
top	$1.5 \pm 0.5$
Total prediction	$35.8 \pm 3.7$
Data	$57 \pm 7.6$

Table 5.11: Event yields in the  $V\gamma$  control region. The  $V\gamma$  scale factor of 1.77 is calculated by scaling up the  $Z\gamma$  and  $Z+jets$  backgrounds to account for the difference between the data and predicted total background.

### 1862 5.3.3 Estimation of backgrounds from charge misidentification

1863 If an electron's charge is mis-reconstructed, it can lead to a real opposite-sign lepton pair passing  
 1864 the same-sign requirement in the event selection. There are two primary reasons this can occur:

- 1865 1. An electron emits a photon via bremsstrahlung which then converts into an electron-positron  
 1866 pair, and the conversion track with the wrong electric charge is matched to the original electron.  
 1867 This is the dominant process leading to charge flip, and it is highly dependent on the electron  
 1868  $\eta$  due to the different amount of detector material the electron passes through.
- 1869 2. The curvature of the electron's track is mis-measured, resulting in the wrong charge being  
 1870 assigned. This process is dependent on the momentum of the electron, as its track becomes  
 1871 more straight as the momentum of the electron increases.

1872 In order to estimate this background, the rate at which an electron's charge is misidentified is  
 1873 calculated from  $Z \rightarrow ee$  MC simulation. It is known that the MC does not perfectly model the  
 1874 material effects leading to charge flip; as a result, scale factors are applied to the MC in order for it  
 1875 to better reflect the real performance. These scale factors are obtained from the ratio of charge  
 1876 mis-ID rates in data and uncorrected MC in [83] following the method outlined in [111]. Once the  
 1877 scale factors are applied, the charge misidentification rate  $\varepsilon$  can be extracted by comparing the

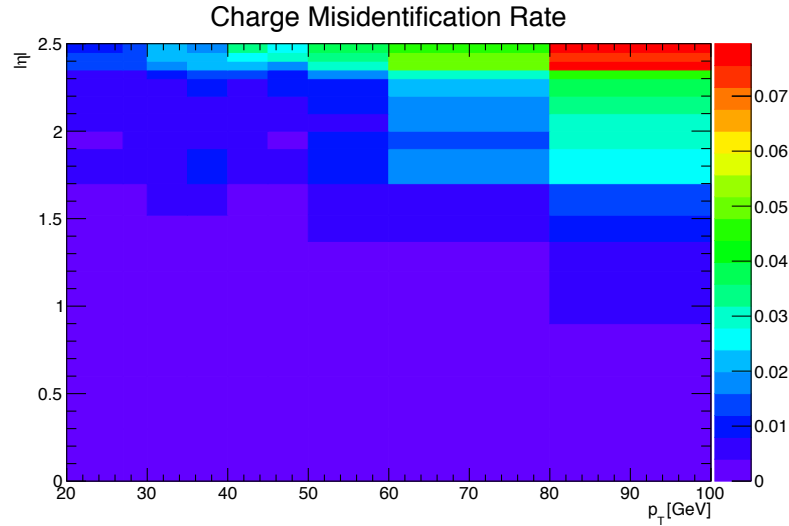


Figure 5.10: Charge misidentification rates for electrons as a function of  $|\eta|$  and  $p_{\text{T}}$ . Rates are calculated from  $Z \rightarrow e^+e^-$  MC after applying scale factors to approximate the charge mis-ID rates in data.

1878 electron's reconstructed charge with the charge of its truth particle:

$$\varepsilon(\eta, p_{\text{T}}) = \frac{N_{\text{wrong charge}}}{N_{\text{prompt electrons}}} . \quad (5.1)$$

1879 The charge mis-ID rate is calculated in bins of electron  $|\eta|$  and  $p_{\text{T}}$ , and it varies from below 0.1%  
 1880 in the central region of the detector up to 8% in the forward regions for high  $p_{\text{T}}$  (above 80 GeV)  
 1881 electrons. A two-dimensional plot of  $\varepsilon$  can be found in Figure 5.10.

1882 Given the charge flip rate  $\varepsilon(\eta, p_{\text{T}})$ , the rate at which an electron has its charge correctly recon-  
 1883 structed is  $(1 - \varepsilon)$ . Thus there are three possible combinations of charge identification, assuming a  
 1884 two-electron event:

- 1885 1. Both electrons are reconstructed correctly:  $(1 - \varepsilon)^2$
- 1886 2. Both electrons are mis-reconstructed:  $\varepsilon^2$
- 1887 3. Only one electron is mis-reconstructed:  $2\varepsilon(1 - \varepsilon)$

1888 In order to estimate the size of the background from charge misidentification, opposite-sign events  
 1889 are selected using the default event selection for a given signal or control region with the same-sign  
 1890 requirement inverted. These events are then weighted by the probability for one of the electrons to

1891 be reconstructed with the wrong charge:

$$\omega = \frac{\varepsilon_1(1 - \varepsilon_2) + \varepsilon_2(1 - \varepsilon_1)}{(1 - \varepsilon_1)(1 - \varepsilon_2) + \varepsilon_1\varepsilon_2}, \quad (5.2)$$

1892 where the subscripts 1 and 2 refer to the leading and subleading electrons, respectively, and  $\varepsilon_i$  is a  
 1893 function of the  $\eta$  and  $p_T$  of the  $i^{\text{th}}$  electron. In the case of an event with one electron and one muon  
 1894 ( $\varepsilon_\mu = 0$ ), Equation 5.2 simplifies to

$$\omega = \frac{\varepsilon}{1 - \varepsilon}. \quad (5.3)$$

1895 This method assumes that there is little contamination from fake electrons in the opposite-sign  
 1896 sample, and this has been verified with MC simulation.

1897 Additionally, charge-flipped electrons tend to be reconstructed with lower energy when compared  
 1898 to electrons with the correct charge. This is due to energy loss from the material interactions that  
 1899 can cause the charge to be misidentified in the first place. A correction factor is calculated from  
 1900 MC simulations, comparing the  $p_T$  of the truth electron to its reconstructed counterpart:

$$\alpha = \frac{\left(\frac{p_T^{\text{reco}}}{p_T^{\text{truth}}} - 1\right)_{\text{correct charge}}}{\left(\frac{p_T^{\text{reco}}}{p_T^{\text{truth}}} - 1\right)_{\text{wrong charge}}}. \quad (5.4)$$

1901 The correction is then applied to the  $p_T$  of the charge-flipped electron via

$$p_T = p_T^0 / (1 + \alpha) + dE, \quad (5.5)$$

1902 where  $p_T^0$  is the uncorrected  $p_T$  of the electron and  $dE$  is a gaussian smearing factor centered at zero  
 1903 with a width related to the energy resolution. Since which electron is mis-reconstructed is never  
 1904 determined in this method, in the case of a two-electron event, the energy correction is applied  
 1905 randomly to one of the two electrons based on the probabilities for them to be charge-flipped. This  
 1906 also determines the overall sign of the event; the charge of the electron that does not receive the  
 1907 correction is taken to be the charge for both.

1908 Systematic uncertainties on the charge mis-ID rates are calculated by generating two additional  
 1909 sets of rates with the uncertainties on the scale factors varied up and down. The size of the esti-  
 1910 mated charge flip background without the energy correction applied is also taken as a systematic  
 1911 uncertainty. These systematic uncertainties are estimated to be approximately  $\pm 15\%$ .

### 1912 5.3.3.1 Validation of the charge misidentification estimate

1913 The performance of the charge misidentification estimation is tested in the same-sign inclusive  
 1914 validation region (VR), defined in Table 5.12. For  $ee$  events, the mass of the dilepton pair is required

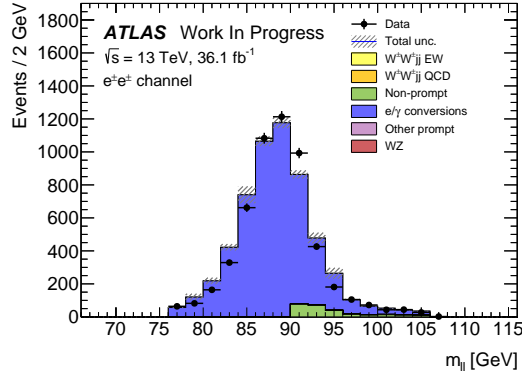


Figure 5.11: Dilepton invariant mass distribution  $m_{ll}$  for the  $ee$  channel in the same-sign inclusive VR.

1915 to lie within 15 GeV of the  $Z$  boson mass to increase the purity of the charge flip background.  
 1916  $t\bar{t}$  production, which can contribute to both the charge mis-ID and fake lepton backgrounds, is  
 1917 suppressed by the  $b$ -jet veto. The di-electron invariant mass is shown in Figure 5.11, and distributions  
 1918 of the leading and subleading electron  $p_T$  in the  $ee$ -channel are shown in Figure 5.12 with the  $Z$   
 1919 mass cut inverted. Agreement between data and prediction is seen within the total statistical and  
 1920 systematic uncertainties in the VR.

Same-sign inclusive VR
Exactly 2 same-sign signal leptons
$p_T > 27$ GeV for both leptons
$m_{ll} > 20$ GeV
$ m_{ee} - m_Z  > 15$ GeV ( $e^\pm e^\pm$ -channel only)
$N_{b\text{-jet}} = 0$

Table 5.12: Selection criteria for the same-sign inclusive validation region.

### 1921 5.3.4 Estimation of non-prompt backgrounds with the fake-factor method

1922 Events with one prompt lepton produced in association with hadronic jets can pass the event selection  
 1923 if a jet is misidentified as a charged lepton or if a non-prompt lepton from the decay of a heavy  
 1924 flavor particle (such as  $b$ - and  $c$ -hadrons) passes the signal lepton criteria. These misidentified jets  
 1925 and non-prompt leptons are collectively referred to as *fake leptons*, or simply *fakes*. The rate at  
 1926 which a fake lepton is misidentified is generally not modelled well enough by the MC to accurately  
 1927 estimate their contributions directly from simulation. Therefore, a data-driven technique called the

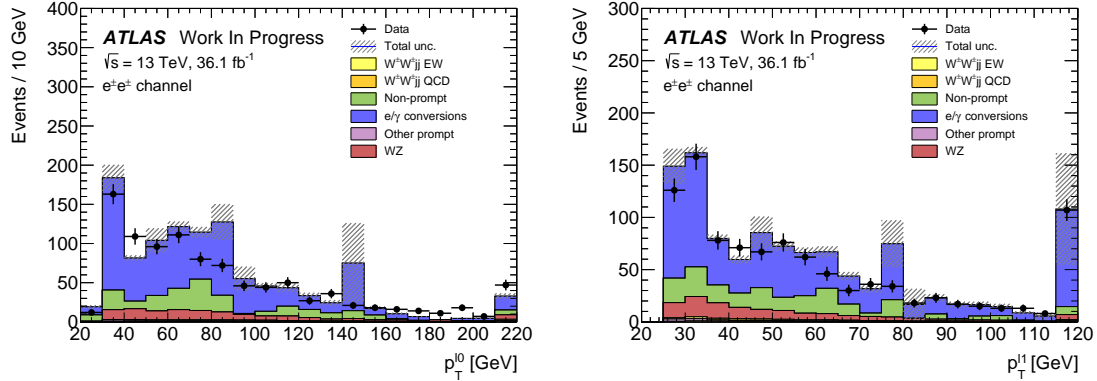


Figure 5.12:  $p_T$  distributions for the leading (left) and subleading (right) electron for the  $ee$  channel in the same-sign inclusive VR. In these plots, the cut requiring  $m_{ee}$  to fall within the  $Z$  mass window has been inverted in order to test the modelling away from the  $Z$  peak.

1928    *fake-factor* is used to estimate the size and shape of background processes from fake leptons. In this  
 1929    analysis, a new modification to the fake-factor is used involving the particle isolation variables; the  
 1930    method is outlined first in the context of the *default* fake-factor in Section 5.3.4.1, and the modified  
 1931    fake-factor is covered in Section 5.3.4.2.

### 1932    5.3.4.1    Overview of the default fake-factor method

1933    The goal of the fake-factor method is to measure the fake rate from real collision events in a region  
 1934    enriched in fake leptons and use it to estimate the size of the fake lepton background in a chosen  
 1935    signal or control region. This is done by creating two samples using different lepton definitions:

- 1936    1. The *nominal* sample is made up of leptons passing the signal selection.  
 1937    2. The *loose* sample is made up of leptons that fail the signal selection while still passing a  
 1938    loosened set of criteria. This sample is enriched in fake leptons and is orthogonal to the set of  
 1939    nominal leptons.

1940    Using the sets of nominal and loose leptons, a fake-factor  $f$  can be calculated from a region enriched  
 1941    in processes that are prone to producing fake leptons:

$$f = \frac{N_{\text{nominal}}}{N_{\text{loose}}} . \quad (5.6)$$

1942    Since the fake rate is not expected to be constant over the entire phase space, the fake-factor can  
 1943    be divided into bins:

$$f(b) = \frac{N_{\text{nominal}}(b)}{N_{\text{loose}}(b)} , \quad (5.7)$$

1944 where  $b$  represents the bin number. In this analysis, the fake-factor is binned in lepton  $p_T$ .

1945 In order to estimate the fake background contribution in a given signal or control region, the  
 1946 fake-factor is applied to a second control region with a selection identical to the region of interest  
 1947 except one of the leptons required to satisfy the loose criteria. The region for which the background  
 1948 is estimated contains two nominal leptons and is referred to as *nominal+nominal* (*NN*), and the  
 1949 associated control region where the fake-factor is applied contains one nominal and one loose lepton  
 1950 and is referred to as *nominal+loose* (*NL*). The fake background in a *NN* region can then be  
 1951 calculated as

$$N_{NN}^{\text{fake bkg.}} = \sum_b f(b) N_{NL}(b). \quad (5.8)$$

1952 Backgrounds containing two prompt leptons can also enter the *NL* region if one of the leptons  
 1953 passes the nominal selection and the other passes the loose selection. Since the fake-factor method  
 1954 estimates the fake background by scaling the amount of non-prompt events in the *NL* region, if these  
 1955 prompt contributions are not removed, they will be included in the scaling, and the background will  
 1956 be overpredicted. The final estimate of the fake background becomes

$$N_{NN}^{\text{fake bkg.}} = \sum_b f(b) (N_{NL}(b) - N_{NL}^{\text{prompt}}(b)). \quad (5.9)$$

1957 A visual representation of the fake background estimation process is shown in Figure 5.13.

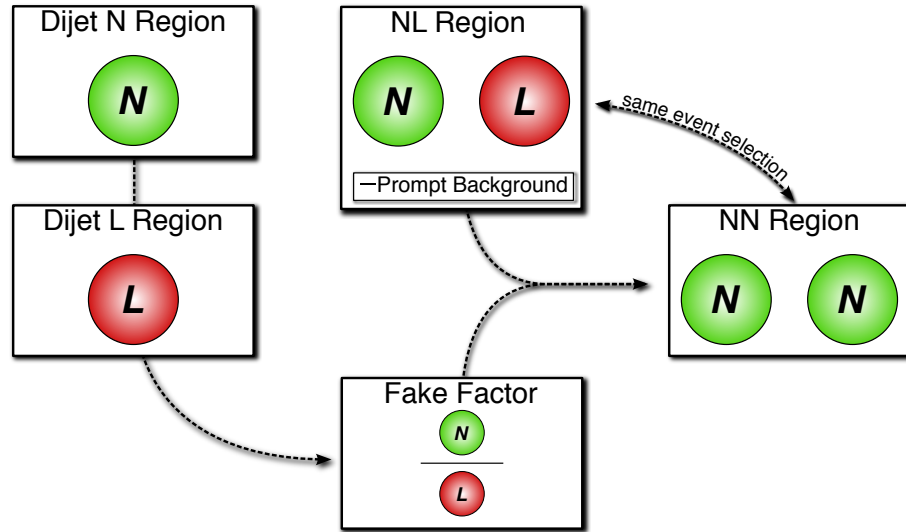


Figure 5.13: Graphical representation of how the fake factor method is used to estimate the fake background in a given *NN* region.

1958    **5.3.4.2 The fake-factor with  $p_T^{\text{cone}}$**

1959    When a jet produces a non-prompt lepton, that lepton only carries a fraction of the underlying jet's  
 1960    total momentum. Due to the isolation cut applied to the nominal leptons, they typically carry a  
 1961    much larger percentage of the underlying jet momentum than the loose leptons. Since the isolation  
 1962    essentially sets a limit on the amount of detector activity allowed around the lepton, if other nearby  
 1963    particles carried a significant amount of momentum, the lepton would likely fail this cut.

1964    This discrepancy in the underlying jet momentum fraction can cause problems in the calculation  
 1965    of the fake-factor  $f$ . Consider the case of two separate events with muons of identical momentum,  
 1966    but one passes the nominal selection, and the other passes the loose selection. The loose lepton on  
 1967    average will originate from a jet with higher  $p_T$  than the one corresponding to the nominal lepton  
 1968    despite both muons having the same momentum. This can be seen explicitly when comparing the  
 1969     $p_T$  of a muon to its associated truth jet:

$$\Delta p_T(\mu, j) = \frac{p_T(j) - p_T(\mu)}{p_T(j) + p_T(\mu)}. \quad (5.10)$$

1970    Since muons are not included in the jet reconstruction algorithm,  $\Delta p_T$  approximates the momentum  
 1971    of the muon compared to the rest of the jet. For muons that carry more than 50% of the jet's  
 1972    momentum,  $\Delta p_T$  will be negative and vice-versa. The  $\Delta p_T$  distributions for nominal and loose  
 1973    muons in  $t\bar{t}$  MC events is shown Figure 5.14, where a 25 GeV nominal muon on average corresponds  
 1974    to a 35 GeV jet, and a 25 GeV loose muon on average corresponds to a 62 GeV jet<sup>17</sup>.

1975    Since the default fake-factor defined in Equation 5.7 is binned in lepton  $p_T$ , the 25 GeV muons  
 1976    in the example above would occupy the same bin despite originating from very different jets. As  
 1977    a result, within a given bin, the underlying jet  $p_T$  spectrum can differ substantially between the  
 1978    numerator and the denominator. Additionally, these differences can vary depending on the process  
 1979    producing the non-prompt leptons or on the specific kinematic selections of the signal or control  
 1980    regions where the fake-factor is applied.

1981    Fortunately, the majority of the jet momentum not carried by the non-prompt lepton (excluding  
 1982    neutrinos) can be recovered using isolation variables. A track-based isolation is chosen, referred  
 1983    to as  $p_T^{\text{cone}}$ , and it contains the sum of the  $p_T$  of all particle tracks with  $p_T > 1$  GeV originating  
 1984    from the primary vertex within a cone of  $\Delta R < 0.3$  around the lepton. Thus, the sample of loose  
 1985    leptons in the denominator of the fake-factor calculation is binned in  $p_T + p_T^{\text{cone}}$  rather than simply

---

<sup>17</sup>To better illustrate the point, here the muon is added back into the jet  $p_T$ , and the corresponding muon  $p_T$  is obtained via  $\Delta p_T(\mu, j) = \frac{(p_T(j) - p_T\mu) - p_T(\mu)}{(p_T(j) - p_T\mu) + p_T(\mu)} = \frac{p_T(j) - 2p_T(\mu)}{p_T(j)}$ .

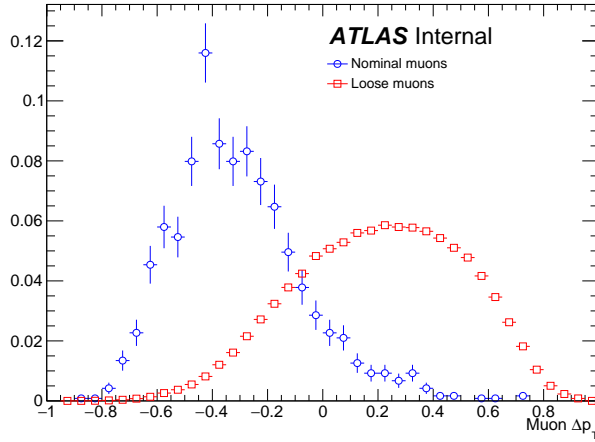


Figure 5.14:  $\Delta p_T$  distributions for nominal (blue) and loose (red) muons in simulated  $t\bar{t}$  events. Each muon has been matched to a truth-level jet. Both distributions are normalized to unit area.

lepton  $p_T$ . Adding the isolation cone greatly reduces the difference in the fraction of the underlying jet momentum carried by the nominal and loose leptons. To check this, a new  $\Delta p_T$  is calculated between a lepton and its matched truth jet, where the truth jet  $p_T$  has been corrected to include all muons within a cone of  $\Delta R < 0.4$ :

$$p_T(j) = p_T(j_{\text{truth}}) + \sum_{\Delta R < 0.4} p_T(\mu_{\text{truth}}). \quad (5.11)$$

The  $\Delta p_T$  distributions comparing  $p_T$  and  $p_T + p_T^{\text{cone}}$  for nominal and loose leptons using the corrected jet  $p_T$  are found in Figure 5.15, and better agreement is seen between the numerator (nominal) and denominator (loose with  $p_T + p_T^{\text{cone}}$ ) distributions.

The numerator remains binned in lepton  $p_T$ , due to the fact that it is meant to mirror the signal region as closely as possible, and the signal lepton selection does not use  $p_T + p_T^{\text{cone}}$ . The impact of this is expected to be negligible due to the  $p_T^{\text{cone}}$  isolation being small for signal leptons, as shown for muons in Figure 5.16. Finally, the fake-factor  $f$  becomes

$$f(b) = \frac{N_{\text{nominal}}(b(p_T))}{N_{\text{loose}}(b(p_T + p_T^{\text{cone}}))}. \quad (5.12)$$

### 5.3.4.3 Application of the fake-factor

The fake-factor itself is measured from a sample of collision events passing a dijet selection that requires exactly one lepton (either passing the nominal or loose selections) and at least one jet.

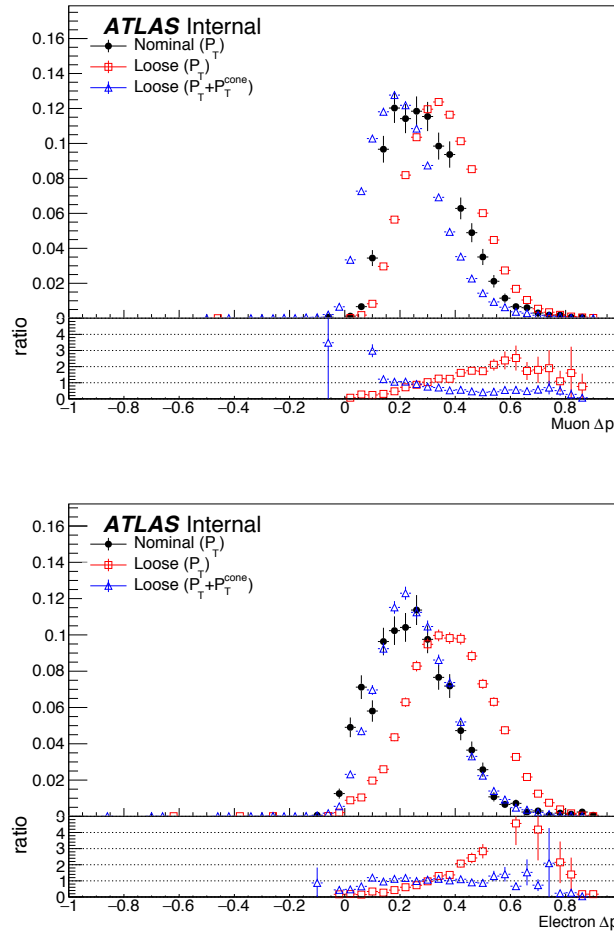


Figure 5.15:  $\Delta p_T$  distributions for muons (top) and electrons (bottom) in simulated  $t\bar{t}$  events. Each lepton has been matched to a truth-level jet, and that truth jet has had its  $p_T$  corrected to include all truth muons within a cone of  $\Delta R < 0.4$ . The nominal leptons are in black.  $\Delta p_T$  is calculated for the loose leptons using  $p_T$  (red) and  $p_T + p_T^{\text{cone}}$  (blue).

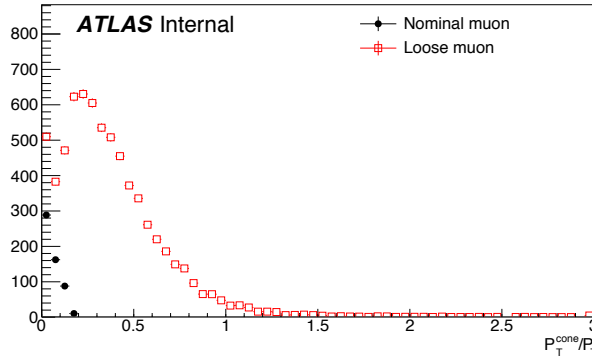


Figure 5.16: Distributions of  $p_T^{\text{cone}}/p_T$  for nominal (black) and loose (red) muons in simulated  $t\bar{t}$  events.

2000 The leading jet must also be  $b$ -tagged and approximately back-to-back with the lepton in order to  
 2001 enhance non-prompt lepton contributions while reducing contributions from processes involving  $W$   
 2002 and  $Z$  bosons.  $W$  boson events are further suppressed by requiring the sum of the  $E_T^{\text{miss}}$  and the  
 2003 transverse mass of the lepton to be less than 50 GeV. The full event selection for the dijet region is  
 2004 summarized in Table 5.13.

Dijet event selection
Event preselection
Exactly one lepton with $p_T > 15$ GeV
$N_{\text{jet}} > 0$
Leading jet is $b$ -tagged
$p_T^{\text{lead. jet}} > 25$ GeV
$p_T^{\text{lead. jet}} > 30$ GeV if $ \eta_j  > 2.5$
$ \Delta\phi(l, \text{lead. jet})  > 2.8$
$m_T(l, E_T^{\text{miss}}) + E_T^{\text{miss}} < 50$ GeV

Table 5.13: Event selection for the dijet region used for calculating the fake-factor. The selected lepton can pass either the nominal (signal) or loose selections. In the case of the nominal leptons, the  $p_T > 27$  GeV requirement is replaced with  $p_T > 15$  GeV.

2005 The numerator sample is constructed from dijet events in which the lepton passes the nominal  
 2006 (signal) selection and is binned in the lepton  $p_T$ . Similarly, the denominator sample is made up of  
 2007 the remaining dijet events where the lepton passes the loose selection and is binned in the lepton  
 2008  $p_T + p_T^{\text{cone}}$ . The nominal and loose leptons pass the signal selection<sup>18</sup> and loose selection, respectively,  
 2009 defined earlier in Table 5.3 for muons and Table 5.4 for electrons. Backgrounds from  $W + \text{jets}$ ,  $Z + \text{jets}$ ,

<sup>18</sup>The  $p_T > 27$  GeV cut in the signal lepton selection is dropped in favor of the  $p_T > 15$  GeV requirement in the dijet selection.

2010  $t\bar{t}$ , and single top processes are estimated from MC simulations requiring one lepton to be prompt  
 2011 using the truth information; these contributions are subtracted from the dijet data. The fake-factor  
 2012 is then calculated using Equation 5.12 for muons and for central and forward electrons separately.  
 2013 The muon fake-factor is shown in Figure 5.17, and the two electron fake-factors (one each for central  
 2014 and forward electrons) are shown in Figure 5.18. The numerical values of the fake-factors, including  
 2015 their systematic uncertainties (which will be discussed in Section 5.3.4.4) are listed in Table 5.14.

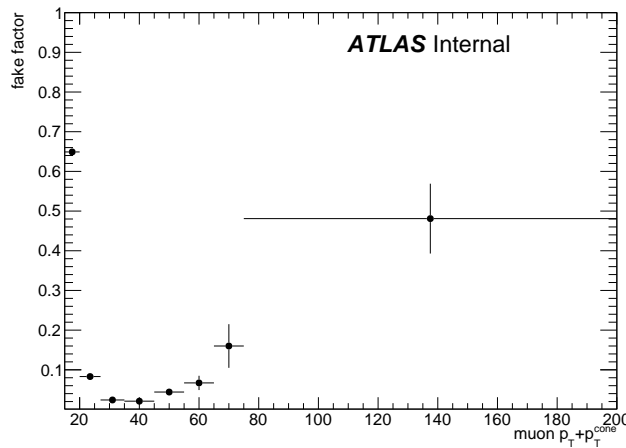


Figure 5.17: The measured fake-factor as a function of muon  $p_T + p_T^{\text{cone}}$ . The error bars represent the statistical uncertainty only.

2016 In order to properly account for the denominator being binned in  $p_T + p_T^{\text{cone}}$ , special care needs  
 2017 to be taken when estimating the fake background from the *NL* regions. For the purposes of the  
 2018 fake-factor calculation, it is perhaps more intuitive to consider a loose *object* with  $p_T = p_T + p_T^{\text{cone}}$   
 2019 instead of simply a loose lepton, as the lepton and the underlying jet are treated as a whole with this  
 2020 method. When the lepton  $p_T$  cuts required by a particular signal or control region are applied to  
 2021 nominal and loose leptons, the cut is applied to the  $p_T$  of the nominal lepton and to the  $p_T + p_T^{\text{cone}}$  of  
 2022 the loose object. Similarly, when looking up the fake-factor weight for a given *NL* event, the value  
 2023 is taken from the bin corresponding to the  $p_T + p_T^{\text{cone}}$  of the loose object. Finally, when applying the  
 2024 weight to the *NL* event,  $p_T + p_T^{\text{cone}}$  is assigned as the  $p_T$  of the loose object. This can be visualized  
 2025 by referring back to Figure 5.13; every time a loose lepton is used (the red circles in the Figure),  
 2026  $p_T + p_T^{\text{cone}}$  is used in place of  $p_T$ .

2027 Finally, it should be noted that the addition of  $p_T^{\text{cone}}$  to the loose object may cause the loose  
 2028 leptons in the denominator sample to migrate into higher bins. This results in an overall decrease in

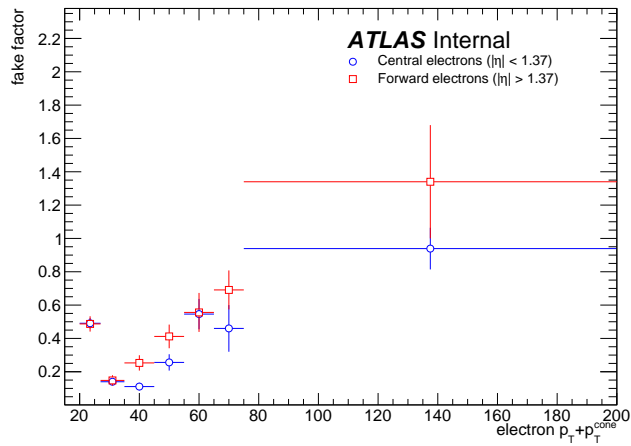


Figure 5.18: The measured fake-factor as a function of electron  $p_T + p_T^{\text{cone}}$  in the central ( $|\eta| < 1.37$ , blue) and forward ( $|\eta| > 1.37$ , red) regions of the detector. The error bars represent the statistical uncertainty only.

2029 the number of loose objects in the lower  $p_T + p_T^{\text{cone}}$  bins due to there not being additional leptons at  
 2030 lower  $p_T$  to replace them. Since the fake-factor is a ratio of the number of events in a bin, this effect  
 2031 causes the first few bins of the fake-factor to increase, as can be seen clearly in Figure 5.17. However,  
 2032 the signal and control regions (and their corresponding  $NL$  regions) contain a  $p_T > 27$  GeV cut that  
 2033 prevents these migrations from negatively impacting the fake estimation.

2034 **5.3.4.4 Systematic uncertainties**

2035 Four sources of systematic uncertainty are considered: the dijet event selection, prompt background  
 2036 subtraction, jet flavor composition, and residual dependence on the underlying jet  $p_T$  spectrum. In  
 2037 order to measure the impact of these systematics, new fake-factors are computed with variations  
 2038 in each of the systematic sources and the differences from the nominal values are taken as the  
 2039 uncertainty.

- 2040 1. In order to estimate uncertainties due to the dijet selection, the cut on  $M_T + E_T^{\text{miss}}$  is varied  
 2041 by  $\pm 5$  GeV, the jet-lepton separation  $\Delta\phi(l, j)$  by  $\pm 0.1$ , and the jet  $p_T$  cut by  $\pm 5$  GeV.  
 2042 2. To estimate the systematic uncertainty on the prompt background subtraction, the MC pre-  
 2043 diction in a  $W+\text{jets}$  control region is compared to data. The discrepancy between data and  
 2044 MC is found to be approximately 10% [83]. Therefore, the prompt background used for the  
 2045 subtraction is scaled up and down by  $\pm 10\%$ .

- 2046     3. The difference in the jet flavor composition between the dijet events and the events in the  
 2047     NL regions can affect the accuracy of the fake background estimation. The dijet sample is  
 2048     dominated by light jets, while the NL regions tend to be dominated by heavy flavor from  $t\bar{t}$ .  
 2049     To account for this, the fake-factor is computed with a  $b$ -jet veto.
- 2050     4. To measure any residual dependence on the underlying jet  $p_T$  spectrum, the leading jet  $p_T$   
 2051     distribution is reweighted to match the  $p_T$  spectrum of truth jets that produce fake leptons  
 2052     in MC simulations. This results in an increase in the number of nominal and loose leptons at  
 2053     high momentum [83].

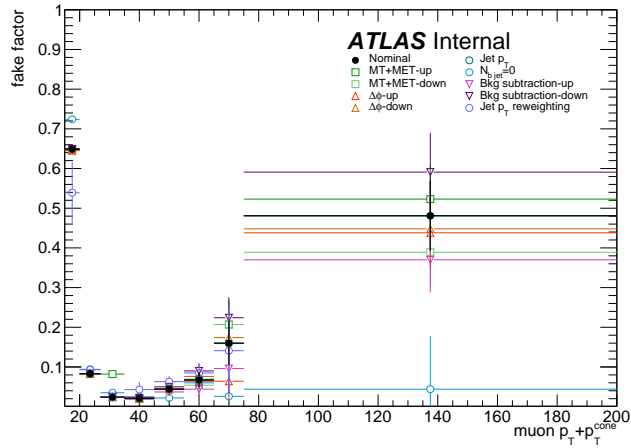


Figure 5.19: Systematic variations in the fake-factor as a function of muon  $p_T + p_T^{\text{cone}}$ . The individual fake-factors obtained for each systematic variation are displayed with their statistical uncertainties.

2054     **5.3.4.5 Results of the fake-factor**

- 2055     The fake background contribution in the signal region is estimated by applying the fake-factors  
 2056     to the equivalent NL region using Equation 5.9, where the fake-factor used corresponds to the  
 2057     flavor of the loose lepton in the event. As usual, the prompt background is subtracted from the  
 2058     NL events using MC simulation. Charge misidentification is handled using the same method as  
 2059     in Section 5.3.3, with an additional set of charge flip rates calculated for loose leptons. The fake  
 2060     background yields in the signal region are listed in Table 5.15. An overall uncertainty of 50% is  
 2061     assigned to the fake background estimation in  $\mu^\pm\mu^\pm$  events, and between 40% to 90% for  $e^\pm e^\pm$  and  
 2062      $\mu^\pm e^\pm$  events, including both statistical and systematic effects.

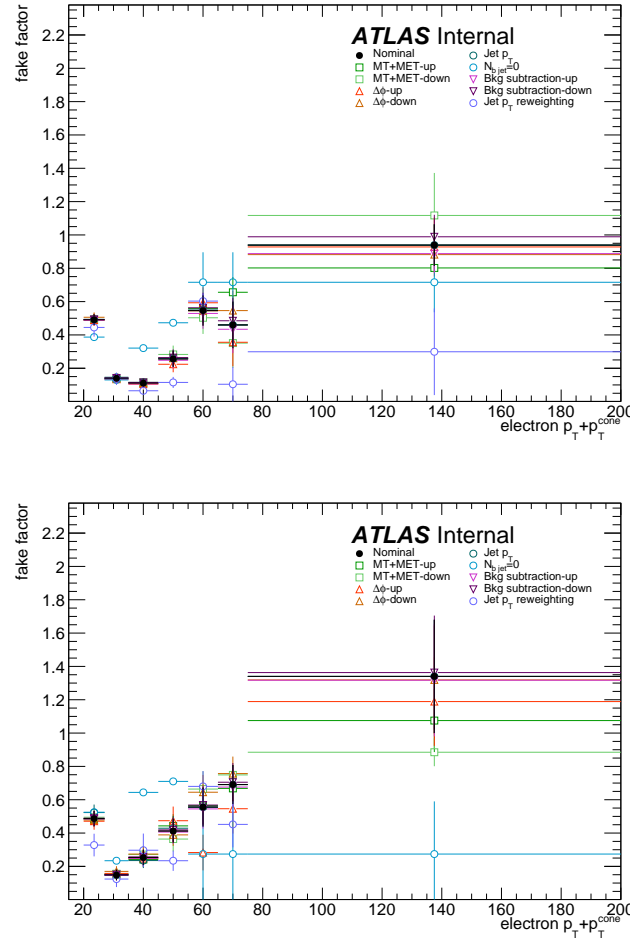


Figure 5.20: Systematic variations in the fake-factor as a function of electron  $p_T + p_T^{\text{cone}}$  in the central ( $|\eta| < 1.37$ , top) and forward ( $|\eta| > 1.37$ , bottom) regions of the detector. The individual fake-factors obtained for each systematic variation are displayed with their statistical uncertainties.

fake-factor	$p_T[15, 20]$	$p_T[20, 27]$	$p_T[27, 35]$	$p_T[35, 45]$	$p_T[45, 55]$	$p_T[55, 65]$	$p_T[65, 75]$	$p_T[75, 200]$
nominal	0.649 ± 0.007	0.083 ± 0.002	0.024 ± 0.002	0.021 ± 0.003	0.044 ± 0.007	0.067 ± 0.018	0.160 ± 0.055	0.481 ± 0.088
MT+MET	0.649 ± 0.007	0.082 ± 0.002	0.082 ± 0.002	0.020 ± 0.003	0.045 ± 0.007	0.068 ± 0.018	0.207 ± 0.062	0.523 ± 0.086
$\Delta\phi(\ell, j)$	0.648 ± 0.007	0.083 ± 0.003	0.024 ± 0.002	0.022 ± 0.004	0.044 ± 0.007	0.054 ± 0.020	0.207 ± 0.060	0.389 ± 0.081
Jet $p_T$	0.645 ± 0.008	0.083 ± 0.003	0.024 ± 0.002	0.021 ± 0.004	0.045 ± 0.008	0.064 ± 0.021	0.064 ± 0.058	0.438 ± 0.092
$N_{b\text{-jet}} = 0$	0.646 ± 0.006	0.083 ± 0.002	0.024 ± 0.002	0.020 ± 0.003	0.043 ± 0.006	0.076 ± 0.017	0.174 ± 0.050	0.448 ± 0.078
Bkg. subtraction	0.650 ± 0.007	0.083 ± 0.002	0.024 ± 0.002	0.021 ± 0.003	0.045 ± 0.007	0.069 ± 0.018	0.159 ± 0.018	0.481 ± 0.088
Jet $p_T$ Reweighting	0.724 ± 0.003	0.094 ± 0.001	0.035 ± 0.001	0.025 ± 0.002	0.022 ± 0.004	0.060 ± 0.015	0.026 ± 0.053	0.044 ± 0.134
	0.648 ± 0.007	0.083 ± 0.002	0.024 ± 0.002	0.019 ± 0.003	0.037 ± 0.007	0.044 ± 0.019	0.096 ± 0.062	0.370 ± 0.082
	0.649 ± 0.007	0.083 ± 0.002	0.025 ± 0.002	0.022 ± 0.003	0.050 ± 0.007	0.090 ± 0.017	0.224 ± 0.052	0.591 ± 0.099
	0.539 ± 0.077	0.093 ± 0.007	0.025 ± 0.004	0.043 ± 0.019	0.063 ± 0.014	0.085 ± 0.025	0.141 ± 0.110	1.962 ± 0.492

(a) Fake-factor values for muons.

fake-factor	$p_T[20, 27]$	$p_T[27, 35]$	$p_T[35, 45]$	$p_T[45, 55]$	$p_T[55, 65]$	$p_T[65, 75]$	$p_T[75, 200]$
nominal	0.491 ± 0.031	0.140 ± 0.020	0.111 ± 0.023	0.256 ± 0.049	0.546 ± 0.091	0.460 ± 0.140	0.939 ± 0.125
MT+MET	0.493 ± 0.030	0.138 ± 0.019	0.115 ± 0.022	0.261 ± 0.045	0.559 ± 0.084	0.656 ± 0.091	0.802 ± 0.016
$\Delta\phi(\ell, j)$	0.488 ± 0.032	0.137 ± 0.020	0.110 ± 0.025	0.283 ± 0.053	0.503 ± 0.097	0.351 ± 0.149	1.117 ± 0.255
Jet $p_T$	0.489 ± 0.035	0.134 ± 0.021	0.105 ± 0.025	0.224 ± 0.048	0.593 ± 0.093	0.356 ± 0.144	0.928 ± 0.177
$N_{b\text{-jet}} = 0$	0.506 ± 0.029	0.140 ± 0.018	0.111 ± 0.022	0.260 ± 0.046	0.545 ± 0.084	0.546 ± 0.120	0.882 ± 0.103
Jet $p_T$	0.493 ± 0.032	0.146 ± 0.021	0.115 ± 0.024	0.259 ± 0.049	0.550 ± 0.091	0.460 ± 0.140	0.939 ± 0.125
$N_{b\text{-jet}} = 0$	0.387 ± 0.009	0.130 ± 0.008	0.321 ± 0.012	0.473 ± 0.015	0.716 ± 0.180	0.716 ± 0.180	0.716 ± 0.180
Bkg. subtraction	0.488 ± 0.031	0.138 ± 0.020	0.106 ± 0.023	0.248 ± 0.049	0.529 ± 0.092	0.434 ± 0.143	0.888 ± 0.115
Jet $p_T$ Reweighting	0.493 ± 0.031	0.142 ± 0.020	0.115 ± 0.023	0.264 ± 0.049	0.563 ± 0.090	0.485 ± 0.136	0.989 ± 0.132

(b) Fake-factor values for central electrons ( $|\eta| < 1.37$ ).

fake-factor	$p_T[20, 27]$	$p_T[27, 35]$	$p_T[35, 45]$	$p_T[45, 55]$	$p_T[55, 65]$	$p_T[65, 75]$	$p_T[75, 200]$
nominal	0.487 ± 0.046	0.148 ± 0.031	0.253 ± 0.046	0.412 ± 0.071	0.556 ± 0.117	0.691 ± 0.117	1.340 ± 0.340
MT+MET	0.483 ± 0.045	0.152 ± 0.031	0.241 ± 0.043	0.443 ± 0.070	0.565 ± 0.106	0.668 ± 0.117	1.075 ± 0.189
$\Delta\phi(\ell, j)$	0.495 ± 0.047	0.156 ± 0.033	0.271 ± 0.052	0.364 ± 0.074	0.664 ± 0.107	0.749 ± 0.056	0.885 ± 0.084
Jet $p_T$	0.471 ± 0.051	0.158 ± 0.035	0.247 ± 0.051	0.474 ± 0.085	0.283 ± 0.107	0.546 ± 0.149	1.189 ± 0.266
$N_{b\text{-jet}} = 0$	0.478 ± 0.042	0.170 ± 0.031	0.274 ± 0.046	0.389 ± 0.066	0.645 ± 0.104	0.757 ± 0.102	1.319 ± 0.326
Jet $p_T$	0.523 ± 0.048	0.149 ± 0.033	0.235 ± 0.045	0.429 ± 0.073	0.555 ± 0.117	0.691 ± 0.117	1.340 ± 0.340
$N_{b\text{-jet}} = 0$	0.525 ± 0.011	0.234 ± 0.013	0.644 ± 0.016	0.710 ± 0.014	0.274 ± 0.316	0.274 ± 0.316	0.274 ± 0.316
Bkg. subtraction	0.484 ± 0.046	0.146 ± 0.031	0.248 ± 0.046	0.406 ± 0.071	0.545 ± 0.118	0.676 ± 0.118	1.317 ± 0.337
Jet $p_T$ Reweighting	0.489 ± 0.046	0.151 ± 0.031	0.257 ± 0.046	0.419 ± 0.071	0.568 ± 0.117	0.705 ± 0.115	1.363 ± 0.342

(c) Fake-factor values for forward electrons ( $1.37 < |\eta|$ ).Table 5.14: Values of the fake-factor in each  $p_T$  bin and for each individual systematic source.

	estimated yield	$f_e$ stat. up	$f_e$ stat. dn	$f_e$ syst. up	$f_e$ syst. dn	$f_\mu$ stat. up	$f_\mu$ stat. dn	$f_\mu$ syst. up	$f_\mu$ syst. dn
$e^\pm e^\pm$	11.42 ± 3.13	—	—	—	—	—	—	—	—
$\mu^\pm \mu^\pm$	4.82 ± 0.77	—	—	—	—	0.65	-0.65	3.64	-0.61
$\mu^\pm e^\pm$	37.08 ± 5.16	4.90	-4.90	5.59	-14.34	1.39	-1.39	16.10	-1.98

Table 5.15: Estimated yields for the fake lepton background. The estimated yield is shown in the first column together with the statistical uncertainty followed by the systematic uncertainties from variations of the the fake-factors within their statistical (stat.) and systematic (syst.) uncertainties. The labels  $f_e$  and  $f_\mu$  indicate the fake-factors for electrons and muons, respectively.

2063 **5.3.4.6 Validation of the fake-factor**

2064 The accuracy of the fake-factor method is tested in several validation regions, the most sensitive  
 2065 of which is the same-sign top fakes VR (SS top VR), defined in Table 5.16. This region inverts  
 2066 the signal region's  $b$ -jet veto to accept events with exactly one  $b$ -jet. Due to this requirement, the  
 2067 dominant source of events comes from the  $t\bar{t}$  process where a  $b$ -jet fakes an isolated lepton. The  
 2068 distribution of the subleading lepton  $p_T$  in this VR is shown in Figure 5.21 for all lepton flavor  
 2069 combinations. There is good agreement between the data and the prediction, even when only taking  
 2070 into account the statistical uncertainty and not the large systematic uncertainties assigned to the  
 2071 fake estimation.

Same-sign top fakes VR
Exactly 2 same-sign signal leptons
$p_T > 27$ GeV for both leptons
$m_{ll} > 20$ GeV
$ m_{ee} - m_Z  > 15$ GeV ( $e^\pm e^\pm$ -channel only)
$N_{b\text{-jet}} = 1$
$N_{\text{jet}} \geq 2$
Leading jet $p_T > 65$ GeV
Subleading jet $p_T > 35$ GeV

Table 5.16: Selection criteria for the same-sign top fakes validation region.

2072 **5.3.5 Reduction of  $WZ$  background using custom overlap removal**

2073 The dominant source of prompt background in this analysis comes from  $WZ$  events where both  
 2074 bosons decay leptonically. Traditionally, the background is dealt with by imposing a veto on any  
 2075 event with a third lepton passing some loose identification criteria (the so-called *trilepton veto*).  
 2076 In the case of this analysis, if one or more leptons in addition to the two signal leptons pass the  
 2077 preselection criteria, the event is rejected. However,  $WZ$  events can still enter the signal region if  
 2078 one of the leptons fails the preselection or falls outside of the detector's acceptance.

2079 In order to understand the sources of  $WZ$  events that are not removed by the trilepton veto,  
 2080 a study was performed on truth-level leptons in  $W^\pm W^\pm jj$  and  $WZ$  MC samples. Events with  
 2081 three truth leptons are selected, and each is matched to its reconstruction-level partner by finding  
 2082 the closest match in  $\Delta R(\text{truth}, \text{reco})$  and  $\Delta p_T(\text{truth}, \text{reco})$ . For events surviving the trilepton veto,  
 2083 the two signal leptons are removed, and the remaining leptons represent real leptons that fail to  
 2084 be selected for the veto. Between 40-50% of these leptons fall outside of the eta acceptance of the

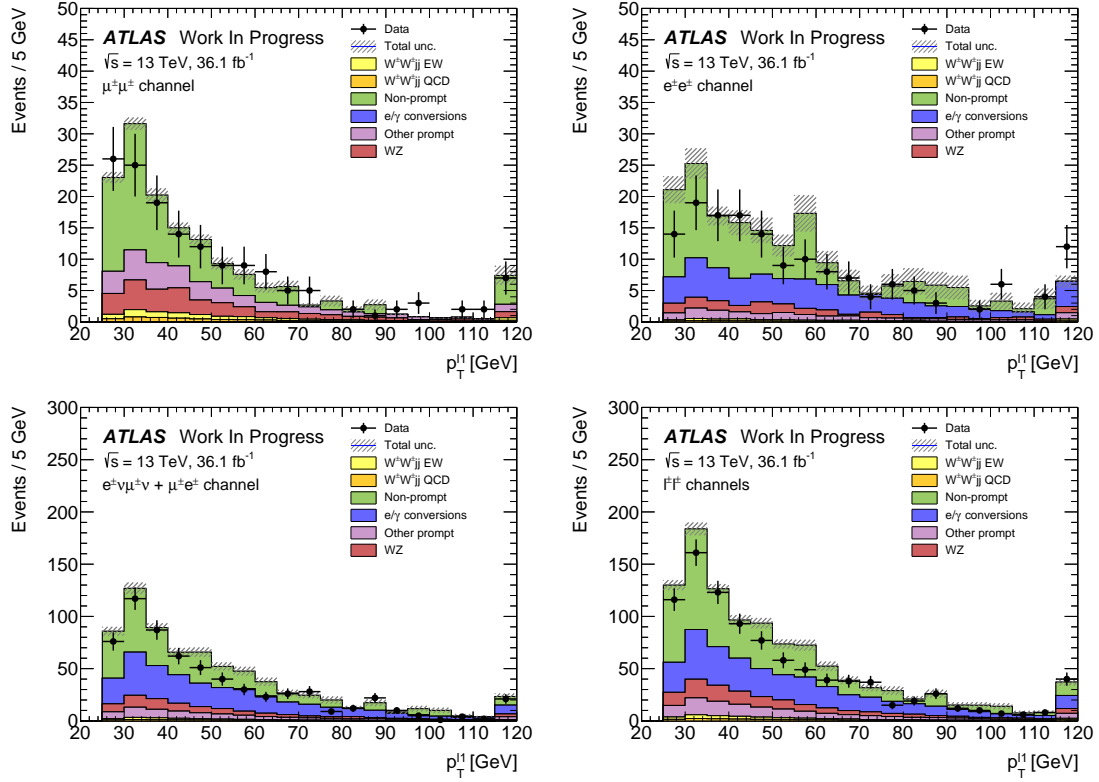


Figure 5.21: Distributions of the subleading lepton  $p_T$  in the same-sign top fakes VR for  $\mu^\pm\mu^\pm$  events (top right),  $e^\pm e^\pm$  events (top left),  $\mu^\pm e^\pm$  events (bottom left), and all events combined (bottom right). All errors are statistical only.

analysis (see Figure 5.22) and are unrecoverable. The second largest source of leptons failing the preselection is the OR, defined in Section 5.2.1.4. The standard OR procedure appears to be too aggressive in removing leptons in favor of jets, causing many three lepton events to “lose” their third lepton and pass the trilepton veto. Therefore a *custom OR* is investigated which would replace the standard OR in the preselection and allow for better  $WZ$  rejection by removing fewer third leptons.

In order to construct this custom OR, a new quantity is defined between a lepton ( $l$ ) and a nearby jet ( $j$ ):

$$p_{T,\text{ratio}}(l, j) = \frac{p_{Tl}}{p_{Tj}}, \quad (5.13)$$

which, along with  $\Delta R(l, j)$ , will make up the custom OR criteria. The idea behind including  $p_{T,\text{ratio}}$  is to be able to preferentially remove background leptons originating from jets (those that carry a low percentage of the total jet momentum) instead of removing *any* lepton near a jet. The distributions of  $p_{T,\text{ratio}}$  and the associated efficiency curves for muons and electrons can be found in Figures 5.23

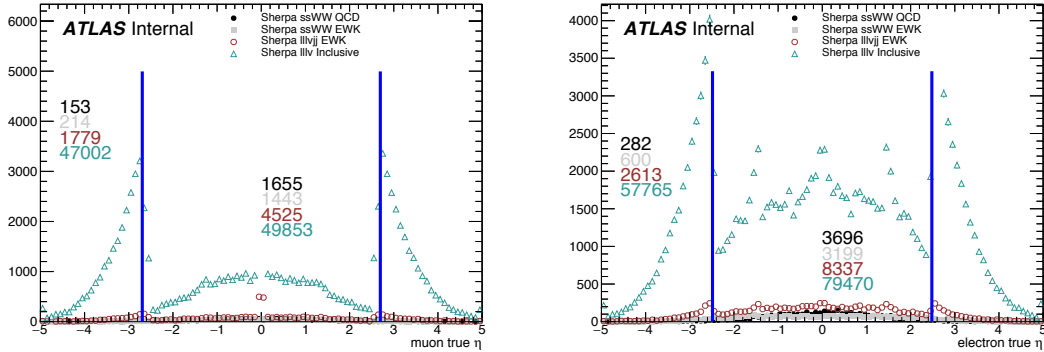


Figure 5.22: Pseudorapidity ( $\eta$ ) distributions of truth muons (top) and electrons (bottom) for Sherpa  $W^\pm W^\pm jj$  and  $WZ$  MC samples. The blue vertical lines represent the allowed  $\eta$  range for each lepton flavor. The numbers correspond to the number of raw MC events that fall within and outside of the allowed  $\eta$  range for each MC sample.

and 5.25, respectively, and the distributions for  $\Delta R(\mu, j)$  for muons can be found in Figure 5.24. Since all electrons have an associated jet in the calorimeters, the  $\Delta R(e, j)$  variable is not a good quantity to use for this custom OR.

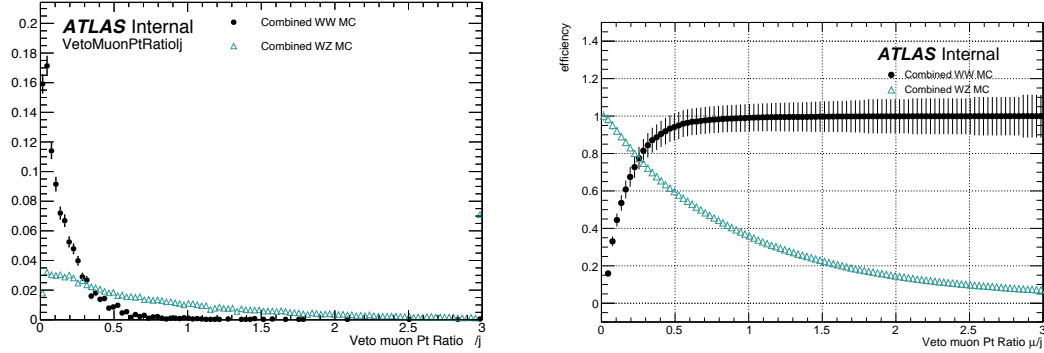


Figure 5.23: Distributions of  $p_{T,\text{ratio}}(\mu, j)$  for EWK and QCD  $W^\pm W^\pm jj$  signal (black) and  $WZ$  background (teal) for truth-matched third muons in events that pass the trilepton veto. Both distributions are normalized to unit area. The associated efficiency curves are on the right where efficiency is defined as the percentage of total events that would pass a cut on  $p_{T,\text{ratio}}(\mu, j)$  at a given value on the  $x$ -axis.

A working point for the Custom OR was chosen by requiring 90% signal retention for muons and 90% background rejection for electrons. The cut on electrons was allowed to be much tighter because the number of signal events with a third electron is considerably smaller than for muons. It should be emphasized that the signal events present in Figures 5.23-5.25 do not represent the full

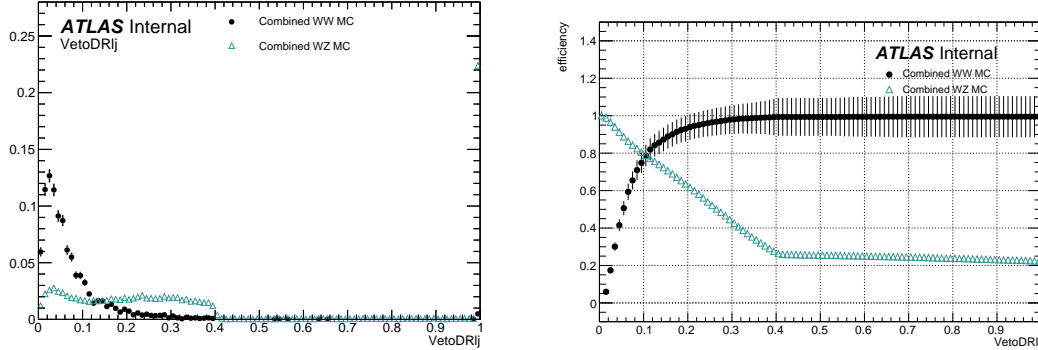


Figure 5.24: Distributions of  $\Delta R(\mu, j)$  for EWK and QCD  $W^\pm W^\pm jj$  signal (black) and  $WZ$  background (teal) for truth-matched third muons in events that pass the trilepton veto. Both distributions are normalized to unit area. The associated efficiency curves are on the right where efficiency is defined as the percentage of total events that would pass a cut on  $\Delta R(\mu, j)$  at a given value on the  $x$ -axis.

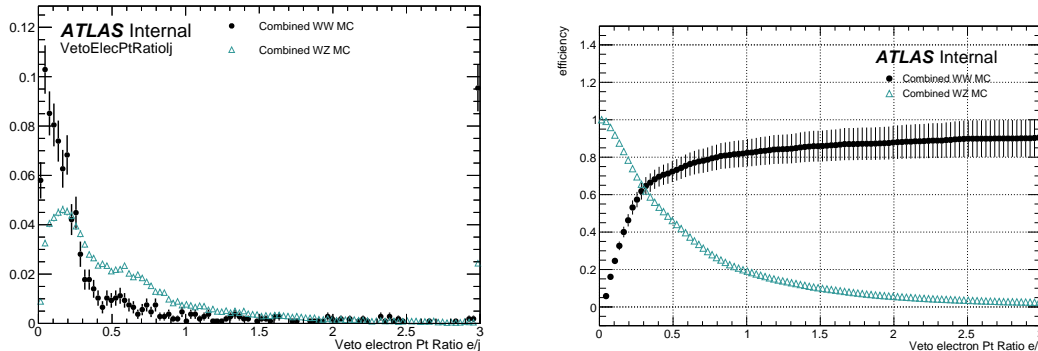


Figure 5.25: Distributions of  $p_{T,\text{ratio}}(e, j)$  for EWK and QCD  $W^\pm W^\pm jj$  signal (black) and  $WZ$  background (teal) for truth-matched third electrons in events that pass the trilepton veto. Both distributions are normalized to unit area. The associated efficiency curves are on the right where efficiency is defined as the percentage of total events that would pass a cut on  $p_{T,\text{ratio}}(e, j)$  at a given value on the  $x$ -axis.

set of signal events, but only those with a real third lepton (which must come from some source other than the signal  $W^\pm W^\pm jj$  process). For muons, a logical ‘or’ of  $p_{T,\text{ratio}}(\mu, j)$  and  $\Delta R(\mu, j)$  is used to maximize the third lepton acceptance due to correlations between the quantities, as shown in Figure 5.26; for electrons, only a cut on  $p_{T,\text{ratio}}(e, j)$  is used. The Custom OR working point is defined in Table 5.17.

Custom OR Definition	
Muons	$p_{T,\text{ratio}}(\mu, j) > 0.40$ or $\Delta R(\mu, j) > 0.15$
Electrons	$p_{T,\text{ratio}}(e, j) > 0.18$

Table 5.17: Custom OR definition. Leptons must pass this selection in order to be counted for the trilepton veto.

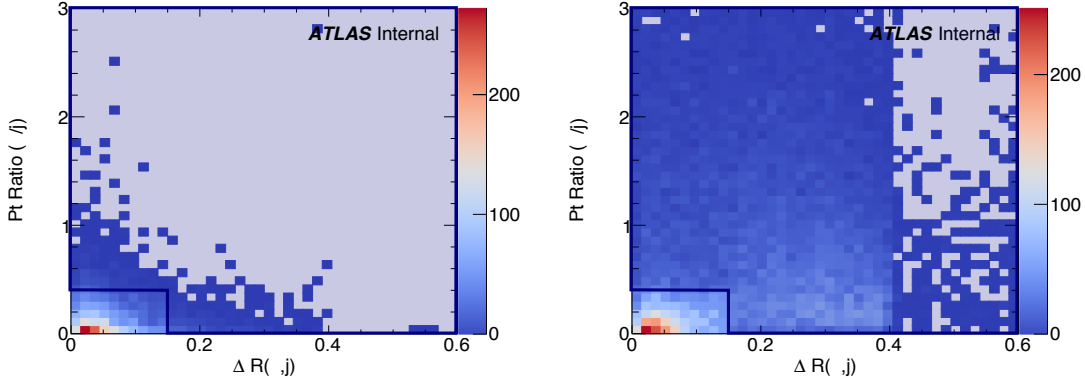


Figure 5.26: Two-dimensional plots of  $p_{T,\text{ratio}}(\mu, j)$  vs  $\Delta R(\mu, j)$  for truth-matched third muons in events that pass the trilepton veto for EWK and QCD  $W^\pm W^\pm jj$  signal (left) and  $WZ$  background (right). The blue overlay indicates the area in which the third leptons will pass the custom OR and result in the event failing the trilepton veto.

Initial tests of the performance of the Custom OR yielded promising results, with approximately 20% reduction in  $WZ$  background compared to less than 2% signal loss in the signal region. Unfortunately, due to differences between the primary analysis framework and the one used for testing, in practice the gains in  $WZ$  rejection were not nearly as substantial, and ultimately the Custom OR was not included in the final analysis. However, it is still a potentially useful tool for improving background rejection based on lepton counting in analyses with overly aggressive OR procedures.

2114 **5.4 Cross section measurement**

2115 The  $W^\pm W^\pm jj$  EWK cross section is extracted from the signal region using a maximum-likelihood  
 2116 fit applied simultaneously to four  $m_{jj}$  bins in the signal region as well as to the low- $m_{jj}$  and  $WZ$   
 2117 control regions. For the fit and cross section extraction, the signal region is defined as in Table 5.8  
 2118 with the dijet invariant mass requirement raised to  $m_{jj} > 500$  GeV. The low- $m_{jj}$  region is defined  
 2119 to mirror the signal region exactly with the dijet invariant mass inverted to  $200 < m_{jj} < 500$  GeV,  
 2120 and the  $WZ$  control region is as defined previously in Section 5.3.1.

2121 The signal and low- $m_{jj}$  regions are split into six channels based on the flavor and charge of  
 2122 the dilepton pair:  $\mu^+\mu^+$ ,  $\mu^-\mu^-$ ,  $\mu^+e^+$ ,  $\mu^-e^-$ ,  $e^+e^+$ , and  $e^-e^-$ . This split by charge increases the  
 2123 sensitivity of the measurement due to the  $W^+/W^-$  charge asymmetry favoring the production of  
 2124  $W^+$  bosons [112]. Since the signal events contain two  $W$  bosons, the signal strength compared to  
 2125 charge-symmetric backgrounds is much greater in the  $++$  channels than for both charges combined.  
 2126 The  $WZ$  control region is included in the fit as a single bin ( $l^\pm l^\mp l^\pm$ ).

2127 The maximum likelihood fit and cross section extractions are outlined in Sections 5.4.1 and  
 2128 5.4.3, respectively. The results of the cross section measurement and of the analysis as a whole are  
 2129 presented in Section 5.6.

2130 **5.4.1 Maximum likelihood fit**

2131 The number of predicted signal events in each channel  $c$  and  $m_{jj}$  bin  $b$  can be calculated from the  
 2132 SM predicted total production cross section  $\sigma_{\text{theo}}^{\text{tot}}$  scaled by the total integrated luminosity  $\mathcal{L}$ , the  
 2133 signal acceptance  $\mathcal{A}$ , and the efficiency corrections  $\mathcal{C}(\theta)$ :

$$N_{cb}^{\text{sig}}(\theta) = \sigma_{\text{theo}}^{\text{tot}} \mathcal{A}_b \mathcal{C}_b(\theta) \mathcal{L}. \quad (5.14)$$

2134 Here,  $\theta$  represents the set of nuisance parameters that parameterize the effects of each systematic  
 2135 uncertainty on the signal and background expectations. The acceptance and efficiency corrections  
 2136 will be covered in more detail in Section 5.4.2. A signal strength parameter  $\mu$  is defined as the ratio  
 2137 of the measured cross section to the SM predicted cross section. The expected number of events in  
 2138 a given channel and bin can then be expressed as the sum of the estimated background ( $N_{cb}^{\text{bkg}}(\theta)$ )  
 2139 and the number of predicted signal events scaled by  $\mu$ :

$$\begin{aligned} N_{cb}^{\text{exp}}(\theta) &= \mu N_{cb}^{\text{sig}}(\theta) + N_{cb}^{\text{bkg}}(\theta) \\ &= \mu \sigma_{\text{theo}}^{\text{tot}} \mathcal{A}_b \mathcal{C}_b(\theta) \mathcal{L} + N_{cb}^{\text{bkg}}(\theta). \end{aligned} \quad (5.15)$$

2140 The nuisance parameters are constrained by Gaussian probability distribution functions, and  
 2141 the normalization of the  $WZ$  background mentioned in Section 5.3.1 is included in the fit as a free  
 2142 parameter. The expected yields for signal and background processes are adjusted by the set of  
 2143 nuisance parameters within the constraints of the systematic uncertainties. The yields after the fit  
 2144 correspond to the value that best matches the observed data.

2145 The number of events per channel and bin after the fit can be written as a sum of the predicted  
 2146 event yields for each sample  $s$ :

$$\nu_{cb}(\phi, \theta, \gamma_{cb}) = \gamma_{cb} \sum_s [\eta_{cs}(\theta) \phi_{cs}(\theta) \lambda] h_{cbs}(\theta). \quad (5.16)$$

2147 In this equation, the fitted number of events in a given channel and bin is obtained by weighting  
 2148 the histogram of predicted yields  $h_{cbs}$  by the product of a given luminosity  $\lambda$  and any normalization  
 2149 factors  $\phi_{cs}$  that may be given for each channel and sample. The input histogram and the normal-  
 2150 ization factors may depend on the nuisance parameters  $\theta$  taking into account sources of systematic  
 2151 uncertainty. Uncertainties on the normalization factors  $\eta_{cs}(\theta)$  are also included. Finally, bin-by-bin  
 2152 scale factors  $\gamma_{cb}$  are included to parameterize the statistical uncertainties of the MC predictions.

2153 The binned likelihood function is given by a product of Gaussian functions for the luminosity  
 2154 and for the background uncertainties and a product of Poisson functions for the number of observed  
 2155 events in each bin and channel:

$$L(\mu|\theta) = \mathcal{G}(\mathcal{L}|\theta_{\mathcal{L}}, \sigma_{\mathcal{L}}) \cdot \prod_c \prod_b \mathcal{P}(N_{cb}^{\text{meas.}} | \nu_{cb}(\mu)) \prod_p \mathcal{G}(\theta_p^0 | \theta_p), \quad (5.17)$$

2156 where  $\mathcal{G}$  and  $\mathcal{P}$  are the Gaussian and Poisson functions, respectively. As before,  $\mathcal{L}$  represents the  
 2157 integrated luminosity with uncertainty  $\sigma_{\mathcal{L}}$  and associated nuisance parameter  $\theta_{\mathcal{L}}$ . The number of  
 2158 measured events in a given bin and channel is represented by  $N_{cb}^{\text{meas.}}$ , and  $\nu_{cb}(\mu)$  is the predicted  
 2159 number of events defined in Equation 5.16 expressed as a function of the signal strength  $\mu$ . Finally,  
 2160 the set of nuisance parameters  $\theta$  and any auxiliary measurements used to constrain them ( $\theta^0$ ) are  
 2161 multiplied for each parameter  $p$ .

2162 The profile likelihood ratio is defined as

$$q_{\mu} = -2 \ln \frac{L(\mu, \hat{\theta}_{\mu})}{L(\hat{\mu}, \hat{\theta})}, \quad (5.18)$$

2163 where  $\hat{\mu}$  and  $\hat{\theta}$  are the unconditional maximum likelihood estimates, and  $\hat{\theta}$  is the conditional maxi-  
 2164 mum likelihood estimate for a given value of  $\mu$ . The fitted signal strength  $\hat{\mu}$  is obtained by maximiz-  
 2165 ing the likelihood function with respect to all parameters. The compatibility of the observed data

with the background-only hypothesis can then be calculated by setting  $\mu = 0$ . Observation of the  $W^\pm W^\pm jj$  EWK process is claimed if the data is found to be inconsistent with the background-only hypothesis by more than  $5\sigma$ .

### 5.4.2 Definition of the fiducial volume

Before extracting the cross section, it is necessary to define the fiducial volume, or the phase space of measureable events. It is a subset of the total phase space defined by selection requirements designed to mirror those applied in the analysis as closely as possible. The selection criteria for the fiducial volume are listed in Table 5.18.

Fiducial region selection	
Lepton selection	Two prompt leptons ( $e, \mu$ ) $p_T > 27$ GeV and $ \eta  < 2.5$ for both leptons Both leptons with the same electric charge Dilepton invariant mass $m_{ll} > 20$ GeV Dilepton separation $\Delta R(ll) > 0.3$
Missing transverse energy	Two neutrino system with $p_T^{\nu\nu} > 30$ GeV
Jet selection	At least two jets Leading jet $p_T > 65$ GeV Subleading jet $p_T > 35$ GeV Leading and subleading jet $ \eta  < 4.5$ Jet-lepton separation $\Delta R(l, j) > 0.3$ Dijet invariant mass $m_{jj} > 500$ GeV Dijet separation $\Delta y_{jj} > 2.0$

Table 5.18: Definition of the fiducial volume.

The full phase space is generated in MC simulations, providing the total theoretical cross section  $\sigma_{\text{theo}}^{\text{tot}}$  and the total number of signal events  $\mathcal{N}_{\text{sig}}^{\text{tot}}$ <sup>19</sup>. After applying the fiducial selection at truth level, the total number of signal events in the fiducial region  $\mathcal{N}_{\text{sig}}^{\text{fid}}$  is obtained. An acceptance factor  $\mathcal{A}$  is used to represent the efficiency of events falling inside the fiducial region at truth level:

$$\mathcal{A} = \frac{\mathcal{N}_{\text{sig}}^{\text{fid}}}{\mathcal{N}_{\text{sig}}^{\text{tot}}}. \quad (5.19)$$

A correction factor  $\mathcal{C}$  is also necessary to translate from the truth level fiducial volume to the reconstruction level signal region and is defined in terms of the number of reconstruction level MC events in the signal region  $N_{\text{sig},\text{MC}}^{\text{SR}}$ :

$$\mathcal{C} = \frac{N_{\text{sig},\text{MC}}^{\text{SR}}}{\mathcal{N}_{\text{sig}}^{\text{fid}}}. \quad (5.20)$$

<sup>19</sup>For the purpose of clarity, the number of events at truth level is represented by a script  $\mathcal{N}$ , and the number of events at reconstruction level uses a regular  $N$ .

2181 Since the fit is binned in  $m_{jj}$ , the acceptance and efficiency correction factors must be as well.  
 2182 Therefore,  $\mathcal{A}_i$  and  $\mathcal{C}_{ij}$  are written in terms of truth  $m_{jj}$  bins  $i$  and reconstruction  $m_{jj}$  bins  $j$ . A  
 2183 graphical representation of these regions and the use of the acceptance and correction factors can  
 2184 be seen in Figure 5.27.

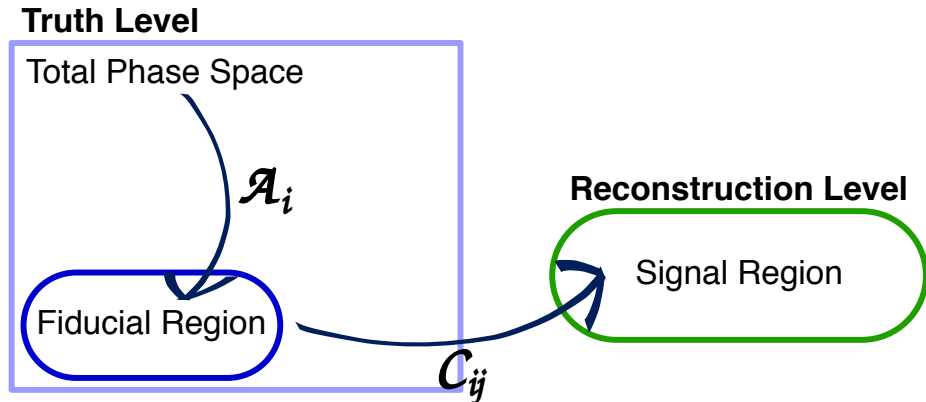


Figure 5.27: Visual representation of the different kinematic regions relevant to the cross section measurement. The acceptance factor  $\mathcal{A}$  converts from the truth level total phase space to the truth level fiducial region, and the efficiency correction  $\mathcal{C}$  translates the fiducial region into the reconstruction level signal region.

#### 2185 5.4.3 Cross section extraction

2186 The  $W^\pm W^\pm jj$  EWK fiducial cross section is measured using the signal strength parameter  $\mu$  that is  
 2187 determined by the maximum likelihood fit. This parameter is dependent on the nuisance parameters  
 2188  $\theta$  and can be written explicitly in terms of the measured and theoretical cross sections as

$$\mu(\theta) = \frac{\sigma_{\text{meas}}^{\text{SR}}}{\sigma_{\text{theo}}^{\text{SR}}} . \quad (5.21)$$

2189 In the simple case with only one bin, the equation for the total number of expected events in the  
 2190 signal region first introduced in Equation 5.15 can be written as

$$N_{\text{exp}}^{\text{SR}}(\theta) = \mu(\theta) \cdot \sigma_{\text{theo}}^{\text{tot}} \cdot \mathcal{L} \cdot \mathcal{A} \cdot \mathcal{C}(\theta) + N_{\text{bkg}}^{\text{SR}}(\theta) \quad (5.22)$$

2191 with the unbinned versions of  $\mathcal{A}$  and  $\mathcal{C}$  defined in Equations 5.19 and 5.20, respectively.

2192 If the measured fiducial cross section is written as

$$\sigma_{\text{meas}}^{\text{fid}} = \mu \cdot \mathcal{A} \cdot \sigma_{\text{theo}}^{\text{tot}} , \quad (5.23)$$

2193 then Equation 5.22 can be rearranged to read

$$\sigma_{\text{meas}}^{\text{fid}} = \frac{N_{\text{exp}}^{\text{SR}}(\theta) - N_{\text{bkg}}^{\text{SR}}(\theta)}{\mathcal{L} \cdot \mathcal{C}(\theta)}. \quad (5.24)$$

2194 The measured fiducial cross section can finally be rewritten in terms of  $\hat{\mu}$ , which is the best estimator  
2195 of the signal strength as extracted from the fit:

$$\begin{aligned} \sigma_{\text{meas}}^{\text{fid}} &= \hat{\mu}(\theta) \cdot \sigma_{\text{theo}}^{\text{tot}} \cdot \mathcal{A} \\ &= \hat{\mu}(\theta) \cdot \sigma_{\text{theo}}^{\text{fid}}. \end{aligned} \quad (5.25)$$

2196 In practice, however, the cross section is not extracted from a single bin, and Equation 5.22  
2197 becomes

$$N_{\text{exp}}^{\text{SR}}(\theta) = \mu(\theta) \cdot \sigma_{\text{theo}}^{\text{tot}} \cdot \mathcal{L} \cdot \sum_i \mathcal{A}_i \sum_j \mathcal{C}_{ij} + \sum_j N_{\text{bkg},j}^{\text{SR}}(\theta) \quad (5.26)$$

2198 for a single channel in truth and reconstruction level  $m_{jj}$  bins  $i$  and  $j$ , respectively, where the binned  
2199 versions of  $\mathcal{A}_i$  and  $\mathcal{C}_{ij}$  are used. This equation can be extended to include all the analysis channels  
2200 by increasing the number of bins  $i$  and  $j$ . Additionally, it can be shown that Equation 5.25 holds  
2201 for this more complex case as well [83], provided care is taken to ensure that all the uncertainties  
2202 are handled properly.

## 2203 5.5 Summary of uncertainties

2204 Systematic uncertainties enter the final fit as nuisance parameters which can impact the estimated  
2205 signal and background yields and the shapes of the  $m_{jj}$  distributions. These uncertainties can arise  
2206 from the experimental methods or from the theoretical calculations used in the analysis. This section  
2207 summarizes the systematic uncertainties; the experimental uncertainties are detailed in Section 5.5.1,  
2208 and the theoretical uncertainties are covered in Section 5.5.2. The impacts of the systematic uncer-  
2209 tainties on the final cross section measurement are summarized in Table 5.19.

### 2210 5.5.1 Experimental uncertainties

2211 Experimental uncertainties include detector effects as well as uncertainties on the background es-  
2212 timation methods. Sources of systematic uncertainty on the measurement of physics objects are  
2213 listed in Table 5.20, grouped by the relevant object type. For backgrounds estimated from MC  
2214 simulations, variations in these sources of uncertainty are propagated through the analysis to obtain  
2215 the corresponding uncertainties on the event yields. Additional experimental uncertainties include

Source	Impact [%]
Reconstruction	$\pm 4.0$
Electrons	$\pm 0.5$
Muons	$\pm 1.2$
Jets and $E_T^{\text{miss}}$	$\pm 2.8$
$b$ -tagging	$\pm 2.0$
Pileup	$\pm 1.5$
Background	$\pm 5.0$
Misid. leptons	$\pm 3.9$
Charge misrec.	$\pm 0.3$
$WZ$	$\pm 1.3$
$W^\pm W^\pm jj$ QCD	$\pm 2.8$
Other	$\pm 0.8$
Signal	$\pm 3.6$
Interference	$\pm 1.0$
EW Corrections	$\pm 1.3$
Shower, Scale, PDF & $\alpha_s$	$\pm 3.2$
Total	$\pm 7.4$

Table 5.19: Impact of various systematic effects on the fiducial cross section measurement. The impact of a given source of uncertainty is computed by performing the fit with the corresponding nuisance parameter varied up or down by one standard deviation from its nominal value.

2216 the integrated luminosity, the photon conversion rate from Section 5.3.2, and the data driven charge  
 2217 misidentification and fake lepton background estimations from Sections 5.3.3 and 5.3.4.5, respec-  
 2218 tively.

2219 The largest sources of experimental uncertainty on the MC estimations come from the jet-related  
 2220 uncertainties and the  $b$ -tagging efficiency, while the largest uncertainty on the background estimation  
 2221 comes from the fake-factor. The effects of the uncertainties on the  $W^\pm W^\pm jj$  EWK signal and the  
 2222 dominant MC estimated background,  $WZ$ , are listed in Tables 5.21 and 5.22, respectively. Since  
 2223 the overall contributions from other processes estimated with MC are small, the uncertainties on  
 2224 these backgrounds have a lesser impact on the final measurement; these tables can be found in  
 2225 Appendix A.1.

### 2226 5.5.2 Theoretical uncertainties

2227 It is also necessary to consider uncertainties on the theoretical predictions in the fiducial region. They  
 2228 include the choice of PDF set, the value of the strong coupling constant  $\alpha_s$ , the renormalization  
 2229 scale  $\mu_R$ , the factorization scale  $\mu_F$ , and the parton showering. The size of these uncertainties are  
 2230 measured by generating new samples with variations in a chosen parameters and comparing them

Experimental uncertainties	
Electrons	Energy resolution
	Energy scale
	Identification efficiency
	Isolation efficiency
	Reconstruction efficiency
	Trigger efficiency
Muons	Energy scale
	Identification efficiency
	Inner detector track resolution
	Muon spectrometer resolution
	Trigger efficiency
$E_T^{\text{miss}}$	Resolution
	Scale
Jets	Energy resolution
	Energy scale
	JVT cut efficiency
	$b$ -tagging efficiency
	Jets from pileup

Table 5.20: List of sources of experimental uncertainties on the reconstruction of physics objects.

$W^\pm W^\pm jj$ EWK	$e^\pm e^\pm$ % Yield	$\mu^\pm e^\pm$ % Yield	$\mu^\pm \mu^\pm$ % Yield
Jet-related Uncertainties	2.28	2.22	2.28
$b$ -tagging efficiency	1.81	1.76	1.74
Pile-up	0.48	0.97	2.42
Trigger efficiency	0.02	0.08	0.47
Lepton reconstruction/ID	1.45	1.14	1.83
MET reconstruction	0.26	0.17	0.21

Table 5.21: Impact of experimental uncertainties for the  $W^\pm W^\pm jj$  EWK processes in all channels.

$WZ$	$e^\pm e^\pm$ % Yield	$\mu^\pm e^\pm$ % Yield	$\mu^\pm \mu^\pm$ % Yield
Jet-related Uncertainties	9.58	5.03	8.45
$b$ -tagging efficiency	2.49	2.23	2.40
Pile-up	2.99	3.49	3.33
Trigger efficiency	0.03	0.09	0.43
Lepton reconstruction/ID	1.52	1.24	3.07
MET reconstruction	0.93	0.79	1.63

Table 5.22: Impact of experimental uncertainties for the  $WZ$  process in all channels.

2231 to samples using the nominal choice of the parameter.

2232 For the signal sample, internal variations on the PDF sets as well as using a different set entirely  
 2233 results in a relative uncertainty of up to 2.25% on the nominal sample. The impact from varying  $\alpha_s$  is  
 2234 very small, on the order of < 0.01%. The factorization and renormalization scales are independently  
 2235 varied between 0.5-2.0 from their nominal values of 1.0. This results in relative uncertainties on the  
 2236 prediction of up to 15%. Finally, varying the parameters in the parton showering results in up to  
 2237 8% uncertainty.

### 2238 5.5.2.1 Uncertainties from EWK-QCD interference

2239 As mentioned in Section 5.0.1,  $W^\pm W^\pm jj$  production consists of both EWK processes. The two  
 2240 production modes cannot be naively separated due to cross terms in the matrix element calculation.  
 2241 These cross terms are referred to as *interference* terms. Since the  $W^\pm W^\pm jj$  EWK production is  
 2242 the focus of the analysis, and the signal region is designed to preferentially select those events, it is  
 2243 important to measure the size of the EWK-QCD interference contributions.

2244 The interference effects are estimated using the `MadGraph` MC generator, as it has a feature that  
 2245 allows direct modelling of the interference term. This allows four samples to be generated:

2246 1. Inclusive: All available diagrams are used in the matrix element calculation

2247 2. EWK only: Only EWK diagrams ( $\mathcal{O}(\alpha_{\text{EWK}}) = 6$ ) are used

2248 3. QCD only: Only QCD diagrams ( $\mathcal{O}(\alpha_s) = 2 \otimes \mathcal{O}(\alpha_{\text{EWK}}) = 4$ ) are used

2249 4. Interference: Only the interference terms are used

2250 A minimal set of generator level cuts, listed in Table 5.23, is applied in order to avoid biasing the  
 2251 sample towards either production mode. The cross sections for each of the four channels can be  
 2252 found in Table 5.24. The size of the interference is found to be approximately 6% of the total cross  
 2253 section and is taken as a systematic uncertainty.

Generator level cuts
$\Delta\eta_{jj} < 10$
Jet $p_T > 20$ GeV
$M_{jj} > 10$ GeV

Table 5.23: The set of generator level cuts used for generating the interference samples with `MadGraph`.

Sample	$\sigma$ (fb)
Inclusive	$3.646 \pm 0.0012$
EWK only	$2.132 \pm 0.0005$
QCD only	$1.371 \pm 0.0008$
Interference	$0.227 \pm 0.0002$

Table 5.24: Cross sections for each different  $W^\pm W^\pm jj$  production mode (inclusive, EWK only, QCD only, and interference only) generated using `MadGraph`. The cross sections are calculated using a minimal set of generator level cuts from events where the  $W$  decays to a muon.

## 5.6 Results

After running the full analysis chain, the event yields in the signal region, low- $m_{jj}$  control region, and  $WZ$  control region as well as associated nuisance parameters representing the uncertainties are passed to the maximum likelihood fit. From this fit, the normalization factor for the  $WZ$  control region  $\mu_{WZ}$  and the signal strength parameter in the signal region  $\mu_{\text{obs}}$  are determined, and the predicted yields in each input bin have been shifted according to the process detailed in Section 5.4.1.

The  $WZ$  normalization factor is measured to be

$$\mu_{WZ} = 0.88^{+0.07}_{-0.07}(\text{stat})^{+0.31}_{-0.21}(\text{model sys})^{+0.22}_{-0.11}(\text{experimental sys}) \quad (5.27)$$

and is constrained primarily by the number of data events in the  $WZ$  control region. The observed signal strength of  $W^\pm W^\pm jj$  EWK production, defined in Equation 5.21, is extracted from the fit and measured with respect to the prediction of the `SHERPA v2.2.2` MC generator:

$$\mu_{\text{obs}} = 1.45^{+0.25}_{-0.24}(\text{stat})^{+0.27}_{-0.22}(\text{sys}) . \quad (5.28)$$

This corresponds to a rejection of the background-only hypothesis with a significance of  $6.9\sigma$ .

The observed number of data events are compared to the predicted signal and background yields in the signal region after applying the fit in Table 5.25. The pre-fit event yields can be found in Appendix A.2. 122 candidate events are observed compared to a prediction of 60 signal and 69 background events. The  $m_{jj}$  distributions for data and prediction are shown in Figure 5.28 after the fit, and the fitted event yields in the low- $m_{jj}$  and  $WZ$  control regions are shown in Figure 5.29.

The last ingredient necessary to measure the  $W^\pm W^\pm jj$  EWK cross section is the theory predicted cross section in the fiducial region defined in Table 5.18. `SHERPA v2.2.2` is used for the calculation, and the cross section in the total generator phase space is  $40.81 \pm 0.05$  fb, and the fiducial cross section is  $2.01 \pm 0.02$  fb. This corresponds to an acceptance factor of  $\mathcal{A} = 0.0493 \pm 0.0002$ . Uncertainties on the simulation are estimated using variations of the scale, parton shower, and PDF set. The final

	$e^+e^+$	$e^-e^-$	$\mu^+e^+$	$\mu^-e^-$	$\mu^+\mu^+$	$\mu^-\mu^-$	combined
$WZ$	$1.49 \pm 0.30$	$1.10 \pm 0.26$	$11.7 \pm 1.7$	$8.0 \pm 1.3$	$5.0 \pm 0.6$	$3.5 \pm 0.6$	$31 \pm 4$
Non-prompt	$2.2 \pm 1.3$	$1.2 \pm 0.7$	$5.7 \pm 2.8$	$4.5 \pm 1.8$	$0.57 \pm 0.06$	$0.65 \pm 0.14$	$15 \pm 6$
$e/\gamma$ conversions	$1.6 \pm 0.4$	$1.6 \pm 0.5$	$6.3 \pm 1.6$	$4.3 \pm 1.1$	—	—	$13.8 \pm 2.9$
Other prompt	$0.16 \pm 0.04$	$0.14 \pm 0.04$	$0.90 \pm 0.19$	$0.63 \pm 0.13$	$0.39 \pm 0.09$	$0.22 \pm 0.05$	$2.4 \pm 0.5$
$W^\pm W^\pm jj$ QCD	$0.35 \pm 0.13$	$0.15 \pm 0.05$	$2.9 \pm 1.0$	$1.2 \pm 0.4$	$1.8 \pm 0.6$	$0.76 \pm 0.25$	$7.2 \pm 2.4$
Expected background	$5.8 \pm 1.5$	$4.1 \pm 1.1$	$27 \pm 4$	$18.7 \pm 2.6$	$7.7 \pm 0.8$	$5.1 \pm 0.6$	$69 \pm 7$
$W^\pm W^\pm jj$ EWK	$5.6 \pm 1.0$	$2.2 \pm 0.4$	$24 \pm 5$	$9.4 \pm 1.8$	$13.5 \pm 2.5$	$5.2 \pm 1.0$	$60 \pm 11$
Data	10	4	44	28	25	11	122

Table 5.25: Table of the data and prediction event yields in the signal region after the fit. Numbers are shown for the six lepton flavor and charge channels and for all channels combined. The background estimations from the fake-factor are included in the “Non-prompt” category, and backgrounds from  $V\gamma$  production and electron charge misidentification are combined in the “ $e/\gamma$  conversions” category. Finally,  $ZZ$ ,  $VVV$ , and  $t\bar{t}V$  backgrounds are combined in the “Other prompt” category.

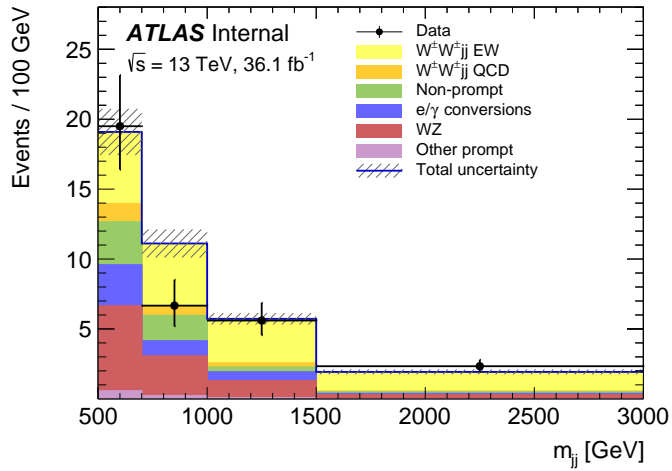


Figure 5.28: The dijet invariant mass  $m_{jj}$  distributions for data and predicted signal and background in the signal region after the fit. The shaded band represents the statistical and systematic uncertainties added in quadrature. Note that the bins have been scaled such that they represent the number of events per 100 GeV in  $m_{jj}$ . The background estimations from the fake-factor are included in the “Non-prompt” category, and backgrounds from  $V\gamma$  production and electron charge misidentification are combined in the “ $e/\gamma$  conversions” category. Finally,  $ZZ$ ,  $VVV$ , and  $t\bar{t} + V$  backgrounds are combined in the “Other prompt” category.

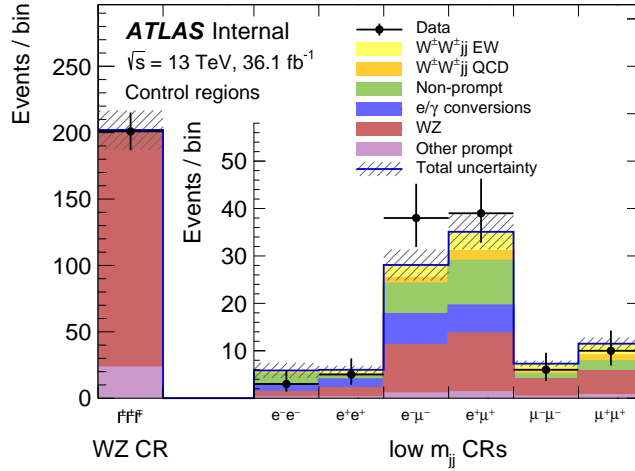


Figure 5.29: The event yields for data and predicted signal and background in the  $WZ$  and low- $m_{jj}$  control regions after the fit. The shaded band represents the statistical and systematic uncertainties added in quadrature. The background estimations from the fake-factor are included in the “Non-prompt” category, and backgrounds from  $V\gamma$  production and electron charge misidentification are combined in the “ $e/\gamma$  conversions” category. Finally,  $ZZ$ ,  $VVV$ , and  $t\bar{t}V$  backgrounds are combined in the “Other prompt” category.

prediction used in the cross section measurement including uncertainties from Section 5.5.2 is

$$\sigma_{\text{SHERPA}}^{\text{fid}} = 2.01 \pm 0.02(\text{stat}) \pm 0.29(\text{scale}) \pm 0.16(\text{parton shower}) \pm 0.05(\text{PDF}) \text{ fb}. \quad (5.29)$$

Combining this **SHERPA** prediction with the measured signal strength  $\mu_{\text{obs}}$  from Equation 5.28, the measured fiducial cross section  $\sigma_{\text{meas}}^{\text{fid}}$  can be calculated using Equation 5.25:

$$\sigma_{\text{meas}}^{\text{fid}} = 2.91^{+0.51}_{-0.47}(\text{stat}) \pm 0.12(\text{model sys}) \pm 0.24(\text{experimental sys}) \pm 0.08(\text{luminosity}) \text{ fb}. \quad (5.30)$$

A plot comparing the measured fiducial cross section to two theoretical calculations is shown in Figure 5.30. The measured value is compared to the **SHERPA** v2.2.2 prediction used to calculate  $\mu_{\text{obs}}$  as well as to **POWHEG-BOX** v2. As mentioned in Section 5.1.1, this **POWHEG** sample does not include the resonant triboson diagrams and is only used here for a visual comparison.

## 5.7 Beyond the Standard Model extensions of $W^\pm W^\pm jj$

Many so-called *Beyond the Standard Model* (BSM) theories exist that incorporate new physics with what has been experimentally observed. BSM theories often manifest as deviations from the expected SM cross sections, either due to additional decay possibilities affecting branching

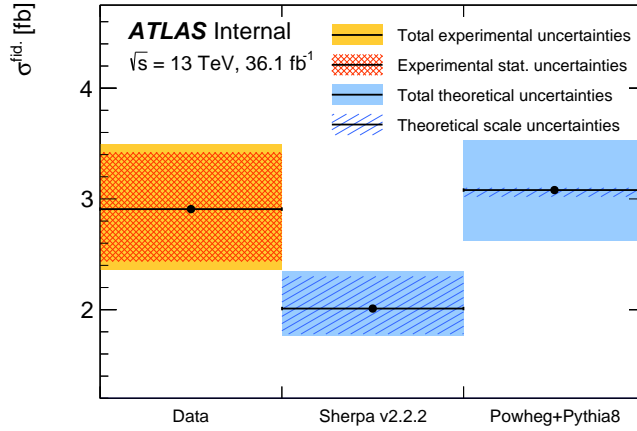


Figure 5.30: Comparison of the measured  $W^\pm W^\pm jj$  EWK fiducial cross section with theoretical calculations from **SHERPA** v2.2.2 and **POWHEG-BOX** v2. The light orange band represents the total experimental uncertainty on the measured value, and the dark orange hashed band is the statistical uncertainty. For the simulations, the light blue band represents the total theoretical uncertainty, and the dark blue hashed band are the scale uncertainties. The theory predictions do not include the interference between the EWK and QCD production.

ratios or modifications of the couplings themselves. One of the most well-known avenues for BSM involving new particles is supersymmetry [113]; however, two popular BSM extensions relevant to the  $W^\pm W^\pm jj$  process involve a doubly-charged Higgs particle ( $H^{\pm\pm}$ ) and anomalous triple and quartic gauge couplings (aTGC and aQGC, respectively)<sup>20</sup>. These two BSM theories will be touched on in the context of  $W^\pm W^\pm jj$  analyses at the LHC.

### 5.7.1 Doubly charged Higgs bosons

Same-sign  $W^\pm W^\pm$  scattering in the SM does not contain the  $s$ -channel diagram shown in Figure 5.1, as there is no SM resonance with  $\pm 2$  electric charge; however, there are BSM theories that involve expanded Higgs sectors that do include such a particle.

One popular model is the Georgi-Machacek (GM) Higgs-triplet model [114]. The GM model proposes a Higgs triplet field  $\chi$  in addition to the usual Higgs doublet  $\phi$ . After symmetry breaking, each field obtains its own VEV,  $v_\chi$  and  $v_\phi$ , and the SM VEV is made up of a combination of the

<sup>20</sup>The aQGC's are the focus in this section since the  $WWWW$  QGC vertex is accessible through  $W^\pm W^\pm$  scattering, as well as the fact that aTGC's have been studied in far greater detail due to being accessible through a larger number of processes.

2298 two:

$$v_{\text{SM}}^2 = v_\phi^2 + 8v_\chi^2 \approx (246 \text{ GeV})^2. \quad (5.31)$$

2299 As a result, the  $W^\pm$  and  $Z$  boson masses, which are determined by  $v_{\text{SM}}$  in the SM, receive con-  
 2300 tributions from both VEV's here. It is important to note that even though this fixes the value of  
 2301  $v_\phi^2 + 8v_\chi^2$ , the ratio  $v_\phi/v_\chi$  is not determined. Thus, there is no required hierarchy  $v_\chi \ll v_\phi$ , and  
 2302 the phenomenology of electroweak bosons can differ from the SM without conflicting with current  
 2303 experimental results [115]. Ultimately, the GM model predicts additional Higgs particles, including  
 2304 a doubly-charged  $H^{\pm\pm}$ .

2305 The GM model has been tested experimentally by CMS at  $\sqrt{s} = 8$  and 13 TeV for the process  
 2306  $H^{\pm\pm} \rightarrow W^\pm W^\pm$  [80, 82]. The coupling depends on the mass of the  $H^{\pm\pm}$  as well as  $s_H$ , where  $s_H^2$  is  
 2307 the fraction of the  $W$  boson mass that is generated by  $v_\chi$ . The resulting 95% confidence level (CL)  
 2308 limits on the VBS cross section are shown in Figure 5.31. Values of  $s_H$  greater than 0.18 and 0.44  
 2309 are excluded for  $m_{H^{\pm\pm}} = 200$  GeV and 1 TeV, respectively.

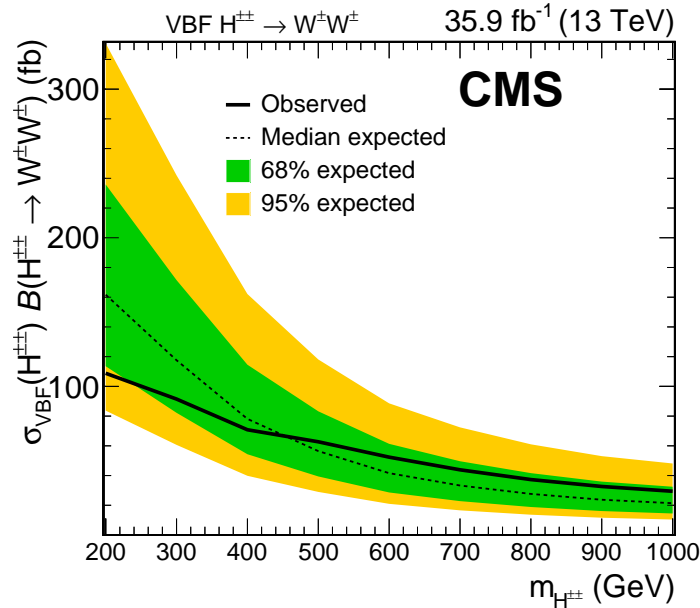


Figure 5.31: CMS observed and expected upper limits for the  $H^{\pm\pm} \rightarrow W^\pm W^\pm$  cross section at 95% CL at  $\sqrt{s} = 13$  TeV as a function of  $H^{\pm\pm}$  mass. The region above the observed limit is excluded by the measurement. Plot taken from [82].

2310 A second model accounts for neutrino masses via a *type II seesaw* mechanism, which involves  
 2311 extending the SM Higgs sector by a complex triplet of scalar fields with hypercharge  $Y = 2$  [116].

This results in a similar situation as the GM model, with two VEV's  $v_d$  and  $v_t$  corresponding to the doublet and triplet fields, respectively, and multiple Higgs bosons, including a doubly-charged  $H^{\pm\pm}$ . In this model, the relative sizes of the two VEV's is important for the context of the same-sign  $W^\pm W^\pm$  process. The observed neutrino masses are proportional to the size of  $v_t$ , which motivates a small value of the triplet VEV. However, the  $H^{\pm\pm}$  coupling to  $W^\pm$  is also proportional to  $v_t$ , and for scenarios where  $v_t \ll v_d$ , the  $H^{\pm\pm} \rightarrow W^\pm W^\pm$  decay mode is suppressed [117, 118].

This model has been studied by ATLAS at  $\sqrt{s} = 13$  TeV involving pairs of  $H^{\pm\pm}$  decaying to four  $W^\pm$  bosons [119]. The value of the triplet VEV is set to  $v_t = 0.1$  GeV, and the mass region  $H^{\pm\pm} > 200$  GeV is considered. No significant excess is seen above the SM predictions, and the 95% CL limits on the  $H^{\pm\pm} \rightarrow W^\pm W^\pm$  cross section are reproduced in Figure 5.32.

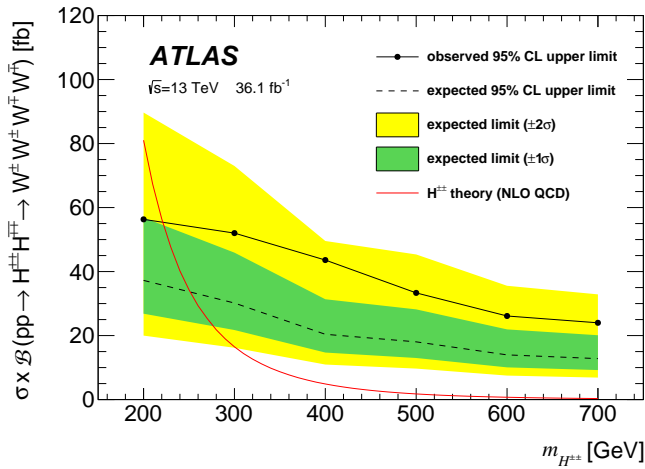


Figure 5.32: ATLAS observed and expected upper limits for the  $H^{\pm\pm}H^{\mp\mp} \rightarrow W^\pm W^\pm W^\mp W^\mp$  cross section at 95% CL at  $\sqrt{s} = 13$  TeV as a function of  $H^{\pm\pm}$  mass. The region above the observed limit is excluded by the measurement. Plot taken from [119].

### 5.7.2 Anomalous quartic couplings

In the event that new physics exists at an energy scale far above what is currently accessible at the LHC, it cannot be directly observed by the experiment; however, its effects can still appear in the interactions between known particles. In this case, the SM is simply the low-energy behavior of a larger *effective field theory* (EFT), which contains additional, higher-dimensional operators that obey the existing SM symmetries:

$$\mathcal{L}_{EFT} = \mathcal{L}_{SM} + \sum_{d>4} \sum_i \frac{\tilde{c}_i}{\Lambda^{d-4}} \mathcal{O}_i, \quad (5.32)$$

where  $\mathcal{O}_i$  are operators of dimension  $d$  with coefficients  $\tilde{c}_i$ , and  $\Lambda$  is the energy scale of the new physics. Here it can be clearly seen that as the energy scale  $\Lambda \rightarrow \infty$ , the SM behavior dominates. In the region where  $E \ll \Lambda$ , operators with high dimensionality contribute less to the total Lagrangian, and the summation may be truncated above a chosen value of  $d$ , at which point  $\mathcal{L}_{EFT}$  becomes predictive and can parametrize any heavy new physics [120].

Only operators with even dimensionality are allowed in order to conserve baryon and lepton numbers. The largest contributions to  $\mathcal{L}_{EFT}$  therefore come from operators with  $d = 6$ ; however, any of these operators which modify the QGC's also modify the TGC's. As a result, these operators are better constrained by existing analyses with greater sensitivity to TGC's. Operators with  $d = 8$  are the lowest that modify exclusively the QGC's, of which there are 18, and nine of them modify the  $WWWW$  QGC accessible through same-sign  $W^\pm W^\pm$  scattering [121, 120]:

$$\begin{aligned}\mathcal{O}_{S,0} &= [(D_\mu \Phi)^\dagger D_\nu \Phi] \times [(D^\mu \Phi)^\dagger D^\nu \Phi], \\ \mathcal{O}_{S,1} &= [(D_\mu \Phi)^\dagger D^\mu \Phi] \times [(D_\nu \Phi)^\dagger D^\nu \Phi], \\ \mathcal{O}_{M,0} &= \text{Tr}[\hat{W}_{\mu\nu} \hat{W}^{\mu\nu}] \times [(D_\beta \Phi)^\dagger D^\beta \Phi], \\ \mathcal{O}_{M,1} &= \text{Tr}[\hat{W}_{\mu\nu} \hat{W}^{\nu\beta}] \times [(D_\beta \Phi)^\dagger D^\mu \Phi], \\ \mathcal{O}_{M,6} &= [(D_\mu \Phi)^\dagger \hat{W}_{\beta\nu} \hat{W}^{\beta\nu} D^\mu \Phi], \\ \mathcal{O}_{M,7} &= [(D_\mu \Phi)^\dagger \hat{W}_{\beta\nu} \hat{W}^{\beta\mu} D^\nu \Phi], \\ \mathcal{O}_{T,0} &= \text{Tr}[\hat{W}_{\mu\nu} \hat{W}^{\mu\nu}] \times \text{Tr}[\hat{W}_{\alpha\beta} \hat{W}^{\alpha\beta}], \\ \mathcal{O}_{T,1} &= \text{Tr}[\hat{W}_{\alpha\nu} \hat{W}^{\mu\beta}] \times \text{Tr}[\hat{W}_{\mu\beta} \hat{W}^{\alpha\nu}], \\ \mathcal{O}_{T,2} &= \text{Tr}[\hat{W}_{\alpha\mu} \hat{W}^{\mu\beta}] \times \text{Tr}[\hat{W}_{\beta\nu} \hat{W}^{\nu\alpha}].\end{aligned}\tag{5.33}$$

Each operator is paired with a coupling in the Lagrangian term:  $\mathcal{L}_{S,0} = \frac{f_{S,0}}{\Lambda^4} \mathcal{O}_{S,0}$  and so on. The SM prediction can be compared to simulations generated with chosen values for the anomalous coupling constants, as shown in Figure 5.33.

Limits on the anomalous couplings generated by the  $d = 8$  operators of Equation 5.33 have been set by CMS in their  $W^\pm W^\pm jj$  analyses at  $\sqrt{s} = 8$  and 13 TeV [80, 82]. ATLAS has also set limits at  $\sqrt{s} = 8$  TeV [79] using a different parameterization of the anomalous couplings outlined in [122]. The limits set in CMS's 13 TeV analysis are reproduced in Table 5.26. The limits are obtained from fits to the  $m_{ll}$  distributions in the signal and  $WZ$  control regions, and 95% confidence intervals are calculated by varying each operator individually.

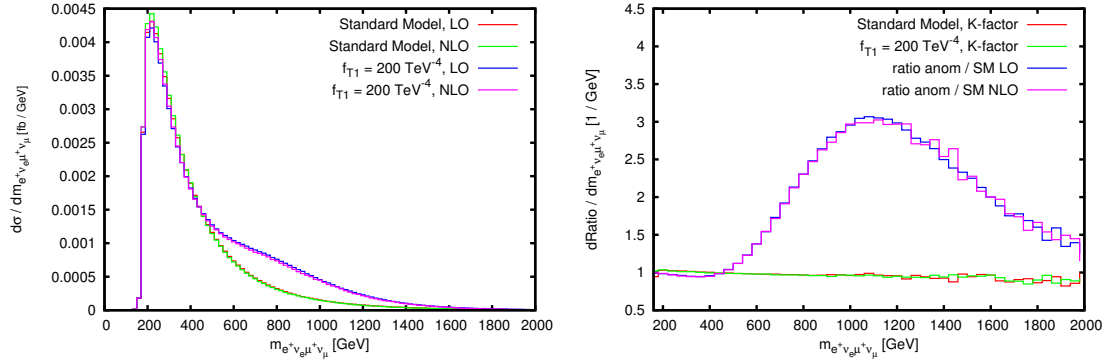


Figure 5.33: Invariant mass distributions of the  $2l2\nu$  system in  $pp \rightarrow e^+\nu_e\mu^+\nu_\mu jj$  events at LO and NLO with the VBFNLO MC generator. SM predictions are compared to those with the anomalous coupling  $\frac{f_{T,1}}{\Lambda^4} = 200 \text{ TeV}^{-4}$ . The left plot shows the differential cross section for each prediction, and the right plot shows the  $K$ -factors for the SM and anomalous coupling predictions as well as the cross section ratio between the anomalous coupling and SM predictions at LO and NLO. Plots taken from [120].

Coupling	Observed limits [ $\text{TeV}^{-4}$ ]
$f_{S,0}/\Lambda^4$	$[-7.7, 7.7]$
$f_{S,1}/\Lambda^4$	$[-21.6, 21.8]$
$f_{M,0}/\Lambda^4$	$[-6.0, 5.9]$
$f_{M,1}/\Lambda^4$	$[-8.7, 9.1]$
$f_{M,6}/\Lambda^4$	$[-11.9, 11.8]$
$f_{M,7}/\Lambda^4$	$[-13.3, 12.9]$
$f_{T,0}/\Lambda^4$	$[-0.62, 0.65]$
$f_{T,1}/\Lambda^4$	$[-0.28, 0.31]$
$f_{T,2}/\Lambda^4$	$[-0.89, 1.02]$

Table 5.26: Observed 95% confidence limits set by CMS at  $\sqrt{s} = 13$  TeV on the nine dimension-eight operators that modify the  $WWWW$  QGC listed in Equation 5.33. Table taken from [82].

## CHAPTER 6

---

# Prospects for same-sign $WW$ at the High Luminosity LHC

---

2351 On December 3, 2018, Run 2 of the LHC officially ended, and the collider was shut down to begin  
 2352 the first of two scheduled extended maintenance periods [123]. During these two long shutdowns,  
 2353 the Phase-I and Phase-II upgrades of the LHC and ATLAS will occur in order to prepare for the  
 2354 High-Luminosity LHC (HL-LHC) which is scheduled to begin operation in 2026 [124].

2355 The HL-LHC is planned to run at a center-of-mass energy of  $\sqrt{s} = 14$  TeV with an instantaneous  
 2356 luminosity of  $\mathcal{L} = 5 \times 10^{34}$  cm $^{-2}$ s $^{-1}$  with up to 200 collisions per beam-crossing. Over the course  
 2357 of operation, the HL-LHC is expected to collect a total integrated luminosity of  $\mathcal{L} = 3000$  fb $^{-1}$  by  
 2358 2035 [125].

2359 These run conditions will be much harsher than what ATLAS has experienced so far, and there  
 2360 are several upgrades planned to adapt the detector to the high luminosity environment. Most  
 2361 notably, the entire ID will be replaced with an all-silicon tracker which will extend the coverage  
 2362 from  $|\eta| \leq 2.7$  up to  $|\eta| \leq 4.0$ . This will allow for forward particle tracks to be reconstructed, which  
 2363 can in turn be matched to clusters in the calorimeters for use in electron identification or forward  
 2364 jet tagging [126].

2365 The upgraded detector, the higher beam energy, and the increased volume of data to be col-  
 2366 lected provides the opportunity to measure rare processes to a much higher precision than what  
 2367 is possible with the current LCH dataset. Same-sign  $W^\pm W^\pm jj$  production is one such process.  
 2368 With greater statistics, the accuracy of the cross section measurement can be improved over the  
 2369 13 TeV analysis detailed in Chapter 5, and it also will allow for more detailed physics studies, such  
 2370 as measuring the polarization state of the scattered  $W$  bosons. A measurement of the cross section

2371 of longitudinally polarized  $W^\pm W^\pm jj$  scattering is one of the most enticing extensions of the existing  
2372  $W^\pm W^\pm jj$  measurements due to its sensitivity to the EWSB mechanism [127], and it is expected to  
2373 be measurable for the first time at the HL-LHC. The analysis detailed in this chapter is based off of  
2374 the 2018 ATLAS HL-LHC  $W^\pm W^\pm jj$  prospects study [128] which extends upon the results of the  
2375 previous year’s study [129].

2376 **6.0.3 Analysis Overview**

2377 The experimental signature of interest is identical to the 13 TeV analysis (see Chapter 5): two  
2378 prompt leptons (either electrons or muons) with the same electric charge, missing transverse energy,  
2379 and two high energy forward jets. These jets are again required to have a large angular separation  
2380 and a high combined invariant mass to preferentially select EWK-produced  $W^\pm W^\pm jj$  events.

2381 Background processes are not expected to change with respect to the 13 TeV analysis and are  
2382 summarized here. The dominant source of prompt background comes from  $WZ+jets$  events where  
2383 both bosons decay leptonically. If the lepton from the  $Z$ -decay with opposite charge from the  $W$   
2384 falls outside of the detector acceptance or is not identified, the remaining two leptons will form a  
2385 same-sign pair, and the event may pass the signal lepton criteria. To a much lesser extent,  $ZZ+jets$   
2386 events can enter the signal region this way provided two leptons are “lost”. Other prompt sources  
2387 include  $t\bar{t}+V$  and multiple parton interactions, however both contributions are small. Overall,  
2388 prompt backgrounds are expected to contribute less in HL-LHC analyses than they do currently  
2389 due to the forward tracking in the upgraded ATLAS detector reducing the probability of leptons  
2390 falling outside the detector acceptance. Jets mis-reconstructed as leptons or leptons from hadronic  
2391 decays (such as  $t\bar{t}$  and  $W+jets$  production) comprise the non-prompt lepton background. Lastly,  
2392 events with two prompt, opposite-charge electrons can appear as a same-sign event provided one of  
2393 the electrons is mis-reconstructed and assigned the wrong charge.

2394 In this analysis, the EWK production of  $W^\pm W^\pm jj$  is studied in the context of the planned  
2395 HL-LHC run conditions and upgraded ATLAS detector. An optimized event selection (referred to  
2396 as the *optimized selection*) is also explored in an effort to gain increased signal significance over the  
2397 *default selection*. The cross section of the inclusive EWK production is measured for both the default  
2398 and optimized selections, and the extraction of the expected longitudinal scattering significance is  
2399 measured with the optimized selection.

2400 **6.1 Theoretical motivation**

2401 The motivation for studying the  $W^\pm W^\pm jj$  process as well as VBS in general has been established  
 2402 previously in Sections 2.3 and 5.0.1. Since only the longitudinally polarized vector bosons that is  
 2403 sensitive to the EWSB mechanism, a direct measurement of this cross section will be very useful for  
 2404 understanding how the Higgs unitarizes the scattering amplitude [127].

2405 **6.1.1 Experimental sensitivity to longitudinal polarization**

2406 There are three possible polarization states for a massive vector boson: two transverse (+ or -)  
 2407 and one longitudinal (0). Therefore, in a system with two  $W$  bosons, the overall polarization can be  
 2408 purely longitudinal (00), purely transverse (++, --, and +-), or mixed (+0 and -0). The three  
 2409 combinations will be referred to as *LL*, *TT*, and *LT* respectively.

2410 In order extract the longitudinal scattering component, it is necessary to find variables that can  
 2411 help distinguish the LL from the TT and LT events. Several were studied, and those with the best  
 2412 discriminating power between the different polarization states are the leading and subleading lepton  
 2413 transverse momenta as well as the azimuthal separation of the two VBS jets  $|\Delta\phi_{jj}|$ . Both leptons  
 2414 in LL events tend to be softer than the TT and LT events (see Figure 6.1), which motivates keeping  
 2415 cuts on the lepton  $p_T$  as low as possible in the event selection. In the case of the dijet separation,  
 2416 LL events prefer the tag jets to be back-to-back (see Figure 6.2). The  $|\Delta\phi_{jj}|$  distribution is chosen  
 2417 to be the discriminating variable between the polarizations, and it is ultimately passed to a binned  
 2418 likelihood fit to extract the longitudinal scattering significance.

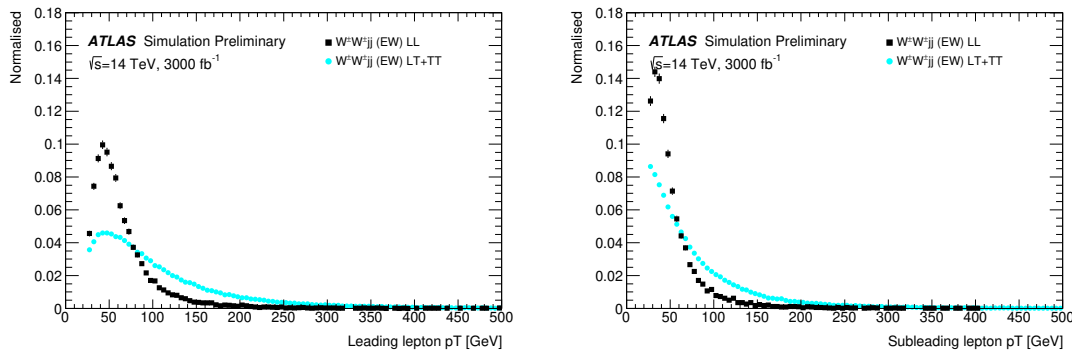


Figure 6.1: Comparison of the leading (left) and subleading (right) lepton  $p_T$  distributions for purely longitudinal (LL, black) and mixed polarization (LT+TT, cyan)  $W^\pm W^\pm jj$  events.

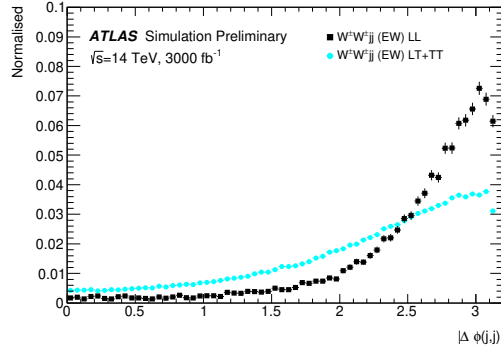


Figure 6.2: Comparison of the azimuthal dijet separation ( $|\Delta\phi_{jj}|$ ) for purely longitudinal (LL, black) and mixed polarization (LT+TT, cyan)  $W^\pm W^\pm jj$  events.

## 6.2 Monte Carlo samples

As this is a prospects study for a future collider, all signal and background processes are modeled using MC simulations. The samples are generated at the expected HL-LHC center of mass energy  $\sqrt{s} = 14$  TeV, and the event yields are scaled to the anticipated integrated luminosity of  $\mathcal{L} = 3000$   $\text{fb}^{-1}$ . The MC samples used in the analysis are generated at particle-level and have not been run through the full simulation of the ATLAS detector. Instead, smearing functions derived from a GEANT4 simulation of the upgraded ATLAS detector are used to estimate detector effects such as momentum resolution. In addition, pileup events are fully simulated. The MC samples used in this analysis are summarized in Table 6.1.

The signal sample consists of both VBS and non-VBS electroweak (EWK)  $W^\pm W^\pm jj$  production, and it is simulated with the `Madgraph5_aMC@NLO` generator using the NNPDF3.0 PDF set and interfaced with PYTHIA v8 [130] for hadronization and parton showering. To study the longitudinal polarization more directly, two additional `Madgraph5_aMC@NLO`  $W^\pm W^\pm jj$  samples are used: one containing only the longitudinal contribution (LL) and a second containing the transverse (TT) and mixed (LT) contributions.

There are many other processes that can produce the same final state as the  $W^\pm W^\pm jj$  and must also be accounted for using MC simulations.  $WZ$  events are generated using `SHERPA v2.2.0`, which includes up to one parton at NLO in the strong coupling constant and up to three additional partons at LO. Both EWK and QCD production are included in these samples.  $ZZ$  and triboson  $VVV$  ( $V = W, Z$ ) events are generated using `SHERPA v2.2.2` with up to two additional partons in the final state. For the triboson backgrounds, the bosons can decay leptonically or hadronically.  $W+jets$

Process	Generator	Comments
$W^\pm W^\pm jj$ (EWK)	Madgraph5_aMC@NLO	Signal sample
$W^\pm W^\pm jj$ (QCD)	Madgraph5_aMC@NLO	
$W^\pm W^\pm jj$ (LL)	Madgraph5_aMC@NLO	Pure longitudinal polarization sample
$W^\pm W^\pm jj$ (TT+LT)	Madgraph5_aMC@NLO	Mixed and transverse polarization sample
Diboson	SHERPA v2.2.0	$WZ$ events
	SHERPA v2.2.2	$ZZ$ events
Triboson	SHERPA v2.2.2	
$W+jets$	Madgraph5_aMC@NLO	
$Z+jets$	POWHEG-BOX v2	
$t\bar{t}$	POWHEG-BOX	
Single top	POWHEG-BOS	

Table 6.1: Summary of MC samples used in the analysis.

backgrounds are generated for electron, muon, and tau final states at LO with Madgraph5\_aMC@NLO and the NNPDF3.0 PDF set with showering from PYTHIA v8.  $Z+jets$  events are produced using POWHEG-BOX v2 and the CT10 PDF set interfaced with PYTHIA v8. Finally,  $t\bar{t}$  and single-top events are generated using POWHEG-BOX with showering from PYTHIA v6.

### 6.3 Background estimations

In this analysis, all background contributions are estimated using MC simulations. Backgrounds from electron charge misidentification and fake electrons from jets, which are traditionally estimated using data-driven techniques, are instead estimated using a set of parameterization functions applied to the MC. These functions calculate the probability that an electron is assigned the wrong charge or a jet is mis-reconstructed as an electron parameterized by the  $p_T$  and  $\eta$  of the respective electron or jet. The probabilities are derived from studies on expected electron performance with the upgraded ATLAS detector [131].

Processes involving two  $W$  or  $Z$  bosons are grouped together as *diboson* backgrounds, with the exception of  $W^\pm W^\pm jj$  events produced via QCD interactions, which are kept separate. Similarly, all backgrounds with three vector bosons are combined and labeled as *triboson*. Any  $W+jets$  or top events that pass selection and do not contain a fake electron, as well as any  $Z+jets$  events without an electron identified as having its charge misidentified are combined as *other non-prompt* backgrounds.

2457 **6.3.1 Truth-based isolation**

2458 The canonical isolation variables used in ATLAS analyses require detailed information from several  
 2459 detector subsystems including particle tracks and calorimeter responses. Since the MC samples used  
 2460 in this analysis have not been run through a full detector simulation, it is not possible to reproduce  
 2461 the official isolation variables. For truth-level analysis, this is generally not a serious concern, as  
 2462 high- $p_T$  signal leptons tend to be well isolated to begin with. However, isolation is one of the  
 2463 most powerful tools for rejecting leptons from non-prompt sources, such as top events, which are  
 2464 produced in association with additional nearby particles from  $b$  and  $c$  hadron decays. It was seen in  
 2465 the early stages of this analysis that without any sort of isolation requirement, contributions from  
 2466 top backgrounds (including single top,  $t\bar{t}$ , and  $t\bar{t} + V$ ) were more than an order of magnitude higher  
 2467 than expected.

2468 As a result, it was necessary to find one or more quantities that are comparable to the isolation  
 2469 information that is available in fully-simulated samples. Analogues to track- and calorimeter-based  
 2470 isolation are constructed by summing the momentum and energy, respectively, of stable truth parti-  
 2471 cles with  $p_T > 1$  GeV within a specified radius of each signal lepton. For the track-based isolation,  
 2472 only charged truth particles are used; both charged and neutral particles (excluding neutrinos) are  
 2473 included for the calorimeter-based isolation. Ultimately, a set of isolation cuts are chosen that are  
 2474 similar to the fixed-cut recommendations for ATLAS Run 2 analyses. The truth-based isolation  
 2475 requirements are listed in Table 6.2.

	Electron Isolation	Muon Isolation
Track-based isolation cone size	$\Delta R < 0.2$	$\Delta R < 0.3$
Track-based isolation requirement	$\sum p_T/p_T^e < 0.06$	$\sum p_T/p_T^\mu < 0.04$
Calorimeter-based isolation cone size	$\Delta R < 0.2$	$\Delta R < 0.2$
Calorimeter-based isolation requirement	$\sum E_T/p_T^e < 0.06$	$\sum E_T/p_T^\mu < 0.15$

Table 6.2: Truth-based isolation requirements for electrons and muons.

2476 With no cut on truth-based isolation, 83% of the total background consisted of top events  
 2477 (without including top contributions to the fake electron background). The isolation requirement  
 2478 reduces the top background by over 99%, and the percentage of the total background from top  
 2479 events is reduced to 2%. Additional studies on the truth-based isolation as well as full event yields  
 2480 with and without the isolation requirement can be found in Appendix B.1.

---

2481 **6.4 Object and event selection**

2482 The majority of the default object and event selections were determined in the preceeding  $W^\pm W^\pm jj$   
 2483 HL-LHC prospects study [129], which focused on the impact of the upgraded detector's forward  
 2484 tracking capabilities. Several different combinations of lepton and jet  $\eta$  ranges were tested, and the  
 2485 results are used in this study.

2486 **6.4.1 Object selection**

2487 Electrons and muons are preselected to have  $p_T > 7$  and  $6$  GeV, respectively, and lie within  $|\eta| \leq 4.0$ .  
 2488 The likelihood of a given lepton to pass the trigger and identification requirements is estimated by  
 2489 calculating an efficiency dependent on the  $p_T$  and  $\eta$  of the lepton. The leptons are also required to  
 2490 pass the isolation criteria detailed in Table 6.2. Jets that have been tagged as a fake electron by the  
 2491 functions described in Section 6.3 are treated as electrons for the purpose of the object selection and  
 2492 are subject to the same criteria. In order to be considered a signal lepton, the transverse momentum  
 2493 requirement is raised to  $p_T > 25$  GeV. The two highest  $p_T$  leptons passing this selection are chosen  
 2494 to be the leading and subleading signal leptons.

2495 Jets are clustered using the anti- $k_t$  algorithm from final-state particles (excluding muons and  
 2496 neutrinos) within a radius of  $\Delta R = 0.4$ . All jets are required to have  $p_T > 30$  GeV and lie within  
 2497  $|\eta| < 4.5$ ; in order to suppress jets from pileup interactions, jets outside of  $|\eta| \geq 3.8$  must pass an  
 2498 higher momentum cut of  $p_T > 70$  GeV. Jets overlapping a preselected electron within  $\Delta R(e, j) <$   
 2499  $0.05$  are removed in order to prevent double counting. The two highest  $p_T$  jets are defined as the  
 2500 leading and subleading tag jets.

2501 **6.4.2 Event selection**

2502 The default event selection is summarized in Table 6.3 and described here. Exactly two signal  
 2503 leptons are required with the same electric charge and separated from each other by  $\Delta R(ll) > 0.3$ .  
 2504 In order to suppress contributions from Drell-Yan backgrounds, the two signal leptons must have  
 2505 an invariant mass  $m_{ll}$  greater than  $20$  GeV. Additionally, if both signal leptons are electrons, their  
 2506 mass must be at least  $10$  GeV away from the  $Z$ -boson mass in order to reduce background from  
 2507  $Z$ -boson decays<sup>21</sup>. The event is required to have at least  $40$  GeV of missing transverse energy ( $E_T^{\text{miss}}$ )

---

<sup>21</sup>The electron charge misidentification rate in the upgraded ATLAS detector is estimated to be high enough that contributions from  $Z \rightarrow ee$  backgrounds are non-negligible.

Selection requirement	Selection value
Lepton kinematics	$p_T > 25 \text{ GeV}$ $ \eta  \leq 4.0$
Jet kinematics	$p_T > 30 \text{ GeV}$ for $ \eta  \leq 4.5$ $p_T > 70 \text{ GeV}$ for $ \eta  > 3.8$
Dilepton charge	Exactly two signal leptons with same charge
Dilepton separation	$\Delta R_{l,l} \geq 0.3$
Dilepton mass	$m_{ll} > 20 \text{ GeV}$
$Z$ boson veto	$ m_{ee} - m_Z  > 10 \text{ GeV}$ ( $ee$ -channel only)
$E_T^{\text{miss}}$	$E_T^{\text{miss}} > 40 \text{ GeV}$
Jet selection	At least two jets with $\Delta R_{l,j} > 0.3$
$b$ jet veto	$N_{\text{b-jet}} = 0$
Dijet separation	$\Delta \eta_{jj} > 2.5$
Trilepton veto	No additional preselected leptons
Dijet mass	$m_{jj} > 500 \text{ GeV}$
Lepton-jet centrality	$\zeta > 0$

Table 6.3: Summary of the signal event selection.

2508 to account for the two final-state neutrinos. Events with additional preselected leptons are vetoed,  
 2509 which greatly reduces  $WZ$  and  $ZZ$  backgrounds.

2510 Each event must have at least two jets, and both tag jets are required to not overlap with the  
 2511 signal leptons. Events with one or more  $b$ -jets are vetoed to suppress backgrounds from heavy-flavor  
 2512 decays. In order to preferentially select EWK production, the tag jets are required to have a large  
 2513 separation between them and a large invariant mass. Finally, a cut on the lepton centrality  $\zeta^{22}$ ,  
 2514 defined in Equation 6.1, further enhances the EWK  $W^\pm W^\pm jj$  signal:

$$\zeta = \min[\min(\eta_{\ell 1}, \eta_{\ell 2}) - \min(\eta_{j 1}, \eta_{j 2}), \max(\eta_{j 1}, \eta_{j 2}) - \max(\eta_{\ell 1}, \eta_{\ell 2})]. \quad (6.1)$$

2515

## 2516 6.5 Selection optimization

2517 The default event selection is optimized in order to improve the strength of the  $W^\pm W^\pm jj$  EWK  
 2518 signal. The expectation is that the increased detector acceptance from the forward tracking combined  
 2519 with an increase in center of mass energy and much higher integrated luminosity will allow tighter  
 2520 selection cuts without jeopardizing signal statistics.

---

<sup>22</sup> $\zeta$  is a measurement of whether the two signal leptons lie between the two tagging jets in  $\eta$ , as is preferred by the VBS topology.

2521 **6.5.1 Random grid search algorithm**

2522 The chosen method for optimizing the event selection is a cut-based algorithm known as the Random  
 2523 Grid Search (RGS) [132]. Consider a simple case of two variables  $x$  and  $y$  chosen to differentiate  
 2524 signal from background. In order to be considered a signal event, a given event would be required to  
 2525 pass a set of selection criteria, called a *cut point*:  $c = \{x > x_c, y > y_c\}$ . A simple method to choose  
 2526 the optimal cut point (the “best” values of the cuts  $x_c$  and  $y_c$ ) would be to construct an  $n \times m$   
 2527 rectangular grid in  $x$  and  $y$  consisting of points  $(x_0, y_0), (x_1, y_1), \dots, (x_n, y_m)$ , as in Figure 6.3a. One  
 2528 can then choose a cut point  $c_k = \{x > x_i, y > y_j\}$  that maximizes the signal significance as given  
 2529 by a chosen metric. This would be considered a *rectangular grid search*.

2530 While effective in principle, a rectangular grid search comes with two major drawbacks:

- 2531 1. The algorithm scales exponentially as the number of variables to be optimized increases, as  
 2532 this is effectively increasing the dimensionality of the grid. In the simple case of a square grid  
 2533 with  $N$  bins per variable  $v$ , the number of cut points to be evaluated grows as  $N^v$ .
- 2534 2. Signal and background samples are rarely evenly distributed over the entire grid, resulting  
 2535 in many cut points being sub-optimal, and evaluating them would be a waste of computing  
 2536 resources.

2537 To combat these limitations, the RGS algorithm constructs a grid of cut points directly from  
 2538 the signal sample itself. In the two-dimensional example, this means that the variables  $x_i$  and  $y_j$   
 2539 making up the cut point  $c_k = \{x > x_i, y > y_j\}$  take their values directly from a given signal event.  
 2540 This creates a *random grid* of cut points that has the benefit of being biased towards regions of high  
 2541 signal concentration by construction. This reduces the need for exponentially increasing numbers of  
 2542 cut points while ensuring that computing resources are not wasted in regions with few to no signal  
 2543 events. An example of a two-dimensional random grid is shown in Figure 6.3b.

2544 Once the random grid of cut points is constructed, the optimal cut point can be chosen using any  
 2545 number of metrics, such as signal to background ratio. For the purpose of the  $W^\pm W^\pm jj$  upgrade  
 2546 study, the optimal cut point is chosen to be the one that maximizes the signal significance  $Z$ , defined  
 2547 as [133]

$$Z = \sqrt{2 \left[ (s + b) \ln \left( \frac{s + b}{b_0} \right) + b_0 - s - b \right] + \frac{(b - b_0)^2}{\sigma_b^2}}, \quad (6.2)$$

2548 where  $s$  and  $b$  are the number of signal and background events, respectively,  $\sigma_b$  is the total uncertainty

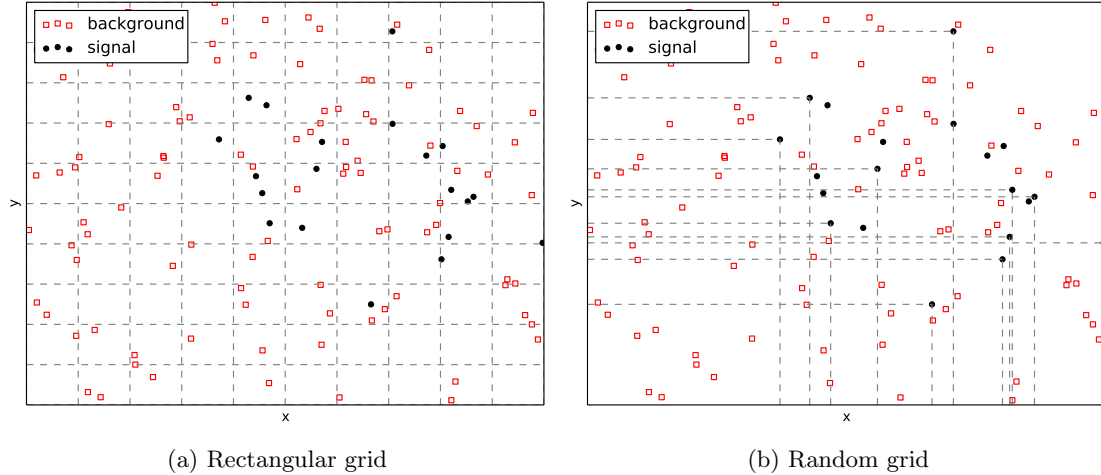


Figure 6.3: A visual representation of a two-dimensional rectangular grid (left) and a random grid (right) in variables  $x$  and  $y$ . The signal events are the black circles, and the red squares are the background events. Each intersection of gray dashed lines represents a cut point to be evaluated by the optimization.

2549 on the background, and  $b_0$  is defined as

$$b_0 = \frac{1}{2} \left( b - \sigma_b^2 + \sqrt{(b - \sigma_b^2)^2 + 4(s + b)\sigma_b^2} \right). \quad (6.3)$$

2550 In the case where the background is known precisely (i.e.  $\sigma_b = 0$ ), Equation 6.2 simplifies to

$$Z = \sqrt{2 \left( b \left[ (1 + s/b) \ln(1 + s/b) - s/b \right] \right)}, \quad (6.4)$$

which further reduces to the familiar  $Z = s/\sqrt{b}$  for the case when  $s \ll b$ .

## 2552 6.5.2 Inputs to the optimization

In order to train the RGS, signal and background samples are prepared from events passing the event selection outlined in Table 6.3 up through the  $b$ -jet veto. The signal sample is chosen to be the longitudinally polarized  $W^\pm W^\pm jj$  EWK events, and the transverse and mixed polarizations are treated as background along with  $W^\pm W^\pm jj$  events from QCD interactions and the traditional backgrounds listed in Section 6.3. Splitting the inclusive  $W^\pm W^\pm jj$  EWK events by polarization allows the optimization to favor the longitudinally polarized events as much as possible, even though they both contribute to the EWK signal.

2560 The following variables are chosen for optimization:

- Leading lepton  $p_T$

2562     • Dilepton invariant mass ( $m_{ll}$ )

2563     • Leading and subleading jet  $p_T$

2564     • Dijet invariant mass ( $m_{jj}$ )

2565     • Lepton-jet centrality ( $\zeta$ )

2566 Subleading lepton  $p_T$  is omitted as it is desirable to keep the cut value as low as possible due  
 2567 to its sensitivity to the longitudinal polarization (as discussed in Section 6.1.1); despite this, the  
 2568 leading lepton  $p_T$  is still allowed to be optimized as it can have strong background rejection power.  
 2569 Additionally, the dijet separation  $\Delta\eta_{jj}$  was included in early studies of the optimization, however it  
 2570 was dropped due to the cut value being motivated by well-studied differences between EWK- and  
 2571 QCD-produced  $W^\pm W^\pm jj$  events (as in Figure 5.6b).

2572 Two additional constraints are imposed on the optimal cut point:

2573 1. At least 1000 signal events must survive in order to prevent the optimization from being too  
 2574 aggressive and unnecessarily reducing signal statistics.

2575 2. The dijet invariant mass may only vary within a 50 GeV range of the default value (from  
 2576 450–550 GeV) due to the cut being physically motivated by the VBS event topology described  
 2577 in Section 5.0.2.

2578 Lastly, the signal significance is calculated without taking into account the uncertainty of the  
 2579 background using Equation 6.4. This is due to the fact that the statistical uncertainties of the fake  
 2580 electron and charge misidentification backgrounds are quite large, owing to poor MC statisces in a  
 2581 few of the samples. If Equation 6.2 were used instead, the optimization would cut unreasonably  
 2582 hard against these backgrounds. Since Monte Carlo statistics is not expected to be a limiting factor  
 2583 when this analysis is performed at the HL-LHC, it is more realistic to simply ignore these large  
 2584 statistical uncertainties for the purpose of the optimization.

### 2585 6.5.3 Results of the optimization

2586 Ultimately, the random grid is constructed from over 38,000 LL-polarized  $W^\pm W^\pm jj$  events in the  
 2587 six variables listed above. After applying the constraints, the optimal cut point reduces the total  
 2588 background from 9900 to 2310 while reducing the signal from 3489 to 2958. This corresponds to  
 2589 an increase in signal significance from  $Z = 33.26$  to  $Z = 52.63$  as calculated by Equation 6.4. The  
 2590 updates to the event selection are listed in Table 6.4.

2591 The large reduction in the background is primarily a result of increasing the leading and sub-  
 2592 leading jet  $p_T$  from 30 GeV to 90 GeV and 45 GeV, respectively. As can be seen in Figure 6.4,  
 2593 this increase removes a significant portion of the backgrounds from jets faking electrons and charge  
 2594 mis-ID. Additionally, the loosening of the lepton-jet centrality cut  $\zeta$  allows more signal events to  
 2595 survive the event selection (see Figure 6.5). Other changes to the event selection are minor and do  
 2596 not individually have a large impact on the signal or background yields; similar distributions for  
 2597 these variables are shown in Appendix B.2.

2598 The full event yields after optimization as well as the cross section measurement are detailed  
 2599 alongside those using the default selection in Section 6.6.

Selection requirement	Selection value
Lepton kinematics	$p_T > 28$ GeV (leading lepton only)
Jet kinematics	$p_T > 90$ GeV (leading jet) $p_T > 45$ GeV (subleading jet)
Dilepton mass	$m_{ll} > 28$ GeV
Dijet mass	$m_{jj} > 520$ GeV
Lepton-jet centrality	$\zeta > -0.5$

Table 6.4: Updates to the  $W^\pm W^\pm jj$  event selection criteria after optimization. Cuts not listed remain unchanged from the default selection in Table 6.3.

## 2600 6.6 Results

### 2601 6.6.1 Event yields

2602 After applying the full event selection, the analysis is broken down into four channels based off of  
 2603 the flavor of the signal leptons:  $\mu\mu$ ,  $ee$ ,  $\mu e$ , and  $e\mu$ . The full signal and background event yields are  
 2604 shown in Table 6.5 for each channel separately and combined using the default event selection. 3489  
 2605 EWK  $W^\pm W^\pm jj$  events are expected compared to 9900 background events. The dominant sources  
 2606 of background are jets faking electrons followed by charge misidentification and diboson processes.  
 2607 Triboson events, QCD  $W^\pm W^\pm jj$ , and other non-prompt sources make up approximately 5% of the  
 2608 total background combined.

2609 The event yields for the optimized selection detailed in Section 6.5.3 are listed in Table 6.6. After  
 2610 optimization, 2958 signal events and just 2310 background events are expected. Diboson events are  
 2611 now the primary source of background, as the optimization greatly reduces the fake and charge  
 2612 mis-ID contributions. As discussed earlier, the increase in the leading and subleading jet  $p_T$  cuts  
 2613 as well as the loosening of the centrality cut are most responsible for the changes in the signal

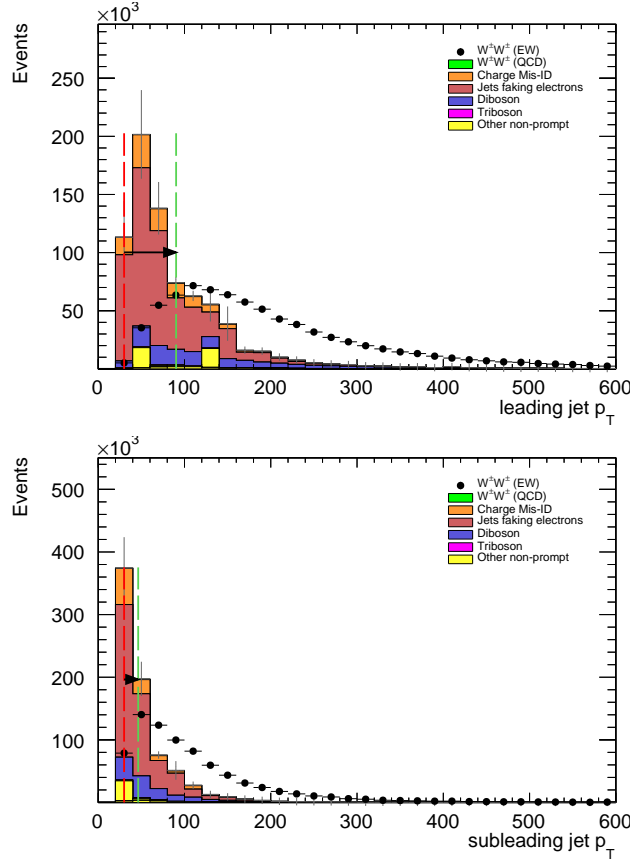


Figure 6.4: Leading (top) and subleading (bottom) jet  $p_T$  distributions. The default and optimized cuts are represented by the red and green dashed lines, respectively. The  $W^\pm W^\pm jj$  EWK signal (black points) is normalized to the same area as the sum of the backgrounds (colored histogram).

	All channels	$\mu\mu$	$ee$	$\mu e$	$e\mu$
$W^\pm W^\pm jj$ (QCD)	206.4	91.1	22.8	38.4	54.1
Charge Misidentification	2300	0.0	2100	90	160
Jets faking electrons	5000	0.0	3400	1200	340
$WZ + ZZ$	2040	500	438	423	680
Tribosons	115	47	15.4	21.6	31.2
Other non-prompt	210	110	20	60	27
Total Background	9900	750	6000	1900	1290
Signal $W^\pm W^\pm jj$ (EWK)	3489	1435	432	679	944

Table 6.5: Signal and background event yields using the default event selection for an integrated luminosity of  $\mathcal{L} = 3000 \text{ fb}^{-1}$ . Events containing a fake or charge-flipped electron are removed from their respective sources and combined into a single entry each.

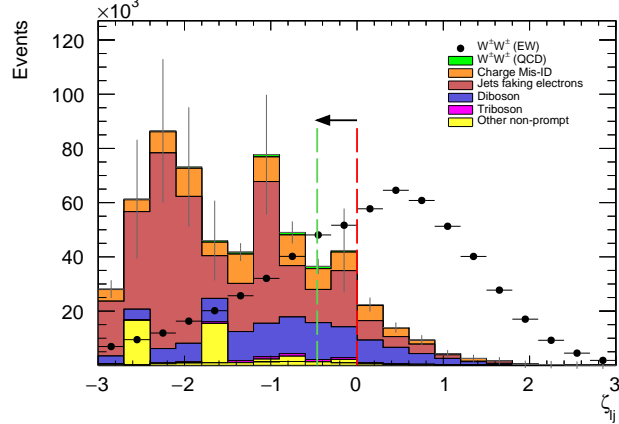


Figure 6.5: Lepton-jet centrality distribution. The default and optimized cuts are represented by the red and green dashed lines, respectively. The  $W^\pm W^\pm jj$  EWK signal (black points) is normalized to the same area as the sum of the backgrounds (colored histogram).

and background yields; distributions of these quantities using the default and the optimized event selections can be found in Figures 6.6, 6.7, and 6.8, respectively.

	All channels	$\mu\mu$	$ee$	$\mu e$	$e\mu$
$W^\pm W^\pm jj$ (QCD)	168.7	74.6	19.7	32.2	42.2
Charge Misidentification	200	0.0	11	30	160
Jets faking electrons	460	0.0	130	260	70
$WZ + ZZ$	1286	322	289	271	404
Tribosons	76	30.1	9.6	15.1	21.6
Other non-prompt	120	29	16.6	50	19
Total Background	2310	455	480	660	710
Signal $W^\pm W^\pm jj$ (EWK)	2958	1228	380	589	761

Table 6.6: Signal and background event yields using the optimized event selection for an integrated luminosity of  $\mathcal{L} = 3000 \text{ fb}^{-1}$ . Events containing a fake or charge-flipped electron are removed from their respective sources and combined into a single entry each.

It is important to note, however, that the MC sample used to estimate  $Z+\text{jets}$  events suffers from poor statistics which results in large per-event weights once scaled to  $\mathcal{L} = 3000 \text{ fb}^{-1}$ . This sample contributes heavily to the fake and charge misidentification backgrounds, and a handful of these events being cut out by the optimization is largely responsible for the dramatic reduction of the corresponding backgrounds. As a result, the optimized results presented here are likely overly optimistic. However, given proper MC statistics, it is still expected that this optimization will outperform the default selection.

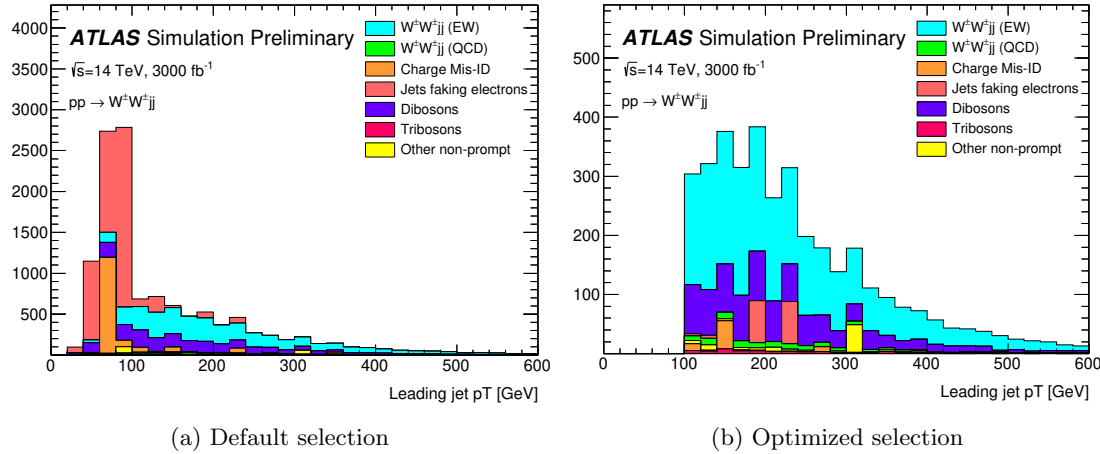


Figure 6.6:  $p_T$  distributions for the leading jet using the default (left) and optimized (right) event selections for all channels combined.

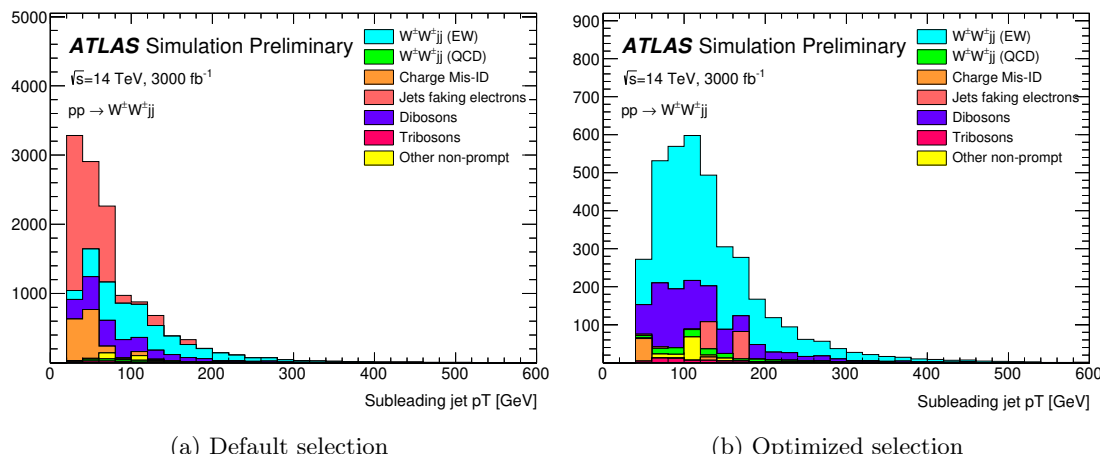


Figure 6.7:  $p_T$  distributions for the subleading jet using the default (left) and optimized (right) event selections for all channels combined.

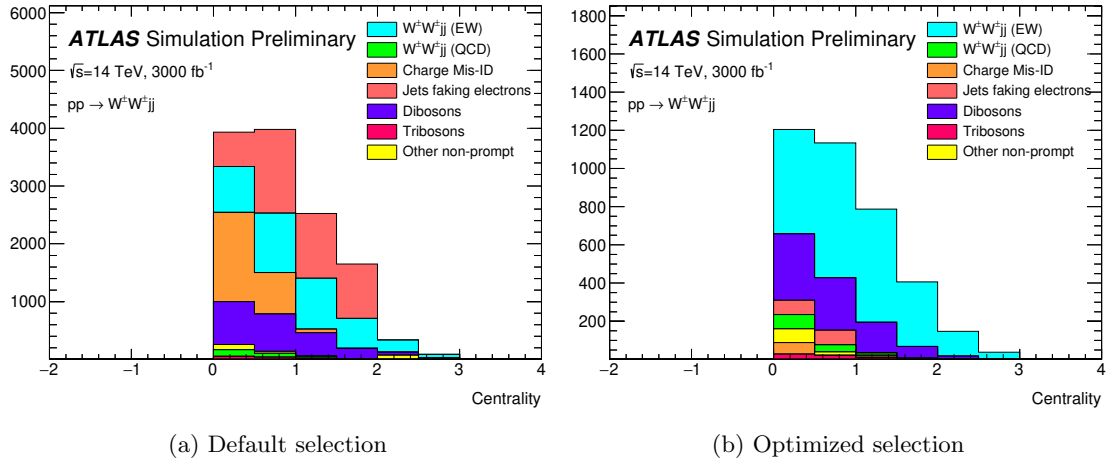


Figure 6.8:  $p_T$  distributions for lepton-jet centrality  $\zeta$  using the default (left) and optimized (right) event selections for all channels combined.

### 6.6.2 Uncertainties

The uncertainties considered for the analysis are summarized in Table 6.7. Values for experimental systematics on the trigger efficiency, lepton and jet reconstruction, and flavor tagging are taken directly from the 13 TeV analysis [81]. The rate uncertainties for the background processes are halved from the 13 TeV values according to ATLAS recommendations. The uncertainty on the fake electron estimation is also halved from the 13 TeV analysis. Finally, a conservative estimate of the uncertainty on the charge flip background is used as the electron charge mis-ID rate due to material interactions is difficult to predict at this stage.

Source	Uncertainty (%)
$W^\pm W^\pm jj$ (EWK)	3
Luminosity	1
Trigger efficiency	0.5
Lepton reconstruction and identification	1.8
Jets	2.3
Flavor tagging	1.8
Jets faking electrons	20
Charge misidentification	25
$W^\pm W^\pm jj$ (QCD)	20
Top	15
Diboson	10
Triboson	15

Table 6.7: Summary of estimated experimental and rate uncertainties.

2631 **6.6.3 Cross section measurement**

2632 The cross section is calculated using the same method as in the 13 TeV analysis, detailed in Sec-  
 2633 tion 5.4. Unlike the previous analysis, however, eight lepton channels are used here instead of six.  
 2634 The  $\mu e$  and  $e\mu$  channels remain separated in addition to the  $\mu\mu$  and  $ee$  channels, and each lepton fla-  
 2635 vor channel is further split by charge, as this increases the sensitivity of the analysis. Each channel's  
 2636  $m_{jj}$  distribution is combined in a profile likelihood fit to extract the EWK  $W^\pm W^\pm jj$  production  
 2637 cross section. Using the default event selection, the expected cross section calculated to be

$$\sigma_{W^\pm W^\pm jj}^{\text{expected}} = 16.89 \pm 0.36 \text{ (stat)} \pm 0.53 \text{ (theory)} \pm 0.84 \text{ (syst)} \text{ fb}. \quad (6.5)$$

2638 With the optimized event selection, the expected cross section is

$$\sigma_{W^\pm W^\pm jj}^{\text{expected}} = 16.94 \pm 0.36 \text{ (stat)} \pm 0.53 \text{ (theory)} \pm 0.78 \text{ (syst)} \text{ fb}. \quad (6.6)$$

2639 The optimized selection should not change the measured value of the cross section, and indeed both  
 2640 are consistent with within uncertainties. The systematic uncertainty is reduced by about 7% with  
 2641 the optimized selection. The total uncertainty on the cross section measurement is approximately  
 2642 6%, compared to the 20% uncertainty on the measured fiducial cross section of the 13 TeV analysis  
 2643 reported in Equation 5.30.

2644 Projections of each uncertainty type and the total uncertainty on the cross section as a function of  
 2645 integrated luminosity are shown in Figure 6.9. The predictions are made by scaling the event yields  
 2646 by different luminosity values and re-running the fitting procedure. As the integrated luminosity  
 2647 increases past  $\mathcal{L} > 3000 \text{ fb}^{-1}$ , the statistical uncertainty continues to reduce; however, the total  
 2648 uncertainty becomes limited by the systematics. Additionally, the total uncertainty is expected to  
 2649 reduce by less than a percent as the integrated luminosity increases past the planned  $3000 \text{ fb}^{-1}$ .  
 2650 This implies that the precision on the cross section measurement will not improve by much even  
 2651 with additional data.

2652 **6.6.4 Longitudinal scattering significance**

2653 The longitudinal scattering significance is extracted in much the same way as the cross section, this  
 2654 time using a binned likelihood fit on the  $|\Delta\phi_{jj}|$  distribution. In order to increase sensitivity, the  
 2655  $|\Delta\phi_{jj}|$  distribution is split into two bins in  $m_{jj}$ , and an additional cut on the pseudorapidity of the  
 2656 subleading lepton is applied ( $|\eta| < 2.5$ ) to reduce background contributions from fake electrons and  
 2657 charge flip. The  $|\Delta\phi_{jj}|$  distributions used in the fit are shown in Figure 6.10. Due to limited statistics

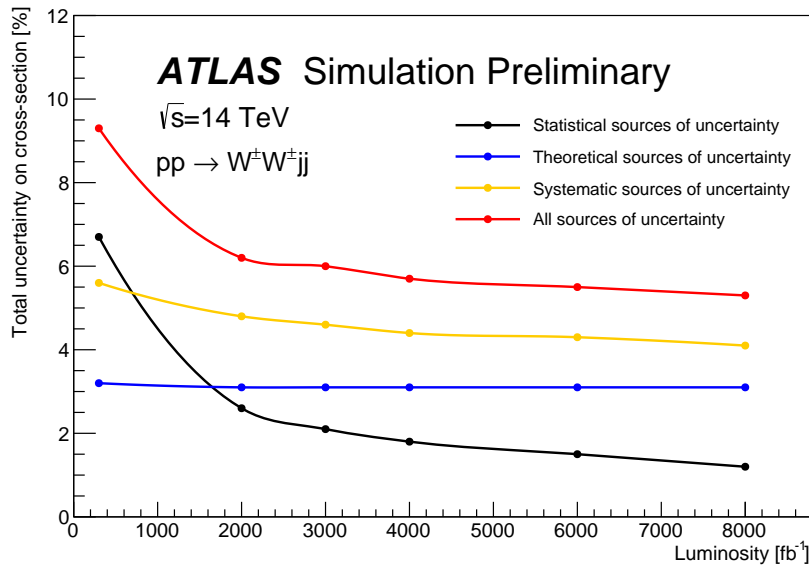


Figure 6.9: Projections of the statistical (black), theoretical (blue), systematic (yellow), and total (red) uncertainties on the measured cross section as a function of integrated luminosity using the optimized event selection.

2658 in the LL events, the four lepton flavor channels are not split by charge. The expected significance  
 2659 of the  $W_L^\pm W_L^\pm jj$  process is  $1.8\sigma$  with a precision of 47% on the measurement. Projections of the  
 2660 expected significance as a function of integrated luminosity is shown in Figure 6.11.

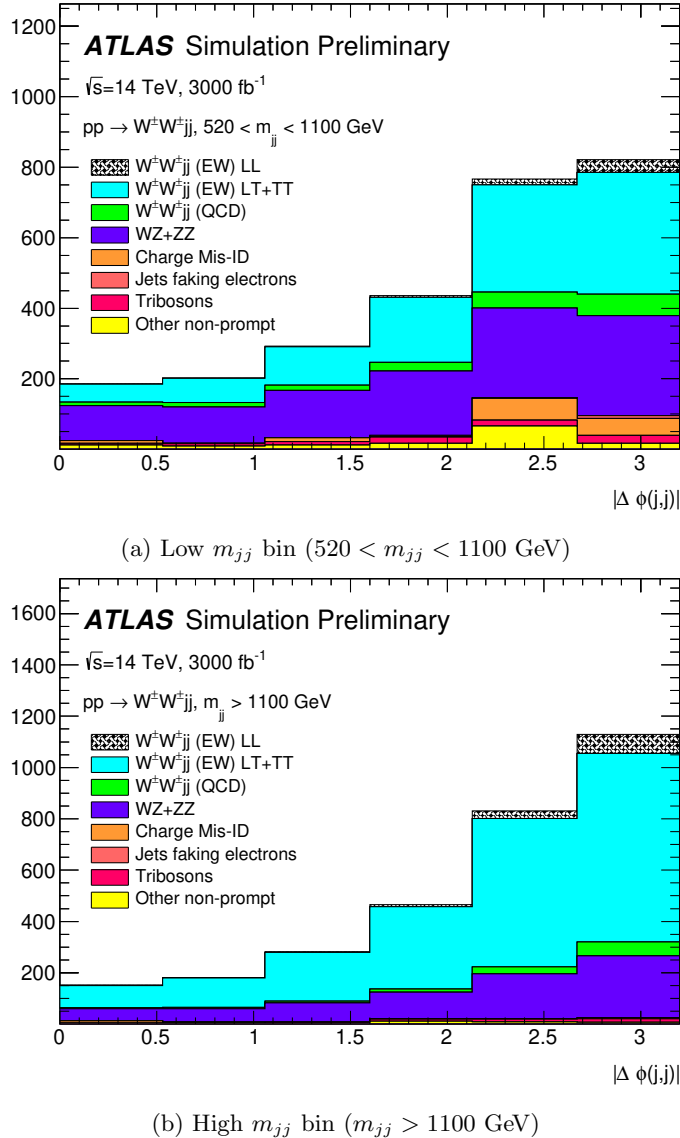


Figure 6.10: Dijet azimuthal separation ( $|\Delta\phi_{jj}|$ ) for the low  $m_{jj}$  region ( $520 < m_{jj} < 1100$  GeV, top) and the high  $m_{jj}$  region ( $m_{jj} > 1100$  GeV, bottom). The purely longitudinal (LL, gray) is plotted separately from the mixed and transverse (LT+TT, cyan) polarizations.

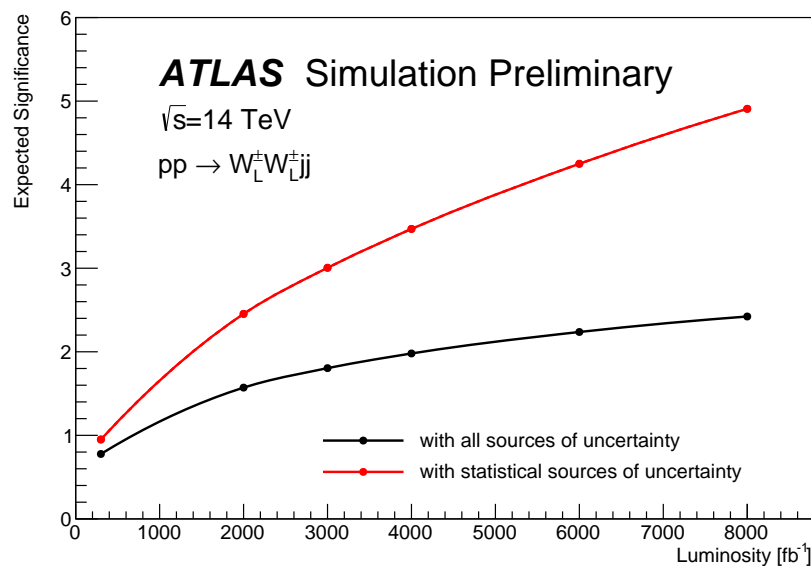


Figure 6.11: Projections of the expected longitudinal scattering significance as a function of integrated luminosity when considering all sources of uncertainties (black) or only statistical uncertainties (red).

2661

## CHAPTER 7

---

2662

## Conclusion

---

2663 Here's where you wrap it up.

2664

## APPENDIX A

2665

2666

---

# Additional material on $W^\pm W^\pm jj$ measurement at $\sqrt{s} = 13$ TeV

---

2667

## A.1 Impact of experimental uncertainty on MC background estimations

Tables A.1-A.6 contain the impact of experimental systematic uncertainties for the remaining backgrounds estimated from MC simulation. The  $W^\pm W^\pm jj$  EWK signal and  $WZ$  background systematics are listed in the main body of the document, in Tables 5.21 and 5.22, respectively. While the percentage of the contributions for some systematics appear large, the size of these backgrounds are quite small compared to the total background.

$W^\pm W^\pm jj$ QCD	$ee$ % Yield	$e\mu$ % Yield	$\mu\mu$ % Yield
Jet-related Uncertainties	3.41	3.04	2.85
b-tagging efficiency	2.56	2.48	2.48
Pile-up	4.99	0.45	0.33
Trigger efficiency	0.02	0.08	0.41
Lepton reconstruction/ID	1.62	1.19	1.89
MET reconstruction	0.41	0.22	0.34

Table A.1: Impact of experimental uncertainties for the  $W^\pm W^\pm jj$  QCD processes in all channels.

Triboson	$ee$ % Yield	$e\mu$ % Yield	$\mu\mu$ % Yield
Jet-related Uncertainties	13.09	13.39	16.85
b-tagging efficiency	2.96	3.77	4.95
Pile-up	19.37	24.66	6.87
Trigger efficiency	0.02	0.07	0.47
Lepton reconstruction/ID	1.66	1.27	2.48
MET reconstruction	0.00	0.46	0.00

Table A.2: Impact of experimental uncertainties for triboson process in all channels.

$t\bar{t}V$	$ee$ % Yield	$e\mu$ % Yield	$\mu\mu$ % Yield
Jet-related Uncertainties	17.65	11.97	14.27
b-tagging efficiency	15.02	9.04	13.83
Pile-up	8.73	10.69	4.18
Trigger efficiency	0.03	0.08	0.39
Lepton reconstruction/ID	2.57	3.27	2.66
MET reconstruction	1.75	4.16	1.62

Table A.3: Impact of experimental uncertainties for  $t\bar{t}V$  processes in all channels.

$W\gamma$	$ee$ % Yield	$e\mu$ % Yield	$\mu\mu$ % Yield
Jet-related Uncertainties	7.05	33.36	—
b-tagging efficiency	1.97	2.94	—
Pile-up	4.11	14.17	—
Trigger efficiency	0.01	0.14	—
Lepton reconstruction/ID	1.40	1.13	—
MET reconstruction	0.00	0.00	—

Table A.4: Impact of experimental uncertainties for the  $W\gamma$  process in all channels.

$Z\gamma$	$ee$ % Yield	$e\mu$ % Yield	$\mu\mu$ % Yield
Jet-related Uncertainties	16.22	370.44	—
b-tagging efficiency	1.08	3.10	—
Pile-up	12.57	11.51	—
Trigger efficiency	0.02	0.07	—
Lepton reconstruction/ID	1.26	22.01	—
MET reconstruction	0.00	0.00	—

Table A.5: Impact of experimental uncertainties for the  $Z\gamma$  process in all channels.

$ZZ$	$ee$ % Yield	$e\mu$ % Yield	$\mu\mu$ % Yield
Jet-related Uncertainties	15.71	15.76	35.18
b-tagging efficiency	2.23	2.35	2.89
Pile-up	1.22	3.20	4.58
Trigger efficiency	0.03	0.10	0.36
Lepton reconstruction/ID	3.59	3.10	5.70
MET reconstruction	4.84	3.26	3.24

Table A.6: Impact of experimental uncertainties for the  $ZZ$  process in all channels.

## 2673 A.2 Pre-fit event yields

2674 Table A.7 contains the event yields for each source and channel before the fit.

	$e^+e^+$	$e^-e^-$	$\mu^+e^+$	$\mu^-e^-$	$\mu^+\mu^+$	$\mu^-\mu^-$	combined
$WZ$	$1.9 \pm 0.6$	$1.3 \pm 0.4$	$14 \pm 4$	$8.9 \pm 2.6$	$5.5 \pm 1.6$	$3.6 \pm 1.1$	$35 \pm 10$
Non-prompt	$4.1 \pm 2.3$	$2.3 \pm 1.7$	$9 \pm 5$	$6 \pm 4$	$0.57 \pm 0.15$	$0.67 \pm 0.25$	$23 \pm 10$
$e/\gamma$ conversions	$1.74 \pm 0.29$	$1.8 \pm 0.4$	$6.1 \pm 1.6$	$3.7 \pm 0.8$	—	—	$13.4 \pm 2.5$
Other prompt	$0.17 \pm 0.05$	$0.14 \pm 0.04$	$0.90 \pm 0.19$	$0.60 \pm 0.14$	$0.36 \pm 0.10$	$0.19 \pm 0.05$	$2.4 \pm 0.5$
$W^\pm W^\pm jj$ QCD	$0.38 \pm 0.13$	$0.16 \pm 0.05$	$3.0 \pm 1.0$	$1.2 \pm 0.4$	$1.8 \pm 0.6$	$0.76 \pm 0.25$	$7.3 \pm 2.5$
Expected background	$8.2 \pm 2.4$	$5.7 \pm 1.8$	$33 \pm 7$	$21 \pm 5$	$8.2 \pm 1.8$	$5.3 \pm 1.2$	$81 \pm 14$
$W^\pm W^\pm jj$ EWK	$3.8 \pm 0.6$	$1.49 \pm 0.22$	$16.5 \pm 2.5$	$6.5 \pm 1.0$	$9.1 \pm 1.4$	$3.5 \pm 0.5$	$41 \pm 6$
Data	10	4	44	28	25	11	122

Table A.7: Table of the data and prediction event yields in the signal region before the fit. Numbers are shown for the six lepton flavor and charge channels and for all channels combined. Here the  $WZ$  background yields are normalized to the data in the  $WZ$  control region. The background estimations from the fake-factor are included in the “Non-prompt” category, and backgrounds from  $V\gamma$  production and electron charge misidentification are combined in the “ $e/\gamma$  conversions” category. Finally,  $ZZ$ ,  $VVV$ , and  $t\bar{t} + V$  backgrounds are combined in the “Other prompt” category.

2675

## APPENDIX B

2676

2677

# Additional material on $W^\pm W^\pm jj$ prospects at the HL-LHC

2678

## B.1 Truth isolation

As mentioned in Section 6.3.1, the size of the background contribution from top processes are much larger than expected when no isolation is applied. The event yields using an earlier version of the event selection with no truth-based isolation requirement are listed in Table B.1. Here, top events make up nearly 90% of the total background, and the contributions from fake and charge-flipped electrons are also large. The event yields using the same event selection with the truth-based isolation included are shown in Figure B.2. When comparing the two tables, the considerable reduction in the top background can be clearly seen.

yields by type	all channels	$\mu\mu$	$ee$	$\mu e$	$e\mu$
signal	4011	1583.2	531.7	793.1	1103.1
ww qcd	252.6	105.8	30.4	48	68.4
charge flip	2528.4	0.0	2075.4	255.1	197.8
fakes	7135.4	0.0	4675.1	1904.3	555.9
diboson	2370.4	581.2	491.8	517.9	779.6
triboson	125.5	49.1	17.8	24.6	34.1
top	90150.5	26618	15301.6	25277.9	22953.1
z+jets	241.2	0.0	0.0	0.0	241.2
w+jets	31.4	3.9	7.6	13.2	6.7
total bkg	102803.9	27354	22592	28027.8	24830.1
signal	4011	1583.2	531.7	793.1	1103.1

Table B.1: Event yields prior to applying any form of truth-based isolation criteria.

2685

2686

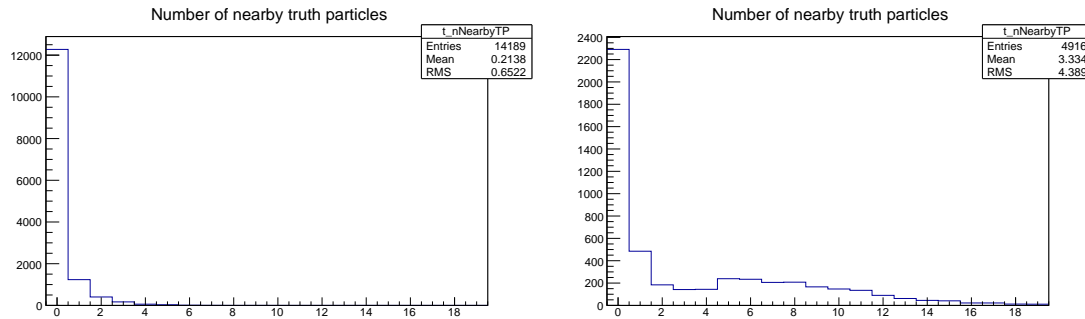
TODO: Add tables for tight vs loose working point, information on the necessity of TRUTH1++

yields by type	all channels	$\mu\mu$	$ee$	$\mu e$	$e\mu$
signal	3470.5	1427.3	428.8	675.8	938.7
ww qcd	205.8	90.8	22.7	38.3	54
charge flip	2398.3	0.0	2104.6	95.8	197.9
fakes	4309.7	0.0	3390.6	750.8	168.3
diboson	1552.4	311.3	355.6	346.8	538.7
triboson	115	46.8	15.4	21.6	31.2
top	156.9	42.3	14.8	76.6	23.3
$z+jets$	0.0	0.0	0.0	0.0	0.0
$w+jets$	0.3	0.0	0.0	0.3	0.0
total bkg	8738.1	491.3	5903.7	1329.8	1013.4
signal	3470.5	1427.3	428.8	675.8	938.7

Table B.2: Event yields after applying a test version of the truth-based isolation.

### 2687 B.1.1 TRUTH1++ derivations

2688 The ATLAS standard TRUTH1 derivations used for this analysis contain a slimmed truth particle  
 2689 container in order to reduce the file size. As a result, many of the truth particles that would be  
 2690 included in the isolation variables are missing, and the truth-based isolation will not accurately  
 2691 model the reconstruction-level isolation variables. In order to recover the performance of the truth-  
 2692 based isolation in the top MC samples (where it is most needed), a custom derivation was produced  
 2693 privately that duplicated the default TRUTH1 data structure but includes the full truth particle  
 2694 record. The reduced size of the truth particle information in the TRUTH1 derivation compared to the  
 2695 TRUTH1++ derivation is shown in Figure B.1.

Figure B.1: Number of truth particles within  $\Delta R < 0.4$  of a selected muon or electron using the ATLAS standard TRUTH1 (left) and the custom TRUTH1++ (right) derivations in  $t\bar{t}$  simulation. The complete truth record is stored in the TRUTH1++ derivation, and this is best seen in the first bin, where the lepton has no nearby truth particles.

---

2696 **B.1.2 Check of truth-based isolation**

2697 Since the isolation variables are constructed from truth particles, there is an expectation that the  
 2698 efficiency of the isolation selection will be higher than what would be seen in the full simulation.  
 2699 In order to test this, a truth-level 13 TeV  $t\bar{t}$  MC sample was run through a selection altered to  
 2700 mimic the 13 TeV  $W^\pm W^\pm jj$  measurement as closely as possible. The results were compared to the  
 2701  $t\bar{t}$  background in the 13 TeV analysis extrapolated to 14 TeV and  $3000 \text{ fb}^{-1}$ , and the truth-based  
 2702 isolation reduces the expected events by a factor of approximately 4. However, the statistics in the  
 2703 13 TeV truth-level sample are low, and it is therefore difficult to measure precisely how much the  
 2704 truth-based isolation overperforms.

2705 **B.1.3 Loose isolation working point**

2706 As another check on the truth-based isolation, a second isolation working point was constructed  
 2707 to match the official ATLAS Fixed Cut Loose isolation working point. The definition of this loose  
 2708 isolation are found in Table B.3.

2709 The primary impact of loosening the isolation is a substantial increase in the non-prompt back-  
 2710 round from top processes, and a moderate increase in the charge mis-ID and fake backgrounds.  
 2711 Backgrounds from prompt leptons only did not see major changes. As a result, the tight working  
 2712 point is chosen for the analysis. The event yields by sample and by background type using the  
 2713 loose working point are in Table B.4, and Table B.5 has the numbers using the tight working point  
 2714 (defined in Table 6.2) for comparison.

	Electron Isolation	Muon Isolation
Track-based isolation cone size	$\Delta R < 0.2$	$\Delta R < 0.3$
Track-based isolation requirement	$\sum p_T/p_T^e < 0.15$	$\sum p_T/p_T^\mu < 0.15$
Calorimeter-based isolation cone size	$\Delta R < 0.2$	$\Delta R < 0.2$
Calorimeter-based isolation requirement	$\sum E_T/p_T^e < 0.2$	$\sum E_T/p_T^\mu < 0.3$

Table B.3: Electron and muon isolation requirements for the loose working point.

run number	all channels			mm			ee			me			em		
	events	stat	sys	events	stat	sys	events	stat	sys	events	stat	sys	events	stat	sys
signal	3783.21	22.08	0.00	1524.99	15.00	0.00	484.74	7.01	0.00	740.76	9.01	0.00	1032.72	11.50	0.00
ww qcd	223.95	3.54	44.79	97.17	2.51	19.43	25.51	1.03	5.10	42.23	1.40	8.45	59.04	1.80	11.81
charge flip	3025.40	1276.74	0.00	0.00	0.00	0.00	2615.30	1267.89	0.00	197.20	87.94	0.00	212.90	121.63	0.00
fakes	5315.55	1775.87	0.00	0.00	0.00	0.00	3524.24	1694.39	0.00	1356.74	450.60	0.00	434.57	282.33	0.00
diboson	2195.61	38.10	219.58	548.72	18.54	54.87	451.27	18.29	45.14	470.61	15.71	47.07	725.01	22.95	72.50
triboson	117.43	5.90	17.62	47.55	4.32	7.13	15.83	1.94	2.37	22.11	2.18	3.32	31.94	2.76	4.80
top	554.63	218.75	83.21	229.26	135.53	34.40	61.15	38.23	9.18	232.30	167.28	34.85	31.92	6.43	4.78
z+jets	0.00	0.00	0.00	0.00	0.00	0.00	0.00	0.00	0.00	0.00	0.00	0.00	0.00	0.00	0.00
w+jets	1.21	0.87	0.00	0.00	0.00	0.00	0.00	0.00	0.00	0.00	0.00	0.00	0.02	0.00	0.00
total bkg	11433.78	2198.44	239.70	922.70	136.88	67.99	6693.30	2116.67	46.41	2322.38	488.89	59.27	1495.40	308.36	73.77
signal	3783.21	22.08	0.00	1524.99	15.00	0.00	484.74	7.01	0.00	740.76	9.01	0.00	1032.72	11.50	0.00

Table B.4: Event yields broken down by sample and by background type using the loose isolation workingpoint. Events containing a fake or charge-flipped electron are removed from their respective sample and added to the ‘fakes’ and ‘charge flip’ rows, respectively. Errors include statistical uncertainty and estimated systematic rate uncertainty based on the background process.

run number	all channels			mm			ee			me			em		
	events	stat	sys	events	stat	sys	events	stat	sys	events	stat	sys	events	stat	sys
signal	3489.49	21.23	0.00	1434.85	14.55	0.00	431.75	6.61	0.00	679.09	8.63	0.00	943.8	11.00	0.00
ww qcd	206.42	3.41	41.28	91.12	2.43	18.22	22.84	0.98	4.57	38.37	1.34	7.67	54.09	1.72	10.82
charge flip	2335.73	1163.47	0.00	0.00	0.00	0.00	2087.78	1159.5	0.00	90.37	33.32	0.00	157.58	90.02	0.00
fakes	4979.27	1756.47	0.00	0.00	0.00	0.00	3406.20	1705.03	0.00	1230.80	362.15	0.00	342.27	216.54	0.00
diboson	2039.94	36.93	204.00	499.69	18.04	49.97	437.60	14.12	43.76	422.90	14.18	42.29	679.75	25.25	67.98
triboson	115.03	5.87	17.29	46.84	4.31	7.03	15.40	1.94	2.32	21.55	2.17	3.24	31.24	2.74	4.70
top	211.74	84.14	31.76	107.96	71.12	16.20	19.58	3.76	2.93	57.21	44.47	8.58	26.99	5.40	4.05
z+jets	0.00	0.00	0.00	0.00	0.00	0.00	0.00	0.00	0.00	0.00	0.00	0.00	0.00	0.00	0.00
w+jets	0.30	0.28	0.00	0.00	0.00	0.00	0.00	0.00	0.00	0.28	0.28	0.00	0.02	0.02	0.00
total bkg	9888.43	2108.87	211.25	745.61	73.54	56.04	5898.40	2061.99	44.16	1861.48	366.67	43.95	1291.94	235.95	69.11
signal	3489.49	21.23	0.00	1434.85	14.55	0.00	431.75	6.61	0.00	679.09	8.63	0.00	943.80	11.00	0.00

Table B.5: Event yields broken down by background type using the tight isolation workingpoint. Events containing a fake or charge-flipped electron are removed from their respective sample and added to the “fakes” and “charge flip” rows, respectively. Errors include statistical uncertainty and estimated systematic rate uncertainty based on the background process.

2715 **B.2 Plots of other optimization variables**

2716 Plots of the remaining optimization variables not shown in Section 6.5.3 are presented here for  
 2717 reference. Figures B.2, B.3, and B.4 compare signal and background distributions for the default  
 2718 and optimized cuts. None of these cuts change by much in the optimized selection and their impacts  
 2719 on the overall event selection is minimal.

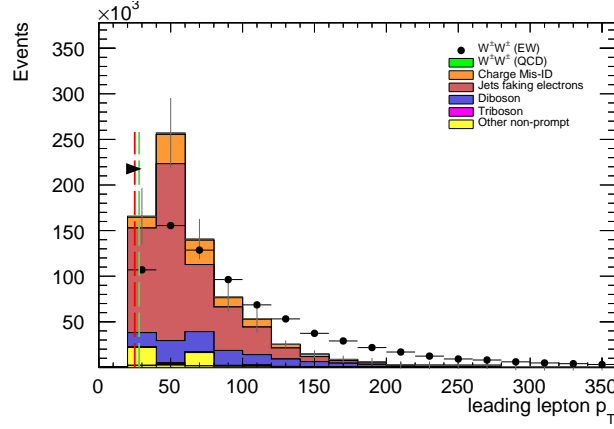


Figure B.2: Leading lepton  $p_T$  distribution. The default and optimized cuts are represented by the red and green dashed lines, respectively. The  $W^\pm W^\pm jj$  EWK signal (black points) is normalized to the same area as the sum of the backgrounds (colored histogram).

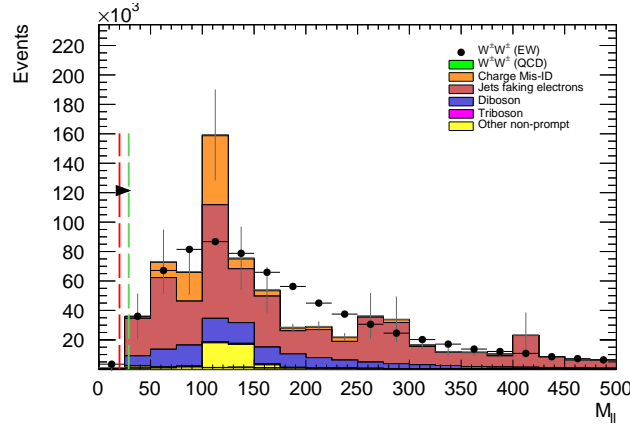


Figure B.3: Dilepton invariant mass distribution. The default and optimized cuts are represented by the red and green dashed lines, respectively. The  $W^\pm W^\pm jj$  EWK signal (black points) is normalized to the same area as the sum of the backgrounds (colored histogram).

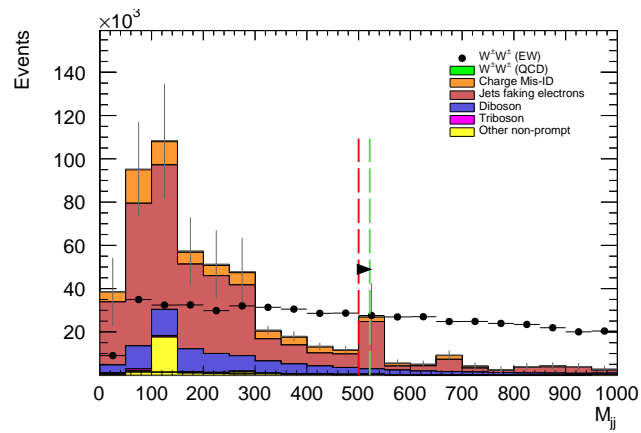


Figure B.4: Dijet invariant mass distribution. The default and optimized cuts are represented by the red and green dashed lines, respectively. The  $W^\pm W^\pm jj$  signal (black points) is normalized to the same area as the sum of the backgrounds (colored histogram).

---

## Bibliography

---

- 2721 [1] ATLAS Collaboration, M. Aaboud et al., *Measurement of the  $W^\pm Z$  boson pair-production*  
 2722 *cross section in  $pp$  collisions at  $\sqrt{s} = 13$  TeV with the ATLAS Detector*, *Phys. Lett.* **B762**  
 2723 (2016) 1–22, [arXiv:1606.04017 \[hep-ex\]](https://arxiv.org/abs/1606.04017). (document)
- 2724 [2] ATLAS Collaboration, *Summary plots from the ATLAS Standard Model physics group*,  
 2725 February, 2019.  
 2726 <https://atlas.web.cern.ch/Atlas/GROUPS/PHYSICS/CombinedSummaryPlots/SM/>. 2.1
- 2727 [3] S. Weinberg, *The Quantum Theory of Fields, Volume 1: Foundations*. Cambridge University  
 2728 Press, 1995. 2.1
- 2729 [4] M. E. Peskin and D. V. Schroeder, *An Introduction to Quantum Field Theory*.  
 2730 Addison-Wesley, 1995. 2.1
- 2731 [5] R. P. Feynman, *Mathematical formulation of the quantum theory of electromagnetic*  
 2732 *interaction*, *Phys. Rev.* **80** (1950) 440–457. 2.1
- 2733 [6] M. Y. Han and Y. Nambu, *Three-triplet model with double SU(3) symmetry*, *Phys. Rev.* **139**  
 2734 (1965) B1006–B1010. 2.1
- 2735 [7] D. J. Gross and F. Wilczek, *Asymptotically Free Gauge Theories - I*, *Phys. Rev.* **D8** (1973)  
 2736 3633–3652. 2.1
- 2737 [8] D. J. Gross and F. Wilczek, *ASYMPTOTICALLY FREE GAUGE THEORIES. 2.*, *Phys.*  
 2738 *Rev.* **D9** (1974) 980–993. 2.1
- 2739 [9] H. D. Politzer, *Reliable Perturbative Results for Strong Interactions?*, *Phys. Rev. Lett.* **30**  
 2740 (1973) 1346–1349. [,274(1973)]. 2.1
- 2741 [10] A. Salam and J. C. Ward, *Weak and Electromagnetic Interactions*, *Nuovo Cimento* **11**  
 2742 (1959) 568–577. 2.1
- 2743 [11] S. L. Glashow, *The Renormalizability of Vector Meson Interactions*, *Nucl. Phys.* **10** (1959)  
 2744 107–117. 2.1
- 2745 [12] ALEPH, DELPHI, L3, OPAL, SLD, LEP Electroweak Working Group, SLD Electroweak  
 2746 Group, SLD Heavy Flavour Group Collaboration, S. Schael et al., *Precision electroweak*

- 2747        *measurements on the  $Z$  resonance*, *Phys. Rept.* **427** (2006) 257–454, [arXiv:hep-ex/0509008](https://arxiv.org/abs/hep-ex/0509008)  
 2748 [hep-ex]. 2.1
- 2749 [13] F. Englert and R. Brout, *Broken symmetry and the mass of gauge vector mesons*, *Phys. Rev. Lett.* **13** (1964) 321–323. 2.1
- 2751 [14] P. W. Higgs, *Broken symmetries, massless particles and gauge fields*, *Physics Letters* **12** (1964) 132–133. 2.1
- 2753 [15] P. W. Higgs, *Broken symmetries and the masses of gauge bosons*, *Phys. Rev. Lett.* **13** (1964) 508–509. 2.1
- 2755 [16] ATLAS Collaboration, *Observation of a new particle in the search for the Standard Model Higgs boson with the ATLAS detector at the LHC*, *Phys. Lett. B* **716** (2012) 1,  
 2756 [arXiv:1207.7214](https://arxiv.org/abs/1207.7214) [hep-ex]. 2.1, 5.0.1
- 2758 [17] CMS Collaboration, *Observation of a new boson at a mass of 125 GeV with the CMS experiment at the LHC*, *Phys. Lett. B* **716** (2012) 30, [arXiv:1207.7235](https://arxiv.org/abs/1207.7235) [hep-ex]. 2.1, 5.0.1
- 2760 [18] UA1 Collaboration, G. Arnison et al., *Experimental Observation of Isolated Large Transverse Energy Electrons with Associated Missing Energy at  $s^{**}(1/2) = 540\text{-GeV}$* , *Phys. Lett. B* **122** (1983) 103–116. [,611(1983)]. 2.2
- 2763 [19] UA1 Collaboration, G. Arnison et al., *Experimental Observation of Lepton Pairs of Invariant Mass Around  $95\text{-GeV}/c^{**2}$  at the CERN SPS Collider*, *Phys. Lett. B* **126** (1983) 398–410.  
 2764 [,7.55(1983)]. 2.2
- 2766 [20] Particle Data Group Collaboration, K. A. Olive et al., *Review of Particle Physics*, *Chin. Phys. C* **38** (2014) 090001. 2.2, 2.2
- 2768 [21] F. Halzen and A. D. Martin, *Quarks and Leptons: An Introductory Course in Modern Particle Physics*. John Wiley & Sons, 1984. 2.2
- 2770 [22] D. R. Green, P. Meade, and M.-A. Pleier, *Multiboson interactions at the LHC*, *Rev. Mod. Phys.* **89** (2017) no. 3, 035008, [arXiv:1610.07572](https://arxiv.org/abs/1610.07572) [hep-ex]. 2.3
- 2772 [23] H.-J. He and W. B. Kilgore, *The Equivalence theorem and its radiative correction - free formulation for all  $R(xi)$  gauges*, *Phys. Rev. D* **55** (1997) 1515–1532, [arXiv:hep-ph/9609326](https://arxiv.org/abs/hep-ph/9609326)  
 2773 [hep-ph]. 2.3
- 2775 [24] B. W. Lee, C. Quigg, and H. B. Thacker, *The Strength of Weak Interactions at Very High-Energies and the Higgs Boson Mass*, *Phys. Rev. Lett.* **38** (1977) 883–885. 2.3
- 2777 [25] S. D. Rindani, *Strong gauge boson scattering at the LHC*, in *Physics at the Large Hadron Collider*, A. Datta, B. Mukhopadhyaya, A. Raychaudhuri, A. K. Gupta, C. L. Khetrapal, T. Padmanabhan, and M. Vijayan, eds., pp. 145–155. 2009. [arXiv:0910.5068](https://arxiv.org/abs/0910.5068) [hep-ph]. 2.3,  
 2778 2.3
- 2781 [26] V. D. Barger, K.-m. Cheung, T. Han, and R. J. N. Phillips, *Strong  $W^+W^+$  scattering signals at pp supercolliders*, *Phys. Rev. D* **42** (1990) 3052–3077. 2.3
- 2783 [27] G. van den Oord, *Recursion, Monte Carlo and Vector Boson Scattering at Hadron Colliders*. PhD thesis, Nijmegen U., 2012.  
 2784 [http://www.nikhef.nl/pub/services/biblio/theses\\_pdf/thesis\\_G\\_v\\_d\\_Oord.pdf](http://www.nikhef.nl/pub/services/biblio/theses_pdf/thesis_G_v_d_Oord.pdf). 2.3,  
 2786 2.3

- 2787 [28] A. Alboteanu, W. Kilian, and J. Reuter, *Resonances and Unitarity in Weak Boson*  
2788 *Scattering at the LHC*, **JHEP** **11** (2008) 010, arXiv:0806.4145 [hep-ph]. 2.7
- 2789 [29] L. R. Evans and P. Bryant, *LHC Machine*, **JINST** **3** (2008) S08001.  
2790 <https://cds.cern.ch/record/1129806>. This report is an abridged version of the LHC  
2791 Design Report (CERN-2004-003). 3.1
- 2792 [30] ATLAS Collaboration, *The ATLAS Experiment at the CERN Large Hadron Collider*, **JINST**  
2793 **3** (2008) S08003. 3.1, 3.5
- 2794 [31] ALICE Collaboration, K. Aamodt et al., *The ALICE experiment at the CERN LHC*, **JINST**  
2795 **3** (2008) S08002. 3.1
- 2796 [32] CMS Collaboration, S. Chatrchyan et al., *The CMS Experiment at the CERN LHC*, **JINST**  
2797 **3** (2008) S08004. 3.1
- 2798 [33] LHCb Collaboration, A. A. Alves, Jr. et al., *The LHCb Detector at the LHC*, **JINST** **3**  
2799 (2008) S08005. 3.1
- 2800 [34] CERN, *The accelerator complex*, February, 2019.  
2801 <https://home.cern/science/accelerators/accelerator-complex>. 3.1
- 2802 [35] E. Mobs, *The CERN accelerator complex. Complexe des accrateurs du CERN*, .  
2803 <https://cds.cern.ch/record/2197559>. General Photo. 3.1
- 2804 [36] W. Herr and B. Muratori, *Concept of luminosity*, . <https://cds.cern.ch/record/941318>.  
2805 3.1
- 2806 [37] ATLAS Collaboration, *ATLAS Experiment – Public Results: Luminosity Public Results Run*  
2807 *2*, February, 2019.  
2808 <https://twiki.cern.ch/twiki/bin/view/AtlasPublic/LuminosityPublicResultsRun2>.  
2809 3.1, 3.2, 3.3, 3.1, 3.4
- 2810 [38] ATLAS Collaboration, *ATLAS inner detector: Technical Design Report*, 1. Technical Design  
2811 Report ATLAS. CERN, Geneva, 1997. <https://cds.cern.ch/record/331063>. 3.2.1, 4
- 2812 [39] ATLAS Collaboration, *ATLAS inner detector: Technical Design Report*, 2. Technical Design  
2813 Report ATLAS. CERN, Geneva, 1997. <https://cds.cern.ch/record/331064>. 3.2.1
- 2814 [40] ATLAS Collaboration, *ATLAS Insertable B-Layer Technical Design Report*, Tech. Rep.  
2815 CERN-LHCC-2010-013. ATLAS-TDR-19, Sep, 2010.  
2816 <https://cds.cern.ch/record/1291633>. 3.2.1.1
- 2817 [41] ATLAS Collaboration, G. Darbo, *Experience on 3D Silicon Sensors for ATLAS IBL*, **JINST**  
2818 **10** (2015) no. 05, C05001, arXiv:1411.6937 [physics.ins-det]. 3.2.1.1
- 2819 [42] E. Stanecka, *ATLAS Inner Tracker Performance at the Beginning of the LHC Run 2*, Tech.  
2820 Rep. ATL-INDET-PROC-2016-002, CERN, Geneva, Apr, 2016.  
2821 <https://cds.cern.ch/record/2147407>. 3.2.1.1
- 2822 [43] ATLAS TRT Collaboration, E. Abat et al., *The ATLAS Transition Radiation Tracker*  
2823 (*TRT*) *proportional drift tube: Design and performance*, **JINST** **3** (2008) P02013. 3.2.1.3
- 2824 [44] ATLAS TRT Collaboration, E. Abat et al., *The ATLAS TRT barrel detector*, **JINST** **3**  
2825 (2008) P02014. 3.2.1.3

- 2826 [45] E. Abat et al., *The ATLAS TRT end-cap detectors*, JINST **3** (2008) P10003. 3.2.1.3
- 2827 [46] ATLAS Collaboration, *ATLAS liquid-argon calorimeter: Technical Design Report*. Technical  
2828 Design Report ATLAS. CERN, Geneva, 1996. <https://cds.cern.ch/record/331061>.  
2829 3.2.2, 3.8
- 2830 [47] ATLAS Collaboration, *ATLAS tile calorimeter: Technical Design Report*. Technical Design  
2831 Report ATLAS. CERN, Geneva, 1996. <https://cds.cern.ch/record/331062>. 3.2.2
- 2832 [48] ATLAS Collaboration, M. Marjanovic, *ATLAS Tile calorimeter calibration and monitoring*  
2833 *systems*, Tech. Rep. arXiv:1806.09156, Jun, 2018. <http://cds.cern.ch/record/2629424>. 8  
2834 pages, 21 figures, IEEE Real Time 2018 proceedings. 3.7
- 2835 [49] ATLAS Collaboration, *ATLAS muon spectrometer: Technical Design Report*. Technical  
2836 Design Report ATLAS. CERN, Geneva, 1997. <https://cds.cern.ch/record/331068>. 3.2.3
- 2837 [50] ATLAS Collaboration, M. Aaboud et al., *Performance of the ATLAS Track Reconstruction*  
2838 *Algorithms in Dense Environments in LHC Run 2*, Eur. Phys. J. **C77** (2017) no. 10, 673,  
2839 arXiv:1704.07983 [hep-ex]. 3.3.1
- 2840 [51] R. Fruhwirth, *Application of Kalman filtering to track and vertex fitting*, Nucl. Instrum.  
2841 Meth. **A262** (1987) 444–450. 3.3.1
- 2842 [52] T. Cornelissen, M. Elsing, I. Gavrilenco, W. Liebig, E. Moyse, and A. Salzburger, *The new*  
2843 *ATLAS track reconstruction (NEWT)*, J. Phys.: Conf. Ser. **119** (2008) 032014.  
2844 <http://cds.cern.ch/record/1176900>. 3.3.1
- 2845 [53] ATLAS Collaboration, *Electron reconstruction and identification in the ATLAS experiment*  
2846 *using the 2015 and 2016 LHC proton-proton collision data at  $\sqrt{s} = 13$  TeV*, Submitted to:  
2847 Eur. Phys. J. (2019) , arXiv:1902.04655 [physics.ins-det]. 3.3.2, 3.3.2, 3.9, 3.10
- 2848 [54] W. Lampl, S. Laplace, D. Lelas, P. Loch, H. Ma, S. Menke, S. Rajagopalan, D. Rousseau,  
2849 S. Snyder, and G. Unal, *Calorimeter Clustering Algorithms: Description and Performance*,  
2850 Tech. Rep. ATL-LARG-PUB-2008-002. ATL-COM-LARG-2008-003, CERN, Geneva, Apr,  
2851 2008. <https://cds.cern.ch/record/1099735>. 3.3.2
- 2852 [55] R. Frhwirth, *A Gaussian-mixture approximation of the BetheHeitler model of electron energy*  
2853 *loss by bremsstrahlung*, Computer Physics Communications **154** (2003) no. 2, 131 – 142.  
2854 <http://www.sciencedirect.com/science/article/pii/S0010465503002923>. 3.3.2
- 2855 [56] ATLAS Collaboration, G. Aad et al., *Electron and photon energy calibration with the*  
2856 *ATLAS detector using LHC Run 1 data*, Eur. Phys. J. **C74** (2014) no. 10, 3071,  
2857 arXiv:1407.5063 [hep-ex]. 3.3.2
- 2858 [57] ATLAS Collaboration, M. Aaboud et al., *Electron and photon energy calibration with the*  
2859 *ATLAS detector using 2015-2016 LHC proton-proton collision data*, Submitted to: JINST  
2860 (2018) , arXiv:1812.03848 [hep-ex]. 3.3.2
- 2861 [58] ATLAS Collaboration, *Electron efficiency measurements with the ATLAS detector using the*  
2862 *2015 LHC proton-proton collision data*, Tech. Rep. ATLAS-CONF-2016-024, CERN,  
2863 Geneva, Jun, 2016. <https://cds.cern.ch/record/2157687>. 3.3.2

- 2864 [59] ATLAS Collaboration, G. Aad et al., *Topological cell clustering in the ATLAS calorimeters*  
2865 *and its performance in LHC Run 1*, *Eur. Phys. J.* **C77** (2017) 490, [arXiv:1603.02934](https://arxiv.org/abs/1603.02934)  
2866 [[hep-ex](#)]. 3.3.2
- 2867 [60] ATLAS Collaboration, G. Aad et al., *Measurement of the muon reconstruction performance*  
2868 *of the ATLAS detector using 2011 and 2012 LHC protonproton collision data*, *Eur. Phys. J.*  
2869 **C74** (2014) no. 11, 3130, [arXiv:1407.3935](https://arxiv.org/abs/1407.3935) [[hep-ex](#)]. 3.3.3
- 2870 [61] ATLAS Collaboration, G. Aad et al., *Muon reconstruction performance of the ATLAS*  
2871 *detector in protonproton collision data at  $\sqrt{s} = 13$  TeV*, *Eur. Phys. J.* **C76** (2016) no. 5, 292,  
2872 [arXiv:1603.05598](https://arxiv.org/abs/1603.05598) [[hep-ex](#)]. 3.3.3, 3.12, 5.2.1.1
- 2873 [62] ATLAS Collaboration, *ATLAS Muon Combined Performance with the full 2016 dataset*,  
2874 March, 2017. <https://atlas.web.cern.ch/Atlas/GROUPS/PHYSICS/PLOTS/MUON-2017-001/index.html>. 3.11
- 2876 [63] ATLAS Collaboration, *ATLAS inner detector: Technical Design Report*, Vol. 1. CERN,  
2877 Geneva, 1997. <https://cds.cern.ch/record/331063>.
- 2878 [64] P. F. Åkesson, T. Atkinson, M. J. Costa, M. Elsing, S. Fleischmann, A. N. Gaponenko,  
2879 W. Liebig, E. Moyse, A. Salzburger, and M. Siebel, *ATLAS Tracking Event Data Model*,  
2880 Tech. Rep. ATL-SOFT-PUB-2006-004. ATL-COM-SOFT-2006-005.  
2881 CERN-ATL-COM-SOFT-2006-005, CERN, Geneva, Jul, 2006.  
2882 <https://cds.cern.ch/record/973401>. 4.1
- 2883 [65] P. Brückman, A. Hicheur, and S. J. Haywood, *Global chi2 approach to the Alignment of the*  
2884 *ATLAS Silicon Tracking Detectors*, Tech. Rep. ATL-INDET-PUB-2005-002.  
2885 ATL-COM-INDET-2005-004. CERN-ATL-INDET-PUB-2005-002, CERN, Geneva, 2005.  
2886 <https://cds.cern.ch/record/835270>. 4.1, 4.1
- 2887 [66] ATLAS Collaboration, *Alignment of the ATLAS Inner Detector Tracking System with 2010*  
2888 *LHC proton-proton collisions at  $\sqrt{s} = 7$  TeV*, Tech. Rep. ATLAS-CONF-2011-012, CERN,  
2889 Geneva, Mar, 2011. <https://cds.cern.ch/record/1334582>. 4, 4.1, 4.2.3, 4.16
- 2890 [67] R. Härtel and S. Bethke, *Iterative local Chi2 alignment approach for the ATLAS SCT*  
2891 *detector*. PhD thesis, Nov, 2005. <http://cds.cern.ch/record/1511044>. Presented 28 Nov  
2892 2005. 4.1
- 2893 [68] ATLAS Collaboration, P. Brückman de Renstrom, *Alignment strategy for the Inner Detector*  
2894 *of ATLAS*, . <https://cds.cern.ch/record/1047114>. 4.1
- 2895 [69] *Alignment of the ATLAS Inner Detector and its Performance in 2012*, Tech. Rep.  
2896 ATLAS-CONF-2014-047, CERN, Geneva, Jul, 2014.  
2897 <https://cds.cern.ch/record/1741021>. 4.1, 4.2.1, 4.4
- 2898 [70] J. J. Peña, *Alignment of the ATLAS Inner Detector Upgraded for the LHC Run II*, *J. Phys.*  
2899 *Conf. Ser.* **664** (2015) no. 7, 072025. 4.1
- 2900 [71] J. Alison and I. J. Kroll, *The Road to Discovery: Detector Alignment, Electron*  
2901 *Identification, Particle Misidentification, WW Physics, and the Discovery of the Higgs*  
2902 *Boson*. PhD thesis, University of Pennsylvania, Dec, 2015.  
2903 <https://cds.cern.ch/record/1536507>. Presented 08 Nov 2012. 10

- 2904 [72] *ATLAS Inner Detector Alignment Performance with February 2015 Cosmic Rays Data*,  
 2905 Tech. Rep. ATL-PHYS-PUB-2015-009, CERN, Geneva, Apr, 2015.  
 2906 <https://cds.cern.ch/record/2008724>. 4.4, 4.2
- 2907 [73] *Alignment of the ATLAS Inner Detector with the initial LHC data at  $\sqrt{s} = 13$  TeV*, Tech.  
 2908 Rep. ATL-PHYS-PUB-2015-031, CERN, Geneva, Jul, 2015.  
 2909 <https://cds.cern.ch/record/2038139>. 4.2
- 2910 [74] *Study of the mechanical stability of the ATLAS Insertable B-Layer*, Tech. Rep.  
 2911 ATL-INDET-PUB-2015-001, CERN, Geneva, Jun, 2015.  
 2912 <https://cds.cern.ch/record/2022587>. 4.2.1
- 2913 [75] *Common Framework Implementation for the Track-Based Alignment of the ATLAS  
 2914 Detector*, Tech. Rep. ATL-SOFT-PUB-2014-003, CERN, Geneva, Mar, 2014.  
 2915 <https://cds.cern.ch/record/1670354>. 4.2.1
- 2916 [76] ATLAS Collaboration, *Study of alignment-related systematic effects on the ATLAS Inner  
 2917 Detector track reconstruction*, Tech. Rep. ATLAS-CONF-2012-141, CERN, Geneva, Oct,  
 2918 2012. <https://cds.cern.ch/record/1483518>. 4.4, 4.4, 4.4.1.1, 4.4.1.2
- 2919 [77] S. Marti-Garcia, S. Camarda, T. Golling, M. Danninger, N. A. Styles, J. Wollrath, W. K.  
 2920 Di Clemente, S. Henkelmann, J. Jimenez Peña, O. Estrada Pastor, A. K. Morley, H. Oide,  
 2921 A. T. Vermeulen, P. Butti, E. Ricci, F. M. Follega, and R. Iuppa, *Studies of radial  
 2922 distortions of the ATLAS Inner Detector*, Tech. Rep. ATL-COM-INDET-2018-010, CERN,  
 2923 Geneva, Mar, 2018. <https://cds.cern.ch/record/2306724>. 4.4
- 2924 [78] ATLAS Collaboration, *Electron and photon energy calibration with the ATLAS detector  
 2925 using data collected in 2015 at  $\sqrt{s} = 13$  TeV*, Tech. Rep. ATL-PHYS-PUB-2016-015, CERN,  
 2926 Geneva, Aug, 2016. <https://cds.cern.ch/record/2203514>. 4.4.1
- 2927 [79] ATLAS Collaboration, ATLAS Collaboration, *Evidence for Electroweak Production  
 2928 of  $W^\pm W^\pm jj$  in  $pp$  Collisions at  $\sqrt{s} = 8$  TeV with the ATLAS Detector*, *Phys. Rev. Lett.*  
 2929 **113** (2014) no. 14, 141803, arXiv:1405.6241 [hep-ex]. 5, 5.7.2
- 2930 [80] CMS Collaboration, V. Khachatryan et al., *Study of vector boson scattering and search for  
 2931 new physics in events with two same-sign leptons and two jets*, *Phys. Rev. Lett.* **114** (2015)  
 2932 no. 5, 051801, arXiv:1410.6315 [hep-ex]. 5, 5.7.1, 5.7.2
- 2933 [81] ATLAS Collaboration, *Observation of electroweak production of a same-sign  $W$  boson pair in  
 2934 association with two jets in  $pp$  collisions at  $\sqrt{s} = 13$  TeV with the ATLAS detector*, Tech.  
 2935 Rep. ATLAS-CONF-2018-030, CERN, Geneva, Jul, 2018.  
 2936 <https://cds.cern.ch/record/2629411>. 5, 5.7, 6.6.2
- 2937 [82] CMS Collaboration, CMS Collaboration, *Observation of electroweak production of same-sign  
 2938  $W$  boson pairs in the two jet and two same-sign lepton final state in proton-proton collisions  
 2939 at  $\sqrt{s} = 13$  TeV*, arXiv:1709.05822 [hep-ex]. 5, 5.7.1, 5.31, 5.7.2, 5.26
- 2940 [83] C. Bittrich, W. K. Di Clemente, et al., *Support note for measurement of electroweak  
 2941  $W^\pm W^\pm jj$  production at  $\sqrt{s} = 13$  TeV*, Tech. Rep. ATL-COM-PHYS-2018-252, CERN,  
 2942 Geneva, Mar, 2018. <https://cds.cern.ch/record/2309552>. 5, 5.3.3, 2, 4, 5.4.3
- 2943 [84] J. M. Campbell and R. K. Ellis, *Higgs Constraints from Vector Boson Fusion and  
 2944 Scattering*, *JHEP* **04** (2015) 030, arXiv:1502.02990 [hep-ph]. 5.0.1, 5.0.2

- 2945 [85] M. Szleper, *The Higgs boson and the physics of WW scattering before and after Higgs*  
 2946 *discovery*, arXiv:1412.8367 [hep-ph]. 5.0.1
- 2947 [86] E. Accomando, A. Ballestrero, A. Belhouari, and E. Maina, *Isolating Vector Boson Scattering*  
 2948 *at the LHC: Gauge cancellations and the Equivalent Vector Boson Approximation vs*  
 2949 *complete calculations*, Phys. Rev. **D74** (2006) 073010, arXiv:hep-ph/0608019 [hep-ph]. 5.0.1
- 2950 [87] C. Gumpert, M. Kobel, B. Heinemann, and U. Klein, *Measurement of Electroweak Gauge*  
 2951 *Boson Scattering in the Channel  $pp \rightarrow W^\pm W^\pm jj$  with the ATLAS Detector at the Large*  
 2952 *Hadron Collider*. PhD thesis, Dec, 2014. <https://cds.cern.ch/record/2003240>.  
 2953 Presented 27 Feb 2015. 5.0.2, 5.1
- 2954 [88] B. Jager, L. Salfelder, M. Worek, and D. Zeppenfeld, *Physics opportunities for vector-boson*  
 2955 *scattering at a future 100 TeV hadron collider*, Phys. Rev. **D96** (2017) no. 7, 073008,  
 2956 arXiv:1704.04911 [hep-ph]. 5.6
- 2957 [89] J. Almond, L. Bianchini, et al., *Search for heavy neutrino,  $W_R$  and  $Z_R$  gauge bosons in*  
 2958 *events with two high- $P_T$  leptons and jets with the ATLAS detector in pp collisions at  $\sqrt{s} = 8$*   
 2959 *TeV*, Tech. Rep. ATL-COM-PHYS-2013-810, CERN, Geneva, Jun, 2013.  
 2960 <https://cds.cern.ch/record/1555805>. Supporting note for EXOT-2012-24, published as  
 2961 JHEP07 (2015) 162. 5.0.3
- 2962 [90] ATLAS Collaboration, M. Aaboud et al., *Luminosity determination in pp collisions at  $\sqrt{s} = 8$  TeV using the ATLAS detector at the LHC*, Eur. Phys. J. **C76** (2016) no. 12, 653,  
 2963 arXiv:1608.03953 [hep-ex]. 5.1
- 2964 [91] G. Avoni et al., *The new LUCID-2 detector for luminosity measurement and monitoring in*  
 2965 *ATLAS*, JINST **13** (2018) no. 07, P07017. 5.1
- 2966 [92] ATLAS Collaboration, G. Aad et al., *The ATLAS Simulation Infrastructure*, Eur. Phys. J. **C70** (2010) 823–874, arXiv:1005.4568 [physics.ins-det]. 5.1.1
- 2967 [93] S. Agostinelli et al., *GEANT4 - a simulation toolkit*, Nucl. Instrum. Meth. **A506** (2003)  
 2968 250–303. 5.1.1
- 2969 [94] T. Sjostrand, S. Mrenna, and P. Skands, *A Brief Introduction to PYTHIA 8.1*, Comput.  
 2970 Phys. Commun. **178** (2008) 852–867, arXiv:0710.3820 [hep-ph]. 5.1.1
- 2971 [95] T. Gleisberg et al., *Event generation with SHERPA 1.1*, JHEP **02** (2009) 007,  
 2972 arXiv:0811.4622 [hep-ph]. 5.1.1
- 2973 [96] S. Schumann and F. Krauss, *A parton shower algorithm based on Catani-Seymour dipole*  
 2974 *factorization*, JHEP **03** (2008) 038, arXiv:0709.1027 [hep-ph]. 5.1.1
- 2975 [97] S. Höche, F. Krauss, S. Schumann, and F. Siegert, *QCD matrix elements and truncated*  
 2976 *showers*, JHEP **05** (2009) 053, arXiv:0903.1219 [hep-ph]. 5.1.1
- 2977 [98] R. D. Ball et al., *Parton distributions for the LHC Run II*, JHEP **04** (2015) 040,  
 2978 arXiv:1410.8849 [hep-ph]. 5.1.1
- 2979 [99] S. Alioli, P. Nason, C. Oleari, and E. Re, *A general framework for implementing NLO*  
 2980 *calculations in shower Monte Carlo programs: the POWHEG BOX*, JHEP **06** (2010) 043,  
 2981 arXiv:1002.2581 [hep-ph]. 5.1.1
- 2982
- 2983

- 2984 [100] A. Ballestrero et al., *Precise predictions for same-sign W-boson scattering at the LHC*, *Eur. Phys. J.* **C78** (2018) no. 8, 671, arXiv:1803.07943 [hep-ph]. 5.1.1
- 2985
- 2986 [101] J. Alwall, R. Frederix, S. Frixione, V. Hirschi, F. Maltoni, O. Mattelaer, H. S. Shao,  
2987 T. Stelzer, P. Torrielli, and M. Zaro, *The automated computation of tree-level and*  
2988 *next-to-leading order differential cross sections, and their matching to parton shower*  
2989 *simulations*, *JHEP* **07** (2014) 079, arXiv:1405.0301 [hep-ph]. 5.1.1
- 2990 [102] H.-L. Lai, M. Guzzi, J. Huston, Z. Li, P. M. Nadolsky, J. Pumplin, and C. P. Yuan, *New*  
2991 *parton distributions for collider physics*, *Phys. Rev. D* **82** (2010) 074024, arXiv:1007.2241  
2992 [hep-ph]. 5.1.1
- 2993 [103] T. Sjostrand, S. Mrenna, and P. Skands, *PYTHIA 6.4 physics and manual*, *JHEP* **05** (2006)  
2994 026, arXiv:0603175 [hep-ph]. 5.1.1
- 2995 [104] M. Cacciari, G. P. Salam, G. Soyez, *The anti- $k_t$  jet clustering algorithm*, *JHEP* **04** (2008)  
2996 063, arXiv:0802.1189 [hep-ph]. 5.2.1.3
- 2997 [105] ATLAS Collaboration, M. Aaboud et al., *Jet energy scale measurements and their systematic*  
2998 *uncertainties in proton-proton collisions at  $\sqrt{s} = 13$  TeV with the ATLAS detector*, *Phys.*  
2999 *Rev. D* **96** (2017) no. 7, 072002, arXiv:1703.09665 [hep-ex]. 5.2.1.3
- 3000 [106] *Tagging and suppression of pileup jets with the ATLAS detector*, Tech. Rep.  
3001 ATLAS-CONF-2014-018, CERN, Geneva, May, 2014.  
3002 <http://cds.cern.ch/record/1700870>. 5.2.1.3
- 3003 [107] D. Adams, C. Anastopoulos, et al., *Recommendations of the Physics Objects and Analysis*  
3004 *Harmonisation Study Groups 2014*, Tech. Rep. ATL-PHYS-INT-2014-018, CERN, Geneva,  
3005 Jul, 2014. <https://cds.cern.ch/record/1743654>. 5.2.1.4
- 3006 [108] ATLAS Collaboration, M. Aaboud et al., *Measurement of the cross-section for producing a*  
3007 *W boson in association with a single top quark in pp collisions at  $\sqrt{s} = 13$  TeV with ATLAS*,  
3008 *JHEP* **01** (2018) 063, arXiv:1612.07231 [hep-ex]. 5.2.1.4
- 3009 [109] ATLAS Collaboration, M. Aaboud et al., *Performance of missing transverse momentum*  
3010 *reconstruction with the ATLAS detector using proton-proton collisions at  $\sqrt{s} = 13$  TeV*,  
3011 *Eur. Phys. J.* **C78** (2018) no. 11, 903, arXiv:1802.08168 [hep-ex]. 5.2.2
- 3012 [110] ATLAS Collaboration, M. Aaboud et al., *Measurements of b-jet tagging efficiency with the*  
3013 *ATLAS detector using  $t\bar{t}$  events at  $\sqrt{s} = 13$  TeV*, *JHEP* **08** (2018) 089, arXiv:1805.01845  
3014 [hep-ex]. 5.2.2
- 3015 [111] J.-F. Arguin, J. Claude, G. Gonella, B. P. Kersevan, K. Koneke, K. Lohwasser,  
3016 K. Mochizuki, M. Muskinja, C. Piaulet, and P. Sommer, *Support Note for Electron ID:*  
3017 *charge mis-identification*, Tech. Rep. ATL-COM-PHYS-2017-1014, CERN, Geneva, Jul,  
3018 2017. <https://cds.cern.ch/record/2273365>. 5.3.3
- 3019 [112] C.-H. Kom and W. J. Stirling, *Charge asymmetry in  $W + \text{jets}$  production at the LHC*, *Eur.*  
3020 *Phys. J.* **C69** (2010) 67–73, arXiv:1004.3404 [hep-ph]. 5.4
- 3021 [113] S. P. Martin, *A Supersymmetry primer*, arXiv:hep-ph/9709356 [hep-ph]. [Adv. Ser. Direct.  
3022 High Energy Phys.18,1(1998)]. 5.7

- 3023 [114] H. Georgi and M. Machacek, *Doubly charged Higgs bosons*, Nuclear Physics B **262** (1985)  
 3024 no. 3, 463 – 477.  
 3025 <http://www.sciencedirect.com/science/article/pii/0550321385903256>. 5.7.1
- 3026 [115] C. Englert, E. Re, and M. Spannowsky, *Triplet Higgs boson collider phenomenology after the*  
 3027 *LHC*, Phys. Rev. **D87** (2013) no. 9, 095014, arXiv:1302.6505 [hep-ph]. 5.7.1
- 3028 [116] J. Schechter and J. W. F. Valle, *Neutrino Masses in  $SU(2) \times U(1)$  Theories*, Phys. Rev. **D22**  
 3029 (1980) 2227. 5.7.1
- 3030 [117] P. Fileviez Perez, T. Han, G.-y. Huang, T. Li, and K. Wang, *Neutrino Masses and the CERN*  
 3031 *LHC: Testing Type II Seesaw*, Phys. Rev. **D78** (2008) 015018, arXiv:0805.3536 [hep-ph].  
 3032 5.7.1
- 3033 [118] A. Arhrib, R. Benbrik, M. Chabab, G. Moultaka, M. C. Peyranere, L. Rahili, and  
 3034 J. Ramadan, *The Higgs Potential in the Type II Seesaw Model*, Phys. Rev. **D84** (2011)  
 3035 095005, arXiv:1105.1925 [hep-ph]. 5.7.1
- 3036 [119] M. Aaboud et al., *Search for doubly charged scalar bosons decaying into same-sign W boson*  
 3037 *pairs with the ATLAS detector*, The European Physical Journal C **79** (Jan, 2019) 58.  
 3038 <https://doi.org/10.1140/epjc/s10052-018-6500-y>. 5.7.1, 5.32
- 3039 [120] C. Degrande, O. Éboli, et al., *Monte Carlo tools for studies of non-standard electroweak*  
 3040 *gauge boson interactions in multi-boson processes: A Snowmass White Paper*, in *Proceedings,*  
 3041 *2013 Community Summer Study on the Future of U.S. Particle Physics: Snowmass on the*  
 3042 *Mississippi (CSS2013): Minneapolis, MN, USA, July 29-August 6, 2013.* 2013.  
 3043 arXiv:1309.7890 [hep-ph]. 5.7.2, 5.33
- 3044 [121] O. J. P. Éboli, M. C. Gonzalez-Garcia, and J. K. Mizukoshi,  $pp \rightarrow jj e^\pm \mu^\pm \nu\nu$  and  $jj e^\pm \mu^\pm \nu\nu$   
 3045 at  $\mathcal{O}(\alpha_{em}^6)$  and  $\mathcal{O}(\alpha_{em}^4 \alpha_s^2)$  for the study of the quartic electroweak gauge boson vertex at  
 3046 *CERN LHC*, Phys. Rev. **D74** (2006) 073005, arXiv:hep-ph/0606118 [hep-ph]. 5.7.2
- 3047 [122] J. Reuter, W. Kilian, and M. Sekulla, *Simplified Models for New Physics in Vector Boson*  
 3048 *Scattering - Input for Snowmass 2013*, arXiv:1307.8170 [hep-ph]. 5.7.2
- 3049 [123] R. Steerenberg, *LHC Report: Another run is over and LS2 has just begun...*,  
 3050 [https://home.cern/news/news/accelerators/](https://home.cern/news/news/accelerators/lhc-report-another-run-over-and-ls2-has-just-begun)  
 3051 [lhc-report-another-run-over-and-ls2-has-just-begun](https://home.cern/news/news/accelerators/lhc-report-another-run-over-and-ls2-has-just-begun), 2018. Accessed: 2018-12-14. 6
- 3052 [124] *Letter of Intent for the Phase-I Upgrade of the ATLAS Experiment*, Tech. Rep.  
 3053 CERN-LHCC-2011-012. LHCC-I-020, CERN, Geneva, Nov, 2011.  
 3054 <http://cds.cern.ch/record/1402470>. 6
- 3055 [125] G. Apollinari, I. Bjar Alonso, O. Brning, M. Lamont, and L. Rossi, *High-Luminosity Large*  
 3056 *Hadron Collider (HL-LHC): Preliminary Design Report*. CERN Yellow Reports:  
 3057 Monographs. CERN, Geneva, 2015. <https://cds.cern.ch/record/2116337>. 6
- 3058 [126] ATLAS Collaboration, ATLAS Collaboration, *ATLAS Phase-II Upgrade Scoping Document*,  
 3059 Cern-lhcc-2015-020, Geneva, Sep, 2015. <http://cds.cern.ch/record/2055248>. 6
- 3060 [127] D. Espriu and B. Yencho, *Longitudinal WW scattering in light of the “Higgs boson”*  
 3061 *discovery*, Phys. Rev. D **87** (2013) 055017, arXiv:1212.4158 [hep-ph]. 6, 6.1

- 3062 [128] ATLAS Collaboration, *Prospects for the measurement of the  $W^\pm W^\pm$  scattering cross section*  
3063 *and extraction of the longitudinal scattering component in  $pp$  collisions at the*  
3064 *High-Luminosity LHC with the ATLAS experiment*, Tech. Rep. ATL-PHYS-PUB-2018-052,  
3065 CERN, Geneva, Dec, 2018. <http://cds.cern.ch/record/2652447>. 6
- 3066 [129] ATLAS Collaboration, *Studies on the impact of an extended Inner Detector tracker and a*  
3067 *forward muon tagger on  $W^\pm W^\pm$  scattering in  $pp$  collisions at the High-Luminosity LHC*  
3068 *with the ATLAS experiment*, Tech. Rep. ATL-PHYS-PUB-2017-023, CERN, Geneva, Dec,  
3069 2017. <https://cds.cern.ch/record/2298958>. 6, 6.4
- 3070 [130] T. Sjöstrand, S. Ask, J. R. Christiansen, R. Corke, N. Desai, P. Ilten, S. Mrenna, S. Prestel,  
3071 C. O. Rasmussen, and P. Z. Skands, *An Introduction to PYTHIA 8.2*, *Comput. Phys.*  
3072 *Commun.* **191** (2015) 159–177, <arXiv:1410.3012> [hep-ph]. 6.2
- 3073 [131] ATLAS Collaboration, *Expected performance for an upgraded ATLAS detector at*  
3074 *High-Luminosity LHC*, Tech. Rep. ATL-PHYS-PUB-2016-026, CERN, Geneva, Oct, 2016.  
3075 <http://cds.cern.ch/record/2223839>. 6.3
- 3076 [132] P. C. Bhat, H. B. Prosper, S. Sekmen, and C. Stewart, *Optimizing Event Selection with the*  
3077 *Random Grid Search*, *Comput. Phys. Commun.* **228** (2018) 245–257, <arXiv:1706.09907>  
3078 [hep-ph]. 6.5.1
- 3079 [133] G. Cowan, K. Cranmer, E. Gross, and O. Vitells, *Asymptotic formulae for likelihood-based*  
3080 *tests of new physics*, *Eur. Phys. J.* **C71** (2011) 1554, <arXiv:1007.1727> [physics.data-an].  
3081 [Erratum: *Eur. Phys. J.* C73,2501(2013)]. 6.5.1